

This electronic thesis or dissertation has been downloaded from the King's Research Portal at <https://kclpure.kcl.ac.uk/portal/>



Dynamics from statics: A conceptual reformulation of Green's function perturbation theories

Backhouse, Ollie

*Awarding institution:*  
King's College London

The copyright of this thesis rests with the author and no quotation from it or information derived from it may be published without proper acknowledgement.

#### END USER LICENCE AGREEMENT



**Unless another licence is stated on the immediately following page** this work is licensed

under a Creative Commons Attribution-NonCommercial-NoDerivatives 4.0 International

licence. <https://creativecommons.org/licenses/by-nc-nd/4.0/>

You are free to copy, distribute and transmit the work

Under the following conditions:

- Attribution: You must attribute the work in the manner specified by the author (but not in any way that suggests that they endorse you or your use of the work).
- Non Commercial: You may not use this work for commercial purposes.
- No Derivative Works - You may not alter, transform, or build upon this work.

Any of these conditions can be waived if you receive permission from the author. Your fair dealings and other rights are in no way affected by the above.

#### Take down policy

If you believe that this document breaches copyright please contact [librarypure@kcl.ac.uk](mailto:librarypure@kcl.ac.uk) providing details, and we will remove access to the work immediately and investigate your claim.

---

**Dynamics from statics:**  
**A conceptual reformulation of Green's  
function perturbation theories**

---

*Author:*

**Oliver James Backhouse**

*Supervisor:*

**Dr George H. Booth**

A thesis presented for the degree of

*Doctor of Philosophy*

Department of Physics

Faculty of Natural, Mathematical & Engineering Sciences

KING'S COLLEGE LONDON

**Version**

This document was generated using <https://github.com/obackhouse/thesis> on commit 897ede of branch master at 12:24 on Monday 17<sup>th</sup> April, 2023.

# Dynamics from statics:

## A conceptual reformulation of Green's function perturbation theories

### Abstract

The use of the single-particle Green's function in quantum chemistry has become widespread as a result of its correspondence with the spectral function, allowing the study of a wide range of materials. The spectral function is a quantity central to spectroscopic investigations and characterisations, and there exists many paradigms and methods to probe it. In this thesis, an approach to finding the Green's function will be presented. This method, based on the block Lanczos algorithm, has been investigated previously in the literature, however a new formulation that permits the access of 'full-frequency' dynamic Green's functions and self-energies using only a set of static expectation values is presented. These expectation values, taking the form of the spectral moments of the particular function, are conserved through the familiar Lanczos recursion in order to physically inform the solution, and allow a systematic improvability with respect to the number of moments conserved.

The reformulations of the block Lanczos algorithm will be presented, along with necessary considerations and a discussion of their application to the Dyson equation. Following this, a number of specific examples of their use for efficiently performing existing quantum chemical methods will be presented, based on many-body perturbation theory and coupled cluster theories. These discussions will include deriving and outlining the working equations, discussing any algorithmic considerations important to their implementation, and comparisons to existing solvers with respect to the existence of multiple solutions.

The performance of these methods will then be benchmarked using a number of datasets in order to quantify the change in accuracy of the methods with the number of spectral moments conserved. This data will be used to show that few spectral moments must be conserved in order to faithfully represent the spectral function within the regimes of interest, such as the frontier excitations close to the Fermi energy defining the ionisation potential and electron affinity of the particular material. Furthermore, in the case of self-consistent many-body perturbation theory, similar discussions will be used to show that an increase in the resolution of the dynamics via additional moments is actually a detriment to the accuracy of the resulting excitations, leading to an accurate and efficient approach. This approach will be applied to the important drug molecule artemisinin as an example of its applicability in elucidating physical properties, and early investigations into the suitability of the method for extended solids will be presented.





## Acknowledgement

First and foremost I would like to express thanks to my supervisor, Dr George Booth, for the opportunity to conduct my PhD under his guidance. George's comprehensive expertise in the field, combined with his supportive and attentive approach to supervision, has made for an extremely productive and enjoyable environment for research. The Booth group at King's has offered diverse collaboration that has been indispensable to my studies, and in particular I would like to thank Max and Charlie for their tutorship and guidance, as well as the many other members of the group. I also extend my gratitude to Alejandro for his technical and computing advice. Many calculations performed during this work made use of computational resources granted by the UK Materials and Molecular Modelling Hub, along with the embedded CSE programme of the ARCHER2 UK National Supercomputing Service, both of which have been indispensable. Additionally, I am very grateful to Dr Crespo-Otero and Prof. Loos for agreeing to examine my thesis.

I would like to thank my family, particularly my mother Ruth, my father Graeme, and my brother Theo. They have never failed to support me even if I fail to explain to them exactly what it is that I do. I must also extend my scarcely uttered though sincere thanks toward my friends Dom, Sam, Tom, and Lewis. Though in recent years our visits have been infrequent, I am always mindful of their fellowship, and I will forever hold dear my undergraduate years in Manchester, particularly in and around Fallowfield. I would also like to thank my housemates over the past four years, who were extremely welcoming upon my move to London, many of whom also made the various COVID-19 lockdowns quite bearable.

Last but not least, my profound and heartfelt thanks go to my partner Margarida. Having met Margi shortly after beginning my PhD, she has never failed to support me through the best and worst of times during the entire length of my studies, and I look forward to whatever our future should hold.

OLIVER JAMES BACKHOUSE  
LONDON  
DECEMBER 2022



---

# Contents

<b>Version</b>	<b>ii</b>
<b>Abstract</b>	<b>iii</b>
<b>Acknowledgement</b>	<b>v</b>
<b>Contents</b>	<b>vii</b>
<b>List of Figures</b>	<b>xi</b>
<b>List of Tables</b>	<b>xii</b>
<b>List of Algorithms</b>	<b>xii</b>
<b>Glossary</b>	<b>xiii</b>
<b>1 Introduction</b>	<b>1</b>
<b>2 Background</b>	<b>7</b>
2.1 Quantum chemistry . . . . .	8
2.1.1 Born–Oppenheimer approximation . . . . .	8
2.1.2 Linear combination of atomic orbitals . . . . .	9
2.1.3 Slater determinants . . . . .	10
2.1.4 Second quantisation . . . . .	10
2.2 Hartree–Fock . . . . .	12
2.2.1 Restricted Hartree–Fock . . . . .	14
2.2.2 Unrestricted Hartree–Fock . . . . .	14
2.2.3 Solving the eigenproblem . . . . .	15
2.2.4 Koopmans’ theorem . . . . .	16
2.3 Diagrammatic notation . . . . .	17
2.4 Green’s functions in quantum chemistry . . . . .	21
2.4.1 Single particle Green’s function . . . . .	21
2.4.2 Dyson equation and the self-energy . . . . .	24
2.4.3 Solving the Dyson equation . . . . .	28
2.4.4 Spectral moments . . . . .	32
2.4.5 Energy functionals . . . . .	34
2.5 Møller–Plesset perturbation theory . . . . .	35

---

2.5.1	Many-body Green's functions . . . . .	38
2.5.2	Algebraic diagrammatic construction . . . . .	40
2.5.3	Green's function perturbation theory . . . . .	42
2.6	Electron propagator theory . . . . .	44
2.7	Coupled cluster . . . . .	46
2.7.1	Equation-of-motion coupled cluster . . . . .	48
2.7.2	Green's function coupled cluster . . . . .	49
2.8	$GW$ approximation . . . . .	51
2.9	Configuration interaction . . . . .	54
<b>3</b>	<b>Block Lanczos</b> . . . . .	<b>57</b>
3.1	Introduction . . . . .	58
3.2	Lanczos algorithm . . . . .	59
3.3	Block Lanczos algorithm . . . . .	62
3.4	Application to the Dyson equation . . . . .	64
3.5	Self-energy recurrence relations . . . . .	66
3.6	Green's function recurrence relations . . . . .	70
3.7	Comparison . . . . .	74
3.8	Moment extrapolation . . . . .	76
<b>4</b>	<b>Second-order auxiliary Green's function perturbation theory</b> . . . . .	<b>79</b>
4.1	Introduction . . . . .	80
4.2	Method . . . . .	81
4.3	Energy functionals . . . . .	83
4.4	Density matrices . . . . .	85
4.5	Algorithm . . . . .	87
4.6	Application to solids . . . . .	91
4.7	Multiple solutions . . . . .	92
<b>5</b>	<b>Auxiliary <math>GW</math> approximation</b> . . . . .	<b>97</b>
5.1	Introduction . . . . .	98
5.2	Method . . . . .	99
5.3	Efficient evaluation of moments . . . . .	100
5.4	Calculation of self-energy moments . . . . .	102
5.5	Multiple solutions . . . . .	103
<b>6</b>	<b>Moment-resolved coupled cluster Green's function</b> . . . . .	<b>107</b>
6.1	Introduction . . . . .	108
6.2	Method . . . . .	109
6.3	Explicit self-energy construction . . . . .	112
6.4	Algorithm . . . . .	114

---

<b>7</b>	<b>Results</b>	<b>117</b>
7.1	Introduction . . . . .	118
7.2	Water . . . . .	119
7.2.1	Ionisation potential and electron affinity . . . . .	119
7.2.2	Spectral functions . . . . .	120
7.3	W4-11 . . . . .	124
7.4	GW100 dataset . . . . .	128
7.4.1	System details . . . . .	128
7.4.2	ADC(2) moments . . . . .	129
7.4.3	GW moments . . . . .	131
7.4.4	GF-CCSD moments . . . . .	134
7.4.5	$\Delta$ CCSD(T) benchmark . . . . .	135
7.4.6	Multiple solutions . . . . .	139
7.5	Artemisinin . . . . .	142
7.6	Solids . . . . .	146
7.6.1	Benchmark . . . . .	146
7.6.2	Silicon bands . . . . .	149
<b>8</b>	<b>Conclusion</b>	<b>153</b>
<b>9</b>	<b>Appendices</b>	<b>159</b>
A	Slater–Condon rules . . . . .	160
B	Brillouin’s theorem . . . . .	161
C	Spectral product integral . . . . .	162
D	GW100 scatter plots . . . . .	163
E	GW100 data . . . . .	168
	<b>Bibliography</b>	<b>171</b>



# List of Figures

2.1	Schematic showing poles of the time-ordered Green's function . . . . .	24
2.2	Spectral functions for $N_2$ with different broadening values . . . . .	25
2.3	Schematic representations of the $ADC(n)$ series of secular matrices . . . . .	41
3.1	Loss in orthogonality for the Lanczos algorithm . . . . .	60
3.2	Loss in orthogonality for the block Lanczos algorithm . . . . .	63
3.3	Moment extrapolation example . . . . .	77
4.1	Benchmark of AGF2 implementation in PySCF on a guanine molecule . . . . .	90
4.2	Discontinuities in $H_2$ energy surfaces with AGF2 . . . . .	93
5.1	Discontinuities in $H_2$ energy surfaces with AGW . . . . .	104
7.1	Convergence of the first IP and EA for $H_2O$ . . . . .	119
7.2	Convergence of $ADC(2)$ spectra for $H_2O$ . . . . .	121
7.3	Convergence of $ADC(3)$ spectra for $H_2O$ . . . . .	122
7.4	Convergence of GF-CCSD spectra for $H_2O$ . . . . .	122
7.5	Error in different types of AGF2 for IPs and EAs of W4-11 . . . . .	124
7.6	Error in moment-resolved $ADC(2)$ calculations for IPs and EAs of $GW100$ . . . . .	130
7.7	Error in moment-resolved $GW$ calculations for IPs and EAs of $GW100$ . . . . .	132
7.8	Error in moment-resolved GF-CCSD calculations for IPs and EAs of $GW100$ . . . . .	133
7.9	Error in methods vs. CCSD(T) for IPs and EAs of $GW100$ . . . . .	136
7.10	$GW$ self-energies around the IP for $GW100$ systems . . . . .	140
7.11	Artemisinin molecular structure with oxygen types labelled . . . . .	142
7.12	Spectral functions for artemisinin . . . . .	143
7.13	Projected spectral functions for artemisinin . . . . .	144
7.14	Dyson orbitals for artemisinin . . . . .	144
7.15	Error in AGF2 calculations for the direct band gap of solids . . . . .	147
7.16	Band structure of silicon at the level of AGF2 . . . . .	150
D.1	Scatter plots of calculations for IPs and EAs of $GW100$ . . . . .	163
D.2	Scatter plot of moment-resolved $ADC(2)$ calculations for IPs and EAs of $GW100$ . . . . .	164
D.3	Scatter plot of moment-resolved $GW$ calculations for IPs and EAs $GW100$ . . . . .	165
D.4	Scatter plot of moment-resolved GF-CCSD calculations for IPs and EAs of $GW100$ . . . . .	166



# List of Tables

2.1	Scaling of the electron propagator methods . . . . .	45
3.1	Comparison of the block Lanczos recurrence schemes . . . . .	74
7.1	Error in different types of AGF2 for IPs and EAs of W4-11 . . . . .	125
7.2	Error in moment-resolved ADC(2) calculations for IPs and EAs of <i>GW100</i> . . . . .	130
7.3	Error in moment-resolved <i>GW</i> calculations for IPs and EAs of <i>GW100</i> . . . . .	132
7.4	Error in moment-resolved GF-CCSD calculations for IPs and EAs of <i>GW100</i> . . . . .	133
7.5	GF-CCSD quasiparticle weights of the IPs of H <sub>2</sub> O and HCN . . . . .	134
7.6	Error in methods vs. CCSD(T) for IPs and EAs of <i>GW100</i> . . . . .	136
7.7	Error in moment-resolved calculations for IPs and EAs of <i>GW100</i> . . . . .	138
7.8	Systems in the solid benchmark set . . . . .	146
7.9	Error in AGF2 calculations for the direct band gap of solids . . . . .	148
E.1	List of IPs for the <i>GW100</i> dataset using several quantum chemical methods . . . . .	168
E.2	List of EAs for the <i>GW100</i> dataset using several quantum chemical methods . . . . .	169

# List of Algorithms

4.1	Calculation of self-energy moments in AGF2 . . . . .	87
4.2	Relaxation of density matrices in AGF2 . . . . .	88
4.3	Full AGF2 calculation . . . . .	89
6.1	Calculation of CC moments . . . . .	114

# Glossary

<b>AGW</b>	auxiliary <i>GW</i>
<b>ADC</b>	algebraic diagrammatic construction
<b>ADC(0)</b>	zeroth-order algebraic diagrammatic construction
<b>ADC(1)</b>	first-order algebraic diagrammatic construction
<b>ADC(2)</b>	second-order algebraic diagrammatic construction
<b>ADC(2)-x</b>	extended second-order algebraic diagrammatic construction
<b>ADC(3)</b>	third-order algebraic diagrammatic construction
<b>AGF2</b>	second-order auxiliary Green's function perturbation theory
<b>AO</b>	atomic orbital
<b>BLAS</b>	basic linear algebra subprogram
<b>CC</b>	coupled cluster
<b>CCSD</b>	coupled cluster singles and doubles
<b>CCSD(T)</b>	coupled cluster singles and doubles with perturbative triples
<b>CD</b>	Cholesky decomposition
<b>CI</b>	configuration interaction
<b>CPU</b>	central processing unit
<b>DF</b>	density fitting
<b>DFT</b>	density functional theory
<b>DIIS</b>	direct inversion of the iterative subspace
<b>DLPNO</b>	domain-based local pair natural orbital
<b>EA</b>	electron affinity
<b>ECP</b>	effective core potential
<b>EE</b>	electron excitation
<b>EKT</b>	extended Koopmans' theorem
<b>EOM-CC</b>	equation-of-motion coupled cluster
<b>EOM-CCSD</b>	equation-of-motion coupled cluster singles and doubles
<b>EP</b>	electron propagator
<b>ERI</b>	electronic repulsion integral
<b>FCI</b>	full configuration interaction
<b>FLOP</b>	floating-point operation
<b>GAE</b>	greatest absolute error

<b>GEMM</b>	general matrix-multiplication
<b>GF<math>n</math></b>	Green's function perturbation theory
<b>GF-CC</b>	Green's function coupled cluster
<b>GF-CCSD</b>	Green's function coupled cluster singles and doubles
<b>GF2</b>	second-order Green's function perturbation theory
<b>GTO</b>	Gaussian-type orbital
<b>HF</b>	Hartree–Fock
<b>HOMO</b>	highest occupied molecular orbital
<b>HPC</b>	high performance computing
<b>IP</b>	ionisation potential
<b>IPES</b>	inverse photoelectron spectroscopy
<b>LCAO</b>	linear combination of atomic orbitals
<b>LDA</b>	local density approximation
<b>LUMO</b>	lowest unoccupied molecular orbital
<b>MAE</b>	mean absolute error
<b>MO</b>	molecular orbital
<b>MP</b>	Møller–Plesset perturbation theory
<b>MP1</b>	first-order Møller–Plesset perturbation theory
<b>MP2</b>	second-order Møller–Plesset perturbation theory
<b>MP3</b>	third-order Møller–Plesset perturbation theory
<b>MPI</b>	message passing interface
<b>MSE</b>	mean signed error
<b>OpenMP</b>	open multi-processing
<b>OVGF</b>	outer-valence Green's function
<b>PBE</b>	Perdew–Burke–Ernzerhof
<b>PES</b>	photoelectron spectroscopy
<b>PW</b>	plane wave
<b>QMO</b>	quasi-molecular orbital
<b>RAM</b>	random-access memory
<b>RHF</b>	restricted Hartree–Fock
<b>RI</b>	resolution of the identity
<b>RPA</b>	random phase approximation
<b>RSPT</b>	Rayleigh–Schrödinger perturbation theory
<b>SCF</b>	self-consistent field
<b>SCS</b>	spin-component scaled
<b>SOS</b>	scaled opposite-spin
<b>SOSEX</b>	second-order screened exchange
<b>STD</b>	standard deviation
<b>STO</b>	Slater-type orbital
<b>TDA</b>	Tamm–Dancoff approximation
<b>UHF</b>	unrestricted Hartree–Fock
<b>VB</b>	valence-bond





# Chapter 1

## Introduction

In their application of the novel *quantum mechanics* to the study of diatomic hydrogen and helium molecules, the seminal 1927 paper of London and Heitler presented proof of stability in the former, but not the latter, a finding that Pauling remarked “*marks the genesis of the science of subatomic theoretical chemistry*”.<sup>1,2</sup> The mathematical basis upon which quantum chemistry is built had already been laid by Schrödinger in 1926, then applied only to the hydrogen atom.<sup>3,4</sup> A comprehensive account of the discoveries and developments which therein led to the state of the art would be exhausting, with notable advances in Hund and Mulliken’s molecular orbital (MO) theory,<sup>5</sup> Slater and Pauling’s valence-bond (VB) theory,<sup>6,7</sup> and the long-neglected contributions of Hückel in applying such descriptions to conjugated hydrocarbons, thereby realising many of the advances thus far in the interpretation of organic molecules.<sup>8–10</sup> Owing to observations by Born and Oppenheimer, the problem of determining the properties and behaviour of chemical systems according to the laws of quantum mechanics became essentially an issue of determining the electronic wavefunction, and hence the field is often referred to as *electronic structure theory*.

The apparatus developed during the early twentieth century led to a detailed understanding of the mathematical theory required to explain chemical properties, with Dirac claiming that “*the difficulty is only that the exact application of these laws leads to equations much too complicated to be soluble*”.<sup>11</sup> In the near century since this remark, a bifaceted approach to overcoming such difficulty has ensued, with the increasing sufficiency of approximations complemented by increases in available computing resources such as that observed by Moore’s law. As a result, the elucidation of chemical activity and properties has continuously progressed, with a focus on quantifying the effects of electron correlation—that is, the quantum mechanical interaction between electrons, both due to electron dynamics (dynamic correlation) and as a result of the multideterminantal nature of the true ground state (static correlation). Moving beyond an independent-particle picture is crucial to the quantification of correlation, within which many physical phenomena are unexplained. These include the broadening and finite lifetime of excited states, along with the components of van der Waals interactions that involve induced dipoles.<sup>12</sup> The latter gives rise to many macroscopic phenomena such as droplet formation and surface tension, and the extraordinary climbing ability

of many animals.<sup>13,14</sup> The term *correlation* was first coined by Löwdin in 1955, having been previously studied by Wigner in 1934.<sup>15,16</sup> An exact computational model to quantify the electron correlation suffers from a *dimensionality problem*, with the number of floating-point operations (FLOPs) required to achieve it increasing exponentially with the number of electrons in the system. Calculation of the exact many-body wavefunction in this manner is not required for an accurate description of many properties, and feasibility of calculations can be improved substantially by employing a diverse range of approximations such as perturbation theories, stochastic formulations, and renormalisation approaches.

The study of electronic structure has connections to and ramifications in many other fields, with many larger scale biological models basing their parameterisation on more accurate calculations on a smaller scale, and methodological development requiring contemporary tools and concepts from mathematics and computer science. A multitude of computer implementations for quantum chemical methods have been established, both open-source and proprietary, specialising in different regimes, properties, and methods.<sup>17,18</sup> A number of these packages are significantly optimised for modern hardware, and support massively parallel calculations to extend the applicability of electronic structure theory to high performance computing (HPC) platforms.<sup>19–24</sup> Many of these packages further facilitate the rapid development of new tools and methods through convenient high-level programming languages, leveraging low-level compiled code to maintain competitive speeds,<sup>25–29</sup> thereby assisting in the modernisation of the field. No single method or codebase reigns omnipotent, with choices of approximations and algorithms introducing diverse options depending on the required accuracy, desired speed, and available resources. Electronic structure is intimately related to the field of quantum computing, presenting a proliferating area of research that may be pivotal to future developments, and quantum chemistry has also been applied to other less conventional architectures such as the blockchain.<sup>30</sup> Three Nobel Prizes in Chemistry can be attributed to the field of quantum chemistry, that of Mulliken in 1966, of Pople and Kohn in 1998, and Karplus, Levitt and Warshel in 2013. The advances made in the years since the pioneering works can be no better evidenced than a final quote, demonstrating the vast difference in capabilities nearly a century has afforded:

*The calculation of a wave function took about two afternoons, and five wave functions were calculated on the whole.*

---

E. Wigner and F. Seitz, May 1933<sup>31</sup>

The prediction and mathematical modelling of physical phenomena is not complete without observation in nature through experiment. One such category of experiment probing the electronic structure of materials is photoelectron spectroscopy (PES) and its counterpart inverse photoelectron spectroscopy (IPES).<sup>32–37</sup> These methods are general monikers for various techniques to ionise or inject an electron, respectively, typically via irradiation with ultraviolet or X-ray light. By doing so, one can probe the energy of the bound state in the case of PES, which defines the ionisation potential (IP) of the material after multiplying by a factor of minus one.

---

This can be interpreted as the energy required to remove an electron from the state, and the IP is always a positive number. In IPES an incident electron transitions into an unbound state and the emitted photon provides its energy, giving the electron affinity (EA), which can be positive or negative. The sum of the IP and EA is often referred to as the *fundamental band gap*, reflecting its role as the energy difference between the valence and conduction bands when energy levels are represented by continua, e.g. in the solid state. The theoretical counterpart to experiments of this kind is the spectral function, related to the photocurrent, and which can be calculated using an object called the single-particle Green's function. This object gives the probability amplitude of a particle created (destroyed) at one time being destroyed (created) at another, and its determination will to a large extent make up the contents of the present work. The structure of the spectral function is influenced by the interaction between electrons in the material, and therefore accurate descriptions of electron correlation are of crucial importance in its quantitative study. Spectroscopic techniques of this kind involve perturbing a system and then considering how the system responds, and therefore perturbation theories can be readily applied as the mathematical framework for the determination of the single-particle Green's function. Spectroscopy is of vital importance in material characterisation in many areas such as atmospheric chemistry,<sup>38</sup> photovoltaics and dyes,<sup>39,40</sup> and determining band structure edges.<sup>41,42</sup>

The aim of this thesis will be to introduce a new perspective on the solution of the Dyson equation. This includes an efficient reformulation of the block Lanczos algorithm, which has been applied to the single-particle Green's function previously in the literature, though in many cases it is not efficient enough to be practical within the many frameworks to be discussed.<sup>43-50</sup> These reformulations will be used to outline a number of novel approaches with utility in the field both for improving the efficiency of existing formulations, and also as alternatives to existing methodology offering superiority in some regimes. This will be shown using both pedagogical examples and diverse benchmark sets. Reformulating the block Lanczos solver in this way also lends connections to the idea of self-energies as an auxiliary space with which the physical space couples in order to mimic the effects of a dynamic function, with the auxiliary space compressed according to conservation in its moments by the Lanczos recursion. This property of moment conservation is central to the efficacy of Lanczos-based recurrence schemes in coarse-graining the dynamics in this way.

The structure of this thesis is as follows:

- **Chapter 1: Introduction**

This Chapter, outlining the context of the work in terms of the history of the field and aims.

- **Chapter 2: Background**

A summary of the fundamental principles and mathematical detail of the state of the art, upon which the novel approaches will be built. Section 2.1 begins with an outline of the mathematical details and theorems fundamental to quantum chemistry, followed by a description of the Hartree–Fock (HF) method that forms a basis for the correlated methods in Section 2.2. Section 2.3 further builds upon Section 2.1 by describing a shorthand diagrammatic notation important in the discussion of methods based in perturbation



theory. Section 2.4 introduces the central quantities this work will be concerned with, the Green's function and the self-energy, linked by the Dyson equation. Sections 2.5 to 2.9 then turn to describing common and relevant methods for quantifying electron correlation, some of which will be recalled in later Chapters from an alternative perspective.

- **Chapter 3: Block Lanczos**

Section 3.2 discusses the common Lanczos method for the iterative solution of eigenproblems, and its extension to the block Lanczos method is discussed thereafter in Section 3.3. Whilst these Sections concern the eigenproblem in a general sense, Section 3.4 will discuss their role specifically in the case of solving the Dyson equation introduced in Section 2.4. The important developments leading to efficient formulations of this problem in the context of self-energies and Green's functions will then be introduced in Sections 3.5 and 3.6, followed by a final note on extrapolation within this formulation.

- **Chapter 4: Second-order auxiliary Green's function perturbation theory**

Application of both the self-energy and Green's function recurrence relations to many-body Green's function perturbation theory, specifically in the case of the second-order self-energy. This results in a method that can be made to be extremely efficient and accurate. Section 4.2 will introduce this method, followed by derivations of functionals for the energy and density matrices in Sections 4.3 and 4.4. Algorithmic considerations will be discussed in Section 4.5. The extension of this method to the solid state is briefly outlined in Section 4.6, and finally a discussion on the existence of multiple solutions in this method compared to other perturbation theories in Section 4.7.

- **Chapter 5: Auxiliary  $GW$  approximation**

Application of the self-energy recurrence relations to the  $GW$  method. Section 5.2 introduces this method. This requires the efficient calculation of moments at the level of the random phase approximation (RPA), introduced in Section 5.3.

- **Chapter 6: Moment-resolved coupled cluster Green's function**

Application of the Green's function recurrence relations to the Green's function coupled cluster (GF-CC) method, introduced in Section 6.2 and discussed algorithmically in Section 6.4.

- **Chapter 7: Results**

Presentation and discussion of various results, with data generated for both existing quantum chemical methods along with the new contributions outlined throughout this work. Section 7.2 will introduce the simple example of a  $\text{H}_2\text{O}$  molecule to initiate analysis of the accuracy of the moment-conserving solvers in a qualitative sense. Sections 7.3 and 7.4 will then perform more quantitative analyses on diverse molecular benchmark datasets. Section 7.5 presents an example of a larger calculation and comparison to experimental data in an important drug molecule. Finally, Section 7.6 discusses results in solid state systems, both for a benchmark dataset and for the band structure of silicon.

- **Chapter 8: Conclusion**

Wrap up of the work by recapping the developments, the conclusions based on the results and their discussion, and the outlook of the project including both future aims and directions.

The work contained in this thesis was done by the author between October 2018 and December 2022 in partial fulfilment for the degree of Doctor of Philosophy at King's College London. The work of Section 3.6 and Chapter 5 build upon work performed by other members of the Booth group, with subsequent collaboration leading to the methods for which results are presented in Chapter 7. The results at the level of  $\Delta\text{CCSD(T)}$  were computed by A. Santana-Bonilla, in the case of *GW100* for Ref. 51 and in the case of *W4-11* specifically for this thesis. The other methodological accounts of Chapters 3 to 6 were developed by the author, along with all data collection and plotting. The applications of the block Lanczos solvers outlined in Chapters 4 to 6 have resulted in four publications, and a further one in preparation:

- **Chapter 4:**

- **Backhouse, O. J.**; Nusspickel, M.; Booth, G. H. *J. Chem. Theory Comput.* **2020**, *16*, 1090–1104.<sup>52</sup>
- **Backhouse, O. J.**; Booth, G. H. *J. Chem. Theory Comput.* **2020**, *16*, 6294–6304.<sup>53</sup>
- **Backhouse, O. J.**; Santana-Bonilla, A.; Booth, G. H. *J. Phys. Chem. Lett.* **2021**, *12*, 7650–7658.<sup>51</sup>

- **Chapter 6:**

- **Backhouse, O. J.**; Booth, G. H. *J. Chem. Theory Comput.* **2022**, *18*, 6622–6636.<sup>53</sup>

- **Chapter 5:**

- Scott, C. J. C.; **Backhouse, O. J.**; Booth, G. H. *in preparation*.<sup>54</sup>



## Chapter 2

# Background

## 2.1 Quantum chemistry

The field of quantum chemistry principally seeks to find approximate and tractable solutions to the Schrödinger equation for elucidating the properties of molecules and materials. In the case of the present work, we are concerned with the non-relativistic time-independent Schrödinger equation<sup>3</sup>

$$\hat{H}|\Psi\rangle = E|\Psi\rangle, \quad (2.1)$$

where  $E$  is the energy corresponding to solution (wavefunction)  $\Psi$ , and  $\hat{H}$  is the Hamiltonian operator for a system composed of  $M$  atomic nuclei and  $N$  electrons<sup>a</sup>

$$\begin{aligned} \hat{H} = & \underbrace{-\sum_{i=1}^N \frac{1}{2} \nabla_i^2}_{\text{electronic kinetic energy}} - \underbrace{\sum_{A=1}^M \frac{1}{2\mu_A} \nabla_A^2}_{\text{nuclear kinetic energy}} - \underbrace{\sum_{i=1}^N \sum_{A=1}^M \frac{Z_A}{|\mathbf{r}_i - \mathbf{R}_A|}}_{\text{nuclear-electron attraction}} \\ & + \underbrace{\sum_{i=1}^N \sum_{j>i}^N \frac{1}{|\mathbf{r}_i - \mathbf{r}_j|}}_{\text{electron-electron repulsion}} + \underbrace{\sum_{A=1}^M \sum_{B>A}^M \frac{Z_A Z_B}{|\mathbf{R}_A - \mathbf{R}_B|}}_{\text{nuclear-nuclear repulsion}}. \end{aligned} \quad (2.2)$$

In the above equation  $\mu_A$  is the nuclear-electron mass ratio for the nucleus  $A$ ,  $Z_A$  its proton number (nuclear charge), and  $\nabla_i^2$  and  $\nabla_A^2$  a pair of Laplacian operators involving differentiation with respect to the positions of the  $i$ th electron and  $A$ th nucleus,  $\mathbf{r}_i$  and  $\mathbf{R}_A$ , respectively. These terms can be classified as operators corresponding to different interactions, as labelled in Equation 2.2.

### 2.1.1 Born–Oppenheimer approximation

Central to quantum chemistry is the Born–Oppenheimer approximation, based upon the observation that nuclei are significantly heavier than electrons (i.e.  $\mu_A \gg 1$ ) and as such their motion is far slower than that of the electrons.<sup>55</sup> It is therefore a reasonable approximation to assume the nuclei to be fixed and the remaining electrons existing in a field resulting from these fixed nuclei. The result of this approximation on Equation 2.2 is that the nuclear kinetic energy term can be approximated as zero, and the nuclear-nuclear repulsion term a constant for any given system of nuclei. Thus, we define an ‘electronic’ Hamiltonian

$$\begin{aligned} \hat{H}_{\text{elec}} &= -\sum_{i=1}^N \frac{1}{2} \nabla_i^2 - \sum_{i=1}^N \sum_{A=1}^M \frac{Z_A}{|\mathbf{r}_i - \mathbf{R}_A|} + \sum_{i=1}^N \sum_{j>i}^N \frac{1}{|\mathbf{r}_i - \mathbf{r}_j|} \\ \hat{H}_{\text{elec}} &= -\sum_{i=1}^N \left( \frac{1}{2} \nabla_i^2 + v_{\text{ext}}(\mathbf{r}_i) \right) + \sum_{i=1}^N \sum_{j>i}^N \frac{1}{|\mathbf{r}_i - \mathbf{r}_j|} \\ &= \hat{h}_{\text{core}} + \hat{v}_{\text{ee}}, \end{aligned} \quad (2.3)$$

where  $\hat{h}_{\text{core}}$  is often referred to as the *core* Hamiltonian and contains the electronic kinetic energy and nuclear-electron attraction terms, the latter of which is considered an external potential and denoted  $v_{\text{ext}}$ , and  $\hat{v}_{\text{ee}}$  is the electron-electron repulsion.

<sup>a</sup>Unless explicitly stated, atomic units are used throughout this work.

One can then write an electronic Schrödinger equation

$$\hat{H}_{\text{elec}} |\Psi_{\text{elec}}\rangle = E_{\text{elec}} |\Psi_{\text{elec}}\rangle, \quad (2.4)$$

where the electronic wavefunction  $\Psi_{\text{elec}}$  and energy  $E_{\text{elec}}$  depend only parametrically on the nuclear coordinates. The total energy can then be recovered by including the nuclear-nuclear repulsion term of Equation 2.2

$$E = E_{\text{elec}} + \sum_{A=1}^M \sum_{B>A}^M \frac{Z_A Z_B}{|\mathbf{R}_A - \mathbf{R}_B|} = E_{\text{elec}} + E_{\text{nuc}}. \quad (2.5)$$

### 2.1.2 Linear combination of atomic orbitals

In quantum chemistry, one is typically concerned with single-particle orbitals  $\psi$ , for which a common choice are molecular orbitals (MOs). These delocalised orbitals are expanded as a superposition of a chosen basis of atomic-centred functions called atomic orbitals (AOs)

$$\psi_p(\mathbf{r}) = \sum_{\alpha}^{\text{AOS}} C_{\alpha p} \phi_{\alpha}(\mathbf{r}). \quad (2.6)$$

This technique is commonly referred to as the linear combination of atomic orbitals (LCAO) approach. A common choice of AOs in molecular quantum chemistry are Gaussian-type orbitals (GTOs) due to their mathematical convenience, whilst Slater-type orbitals (STOs) are more physically relevant however are harder to work with.<sup>a</sup> Periodic solid state calculations often make use of other basis sets, such as plane waves (PWs). This work will only consider basis sets consisting of GTOs.

The orbital  $\psi_p(\mathbf{r})$  is sufficient to describe the spatial distribution of the electron it is associated with, and in the case of MOs belongs to an orthonormal set

$$\int d\mathbf{r} \psi_p^*(\mathbf{r}) \psi_q(\mathbf{r}) = \delta_{pq}. \quad (2.7)$$

The complete description of an electronic wavefunction also requires one to specify its spin. For orbitals that are eigenfunctions of  $\hat{S}_z$ , the spin takes the values  $\sigma = \pm \frac{1}{2}$ , often referred to as  $\alpha$  and  $\beta$  or spin-up and spin-down. We introduce the composite spatial and spin coordinate  $\mathbf{x}_i = (\mathbf{r}_i, \sigma_i)$ , and each spatial orbital contributes two possible spin orbitals depending on the value of  $\sigma$ .

---

<sup>a</sup>Unlike GTOs, STOs possess a physical cusp condition akin to the Coulomb potential, however any product of two GTOs on different atomic centres can be written as a finite sum of GTOs at some position along the straight line connecting them. As such, high-order integrals of GTOs can be recursively computed as finite sums over one-centre integrals, and therefore one is still afforded speedups when using a relatively large GTO basis.

### 2.1.3 Slater determinants

Taking into account the positions and spins of the electrons, the  $N$ -electron wavefunction can be written  $\Psi(\mathbf{x}_0, \mathbf{x}_1, \dots, \mathbf{x}_N)$ . Electrons are indistinguishable and cannot share quantum states as a result of the Pauli exclusion principle. In order to satisfy this condition, the probability density associated with a wavefunction must be invariant under the exchange of two particles

$$|\Psi(\mathbf{x}_0, \dots, \mathbf{x}_i, \dots, \mathbf{x}_j, \dots, \mathbf{x}_N)|^2 = |\Psi(\mathbf{x}_0, \dots, \mathbf{x}_j, \dots, \mathbf{x}_i, \dots, \mathbf{x}_N)|^2, \quad (2.8)$$

which restricts the factor associated with particle exchange to  $\pm 1$ . It is a fact of nature that fermions obey antisymmetry and bosons obey symmetry with respect to particle exchange, i.e. fermions possess a factor  $-1$  and bosons  $+1$ . Therefore, for our purely fermionic wavefunctions we can write

$$|\Psi(\mathbf{x}_0, \dots, \mathbf{x}_i, \dots, \mathbf{x}_j, \dots, \mathbf{x}_N)\rangle = -|\Psi(\mathbf{x}_0, \dots, \mathbf{x}_j, \dots, \mathbf{x}_i, \dots, \mathbf{x}_N)\rangle. \quad (2.9)$$

Simply taking the product of the orbitals<sup>a</sup> is therefore insufficient to satisfy the antisymmetry of electrons. The most obvious way to write an  $N$ -body wavefunction that satisfies the antisymmetry principle is to use a determinant

$$\Psi(\mathbf{x}_1, \mathbf{x}_2, \dots, \mathbf{x}_N) = \frac{1}{\sqrt{N!}} \begin{vmatrix} \psi_i(\mathbf{x}_1) & \psi_i(\mathbf{x}_2) & \dots & \psi_i(\mathbf{x}_N) \\ \psi_j(\mathbf{x}_1) & \psi_j(\mathbf{x}_2) & \dots & \psi_j(\mathbf{x}_N) \\ \vdots & \vdots & \ddots & \vdots \\ \psi_k(\mathbf{x}_1) & \psi_k(\mathbf{x}_2) & \dots & \psi_k(\mathbf{x}_N) \end{vmatrix}, \quad (2.10)$$

and this is commonly referred to as the Slater determinant.<sup>56</sup> Including the normalisation factor, the determinant explicitly respects fermionic antisymmetry. The cumbersome nature of the determinant makes it necessary to introduce a shorthand notation for the Slater determinant

$$\Psi(\mathbf{x}_1, \mathbf{x}_2, \dots, \mathbf{x}_N) = |\psi_i(\mathbf{x}_1)\psi_j(\mathbf{x}_2) \dots \psi_k(\mathbf{x}_N)\rangle = |\psi_i\psi_j \dots \psi_k\rangle, \quad (2.11)$$

where the dropped coordinate labels are always assumed to be in numerical order, and the shorthand notations implicitly include the normalisation factor.

### 2.1.4 Second quantisation

In the notation of second quantisation Equation 2.3 can be written

$$\hat{H} = \sum_{pq} h_{pq} \hat{a}_p^\dagger \hat{a}_q + \frac{1}{2} \sum_{pqrs} v_{pqrs} \hat{a}_p^\dagger \hat{a}_q^\dagger \hat{a}_s \hat{a}_r, \quad (2.12)$$

where the subscript denoting the electronic Hamiltonian has been dropped for brevity, and the operators  $\hat{a}_p^\dagger$  and  $\hat{a}_p$  denote the creation and annihilation of an electron in the orbital labelled  $p$ , respectively. These operators can be defined using the Slater determinant notation as

$$\hat{a}_i^\dagger |\psi_j \dots \psi_k\rangle = |\psi_i \psi_j \dots \psi_k\rangle, \quad (2.13a)$$

$$\hat{a}_i |\psi_i \psi_j \dots \psi_k\rangle = |\psi_j \dots \psi_k\rangle, \quad (2.13b)$$

<sup>a</sup>Also known as a Hartree product.

and they are related by an adjoint operation. The antisymmetry of the Slater determinant is respected by each of the operators owing to their anticommutativity

$$\hat{a}_i^\dagger \hat{a}_j^\dagger + \hat{a}_j^\dagger \hat{a}_i^\dagger = \{\hat{a}_i^\dagger, \hat{a}_j^\dagger\} = 0, \quad (2.14a)$$

$$\hat{a}_j \hat{a}_i + \hat{a}_i \hat{a}_j = \{\hat{a}_j, \hat{a}_i\} = 0, \quad (2.14b)$$

and in the case of  $i = j$

$$\hat{a}_i^\dagger \hat{a}_i^\dagger = 0, \quad (2.15a)$$

$$\hat{a}_i \hat{a}_i = 0, \quad (2.15b)$$

where Equation 2.15a can be read as the Pauli exclusion principle, and Equation 2.15b as the fact that you cannot remove an electron twice. A further anticommutation relation exists between the creation and annihilation operators

$$\hat{a}_i \hat{a}_j^\dagger + \hat{a}_j^\dagger \hat{a}_i = \{\hat{a}_i, \hat{a}_j^\dagger\} = \delta_{ij}. \quad (2.16)$$

The matrix elements  $h_{pq}$  and  $v_{pqrs}$  result from the expression of the operators of Equation 2.3 in a basis of single particle orbitals  $\psi$

$$h_{pq} = \int d\mathbf{x}_1 \psi_p^*(\mathbf{x}_1) \hat{h}_{\text{core}} \psi_q(\mathbf{x}_1), \quad (2.17)$$

$$v_{pqrs} = \int d\mathbf{x}_1 d\mathbf{x}_2 \psi_p^*(\mathbf{x}_1) \psi_q^*(\mathbf{x}_2) \hat{v}_{\text{ee}} \psi_r(\mathbf{x}_1) \psi_s(\mathbf{x}_2), \quad (2.18)$$

the latter of which shall be referred to as electronic repulsion integrals (ERIs) and are commonly written in two alternative notations

$$v_{pqrs} = \underbrace{\langle pq|rs \rangle}_{\text{physicists' notation}} = \underbrace{(pr|qs)}_{\text{chemists' notation}}, \quad (2.19)$$

where an additional notation exists for the physicists' notation to denote antisymmetrised ERIs

$$\langle pq||rs \rangle = \langle pq|rs \rangle - \langle ps|rq \rangle. \quad (2.20)$$



## 2.2 Hartree–Fock

The Hartree–Fock (HF) approximation considers the  $N$ -electron wavefunction to be a single Slater determinant.<sup>57</sup> As discussed in Section 2.1.3 this satisfies antisymmetry with respect to exchange in particles, which is neglected by the simple Hartree method. Additionally, the determinant explicitly respects the Pauli exclusion principle.<sup>58</sup> Since electrons are treated independently, save a Coulomb interaction with the *average* positions of the other electrons in the systems, this approach is classified as a *mean-field* method and is solved in a self-consistent field (SCF). The total energy in HF can be evaluated as

$$E_{\text{HF}} = \langle \Psi_{\text{HF}} | \hat{H}_{\text{elec}} | \Psi_{\text{HF}} \rangle = \sum_p h_{pp} + \frac{1}{2} \sum_{pq} \langle pp || qq \rangle, \quad (2.21)$$

where  $\Psi_{\text{HF}}$  is the Slater determinant that will be referred to in this context as the HF wavefunction. The energy obeys the variational principle, stating that the exact energy for a given Hamiltonian is a minimum, and any approximation to the energy is therefore an upper bound. The usual form of the HF equations used to minimise  $E_{\text{HF}}$  with respect to choice of spin orbitals  $\psi$  is written as the pseudo-eigenproblem<sup>a</sup>

$$\hat{f}(\mathbf{x})\psi_i(\mathbf{x}) = \varepsilon_i\psi_i(\mathbf{x}), \quad (2.22)$$

where the eigenpairs  $\psi_i, \varepsilon_i$  indicate the  $i$ th orbital and its energy, and  $\hat{f}$  is the Fock operator which takes the form

$$\begin{aligned} \hat{f}(\mathbf{x}) &= \hat{h}_{\text{core}}(\mathbf{x}) + v_{\text{HF}}(\mathbf{x}) \\ &= \hat{h}_{\text{core}}(\mathbf{x}) + \sum_q \left[ \hat{\mathcal{J}}_q(\mathbf{x}) - \hat{\mathcal{K}}_q(\mathbf{x}) \right]. \end{aligned} \quad (2.23)$$

In Equation 2.23 the electron–electron interaction of Equation 2.3 is replaced by the HF potential  $v_{\text{HF}}$ , which incorporates the Coulomb and exchange operators  $\hat{\mathcal{J}}$  and  $\hat{\mathcal{K}}$ , respectively. The operators can be written as

$$\hat{\mathcal{J}}_q(\mathbf{x}_1)\psi_p(\mathbf{x}_1) = \left[ \int d\mathbf{x}_2 \psi_q^*(\mathbf{x}_2) \frac{1}{|\mathbf{r}_1 - \mathbf{r}_2|} \psi_q(\mathbf{x}_2) \right] \psi_p(\mathbf{x}_1), \quad (2.24a)$$

$$\hat{\mathcal{K}}_q(\mathbf{x}_1)\psi_p(\mathbf{x}_1) = \left[ \int d\mathbf{x}_2 \psi_q^*(\mathbf{x}_2) \frac{1}{|\mathbf{r}_1 - \mathbf{r}_2|} \psi_p(\mathbf{x}_2) \right] \psi_q(\mathbf{x}_1). \quad (2.24b)$$

The exchange operator is non-local, with no existing potential defined at a single point in space.

We must now consider the HF equations in a basis, following the procedure of Section 2.1.2. Since the GTOs we typically use as basis functions are non-orthogonal, we introduce an overlap matrix  $S$  with matrix elements

$$S_{pq} = \int d\mathbf{x} \phi_p^*(\mathbf{x}) \phi_q(\mathbf{x}), \quad (2.25)$$

---

<sup>a</sup>The HF equations can be described as a pseudo-eigenvalue equation as the Fock operator has a functional dependence on the solution eigenvectors  $\psi$ .

and allows us to recast Equation 2.22 as

$$\sum_{\alpha}^{\text{MOS}} \hat{f}(\mathbf{x}) C_{\alpha q} \phi_{\alpha}(\mathbf{x}) = \varepsilon_i \sum_{\alpha}^{\text{MOS}} C_{\alpha q} \phi_{\alpha}(\mathbf{x}). \quad (2.26)$$

Multiplying by  $\phi_q(\mathbf{x})$  and integrating over the coordinate gives a generalised eigenproblem<sup>a</sup> including the overlap matrix<sup>59,60</sup>

$$\sum_{\alpha}^{\text{AOS}} F_{pq} C_{\alpha q} = \varepsilon_i \sum_{\alpha}^{\text{AOS}} S_{pq} C_{\alpha q}, \quad (2.27)$$

which in matrix notation is

$$\mathbf{FC} = \mathbf{SC}\boldsymbol{\varepsilon}. \quad (2.28)$$

The eigenvectors  $\mathbf{C}$  are known as the MO coefficients, and constitute a unitary matrix that is sufficient to rotate from a basis of AOs to MOs, and the eigenvalues  $\boldsymbol{\varepsilon}$  are referred to as the MO energies. The coefficients can be used to calculate the density matrix

$$\gamma_{\mu\nu} = \sum_i^{\text{occ}} C_{\mu i} C_{\nu i}^*, \quad (2.29)$$

where  $i$  runs over occupied MOs. We can write the matrix elements of Equation 2.22 as

$$\begin{aligned} \langle \mu | \hat{f} | \nu \rangle &= F_{\mu\nu} = \langle \mu | \hat{h}_{\text{core}} | \nu \rangle + \langle \mu | \hat{\mathcal{J}} | \nu \rangle - \langle \mu | \hat{\mathcal{K}} | \nu \rangle \\ &= h_{\mu\nu} + J_{\mu\nu} - K_{\mu\nu}, \end{aligned} \quad (2.30)$$

and with the basis expansion we can write the matrix elements of the Coulomb and exchange operators as

$$\langle \mu | \hat{\mathcal{J}} | \nu \rangle = J_{\mu\nu} = \sum_i^{\text{occ}} \sum_{\sigma\lambda}^{\text{AOS}} \langle \mu\sigma | \nu\lambda \rangle C_{\sigma i}^* C_{\lambda i}, \quad (2.31a)$$

$$\langle \mu | \hat{\mathcal{K}} | \nu \rangle = K_{\mu\nu} = \sum_i^{\text{occ}} \sum_{\sigma\lambda}^{\text{AOS}} \langle \mu\sigma | \lambda\nu \rangle C_{\sigma i}^* C_{\lambda i}, \quad (2.31b)$$

where  $i$  runs over occupied MOs. As such, we can replace the coefficients with the density matrix of Equation 2.29, and combine the two terms using the notation of Equation 2.20 to write a compact expression for the Fock matrix

$$F_{\mu\nu} = h_{\mu\nu} + \sum_{\sigma\lambda}^{\text{AOS}} \gamma_{\lambda\sigma} \langle \mu\sigma | \nu\lambda \rangle. \quad (2.32)$$

The energy can be computed using the Fock matrix with the expression

$$E_{\text{HF}} = \frac{1}{2} \sum_{\mu\nu}^{\text{AOS}} \gamma_{\mu\nu} [h_{\mu\nu} + F_{\mu\nu}]. \quad (2.33)$$

---

<sup>a</sup>The eigenproblem is sometimes referred to as the Roothaan equation, or Roothaan–Hall equation, acknowledging an independent development of the same year.

### 2.2.1 Restricted Hartree–Fock

The equations derived thus far have considered MOs to be spin orbitals of a general nature. Whilst this serves as a platform for deriving theory, in practical calculations one can typically exploit symmetries in the nature of the spin orbitals in order to reduce the computational requirements. We will consider two such symmetries, the first being restricted Hartree–Fock (RHF) which considers pairs of  $\alpha$  and  $\beta$  spin orbitals to be constrained to have the same spatial coordinate. This means that each occupied MO is now occupied by a pair of electrons rather than a single electron of specified spin, and we must consider  $\frac{N}{2}$  spatial MOs, where  $N$  is the number of spin orbitals. In this basis, the density matrix must be prepended by a factor two to account for the double occupancy

$$\gamma_{\mu\nu} = 2 \sum_i^{\text{occ}} C_{\mu i} C_{\nu i}^* \quad (2.34)$$

and the Fock matrix elements are equal to

$$F_{\mu\nu} = h_{\mu\nu} + 2J_{\mu\nu} - K_{\mu\nu}. \quad (2.35)$$

The factor two appears before the Coulomb matrix due to the equality in integrating over functions with  $\alpha$  or  $\beta$  spins in Equation 2.24, however not in front of the exchange matrix since the integration over pairs of functions that differ in spin is zero. Bringing this together, we can write the Fock matrix in RHF as

$$F_{\mu\nu} = h_{\mu\nu} + \frac{1}{2} \sum_{\sigma\lambda}^{\text{AOS}} \gamma_{\lambda\sigma} [2(\mu\nu|\sigma\lambda) - (\mu\lambda|\sigma\nu)], \quad (2.36)$$

where the Chemists’ notation has been used for the ERIs, as is the common choice in the case of spatial orbitals. The energy can be computed in the same fashion as Equation 2.33

$$E_{\text{HF}} = \frac{1}{2} \sum_{\mu\nu}^{\text{AOS}} \gamma_{\mu\nu} [h_{\mu\nu} + F_{\mu\nu}]. \quad (2.37)$$

### 2.2.2 Unrestricted Hartree–Fock

Since RHF considers orbitals containing pairs of electrons when occupied, it is insufficient to apply to open shell systems. Instead, the unrestricted Hartree–Fock (UHF) method allows the spatial orbitals associated with  $\alpha$  and  $\beta$  electrons to be different, and one must consider  $\frac{N}{2}$  spatial MOs for each spin channel, where  $N$  is the number of spin orbitals. This results in separate generalised eigenproblems for each spin

$$\mathbf{F}^{\alpha} \mathbf{C}^{\alpha} = \mathbf{S} \mathbf{C}^{\alpha} \boldsymbol{\epsilon}^{\alpha}, \quad (2.38a)$$

$$\mathbf{F}^{\beta} \mathbf{C}^{\beta} = \mathbf{S} \mathbf{C}^{\beta} \boldsymbol{\epsilon}^{\beta}, \quad (2.38b)$$

which are sometimes referred to as the Pople–Nesbet equations.<sup>61</sup> The coefficients yield separate density matrices for each spin channel

$$\gamma_{\mu\nu}^{\alpha} = \sum_i^{\text{occ } \alpha} C_{\mu i}^{\alpha} C_{\nu i}^{\alpha,*}, \quad (2.39a)$$

$$\gamma_{\mu\nu}^{\beta} = \sum_i^{\text{occ } \beta} C_{\mu i}^{\beta} C_{\nu i}^{\beta,*}. \quad (2.39b)$$

Whilst these eigenproblems are independent, they are coupled through the fact that both  $\mathbf{F}^{\alpha}$  and  $\mathbf{F}^{\beta}$  are functions of the coefficients of both spins. The Fock matrices are defined as

$$F_{\mu\nu}^{\alpha} = h_{\mu\nu} + J_{\mu\nu}^{\alpha} + J_{\mu\nu}^{\beta} - K_{\mu\nu}^{\alpha}, \quad (2.40a)$$

$$F_{\mu\nu}^{\beta} = h_{\mu\nu} + J_{\mu\nu}^{\beta} + J_{\mu\nu}^{\alpha} - K_{\mu\nu}^{\beta}, \quad (2.40b)$$

where the opposite spin exchange contributions are zero as discussed in Section 2.2.1, and  $h$  has no spin dependence in the AO basis. Matrix elements of the Fock matrices can therefore be expanded as

$$F_{\mu\nu}^{\alpha} = h_{\mu\nu} + \sum_{\sigma\lambda}^{\text{AOS}} [(\mu\nu|\sigma\lambda) - (\mu\lambda|\sigma\nu)] \gamma_{\lambda\sigma}^{\alpha} + \sum_{\sigma\lambda}^{\text{AOS}} (\mu\nu|\sigma\lambda) \gamma_{\lambda\sigma}^{\beta}, \quad (2.41a)$$

$$F_{\mu\nu}^{\beta} = h_{\mu\nu} + \sum_{\sigma\lambda}^{\text{AOS}} [(\mu\nu|\sigma\lambda) - (\mu\lambda|\sigma\nu)] \gamma_{\lambda\sigma}^{\beta} + \sum_{\sigma\lambda}^{\text{AOS}} (\mu\nu|\sigma\lambda) \gamma_{\lambda\sigma}^{\alpha}. \quad (2.41b)$$

The energy can be found by summing the contributions according to Equation 2.37 for both spin channels

$$E_{\text{HF}} = \frac{1}{2} \sum_{\mu\nu}^{\text{AOS}} \gamma_{\mu\nu}^{\alpha} [h_{\mu\nu} + F_{\mu\nu}^{\alpha}] + \frac{1}{2} \sum_{\mu\nu}^{\text{AOS}} \gamma_{\mu\nu}^{\beta} [h_{\mu\nu} + F_{\mu\nu}^{\beta}]. \quad (2.42)$$

### 2.2.3 Solving the eigenproblem

To solve the generalised eigenproblem of Equation 2.28, consider an orthogonal matrix  $\mathbf{X}$  satisfying  $\mathbf{X}^{\dagger} \mathbf{S} \mathbf{X} = \mathbf{I}$ . Let  $\mathbf{C} = \mathbf{X} \mathbf{C}'$ , then Equation 2.28 can be transformed into a regular eigenproblem

$$\mathbf{F} \mathbf{X} \mathbf{C}' = \mathbf{S} \mathbf{X} \mathbf{C}' \boldsymbol{\varepsilon}, \quad (2.43a)$$

$$\mathbf{X}^{\dagger} \mathbf{F} \mathbf{X} \mathbf{C}' = \mathbf{X}^{\dagger} \mathbf{S} \mathbf{X} \mathbf{C}' \boldsymbol{\varepsilon}, \quad (2.43b)$$

$$\mathbf{F}' \mathbf{C}' = \mathbf{C}' \boldsymbol{\varepsilon}, \quad (2.43c)$$

where the orthogonalised Fock matrix  $\mathbf{F}' = \mathbf{X}^{\dagger} \mathbf{F} \mathbf{X}$ . An obvious choice is simply  $\mathbf{S}^{\frac{1}{2}}$ , which can be computed using the eigenpairs of the Hermitian matrix  $\mathbf{S}$ .

### 2.2.4 Koopmans' theorem

Koopmans' theorem is a powerful tool in quantum chemistry, allowing the physical interpretation of the orbital energies in Equation 2.28. It states that the negative of the highest occupied molecular orbital (HOMO) is equal to the first IP of a molecule in closed-shell HF.<sup>62</sup> It can be generalised to open-shell excitations and to EAs (where the lowest unoccupied molecular orbital (LUMO) is now used in place of the HOMO), though the latter is sensitive to choice of basis and is less appropriate in the limit of a complete basis set.<sup>63</sup> Koopmans' theorem fails to take into account orbital relaxation, since the same orbitals are used to describe the ground and excited state, with the alternate approach being to take the difference between energies of separate calculations on each system, with the calculations differing in electron number.

At the mean-field level, the Koopmans' excitations are associated with  $\delta$ -functions in the spectrum, reflecting the uncorrelated single-particle picture. This can be extended to the correlated many-particle picture using the concept of Dyson orbitals, which generalise the overlap between the ground and excited state wavefunction.<sup>64,65</sup> This concept will be discussed in more detail in Section 2.4.

## 2.3 Diagrammatic notation

Many-body diagrams are a convenient way to summarise the often cumbersome mathematics associated with many-body perturbation theories. Several closely related notations based on Feynman diagrams are employed to summarise expressions diagrammatically, with the two most common being Goldstone and Hugenholtz diagrams.<sup>66–68</sup> The principal difference in these diagrams is that the Hugenholtz diagrams consider only antisymmetric matrix elements, whereas in Goldstone diagrams one must explicitly enumerate additional diagrams corresponding to the antisymmetry. Goldstone diagrams have the advantage of naturally corresponding to RHF and UHF equations that are the practical basis in which many-body perturbation theories are implemented, however the lack of implicit antisymmetry means they are far greater in number for any given theory. Phase factors are also much more straightforward to determine in Goldstone diagrams, as the order of indices in ( $N > 1$ )-body operators is no longer determined. A simple solution to this scintillating dilemma is to combine the advantages in the form of *antisymmetric Goldstone* diagrams.<sup>69</sup> In this form, a single diagram with the appearance of a Goldstone diagram, complete with determined order of labels, represents the associated Hugenholtz diagram. The Goldstone diagram therefore maintains the antisymmetry in derived expressions. Since there can be many Goldstone diagrams per Hugenholtz diagram, the antisymmetric Goldstone representation for a given expression is not unique, however any expansion of the respective Hugenholtz diagram can be used granted the correct phase is determined by the rules prescribed to Goldstone diagrams. The weight factor of an antisymmetric Goldstone diagram is determined according to the Hugenholtz prescription. Due to the obvious benefits of this representation, we shall consider only antisymmetric Goldstone diagrams.

### Order of operations

As Feynman diagrams arise in time-dependent perturbation theories, the perturbation is ‘switched on’ in a given direction, which represents the flow of time and the sequence of events in the diagram. We are concerned with time-independent perturbation theories only, however one must still consider the order of application of operators and therefore the time axis is retained. We will consider a vertical time axis flowing from the bottom of a diagram to the top, such that the bottommost operators are applied before the uppermost.<sup>a</sup>

### Second quantised operators

The reference state (e.g. the HF wavefunction) is denoted by a position on the time axis where there is nothing. Therein, the creation and annihilation operators introduced in Section 2.1.4 can

---

<sup>a</sup>Other such notations commonly rotate the time axis such that it runs horizontally.

be represented by lines going upwards and downwards from the reference state

$$\hat{a}^\dagger \equiv \uparrow, \quad (2.44a)$$

$$\hat{a} \equiv \downarrow, \quad (2.44b)$$

respectively.

### One-body operators

The point of action for a one-body operator is represented by a vertex, with an interaction line extending to some one-body operator marker

$$\bullet \text{---} \times, \quad (2.45)$$

where the marker indicates the particular one-body operator. In this case  $\times$  indicates the Fock operator, and therefore we can define different contributions to the Fock matrix based on the time-ordering

$$\langle i|\hat{f}|j \rangle \equiv \begin{array}{c} \downarrow \\ \bullet \text{---} \times \\ \uparrow \end{array}, \quad (2.46a)$$

$$\langle a|\hat{f}|i \rangle \equiv \begin{array}{c} \downarrow \\ \bullet \text{---} \times \\ \downarrow \end{array}, \quad (2.46c)$$

$$\langle i|\hat{f}|a \rangle \equiv \begin{array}{c} \uparrow \\ \bullet \text{---} \times \\ \uparrow \end{array}, \quad (2.46b)$$

$$\langle a|\hat{f}|b \rangle \equiv \begin{array}{c} \downarrow \\ \bullet \text{---} \times \\ \downarrow \end{array}. \quad (2.46d)$$

### Two-body operators

Two-body operators are similarly represented by an interaction line, this time the interaction connecting two vertices, each with one incoming and one outgoing line. The order of indices follows the convention

$$\langle \text{left out} \text{ right out} || \text{left in} \text{ right in} \rangle. \quad (2.47)$$

The permutations of antisymmetrised ERIs that are unique under symmetry are therefore

$$\langle ab||cd \rangle \equiv \text{diagram}, \quad (2.48a)$$

$$\langle ia||jk \rangle \equiv \text{diagram}, \quad (2.48f)$$

$$\langle ai||jb \rangle \equiv \text{diagram}, \quad (2.48b)$$

$$\langle ij||ak \rangle \equiv \text{diagram}, \quad (2.48g)$$

$$\langle ab||ic \rangle \equiv \text{diagram}, \quad (2.48c)$$

$$\langle ab||ij \rangle \equiv \text{diagram}, \quad (2.48h)$$

$$\langle ai||bc \rangle \equiv \text{diagram}, \quad (2.48d)$$

$$\langle ai||bj \rangle \equiv \text{diagram}, \quad (2.48i)$$

$$\langle ij||kl \rangle \equiv \text{diagram}, \quad (2.48e)$$

$$\langle ij||ab \rangle \equiv \text{diagram}. \quad (2.48j)$$

The corresponding Hugenholtz representations, for example the  $\langle ai||jb \rangle$  case, would take the form

$$\langle ai||jb \rangle \equiv \text{diagram}, \quad (2.49)$$

from which it is clear to see why the labels are no longer determined, as the integral  $\langle ai||bj \rangle$  is represented by the same diagram.

### Products of operators

Products can be expressed by connecting the lines between vertices, for example

$$\sum_{ia} \langle i|\hat{f}|a \rangle \langle a|\hat{f}|i \rangle \equiv \text{diagram}, \quad (2.50)$$

where the summation indicates that non-external lines are contracted over. In the case of two-body operators, the antisymmetry results in equal diagrams, for example

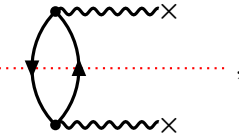
$$\begin{aligned} \frac{1}{4} \sum_{ijab} \langle ij||ab \rangle \langle ab||ij \rangle &\equiv \text{diagram} \\ &\equiv -\frac{1}{4} \sum_{ijab} \langle ij||ab \rangle \langle ab||ji \rangle \equiv \text{diagram}. \end{aligned} \quad (2.51)$$

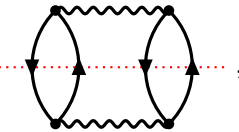


In the (non-antisymmetrised) Goldstone notation, these two diagrams constitute the so-called ‘direct’ and ‘exchange’ diagrams at second-order. The phase (sign of the factor) of each diagram can be determined according to the Goldstone prescription as  $(-1)^{h+l}$ , whereas the weight (magnitude of the factor) is  $(\frac{1}{2})^n$ ,  $n$  being the number of equivalent pairs of lines. Two lines are said to be equivalent if they connect the same pair of vertices with the same directionality. The  $h$  and  $l$  values correspond to the topology of the diagrams,  $l$  being the number of (fermionic) loops and  $h$  the number of hole connections. For a detailed description of their determination, see e.g. Ref. 68.

### Perturbation theory

In perturbation theory, one inserts a resolvent line between each point of interaction, and a denominator contribution appears for every line passing through the resolvent line. This denominator consists of a sum of the orbital energies, with their values being in the occupied or virtual sector, depending on whether the lines are hole or particles ones. As examples, Equations 2.50 and 2.51 can be rewritten with their respective denominators to obtain the full perturbation theoretical expressions

$$\sum_{ia} \frac{\langle i|\hat{f}|a\rangle\langle a|\hat{f}|i\rangle}{\varepsilon_i - \varepsilon_a} = \dots \text{diagram} \dots, \quad (2.52)$$


$$\frac{1}{4} \sum_{ijab} \frac{\langle ij||ab\rangle\langle ab||ij\rangle}{\varepsilon_i + \varepsilon_j - \varepsilon_a - \varepsilon_b} = \dots \text{diagram} \dots, \quad (2.53)$$


where the resolvent lines are marked as the red dashed line. In more complicated diagrams with more positions on the time axis and therefore more resolvent lines, multiple denominators may contribute, resulting in products over said denominators.

## 2.4 Green's functions in quantum chemistry

Green's functions, named after British mathematician George Green,<sup>70</sup> are tools for solving inhomogeneous differential equations within particular boundary conditions. Consider the linear differential operator  $\hat{\mathcal{L}}$  with a corresponding differential equation

$$\hat{\mathcal{L}}f(x_1) = h(x_1), \quad (2.54)$$

one can define the associated Green's function  $G(x_1; x_2)$  as the solution of

$$\hat{\mathcal{L}}G(x_1; x_2) = \delta(x_1 - x_2), \quad (2.55)$$

where  $\delta$  is the  $\delta$ -function. The solution  $f(x_1)$  can then be determined according to

$$f(x_1) = \int dx_2 G(x_1; x_2) h(x_2). \quad (2.56)$$

Green's functions have been used extensively throughout physics and mathematics, and can be readily applied to the Schrödinger (differential) equation. For the time-dependent case of the Schrödinger equation for a single particle, we can transform the differential equation such that its Green's function is the solution to

$$\hat{H}G(\mathbf{r}_1, t_1; \mathbf{r}_2, t_2) = \delta(\mathbf{r}_1 - \mathbf{r}_2)\delta(t_1 - t_2), \quad (2.57)$$

where the solution wavefunctions can be determined as in Equation 2.56

$$\Psi(\mathbf{r}_1, t_1) = \int d\mathbf{r}_2 G(\mathbf{r}_1, t_1; \mathbf{r}_2, t_2) \Psi(\mathbf{r}_2, t_2), \quad (2.58)$$

corresponding to the evolution of the wavefunction  $\Psi$  in space and time. This propagation of the wavefunction through space and time resulted in Green's functions being readily applied as propagators in diagrammatic theories throughout many-body physics.

### 2.4.1 Single particle Green's function

The single particle Green's function is perhaps the most ubiquitous correlation function in electronic structure theory. It is composed of 'greater' and 'lesser' propagators, where the 'lesser' part quantifies the correlation between the annihilation of a particle at time  $t_1$  and creation at  $t_2$

$$G^<(\mathbf{x}_1, t_1; \mathbf{x}_2, t_2) = i \left\langle \hat{\psi}^\dagger(\mathbf{x}_2, t_2) \hat{\psi}(\mathbf{x}_1, t_1) \right\rangle. \quad (2.59)$$

and the 'greater' part quantifies the correlation between the creation of a particle at time  $t_2$  and annihilation at  $t_1$

$$G^>(\mathbf{x}_1, t_1; \mathbf{x}_2, t_2) = -i \left\langle \hat{\psi}(\mathbf{x}_1, t_1) \hat{\psi}^\dagger(\mathbf{x}_2, t_2) \right\rangle, \quad (2.60)$$

For a Hamiltonian  $\hat{H}$  that is translationally invariant in time, Equations 2.59 and 2.60 do not depend on both  $t_1$  and  $t_2$ , but only their difference  $\tau = t_1 - t_2$ . Green's functions of this kind

are the scope of the present work, as we will not consider time-dependent external potentials. For an  $N$ -electron ground-state  $|\Psi_0^N\rangle$  with an associated time-independent Schrödinger equation  $\hat{H}|\Psi_0^N\rangle = E_0^N|\Psi_0^N\rangle$  we can rewrite Equations 2.59 and 2.60 as<sup>71</sup>

$$G_{pq}^<(\tau) = i \left\langle \Psi_0^N \left| \hat{a}_q^\dagger e^{+i(\hat{H}-E_0^N)\tau} \hat{a}_p \right| \Psi_0^N \right\rangle, \quad (2.61a)$$

$$G_{pq}^>(\tau) = -i \left\langle \Psi_0^N \left| \hat{a}_p e^{-i(\hat{H}-E_0^N)\tau} \hat{a}_q^\dagger \right| \Psi_0^N \right\rangle, \quad (2.61b)$$

respectively. By introducing the Heaviside step function

$$\Theta(x) = \begin{cases} 1 & \text{if } x \geq 0, \\ 0 & \text{if } x < 0, \end{cases} \quad (2.62)$$

the hole and particle Green's functions can now be defined as, respectively

$$G_{pq}^H(\tau) = \Theta(-\tau) G_{pq}^<(\tau), \quad (2.63a)$$

$$G_{pq}^P(\tau) = \Theta(\tau) G_{pq}^>(\tau), \quad (2.63b)$$

which give the probability amplitudes for the propagation of a particle or hole through the ground state of an interacting system.

Alternatively we can define different time-orderings in the combined Green's function, for the retarded

$$G_{pq}^R(\tau) = \Theta(\tau) (G_{pq}^>(\tau) - G_{pq}^<(\tau)), \quad (2.64)$$

advanced

$$G_{pq}^A(\tau) = \Theta(-\tau) (G_{pq}^<(\tau) - G_{pq}^>(\tau)), \quad (2.65)$$

and time-ordered

$$\begin{aligned} G_{pq}^T(\tau) &= G_{pq}^R(\tau) + G_{pq}^<(\tau) \\ &= G_{pq}^A(\tau) + G_{pq}^>(\tau), \end{aligned} \quad (2.66)$$

cases. This object can be considered to be a generalisation of the one-particle density matrix in the time domain; the density matrix can be recovered from this object simply by integrating over spin with  $\mathbf{x}_1 = \mathbf{x}_2$  and  $\tau = 0^+$ .

The Fourier transform of Equation 2.66 can be written

$$\begin{aligned} G_{pq}(\omega) &= \left\langle \Psi_0^N \left| \hat{a}_q^\dagger \left[ \omega - (\hat{H} - E_0^N) - i0^+ \right]^{-1} \hat{a}_p \right| \Psi_0^N \right\rangle \\ &\quad + \left\langle \Psi_0^N \left| \hat{a}_p \left[ \omega - (\hat{H} - E_0^N) + i0^+ \right]^{-1} \hat{a}_q^\dagger \right| \Psi_0^N \right\rangle. \end{aligned} \quad (2.67)$$

By introducing completeness relations, one can write an expression for the Lehmann representation of Equation 2.67

$$\begin{aligned} G(\mathbf{x}_1, \mathbf{x}_2; \omega) &= \sum_i \frac{u_i(\mathbf{x}_1) u_i^*(\mathbf{x}_2)}{\omega - (E_0^N - E_i^{N-1}) - i0^+} \\ &\quad + \sum_a \frac{u_a(\mathbf{x}_1) u_a^*(\mathbf{x}_2)}{\omega - (E_a^{N+1} - E_0^N) + i0^+}, \end{aligned} \quad (2.68)$$

where the so-called Dyson orbitals (quasiparticle states)  $u$  are defined as

$$u_i(\mathbf{x}) = \left\langle \Psi_i^{N-1} \left| \hat{\psi}(\mathbf{x}) \right| \Psi_0^N \right\rangle, \quad (2.69a)$$

$$u_a(\mathbf{x}) = \left\langle \Psi_0^N \left| \hat{\psi}(\mathbf{x}) \right| \Psi_a^{N+1} \right\rangle. \quad (2.69b)$$

The  $N \pm 1$  eigenstates  $\Psi_p^{N\pm 1}$  indicate addition or removal of an electron in the  $p$ th orbital, respectively, with energies  $E_p^{N\pm 1}$ . As such, the two terms in Equation 2.68 correspond to hole and particle parts of the Green's function, respectively. These will typically be denoted  $G^<$  and  $G^>$ , respectively, reflecting the time-orderings.

As introduced in Section 2.2.4, the Dyson orbitals generalise the overlap between ground and excited state wavefunctions in a single-particle picture, and are agnostic to whether or not the wavefunction is correlated. In the mean-field (uncorrelated) picture they are simply  $\delta$ -functions, whereas in the correlated picture the Dyson orbitals may enumerate many more states than just those who can be described in a Koopmans' picture and have non-unitary weights. These one-particle wavefunctions describe the transition between a wavefunction with  $N$  and  $N \pm 1$  electrons.<sup>64,65,72–74</sup> The energy differences  $E_0^N - E_i^{N-1}$  and  $E_a^{N+1} - E_0^N$  correspond to the IP and EA, respectively.

Alternatively, one can define a Lehmann representation of the other time-orderings according to the sign of the imaginary infinitesimal, first for the retarded Green's function of Equation 2.64

$$\begin{aligned} G(\mathbf{x}_1, \mathbf{x}_2; \omega + i0^+) &= \sum_i \frac{u_i(\mathbf{x}_1)u_i^*(\mathbf{x}_2)}{\omega - (E_0^N - E_i^{N-1}) + i0^+} \\ &+ \sum_a \frac{u_a(\mathbf{x}_1)u_a^*(\mathbf{x}_2)}{\omega - (E_a^{N+1} - E_0^N) + i0^+}, \end{aligned} \quad (2.70)$$

and for the advanced Green's function of Equation 2.65

$$\begin{aligned} G(\mathbf{x}_1, \mathbf{x}_2; \omega - i0^+) &= \sum_i \frac{u_i(\mathbf{x}_1)u_i^*(\mathbf{x}_2)}{\omega - (E_0^N - E_i^{N-1}) - i0^+} \\ &+ \sum_a \frac{u_a(\mathbf{x}_1)u_a^*(\mathbf{x}_2)}{\omega - (E_a^{N+1} - E_0^N) - i0^+}. \end{aligned} \quad (2.71)$$

Frequency-dependent functions shall be considered to be time-ordered unless their parameter specifies the sign of the infinitesimal in this way.

Figure 2.1 shows a schematic diagram for the poles of the time-ordered Green's function, where the infinitesimal shifts the poles above and below the real frequency axis for the hole and particle parts, respectively. The Lehmann representation of the single-particle Green's function permits the theoretical prediction of the direct and inverse photoelectron spectra via the IP and EA parts. The spectral function is typically defined with respect to the retarded Green's function<sup>75,76</sup>

$$A(\omega) = \frac{1}{\pi} \text{Tr} \left( \text{Im} \left[ G(\omega + i0^+) \right] \right), \quad (2.72)$$

which in the case of an independent particle picture consists of a series of  $\delta$ -functions positioned at the IPs and EAs. At zero temperature these time-orderings are equal within a sign, i.e.  $A(\omega + i0^+) =$

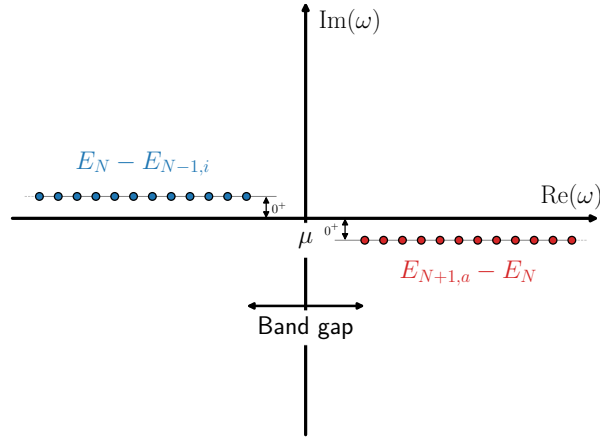


Figure 2.1: Schematic showing the positions of poles on the complex frequency axis for the time-ordered Green’s function. The poles are positioned above and below the real axis, shifted by the infinitesimal factor. The position of the Fermi energy is shifted by the chemical potential  $\mu$ .

$-A(\omega - i0^+)$ . In a correlated (non-independent particle) regime, these peaks have non-unit height and finite lifetimes. The positive infinitesimal displaces the spectral function above or below (depending on the time-ordering) the real axis in the complex plane, for the purpose of plotting and in cases where one requires regularisation of integrals, this is often replaced by a finite broadening parameter  $\eta$ . Figure 2.2 shows an example of broadened spectra at the HF level for the  $N_2$  molecule in a minimal basis. The bottom spectrum with the smallest  $\eta$  is closest to a series of  $\delta$ -functions, with differences in peak height due to resolution and degeneracy of poles in the Green’s function.

### 2.4.2 Dyson equation and the self-energy

When applying Green’s function methods to problems in quantum chemistry, we wish to leverage the frequency dependence to model correlation by shifting the positions and lifetimes of peaks in the (static) one-body density, which the dynamic nature of the Green’s function permits. From this we can derive the Dyson equation, requiring another dynamic quantity known as the self-energy, and this derivation allows us to view the frequency dependence from another perspective that will form a core feature of the present work.

The Green’s function associated with some Hamiltonian, given as a matrix in a basis of single-particle orbitals  $\mathbf{H}$ , can be written

$$(\omega - \mathbf{H}) \mathbf{G} = \mathbf{I}, \quad (2.73)$$

where  $\mathbf{I}$  is an identity matrix, and the behaviour in the complex plane is unspecified. In this case,  $\mathbf{G}$  is the *total* Green’s function corresponding to  $\mathbf{H}$ , and therefore if  $\mathbf{H}$  is the full many-body Hamiltonian  $\mathbf{G}$  is indeed the full many-body Green’s function. We next consider a partition in  $\mathbf{H}$

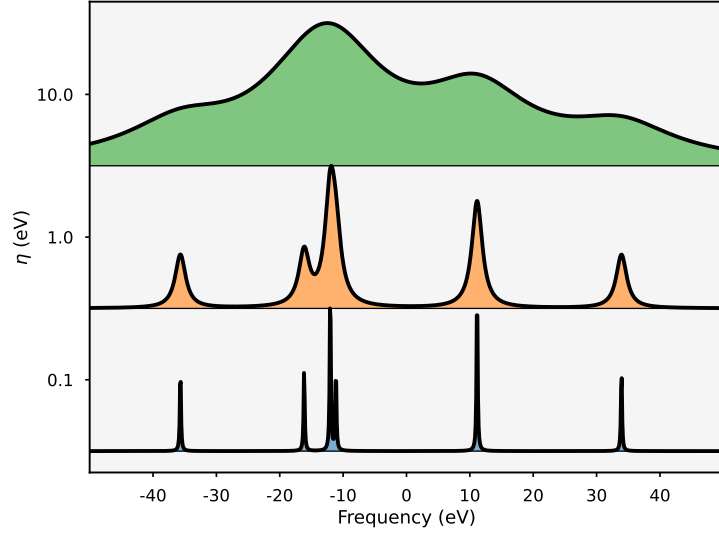


Figure 2.2: Spectral functions for  $N_2$  in a minimal basis at the HF level of theory, for three different values of broadening parameter  $\eta$ . The spectral function has been shifted in energy such that the Fermi level is at zero. The difference in peak height is due to degeneracy of poles (with some small differences due to resolution on a grid).

such that it represents the coupling of a small space to a large space<sup>71</sup>

$$\mathbf{H} = \begin{bmatrix} \mathbf{H}_{SS} & \mathbf{H}_{S\mathcal{L}} \\ \mathbf{H}_{\mathcal{L}S} & \mathbf{H}_{\mathcal{L}\mathcal{L}} \end{bmatrix}, \quad (2.74)$$

where the submatrix  $\mathbf{H}_{SS}$  is of dimension  $n \times n$  and  $\mathbf{H}_{\mathcal{L}\mathcal{L}}$  is  $(m - n) \times (m - n)$ ; here we use  $n$  to denote the size of the smaller space and  $m$  the size of the total space. The small space can be considered a reduced Hilbert space that contains effective interactions among selected degrees of freedom, which differ from the bare interactions via coupling  $\mathbf{H}_{S\mathcal{L}}$  to the larger space. Whereas  $\mathbf{G}$  represents the total Green's function corresponding to the Hamiltonian  $\mathbf{H}$ ,  $\mathbf{G}_{SS}$  instead spans only this reduced space which may incorporate only one-particle states, for example, when we consider the single-particle Green's function.

With this partitioning, we rewrite Equation 2.73

$$\left( \omega - \begin{bmatrix} \mathbf{H}_{SS} & \mathbf{H}_{S\mathcal{L}} \\ \mathbf{H}_{\mathcal{L}S} & \mathbf{H}_{\mathcal{L}\mathcal{L}} \end{bmatrix} \right) \begin{bmatrix} \mathbf{G}_{SS} & \mathbf{G}_{S\mathcal{L}} \\ \mathbf{G}_{\mathcal{L}S} & \mathbf{G}_{\mathcal{L}\mathcal{L}} \end{bmatrix} = \begin{bmatrix} \mathbf{I}_{SS} & \mathbf{0} \\ \mathbf{0} & \mathbf{I}_{\mathcal{L}\mathcal{L}} \end{bmatrix}. \quad (2.75)$$

It is trivial to algebraically manipulate Equation 2.75 to arrive at an expression for  $\mathbf{G}_{SS}$  in terms of the blocks of  $\mathbf{H}$

$$\begin{aligned} \mathbf{G}_{SS}(\omega) &= \left( \omega - \mathbf{H}_{SS} - \mathbf{H}_{S\mathcal{L}} [\omega - \mathbf{H}_{\mathcal{L}\mathcal{L}}]^{-1} \mathbf{H}_{\mathcal{L}S} \right)^{-1} \\ &= \left( \omega - \boldsymbol{\Sigma}(\infty) - \mathbf{V} [\omega - (\mathbf{K} + \mathbf{C})]^{-1} \mathbf{V}^\dagger \right)^{-1} \\ &= \left( [\mathbf{G}_{SS}^0(\omega)]^{-1} - \mathbf{V} [\omega - (\mathbf{K} + \mathbf{C})]^{-1} \mathbf{V}^\dagger \right)^{-1}, \end{aligned} \quad (2.76)$$

where we have introduced a new notation in which  $\mathbf{V}$  is the coupling between the small and large Hamiltonians  $\mathbf{H}_{\mathcal{S}\mathcal{L}}$ , and the Hamiltonian in the large space  $\mathbf{H}_{\mathcal{L}\mathcal{L}}$  is decomposed into two blocks  $\mathbf{K}$  and  $\mathbf{C}$ , the first of which is diagonal and the second of which is not. In this case we assume Hermiticity i.e.  $\mathbf{H}_{\mathcal{S}\mathcal{L}} = \mathbf{H}_{\mathcal{L}\mathcal{S}}$ , and non-Hermitian theories will be explicitly stated as such. The Hamiltonian in the small space  $\mathbf{H}_{\mathcal{S}\mathcal{S}}$  has also been denoted  $\Sigma(\infty)$  in this notation, for reasons that will become clear shortly.  $\mathbf{C}$  represents the coupling (effective interaction) between elements in the large space, and this representation can easily be transformed into a purely diagonal one where these elements are non-interacting, by diagonalising  $(\mathbf{K}+\mathbf{C})$  and appropriately rotating  $\mathbf{V}$  into this diagonal basis. The eigenvalue problem within this ‘arrowhead’ representation of the self-energy has been discussed in Ref. 77. The ‘zeroth-order’ Green’s function in the small space has been defined as  $\mathbf{G}_{\mathcal{S}\mathcal{S}}^0 = (\omega - \mathbf{H}_{\mathcal{S}\mathcal{S}})^{-1}$ . This technique of representing the static problem in the large space as a dynamic problem in the small space is often referred to as Löwdin downfolding.<sup>78–90</sup>

We now arrive at an expression for the Dyson equation

$$\mathbf{G}(\omega) = \left( [\mathbf{G}^0(\omega)]^{-1} - \Sigma(\omega) \right)^{-1}, \quad (2.77)$$

where we have dropped the  $\mathcal{S}$  and  $\mathcal{L}$  subscripts since all the matrices in Equation 2.77 are in the small ( $\mathcal{S}\mathcal{S}$ ) space, and  $\Sigma$  is called the *self-energy*, the dynamic (frequency dependent) part of which is defined as

$$\Sigma(\omega) = \mathbf{V} [\omega - (\mathbf{K}+\mathbf{C})]^{-1} \mathbf{V}^\dagger. \quad (2.78)$$

The non-dynamic (frequency independent) self-energy is given by<sup>91,92</sup>

$$\Sigma_{pq}(\infty) = \sum_{rs}^{\text{MOS}} \langle pr || qs \rangle \left( \frac{1}{2\pi i} \oint d\omega G_{rs}(\omega) \right) \quad (2.79a)$$

$$= \sum_{rs}^{\text{MOS}} \langle pr || qs \rangle \gamma_{rs}, \quad (2.79b)$$

where in this notation the static self-energy also contains the effects of the mean-field Fock matrix, and in the case of  $\mathbf{G} = \mathbf{G}^0$  can be seen to be simply equal to it. The contour integration in Equation 2.79a encloses the upper half-plane of the complex frequency  $\omega$ , i.e. all poles below the Fermi energy.<sup>a</sup> In the case of  $\Sigma(\infty) = \mathbf{F}$ ,  $\mathbf{G}^0$  can be considered the mean-field Green’s function equal to  $(\omega - \mathbf{F})^{-1}$ .<sup>b</sup> Once ‘unfolded’ (i.e. the opposite of downfolded) to remove the frequency dependence we can write

$$\Sigma = \begin{bmatrix} \Sigma(\infty) & \mathbf{V} \\ \mathbf{V}^\dagger & (\mathbf{K}+\mathbf{C}) \end{bmatrix}, \quad (2.80)$$

<sup>a</sup>In the case of the time-ordered Green’s function, where the poles below the Fermi energy are on the upper half-plane, as shown in Figure 2.1.

<sup>b</sup>Other notations often consider the Fock matrix contribution as separate to the static self-energy, which is common in the *GW* community. In this case, Equation 2.79a would integrate over  $G_{rs}(\omega) - G_{rs}^0$  and Equation 2.79b would sum over  $\gamma_{rs} - \gamma_{rs}^0$ .

where columns of  $\mathbf{V}$ , along with the matrices  $\mathbf{K}$  and  $\mathbf{V}$ , are now in the space of the configurations contained in the self-energy. The self-energy is a formally energy dependent object quantifying the effect on a propagator due to the interactions within the system itself, such as screening. It can also be interpreted as a hybridisation between the physical degrees of freedom and an auxiliary space, as shown by the unfolding procedure in Equation 2.80, which represents a coupling between the frequency independent part (including Fock matrix contributions) and a fully static auxiliary space spanning the configurations.

We can rearrange Equation 2.77 to

$$\begin{aligned}\mathbf{G}(\omega) &= (\mathbf{I} - \mathbf{G}^0(\omega)\boldsymbol{\Sigma}(\omega))^{-1} \mathbf{G}^0(\omega) \\ &= \mathbf{G}^0(\omega) + \mathbf{G}^0(\omega)\boldsymbol{\Sigma}(\omega)\mathbf{G}^0(\omega) + \mathbf{G}^0(\omega)\boldsymbol{\Sigma}(\omega)\mathbf{G}^0(\omega)\boldsymbol{\Sigma}(\omega)\mathbf{G}^0(\omega) + \dots \\ &= \mathbf{G}^0(\omega) + \mathbf{G}^0(\omega)\boldsymbol{\Sigma}(\omega)\mathbf{G}(\omega),\end{aligned}\quad (2.81)$$

which can be considered the recursive form of the Dyson equation, since  $\mathbf{G}$  appears on both sides. From this form, we can understand the Dyson equation as that which computes all possible insertions of the  $\boldsymbol{\Sigma}(\omega)$  into the bare propagator  $\mathbf{G}^0$ . These objects can be represented diagrammatically as

$$\mathbf{G}^0(\omega) = \bullet \longrightarrow \bullet, \quad (2.82a)$$

$$\mathbf{G}(\omega) = \bullet \rightleftarrows \bullet, \quad (2.82b)$$

$$\boldsymbol{\Sigma}(\omega) = \textcircled{\boldsymbol{\Sigma}}, \quad (2.82c)$$

and therefore the recursive form of the Dyson equation in Equation 2.81 can be represented as

$$\mathbf{G}^0(\omega) + \mathbf{G}^0(\omega)\boldsymbol{\Sigma}(\omega)\mathbf{G}(\omega) = \bullet \longrightarrow \bullet + \bullet \longrightarrow \textcircled{\boldsymbol{\Sigma}} \rightleftarrows \bullet, \quad (2.83)$$

where the direction of the propagators in time is unspecified in this case.

Another interpretation of the manipulations leading to Equation 2.76 is that the eigenpairs of the unfolded matrix  $\boldsymbol{\Sigma}$

$$\begin{bmatrix} \boldsymbol{\Sigma}(\infty) & \mathbf{V} \\ \mathbf{V}^\dagger & (\mathbf{K} + \mathbf{C}) \end{bmatrix} \begin{bmatrix} \mathbf{u} \\ \mathbf{w} \end{bmatrix} = \lambda \begin{bmatrix} \mathbf{u} \\ \mathbf{w} \end{bmatrix} \quad (2.84)$$

directly give the spectral representation of  $\mathbf{G}(\omega)$  akin to that of Equation 2.68

$$\mathbf{G}(\omega) = \mathbf{u} [\omega - \lambda]^{-1} \mathbf{u}^\dagger, \quad (2.85)$$

for which only the projection of the eigenvectors onto the small space  $\mathbf{u}$  (defining the Dyson orbitals) are required to obtain the Green's function in the small space. Whilst Equation 2.84 is a linear problem, this projection onto the small (physical) space is a non-linear operation. The equivalence of Equation 2.84 with Equation 2.77 in this way will be a common theme of this work. Clearly, a full eigenvalue decomposition of  $\boldsymbol{\Sigma}$  is a very expensive operation scaling as  $\mathcal{O}(m^3)$ , and so rarely will one encounter a method relying on this operation directly.



### 2.4.3 Solving the Dyson equation

A number of ways exist in the literature to obtain energies and Dyson orbitals resulting from a given self-energy. These approaches will be classified into four general categories here, and their details reviewed. This is not an exhaustive review, but rather a generalisation to provide context to discussions going forward.

#### Iterative eigenvalue problem (unfolded)

Once unfolded into its static configuration space, rather than using a dense eigensolver Equation 2.84, can be solved using an iterative eigensolver such as the Lanczos<sup>93,94</sup> or Davidson<sup>95-97</sup> algorithms. The strength of these methods largely comes from the fact that rather than storing the entire matrix  $\Sigma$  in memory and operating on it, one only needs to provide the action that computes the product of  $\Sigma$  with an arbitrary state vector. This benefit is two-fold; the  $\Sigma$  matrix is likely to be very large since it is unfolded into a configuration space typically spanning excitations scaling unfavourably with the size of the system, but also in the fact that the matrix may be sparse, and this sparsity affords reductions in the cost of the diagonalisation. This is particularly apparent in the common scenario where  $\mathbf{C} = \mathbf{0}$ . The frequency independent part  $\Sigma(\infty)$  is typically calculated and stored in RAM since its size only scales quadratically with system size, whilst the other blocks of Equation 2.84 are typically contracted with the vector algebraically in terms of their tensorial components. The disadvantage of these methods is that they can often exhibit numerical instability and their convergent behaviour is subject to limitations. The details of these limitations are largely out of the scope of the present work, though we will revisit such themes in Chapter 3 in the context of the block Lanczos algorithm.

Solutions leveraging an iterative eigensolver do not account for the entire eigenspectrum, but rather target a particular (usually extremal, or otherwise targeted) part of it. This is of no consequence when one wishes to do a one-shot computation of IPs or EAs for a given self-energy, but it offers no opportunity to self-consistently solve the Dyson equation since the propagators are not fully accounted for. In the case of many settings this is of little consequence, since the initial self-energy accounts for most of the correlation-driven changes, whereas renormalisation of the propagators accounts for only small improvements, or in some cases such as equation-of-motion coupled cluster (EOM-CC) the ground state already accounts for the renormalised correlation effects.

#### Self-consistent eigenvalue problem (downfolded)

Rather than solving the eigenvalue problem in the configuration space using an iterative eigensolver, one can also generate eigenpairs via an eigenvalue problem of the downfolded self-energy. Observing that the Green's function has poles where  $\det \mathbf{G}(\omega)$  diverges, we can infer that those poles exist at  $\omega$  where

$$\det \mathbf{G}^{-1}(\omega) = 0. \quad (2.86)$$

Taking the inverse of Equation 2.77 and recasting Equation 2.86 as an eigenvalue problem we can write

$$[\Sigma(\infty) + \Sigma(\omega)] \mathbf{C} = \mathbf{C}\omega. \quad (2.87)$$

This can be considered a generalisation of Equation 2.28 in an orthonormal basis, in which  $\Sigma(\infty)$  can be considered a Fock matrix subjected to a correlated one-particle density matrix, and in which  $\Sigma(\omega)$  provides additional (non-local) correlation and orbital relaxation. At self-consistency in  $\omega$ , the eigenvalues  $\omega$  are equal to the energies  $\lambda$  of the Dyson orbitals and can therefore be interpreted as IPs and EAs, whilst the eigenvectors  $\mathbf{C}$  are proportional to the Dyson orbitals.<sup>98,99</sup> Principally, they recover the quasiparticle weight

$$\left(1 - \mathbf{C}_x^\dagger \frac{\partial \Sigma(\omega)}{\partial \omega} \Big|_{\omega=\lambda_x} \mathbf{C}_x\right)^{-1} = |\mathbf{u}_x|^2, \quad (2.88)$$

and the Dyson orbitals can be interpreted by scaling the eigenvectors according to the square root of the weights

$$\tilde{\mathbf{u}}_x = \left(1 - \mathbf{C}_x^\dagger \frac{\partial \Sigma(\omega)}{\partial \omega} \Big|_{\omega=\lambda_x} \mathbf{C}_x\right)^{-\frac{1}{2}} \mathbf{C}_x. \quad (2.89)$$

In the case of a diagonal self-energy Equation 2.87 can be simplified to

$$\Sigma_{pp}(\infty) + \Sigma_{pp}(\omega) = \omega. \quad (2.90)$$

The diagonal equivalent of Equation 2.88 reads

$$Z_p = \left(1 - \frac{\partial \Sigma_{pp}(\omega)}{\partial \omega} \Big|_{\omega=\lambda_{x_p}}\right)^{-1}, \quad (2.91)$$

where  $\lambda_{x_p}$  is a pole in the Green's function overlapping sufficiently with the  $p$ th MO. That is to say that the  $p$ th MO is a good approximation to the perturbatively determined  $x_p$ th pole in the Green's function; Ref. 99 suggests a threshold in  $Z_p$  of 0.85 to consider the pole of use in characterising an IP or EA under a diagonal approximation. Equation 2.91 is often referred to as the quasiparticle renormalisation factor, as it can be used to linearise Equation 2.90 about the poles to avoid the need for self-consistency.<sup>100</sup> Note that in the case of a diagonal self-energy, the Dyson orbitals are necessarily equal to the MOs, since the density matrix remains diagonal.

The diagonal approximation leads to the quasiparticle equations

$$\lambda_{x_p} = \varepsilon_p + \text{Re}[\Sigma_{pp}(\lambda_{x_p})], \quad (2.92)$$

which is a ubiquitous approximation in the *GW* community. It too is often linearised according to the quasiparticle renormalisation factor, leading to

$$\lambda_{x_p} = \varepsilon_p + Z_p \text{Re}[\Sigma_{pp}(\varepsilon_p)]. \quad (2.93)$$

Ignoring the imaginary part of the self-energy results in infinite quasiparticle lifetimes as one observes at mean-field, however the energies of the quasiparticle states are still adjusted due to correlation as a result of the real part of the (diagonal) self-energy.

Methods of this type have the benefit of not having to store any quantities in the space of the configurations contained in the self-energy, nor does one even have to find analytical expressions for the components of the  $\Sigma$  matrix, but rather just for the downfolded frequency dependent form. However, they target only largely quasiparticle-like poles for which the MOs are good approximations, and a separate self-consistent eigenvalue calculation is required to calculate such a pole corresponding to each MO. This also means that obtaining the full eigenspectrum corresponding to a particular self-energy is not possible, and hence is not a practical method for quantifying spectral functions.

### Self-consistency in Dyson equation (downfolded)

The Dyson equation can be solved numerically for a given self-energy when expressed in the downfolded frequency dependent format. In order to efficiently contract the Green's functions with the interaction in a fashion that represents the diagrammatic expansion of the given self-energy, the update of the self-energy must typically be computed in the time domain.<sup>101</sup> In this domain, the algebraic interpretation of the diagrams and associated time-orderings is particularly simple. This however requires one to perform a Fourier transform in order to return to the frequency domain where the Green's function can be interpreted as a spectrum of electron removals and additions, and equivalently it requires inverse Fourier transforms of the Green's function in order to compute an update for the self-energy. The number of points in the time grid will appear in the formal scaling of the method when the construction of the self-energy is the bottleneck, and the use of non-uniform quadrature is non-trivial, with some recent research looking to remedy this.<sup>102–104</sup> Furthermore, to obtain a smooth and efficient frequency-domain Green's function one must use the Matsubara (imaginary frequency) representation, which is necessarily finite in temperature.<sup>105,106</sup> Whilst this can be an advantage for the expression of some thermal properties and extension to non-equilibrium systems, it can present an obstacle when one wishes to perform calculations at zero temperature, convergence to which can be poor for small-gapped systems. Obtaining the spectral function when one employs a Matsubara axis requires the use of analytic continuation, which is ill-conditioned, exhibiting numerical artefacts and poor precision.<sup>107</sup>

Whilst this allows the self-consistent treatment of self-energies according to the Dyson equation, it does not offer an explicit pole representation, as one obtains when the self-energy is upfolded into the configuration space. One such solution to calculating the IP and EA is to employ the extended Koopmans' theorem (EKT).<sup>101,108–111</sup> This method infers the excitations from the dynamical Green's function in a fashion that uses (and conserves) the first two (zeroth and first) moments of the Green's function.<sup>112,113</sup> The excitations are therefore determined under the lack of conservation of higher-order moments that contribute to the definition of the Green's function. One can also obtain poles of the Green's function by combining the self-consistency in frequency space with the concepts of the self-consistent eigenvalue problem. For a detailed

discussion of the computation of quasiparticle energies and Dyson orbitals from Matsubara Green's functions, see Ref. 110.

Another advantage of self-consistent Green's function theories are their reference independence, with the iteration to a fixed point being irrespective of the initial Green's function. In the case of approximations to the self-energy that can be considered conserving approximations, observables calculated with non-converged Green's functions in a self-consistent scheme may not respect some conservation laws of the Hamiltonian. This can result in unphysical solutions such as ones with an incorrect particle number.<sup>101,114,114</sup> Conserving self-energies are ones that can be obtained according to the functional derivative<sup>101,115</sup>

$$\Sigma(\mathbf{x}_1, \mathbf{x}_2; \tau) = \frac{\partial \Phi}{\partial G(\mathbf{x}_1, \mathbf{x}_2; -\tau)}, \quad (2.94)$$

where  $\Phi[G]$  is some functional of the Green's function such as the Luttinger–Ward functional.<sup>116</sup> Diagrammatically, the partial derivative of Equation 2.94 can be considered to be the cutting of a propagator line in the diagrams contained within  $\Phi$ . We also note that energies calculated with a Green's function in a conserving approximation are in agreement with the virial theorem.<sup>101</sup>

### Reduced dimensionality eigenvalue problem (unfolded)

As discussed previously, solving Equation 2.84 exactly will typically scale unfavourably. Furthermore, since in this case the size of the full eigenspectrum will scale superlinearly with the system size, performing a self-consistency via the Dyson equation in this manner results in a combinatorial explosion of poles that quickly becomes intractable. Therefore, one must apply an approximation that 'freezes' a sufficient number of the configurations in the self-energy that the size of the eigenspectrum does not grow with iterations. One such method originated in the nuclear physics community, in which the block Lanczos algorithm is applied in order to diagonalise the self-energy in a Krylov subspace, thereby conserving its spectral moments.<sup>44,45,117–125</sup> We will save any detailed discussion of this approach since the novel developments of this thesis largely revolve around efficient formulations of this concept, and we will revisit it in detail in Chapter 3. An additional perspective seeks to discretise the frequency variable into intervals which, whilst large in number, do not increase with system size.<sup>126,127</sup>

In a similar fashion to the block Lanczos approach, Ref. 128 applies the single-vector biorthogonal Lanczos algorithm to compute the Green's function at the level of CC in a Krylov subspace. This similarly preserves elements of the moments of the self-energy and circumvents the need for explicit frequency-resolved spectral functions. This is similar to other model-order reduction techniques that also follow the general principle of projecting the problem onto a smaller subspace.<sup>129–132</sup>

### 2.4.4 Spectral moments

The central moments of the spectral function can be defined by the integral

$$\Xi^{(\mathbf{G},n)} = \int_{-\infty}^{\infty} d\omega \mathbf{A}(\omega) \omega^n \quad (2.95a)$$

$$= \frac{1}{\pi} \int_{-\infty}^{\infty} d\omega \operatorname{Im}[\mathbf{G}(\omega + i0^+)] \omega^n, \quad (2.95b)$$

where the Green's function in Equation 2.95b is the retarded variant. The notation  $\Xi^{(\mathbf{G},n)}$  refers to the object with which this moment relates, in this case the Green's function, and the order of the moment  $n$ . The spectral representation in Equation 2.85 can be used to evaluate Equation 2.95b analytically in order to write an expression for the moments in terms of the Dyson orbitals and energies

$$\Xi^{(\mathbf{G},n)} = \mathbf{u} \boldsymbol{\lambda}^n \mathbf{u}^\dagger. \quad (2.96)$$

The dynamic self-energy also possesses an equivalent structure and therefore central moments

$$\Xi^{(\boldsymbol{\Sigma},n)} = \frac{1}{\pi} \int_{-\infty}^{\infty} d\omega \operatorname{Im}[\boldsymbol{\Sigma}(\omega + i0^+)] \omega^n, \quad (2.97)$$

and we can similarly write an analytic expression in terms of the poles and residues in Equation 2.78

$$\Xi^{(\boldsymbol{\Sigma},n)} = \mathbf{V} (\mathbf{K} + \mathbf{C})^n \mathbf{V}^\dagger. \quad (2.98)$$

Both distributions can be represented at large frequencies on the Matsubara axis according to the expansion<sup>133–136</sup>

$$\mathbf{G}(i\omega) = \sum_n \frac{\Xi^{(\mathbf{G},n)}}{(i\omega)^{n+1}}, \quad (2.99)$$

$$\boldsymbol{\Sigma}(i\omega) = \sum_n \frac{\Xi^{(\boldsymbol{\Sigma},n)}}{(i\omega)^{n+1}}. \quad (2.100)$$

Often it will be necessary or convenient to exploit the separability between the hole and particle parts of the self-energy and Green's function, and in both cases the hole and particle distributions possess their own moments. These moments are defined by constraining the integrals in Equations 2.95 and 2.97 to run over the interval  $(\mu, \infty)$  for the particle moment, and over  $(-\infty, \mu)$  for the hole moment, where  $\mu$  indicates the chemical potential. The hole and particle moments of the Green's function can therefore be written as

$$\Xi^{(\mathbf{G}^<,n)} = \frac{1}{\pi} \int_{-\infty}^0 d\omega \operatorname{Im}[\mathbf{G}(\omega + i0^+)] \omega^n, \quad (2.101a)$$

$$= \mathbf{u}^< (\boldsymbol{\lambda}^<)^n \mathbf{u}^{<,\dagger}, \quad (2.101b)$$

$$\Xi^{(\mathbf{G}^>,n)} = \frac{1}{\pi} \int_0^{\infty} d\omega \operatorname{Im}[\mathbf{G}(\omega + i0^+)] \omega^n, \quad (2.101c)$$

$$= \mathbf{u}^> (\boldsymbol{\lambda}^>)^n \mathbf{u}^{>,\dagger}, \quad (2.101d)$$

and of the self-energy as

$$\Xi^{(\Sigma^<,n)} = \frac{1}{\pi} \int_{-\infty}^0 d\omega \operatorname{Im}[\Sigma(\omega + i0^+)] \omega^n, \quad (2.102a)$$

$$= \mathbf{V}^< (\mathbf{K}^< + \mathbf{C}^<)^n \mathbf{V}^{<,\dagger}, \quad (2.102b)$$

$$\Xi^{(\Sigma^>,n)} = \frac{1}{\pi} \int_0^{\infty} d\omega \operatorname{Im}[\Sigma(\omega + i0^+)] \omega^n, \quad (2.102c)$$

$$= \mathbf{V}^> (\mathbf{K}^> + \mathbf{C}^>)^n \mathbf{V}^{>,\dagger}. \quad (2.102d)$$

The intervals defining the central and hole or particle moments constitute Hamburger and Stieltjes moment problems, respectively, in which the moments do not uniquely determine the functions as they would in the case of a bounded interval, the condition required in the Hausdorff moment problem.<sup>137–139</sup> In practice however, the functions both go to zero in the limit of large frequencies, and as such they are bounded by the function values rather than the interval. A sufficiently large number of moments is therefore likely to uniquely define the Green's function or self-energy they represent.

Given that the Green's function and self-energy can be considered probability distribution functions, these moments can be intuited as the moments of such a distribution, with the ordinal names often referred to as the mean, variance, skewness, kurtosis, and so on. One can derive relations between the moments by considering the insertion of the expansions of Equations 2.99 and 2.100 into the recursive expression for the Dyson equation in Equation 2.81

$$\sum_n \frac{\Xi^{(\mathbf{G},n)}}{(i\omega)^{n+1}} = \sum_n \frac{\Xi^{(\mathbf{G}_0,n)}}{(i\omega)^{n+1}} + \sum_n \frac{\Xi^{(\mathbf{G}_0,n)}}{(i\omega)^{n+1}} \sum_n \frac{\Xi^{(\Sigma,n)}}{(i\omega)^{n+1}} \sum_n \frac{\Xi^{(\mathbf{G},n)}}{(i\omega)^{n+1}} \quad (2.103)$$

$$= \sum_n \frac{\Xi^{(\mathbf{G}_0,n)}}{(i\omega)^{n+1}} + \sum_{nmk} \frac{\Xi^{(\mathbf{G}_0,n)} \Xi^{(\Sigma,m)} \Xi^{(\mathbf{G},k)}}{(i\omega)^{n+m+k+3}}. \quad (2.104)$$

By considering separately all terms that are of equal order in  $\frac{1}{i\omega}$ , and noting that  $\mathbf{G}_0(i\omega) = [i\omega - \Sigma(\infty)]^{-1}$  and therefore  $\Xi^{(\mathbf{G}_0,n)} = [\Sigma(\infty)]^n$ , one obtains the following relationships between the moments<sup>134,135</sup>

$$\Xi^{(\mathbf{G},0)} = \mathbf{I}, \quad (2.105a)$$

$$\Xi^{(\mathbf{G},1)} = \Sigma(\infty), \quad (2.105b)$$

$$\begin{aligned} \Xi^{(\mathbf{G},2)} &= [\Sigma(\infty)]^2 + \Xi^{(\Sigma,0)} \Xi^{(\mathbf{G},0)} \\ &= \left[ \Xi^{(\mathbf{G},1)} \right]^2 + \Xi^{(\Sigma,0)}, \end{aligned} \quad (2.105c)$$

$$\begin{aligned} \Xi^{(\mathbf{G},3)} &= [\Sigma(\infty)]^3 + \Sigma(\infty) \Xi^{(\Sigma,0)} \Xi^{(\mathbf{G},0)} + \Xi^{(\Sigma,1)} \Xi^{(\mathbf{G},0)} + \Xi^{(\Sigma,0)} \Xi^{(\mathbf{G},1)} \\ &= \left[ \Xi^{(\mathbf{G},1)} \right]^3 + \Sigma(\infty) \Xi^{(\Sigma,0)} + \Xi^{(\Sigma,1)} + \Xi^{(\Sigma,0)} \Xi^{(\mathbf{G},1)}, \end{aligned} \quad (2.105d)$$

...

For a given self-energy, these expressions can be rearranged to obtain relations in terms of the moments of the self-energy. An important conclusion of Equation 2.105 is that knowledge of the

central moments of the Green's function up to order  $n$  also provides knowledge of the central moments of the self-energy up to order  $n - 2$ . Since the hole and particle moments cannot be separated in the high-frequency expansions of Equations 2.99 and 2.100, this rule does not apply separately to the hole and particle moments of the self-energy.

### 2.4.5 Energy functionals

A significant feature of conserving self-energies is that the total energy computed using the self-consistent Green's function—that which is a fixed point on the Dyson equation—will be identical between a number of different energy functionals. For non-self-consistent theories this does not hold, with different functionals providing differing total energies.<sup>101,140,141</sup> Despite total energies being outside the scope of the present work, their limited discussion will consider the partitioning into one- and two-body contributions.

The one-body contribution is computed as

$$E_{1b} = \frac{1}{2} \sum_{pq}^{\text{MOS}} \gamma_{pq} [H_{pq} + \Sigma_{pq}(\infty)], \quad (2.106)$$

and is therefore identical to the HF energy functional, where the Fock matrix is replaced with the frequency-independent self-energy including both the mean-field Fock contribution along with any non-dynamic correlation contributions, and the one-body density matrix may be correlated.

The two-body energy can be calculated according to a prescription due to the Galitskii–Migdal formula leading to an expression on the Matsubara axis<sup>103,142–144</sup>

$$E_{2b} = \frac{1}{2} \frac{1}{2\pi} \sum_{pq}^{\text{MOS}} \int_{-\infty}^{\infty} d\omega \Sigma_{pq}(i\omega) G_{pq}(i\omega). \quad (2.107)$$

In Section 4.3 it will be shown how this functional can be used to derive analytic expressions for given Green's function theories based on the algebraic structure of their self-energy, as shown in Ref. 52 and similarly for a pedagogical example in Ref. 145. For more detailed discussions of Green's function energy functionals the reader is pointed to Refs. 101,141,144.

## 2.5 Møller–Plesset perturbation theory

A simple method to incorporate the effects of electron correlation to improve upon the wavefunction calculated at the HF level is to apply Rayleigh–Schrödinger perturbation theory (RSPT).<sup>4,146</sup> In this context, the perturbation theory is known as Møller–Plesset perturbation theory (MP), and defines a series of methods depending on the order of perturbation. The most common such method is second-order Møller–Plesset perturbation theory (MP2).<sup>147–150</sup> We introduce an order parameter  $\lambda$  that systematically improves the HF Hamiltonian of Equation 2.4 (where we drop the subscript for brevity)

$$\hat{H} = \hat{f} + \lambda\hat{V}. \quad (2.108)$$

We can then expand the eigenpairs using a Taylor series in  $\lambda$

$$E = E^{(0)} + \lambda E^{(1)} + \lambda^2 E^{(2)} + \dots, \quad (2.109)$$

$$|\Phi\rangle = |\Psi^{(0)}\rangle + \lambda|\Psi^{(1)}\rangle + \lambda^2|\Psi^{(2)}\rangle + \dots, \quad (2.110)$$

where  $E^{(n)}$  and  $|\Psi^{(n)}\rangle$  are the energies and wavefunctions of  $n$ th-order, with the zeroth-order components equal to the unperturbed quantities. One can derive expressions for  $E^{(n)}$  in terms of the perturbation, and manipulate these expressions to yield equations in terms of one- and two-particle quantities in the canonical basis. The details of these derivations can be found in e.g. Ref. 57.

### Zeroth- and first-order

The zeroth-order energy is equal to a sum over the orbital energies

$$\begin{aligned} E^{(0)} &= \langle \Psi^{(0)} | \hat{f} | \Psi^{(0)} \rangle \\ &= \sum_i^{\text{occ}} \varepsilon_i. \end{aligned} \quad (2.111)$$

The first-order energies can be defined as

$$\begin{aligned} E^{(1)} &= \langle \Psi^{(0)} | \hat{V} | \Psi^{(0)} \rangle \\ &= -\frac{1}{2} \sum_{ij}^{\text{occ}} \langle ij || ij \rangle. \end{aligned} \quad (2.112)$$

First-order Møller–Plesset perturbation theory (MP1) can therefore be defined as the sum of the zeroth and first-order energies, which is equal to the HF energy

$$\begin{aligned} E_{\text{MP1}} &= E^{(0)} + E^{(1)} \\ &= \sum_i^{\text{occ}} \varepsilon_i - \frac{1}{2} \sum_{ij}^{\text{occ}} \langle ij || ij \rangle \\ &= E_{\text{HF}}. \end{aligned} \quad (2.113)$$

As such, MP1 energies do not offer any correction due to correlation.

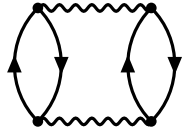


## Second-order

The second-order energy can be evaluated as

$$\begin{aligned} E^{(2)} &= \langle \Psi^{(0)} | \hat{V} | \Psi^{(1)} \rangle \\ &= \frac{1}{4} \sum_{ij}^{\text{occ}} \sum_{ab}^{\text{vir}} \frac{\langle ij || ab \rangle \langle ab || ij \rangle}{\varepsilon_i + \varepsilon_j - \varepsilon_a - \varepsilon_b}, \end{aligned} \quad (2.114)$$

where contributions only originate from doubly excited configurations since  $\langle \Psi^{(0)} | \hat{V} | \Psi_i^a \rangle = 0$  due to Brillouin's theorem (see Appendix B). Similarly, the Slater–Condon rules (see Appendix A) exclude higher-order contributions. The antisymmetric Goldstone diagram associated with the single term at second-order has the form

$$\frac{1}{4} \sum_{ij}^{\text{occ}} \sum_{ab}^{\text{vir}} \frac{\langle ij || ab \rangle \langle ab || ij \rangle}{\varepsilon_i + \varepsilon_j - \varepsilon_a - \varepsilon_b} = \text{Diagram}, \quad (2.115)$$


The MP2 method can therefore be defined as

$$E_{\text{MP2}} = \sum_{n=0}^2 E^{(n)} = E_{\text{HF}} + E^{(2)}. \quad (2.116)$$

Formally, MP2 scales as  $\mathcal{O}(n_{\text{MO}}^4)$  where  $n_{\text{MO}}$  is the number of MOs, however in practice one requires a rotation of the ERIs into the HF basis, an operation which has a  $\mathcal{O}(n_{\text{MO}}^5)$  cost.<sup>a</sup> It accounts for dynamical independent pair correlation, and is commonly applied to problems in quantum chemistry, often with one of many approximations such as local and Laplace-transformed variants, and the use of resolution of the identity (RI) or Cholesky decomposition (CD).<sup>151–154</sup>

## Higher-order

Higher-order corrections can be generated by evaluating the expression

$$E^{(n)} = \langle \Psi^{(0)} | \hat{V} | \Psi^{(n-1)} \rangle, \quad (2.117)$$

which, for example with  $n = 3$ , evaluates to<sup>148,155</sup>

$$\begin{aligned} E^{(3)} &= \frac{1}{8} \sum_{ij}^{\text{occ}} \sum_{abcd}^{\text{vir}} \frac{\langle ab || ij \rangle \langle cd || ab \rangle \langle ij || cd \rangle}{(\varepsilon_i + \varepsilon_j - \varepsilon_a - \varepsilon_b) (\varepsilon_i + \varepsilon_j - \varepsilon_c - \varepsilon_d)} \\ &+ \frac{1}{8} \sum_{ijkl}^{\text{occ}} \sum_{ab}^{\text{vir}} \frac{\langle ab || ij \rangle \langle ij || kl \rangle \langle kl || ab \rangle}{(\varepsilon_i + \varepsilon_j - \varepsilon_a - \varepsilon_b) (\varepsilon_k + \varepsilon_l - \varepsilon_a - \varepsilon_b)} \\ &+ \sum_{ijk}^{\text{occ}} \sum_{abc}^{\text{vir}} \frac{\langle ab || ij \rangle \langle cj || kb \rangle \langle ik || ac \rangle}{(\varepsilon_i + \varepsilon_j - \varepsilon_a - \varepsilon_b) (\varepsilon_i + \varepsilon_k - \varepsilon_a - \varepsilon_c)}, \end{aligned} \quad (2.118)$$

<sup>a</sup>Since only the  $\langle oo|vv \rangle$  blocks of the ERIs are required this operation has a slightly lower prefactor than  $n_{\text{MO}}^5$ , however scales the same with system size.

for which we can again assign antisymmetric Goldstone diagrams to the terms

$$\frac{1}{8} \sum_{ij}^{\text{occ}} \sum_{abcd}^{\text{vir}} \frac{\langle ab||ij \rangle \langle cd||ab \rangle \langle ij||cd \rangle}{(\varepsilon_i + \varepsilon_j - \varepsilon_a - \varepsilon_b)(\varepsilon_i + \varepsilon_j - \varepsilon_c - \varepsilon_d)} = \text{Diagram (2.119a)}, \quad (2.119a)$$

$$\frac{1}{8} \sum_{ijkl}^{\text{occ}} \sum_{ab}^{\text{vir}} \frac{\langle ab||ij \rangle \langle ij||kl \rangle \langle kl||ab \rangle}{(\varepsilon_i + \varepsilon_j - \varepsilon_a - \varepsilon_b)(\varepsilon_k + \varepsilon_l - \varepsilon_a - \varepsilon_b)} = \text{Diagram (2.119b)}, \quad (2.119b)$$

$$\sum_{ijk}^{\text{occ}} \sum_{abc}^{\text{vir}} \frac{\langle ab||ij \rangle \langle cj||kb \rangle \langle ik||ac \rangle}{(\varepsilon_i + \varepsilon_j - \varepsilon_a - \varepsilon_b)(\varepsilon_i + \varepsilon_k - \varepsilon_a - \varepsilon_c)} = \text{Diagram (2.119c)}. \quad (2.119c)$$

General  $\text{MP}n$  energies can be calculated as

$$E_{\text{MP}n} = \sum_{m=0}^n E^{(m)} = E_{\text{HF}} + \sum_{m=2}^n E^{(m)}. \quad (2.120)$$

To obtain energies of  $n$ th-order one can algorithmically generate all diagrams and then apply the rules of e.g. Ref. 57 to write the equivalent mathematical expressions. In the case of Hugenholtz diagrams, this can be done for  $n \geq 2$  by arranging  $n$  vertices in a vertical line, and then enumerating all topologically distinct arrangements of propagator lines such that each diagram satisfies the following rules:

1. Each vertex in the diagram has four propagator lines connected to it.
2. The diagram is linked (connected).
3. Vertices do not have a propagator that both enters and exits itself.

These diagrams can be generated computationally using graph theory, and their number grows extremely rapidly with order.<sup>57,156–167</sup> Alternatively, one can also extract arbitrary-order  $\text{MP}n$  energies from high-order CC ansatzes or from a full configuration interaction (FCI) expansion.<sup>168–170</sup> The  $n$ th-order energies are written in terms of only linked (connected) diagrams, as a consequence of the linked cluster theorem.<sup>171</sup> This theorem proves that unlinked (disconnected) diagrams do not appear in the  $n$ th-order energy and furthermore the algebraic terms proportional to  $N^2$  can be written in terms of these unlinked diagrams; from this we can conclude that the  $\text{MP}n$  energies are size-extensive, i.e. they increase linearly with system size. The equivalence of these diagrams with the mathematical formulae can be seen by following the steps in e.g. Ref. 57. Similarly, one can derive spatial orbital expressions by either algebraically spin adapting Equation 2.114, or by generating the non-antisymmetric Goldstone diagrams corresponding to Equation 2.115, thereby eliminating the antisymmetric matrix elements and resulting in a greater number of diagrams. The  $\text{MP}n$  series tends to be oscillatory in calculated

properties with respect to  $n$ , and in many systems can be erratic or divergent.<sup>169,170,172–176</sup> The deficiencies of the MP series at some orders are often remedied using empirically assigned weights such as the common MP2.5 method, mixing the MP2 and third-order Møller–Plesset perturbation theory (MP3) energy.<sup>177–179</sup>

### 2.5.1 Many-body Green’s functions

Green’s functions and associated self-energies can be derived for MP according to two separate but related formalisms, which will be reviewed in this section.<sup>180–182</sup> The first of these perspectives, which will be referred to as the  $\Delta\text{MP}n$  class of self-energies, can be summarised as the  $n$ th-order perturbation correction to the IP or EA of the  $x$ th electron

$$\bar{\Sigma}_x^{(n)} = \left( E_N^{(n)} - E_{(N-1),x}^{(n)} \right) + \left( E_{(N+1),x}^{(n)} - E_N^{(n)} \right), \quad (2.121)$$

where  $E_{(N\pm 1),x}^{(n)}$  indicates the  $n$ th-order correction to the energy of the  $N \pm 1$  electron determinant in which an electron has been added to or removed from orbital  $x$ . The frequency argument  $\omega$  has been omitted, since the dependency of Equation 2.121 on frequency depends on  $n$ , with some orders being frequency independent and depending on the orbital energy as  $\bar{\Sigma}_x^{(n)}(\epsilon_x)$ , and others being self-consistent in  $\bar{\Sigma}_x^{(n)}(\omega)$ . This class of diagrams corresponds to taking all topologically distinct ways to cut a propagator line in the diagrammatic representations of the  $n$ th-order energy, leaving an external edge, which as discussed in Section 2.4.3 results in a conserving approximation. The external edges correspond to the same physical index, as the self-energy is under a diagonal approximation. We note that the so-called  $\Delta\text{MP}n$  method of calculating IPs and EAs differs from this self-energy since it involves separate determinants for the  $N$  and  $N \pm 1$  reference states.

The second perspective again takes all topologically distinct cuts with two external edges, this time without a diagonal or frequency independent approximation, but also includes a further set of diagrams resulting from the vertex insertion of a ‘bubble’ diagram into the diagrams for the  $(n - 1)$ th order self-energy. This results in additional frequency independent diagrams for  $n \geq 3$ . These self-energies will be referred to as the  $n$ th-order self-energies. Taking a frequency independent diagonal approximation to the  $n$ th-order self-energy yields the  $\Delta\text{MP}n$  self-energy for  $n \leq 3$

$$\bar{\Sigma}_p^{(n)} = \Sigma_{pp}^{(n)}(\epsilon_p) \quad \forall n \leq 3, \quad (2.122)$$

and both self-energies converge systematically to FCI in the limit of infinite order  $n$ .

#### Zeroth- and first-order

The self-energy at zeroth-order is equal to the HF orbital energies,

$$\Sigma_{pq}^{(0)} = \delta_{pq}\epsilon_p, \quad (2.123)$$

and is zero at first-order

$$\Sigma_{pq}^{(1)} = 0, \quad (2.124)$$

both of which are independent of frequency, and as such only contribute to  $\Sigma(\infty)$ . Equation 2.123 explains the notational decision to include the Fock matrix as part of the static self-energy, since it is a member of the perturbation theoretical series.

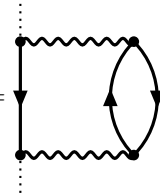
### Second-order

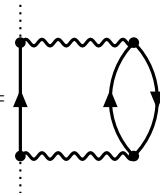
The dynamical self-energy at second-order can be defined as

$$\Sigma_{pq}^{(2)}(\omega) = \frac{1}{2} \sum_{ij}^{\text{occ}} \sum_a^{\text{vir}} \frac{\langle ij||ap \rangle \langle aq||ij \rangle}{\omega - (\varepsilon_i + \varepsilon_j - \varepsilon_a)} \quad (2.125a)$$

$$+ \frac{1}{2} \sum_i^{\text{occ}} \sum_{ab}^{\text{vir}} \frac{\langle pi||ab \rangle \langle ab||qi \rangle}{\omega - (\varepsilon_a + \varepsilon_b - \varepsilon_i)}, \quad (2.125b)$$

where Equation 2.125a corresponds to the occupied ( $2h1p$ ) and Equation 2.125b to the virtual ( $1h2p$ ) spaces. The diagrams associated with the terms can be obtained by taking the two topologically distinct ways to cut a propagator in the diagram shown in Equation 2.115

$$\frac{1}{2} \sum_{ij}^{\text{occ}} \sum_a^{\text{vir}} \frac{\langle ij||ap \rangle \langle aq||ij \rangle}{\omega - (\varepsilon_i + \varepsilon_j - \varepsilon_a)} = \text{Diagram 1}, \quad (2.126a)$$


$$\frac{1}{2} \sum_i^{\text{occ}} \sum_{ab}^{\text{vir}} \frac{\langle pi||ab \rangle \langle ab||qi \rangle}{\omega - (\varepsilon_a + \varepsilon_b - \varepsilon_i)} = \text{Diagram 2}. \quad (2.126b)$$


Equation 2.125 clearly possesses a structure compatible with Equation 2.78, and one can therefore write the occupied self-energy with the substitutions

$$V_{p,ija} = \frac{1}{\sqrt{2}} \langle ij||ap \rangle, \quad (2.127a)$$

$$V_{p,iab} = \frac{1}{\sqrt{2}} \langle pi||ab \rangle, \quad (2.127b)$$

$$K_{ija,klb} = \delta_{ik} \delta_{jl} \delta_{ab} (\varepsilon_i + \varepsilon_j - \varepsilon_a), \quad (2.127c)$$

$$K_{iab,jcd} = \delta_{ij} \delta_{ac} \delta_{bd} (\varepsilon_a + \varepsilon_b - \varepsilon_i), \quad (2.127d)$$

$$C_{ija,klb} = 0, \quad (2.127e)$$

$$C_{iab,jcd} = 0. \quad (2.127f)$$

The diagonal nature of the Hamiltonian in the large space indicates that the  $2h1p$  (and indeed  $1h2p$ ) configurations do not couple with each other at second-order. The expression for the energy

in Equation 2.114 can be recovered from Equation 2.125 by evaluating the Galitskii–Migdal formula in the presence of the HF Green’s function and performing integration over frequency, as shown in Ref. 52, and will be recapped in Section 4.3.

### Higher-order

At third-order, there are 12 frequency dependent diagrams, along with 6 frequency independent ones resulting from vertex insertion. These diagrams can be found in the literature,<sup>183</sup> along with expressions for  $\Sigma^{(3)}$  (including frequency independent parts),<sup>184</sup> and the parameters satisfying  $\mathbf{V}$ ,  $\mathbf{K}$  and  $\mathbf{C}$ .<sup>185,186</sup> At third-order  $\mathbf{C}$  is non-zero, indicating that there exists a coupling between the  $2h1p$  and separately between the  $1h2p$  configurations. The expressions at  $n > 3$  become rather cumbersome, and typically are not defined explicitly, but rather using expansions based on configuration interaction (CI).<sup>181,182</sup> The order of configuration space spanned increases with every other order  $n$ , i.e.  $n = 4, 5$  span also  $3h2p$  and  $2h3p$  spaces,  $n = 6, 7$  span  $4h3p$  and  $3h4p$  spaces, and so forth. This corresponds to an increase in the span of  $\mathbf{K}$  with every even  $n$ , and in the span of  $\mathbf{C}$  with every odd  $n$ .

### 2.5.2 Algebraic diagrammatic construction

The algebraic diagrammatic construction (ADC) can be considered an excited state extension to MP perturbation theory, and whilst several perspectives, derivations, and applications exist in the literature, this work will be concerned with ADC only in the context of the single-particle Green’s function.<sup>91,185,187–195</sup> We note that an alternative and common application of ADC is to the two-particle Green’s function in the form of the polarisation propagator, which serves to calculate neutral excitations energies rather than the IPs and EAs we are concerned with.<sup>196–204</sup> ADC can be considered as a solution to a single iteration of Equation 2.77 where the aforementioned perturbative self-energies are used. Therein, the poles of the Green’s function ( $\lambda$  values of Equation 2.68) are interpreted as IP<sup>a</sup> and EA excitations at the given level of perturbation theory, with the couplings ( $u$  of Equation 2.68) permitting the calculation of transition moments. These calculations typically start with the dynamical self-energy upfolded into its static configuration space, leading to a series of secular matrices in the form of Equation 2.80 that are consistent up to consecutive orders in perturbation theory. Figure 2.3 shows schematic representations of this series of matrices, where the numbers denote the order of each block in the matrix in perturbation theory.

From Equations 2.123 and 2.124 the zeroth-order algebraic diagrammatic construction (ADC(0)) and first-order algebraic diagrammatic construction (ADC(1)) secular matrices can be understood to be equal to the Fock matrix in the canonical basis, and therefore the solutions at these levels of theory are simply the MOs. This reflects the fact that MP1 theory is simply equal to HF, with no frequency dependence existing to alter the spectrum. In second-order algebraic diagrammatic construction (ADC(2)) the frequency-independent self-energies of zeroth and

---

<sup>a</sup>More accurately, in the nomenclature used throughout this work, they are minus one times the IP.

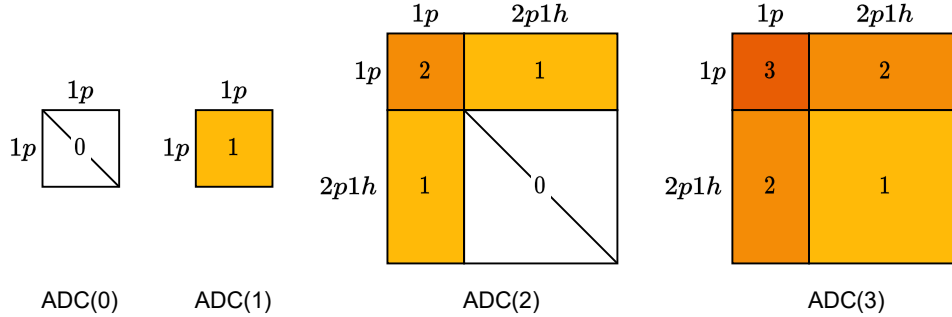


Figure 2.3: Schematic representations of the  $\text{ADC}(n)$  series of matrices for  $n$  between 0 and 3. The numbers denote the order of each block in perturbation theory. Adapted from Ref. 201.

first-order are retained in the small block, however the dynamic  $2h1p$  and  $1h2p$  contributions are unfolded into their respective configuration spaces and concatenated to give  $\mathbf{V}$  and  $\mathbf{K}$ , where the coupling  $\mathbf{C}$  between these configurations is zero. The forms of these quantities are identical to Equation 2.127. Higher-order  $\text{ADC}(n)$  calculations can be derived by similarly unfolding the  $n$ th-order self-energy as discussed in Section 2.5, and matrix elements can be derived diagrammatically or via other frameworks.<sup>181,182,185,188,205</sup> Additionally, the extended second-order algebraic diagrammatic construction ( $\text{ADC}(2)\text{-x}$ ) method is defined by increasing the order in the  $\mathbf{K}+\mathbf{C}$  block to that of third-order algebraic diagrammatic construction ( $\text{ADC}(3)$ ) whilst retaining the  $\mathbf{V}$  and  $\Sigma(\infty)$  of  $\text{ADC}(2)$ . This method however is not rigorously justified diagrammatically, and in the case of excitation energies offers a consistent underestimation.<sup>200</sup>

Iterative eigensolvers, typically the Davidson algorithm, are employed to solve the self-energy in ADC to obtain the poles and transition amplitudes of the Green’s function. This reduces the cost of the eigenproblem to be linear in the cost of the operation computing the dot-product between the self-energy matrix and an arbitrary state vector, but is only sufficient to calculate an  $\mathcal{O}(1)$  number of the smallest eigenvalues. In order to compute the excitations closest to the Fermi level (i.e. the first few IPs and EAs), one requires a separation between the occupied and virtual parts of the self-energy. Whilst these parts are completely separable (c.f. Equation 2.125) there still exists a coupling between the virtual (occupied) MO space and the entire higher-order configuration space, meaning that the solution does not yield purely occupied (purely virtual) poles of the Green’s function. As such, one must employ the ‘non-Dyson’ approximation to fully separate the occupied and virtual Green’s functions, thereby only solving for  $\Sigma_{ij}(\omega)$  in the occupied case and for  $\Sigma_{ab}(\omega)$  in the virtual case.<sup>186,192,206</sup> Solving for the lowest poles of the Green’s function using the  $\text{ADC}(n)$  ansatz in this way exhibits the same scaling as the parent  $\text{MP}n$  method. When referred to as simply ADC, we will mean the ‘non-Dyson’ variant, except when explicitly referred to as Dyson-ADC.

### 2.5.3 Green's function perturbation theory

An alternative method for solving for the Green's function at the level of  $n$ th-order perturbation theory is Green's function perturbation theory. Instead of unfolding the self-energy into the configuration space and solving as an eigenproblem, one instead numerically solves the Dyson equation using the self-energy at a given order. This in turn allows one to reinsert the dressed propagators back into the self-energy, which can in turn be solved for an updated Green's function. As such, this defines an iterative procedure that can be performed self-consistently, and is referred to as Green's function perturbation theory (GF $n$ ).<sup>42,101,103,123,136,143,184,207–214</sup> At the level of second-order Green's function perturbation theory (GF2), diagrammatically this corresponds to inserting in all possible ways the self-energy of Equation 2.126 into Equation 2.83, resulting in a pair of antisymmetric Goldstone diagrams that have the same topology as Equation 2.126 but in which the propagator lines are dressed (renormalised)

$$\Sigma_{pq}^{(2,\text{occ})}[G] = \text{Diagram (2.128a)}, \quad (2.128a)$$

$$\Sigma_{pq}^{(2,\text{vir})}[G] = \text{Diagram (2.128b)}. \quad (2.128b)$$

The two-body component of the total energy can then be calculated by evaluating the Galitskii–Migdal formula as discussed in Section 2.4.5. Diagrammatically, it is equivalent to the MP2 energy of Equation 2.115 with all propagators dressed<sup>a</sup>

$$E_{2b}[\Sigma^{(2)}[G]] = \text{Diagram (2.129)} \quad (2.129)$$

This self-consistency was briefly discussed in Section 2.4.3, involving Fourier transforms between time and frequency grids, and sometimes analytic continuation between real and complex domains. The details of this procedure are out of the scope of this work and can be found in the literature,<sup>42,101,123,143,208,209,212</sup> but it is important to note that these numerical methods are often badly conditioned or hard to converge, and the size of the time grid appears in the formal scaling of method. In addition, self-consistent Green's function methods are inherently

<sup>a</sup>It should be noted that this is referred to as the 'two-body' energy rather than the correlation energy because additional correlation-induced changes to the one-body density matrix result in a one-body energy that is not equal to that of HF, and therefore the correlation energy is actually  $E_{\text{corr}} = (E_{1b} + E_{2b}) - E_{\text{HF}}$ .

hard to converge with respect to the Dyson equation.<sup>145,215,216</sup> On top of the self-consistency in the Dyson equation, one requires that the Fock matrix is self-consistent with the correlation-induced changes to the one-body density matrix, and this in turn requires one to maintain a chemical potential since particle number conservation laws are not strictly obeyed. As such, self-consistent Green's function perturbation theory has only limited use in the literature, with some use of the second-order GF2 method.

Whilst ADC is not traditionally derived from a Green's function perspective, the framework used here to describe both ADC and Green's function perturbation theory allow the conclusion that GF $n$  can be considered a self-consistent extension to Dyson-ADC( $n$ ). GF $n$  however does not allow one to easily obtain an explicit pole representation of the Green's function from which IPs and EAs can be inferred, but rather it provides a grid-resolved Green's function across the entire spectrum. As discussed in Section 2.4.3 one option to obtaining such excitations and effective Dyson amplitudes is to apply the EKT procedure, as outlined in Ref. 109. In Chapter 4 we will look to combine these perspectives in order to define a method that not only self-consistently solves the Dyson equation, but also provides an explicit pole representation of the resulting Green's function.



## 2.6 Electron propagator theory

Electron propagator (EP) theory can be considered an umbrella term that collects the many approximations to the self-energy, in the context of their solution to yield a single-particle Green's function.<sup>65,74,98,183,184,187,188,217–233</sup> The  $n$ th-order self-energies discussed in Section 2.5 are included in this family, including a multitude of approximations incorporating diagrams at different levels of perturbation theory. Typical derivations are performed in the context of superoperator theory however the resulting self-energies can still be applied in identical fashion to those already discussed, with EP implementations typically leveraging a self-consistent eigenvalue equation in order to solve the Dyson equation. As such, we will review some common self-energies employed in EP theory.

Choice of the configuration space to span the  $2h1p$  and  $1h2p$  spaces whilst neglecting couplings between them define the non-diagonal second-order self-energy  $\Sigma^{\text{ND}2}$ , which is identical to the second-order self-energy of Equation 2.125. Considering only diagonal elements  $\Sigma_{pq}^{\text{D}2} = \Sigma_{pq}^{\text{ND}2} \delta_{pq}$  results in the diagonal second-order self-energy which, as per Equation 2.122, is equal to the  $\Delta\text{MP}2$  self-energy when evaluated at the MO energies. Expansion of the spin orbitals and the subsequent neglect of same-spin interactions defines the opposite-spin D2 self-energy  $\Sigma^{\text{os-D}2}$ . Similar approaches exist where the same-spin and opposite-spin interactions are assigned empirically determined weighting factors, with these methods being related to the scaled opposite-spin (SOS) and spin-component scaled (SCS) variants of MP calculations.<sup>234–238</sup> The variants  $\Sigma^{\text{nD-ND}2}$  and  $\Sigma^{\text{nD-D}2}$  employ the non-Dyson approximation as discussed in Section 2.5.2 affording a number of computational advantages. Depending on the solver, this may relax bottlenecks, whilst offering a satisfactory approximation in many applications.<sup>186</sup> ADC(2) is therefore the application of an iterative eigensolver to  $\Sigma^{\text{nD-ND}2}$  upfolded into the space of its configuration space.

Owing to the Tamm–Dancoff approximation (TDA), the  $2p1h$ -TDA self-energy  $\Sigma^{2p1h\text{-TDA}}$  incorporates first-order couplings between the  $2h1p$  couplings and between the  $1h2p$  couplings. This self-energy can be parameterised identically to Equation 2.127 with the additional contributions to the  $\mathbf{C}$  blocks<sup>84,239</sup>

$$C_{ija,klb} = (1 - P_{ij})(1 - P_{kl})\delta_{ik} \langle al||bj \rangle - \delta_{ab} \langle kl||ij \rangle, \quad (2.130a)$$

$$C_{iab,jcd} = \delta_{ij} \langle cd||ab \rangle - (1 - P_{ab})(1 - P_{cd})\delta_{ac} \langle id||jb \rangle, \quad (2.130b)$$

where the permutation operator  $P_{xy}$  permutes the indices  $x$  and  $y$ .

The  $3+$  self-energy  $\Sigma^{3+}$  incorporates all third-order contributions to the self-energy, as discussed in Section 2.5.1. Typical ADC(3) calculations can therefore be considered to be an evaluation of the non-Dyson variant  $\Sigma^{\text{nD-}3+}$ . The subsequent calculation of the resolvent or Dyson orbitals therefore generates terms beyond third-order; one may alternatively neglect terms in the self-energy that result in these higher-order terms defining the third-order  $\Sigma^{\text{ND}3}$  and its associated diagonal approximation  $\Sigma^{\text{D}3}$ , along with associated opposite-spin and non-Dyson variants. As stated for second-order,  $\Sigma^{\text{D}3}$  evaluated at the MO energies returns the so-called

Methods	CPU bottleneck		RAM bottleneck
	Iterative	Non-iterative	
D2	$n_{\text{occ}}n_{\text{vir}}^2$		$n_{\text{occ}}n_{\text{vir}}^2$
ND2	$n_{\text{occ}}n_{\text{vir}}^3$		$n_{\text{occ}}n_{\text{vir}}^3$
D3, OVGf	$n_{\text{occ}}n_{\text{vir}}^4$	$n_{\text{occ}}^2n_{\text{vir}}^3$	$n_{\text{vir}}^4$
P3, P3+	$n_{\text{occ}}^3n_{\text{vir}}^2$	$n_{\text{occ}}^2n_{\text{vir}}^3$	$n_{\text{occ}}n_{\text{vir}}^3$
2p1h-TDA	$n_{\text{occ}}n_{\text{vir}}^4$		$n_{\text{vir}}^4$
NR2	$n_{\text{occ}}^2n_{\text{vir}}^3$	$n_{\text{occ}}^3n_{\text{vir}}^3$	$n_{\text{occ}}n_{\text{vir}}^3$
3+	$n_{\text{occ}}n_{\text{vir}}^4$	$n_{\text{occ}}^2n_{\text{vir}}^4$	$n_{\text{occ}}^2n_{\text{vir}}^2$

Table 2.1: Scaling of the EP methods in terms of the iterative and non-iterative CPU bottlenecks, and the storage bottleneck, with respect to the number of occupied orbitals  $n_{\text{occ}}$  and number of virtual orbitals  $n_{\text{vir}}$ . The non-iterative steps must only be calculated once, typically representing the parts of the self-energy independent of frequency, whilst the iterative steps must be calculated multiple times at each iteration of either an iterative eigensolver or a self-consistent eigenvalue formulation. These costs represent those of the calculation of a single IP or EA, where  $n_{\text{vir}} \gg n_{\text{occ}}$  is assumed. Adapted from Refs. 74,99,233,240,247.

$\Delta$ MP3 self-energy. The terms entering the diagonal third-order  $\Sigma^{\text{D3}}$  can be reformulated into approximate self-energies under the class of outer-valence Green's functions (OVGFs), which are competitive with ADC(3) calculations for the calculation of low-lying IPs.<sup>74,188,224,240</sup> These variants are denoted  $\Sigma^{\text{OVGF-A}}$ ,  $\Sigma^{\text{OVGF-B}}$ , and  $\Sigma^{\text{OVGF-C}}$ , and their form can be found in e.g. Refs. 188,224. The diagonal partial third-order  $\Sigma^{\text{P3}}$  neglects a number of terms in  $\Sigma^{\text{D3}}$ ,<sup>241,242</sup> requiring separate approximations for the IP and EA, and  $\Sigma^{\text{P3+}}$  introduces a renormalisation factor in some terms.<sup>243</sup> Furthermore,  $\Sigma^{\text{NR2}}$  can be considered a non-diagonal extension to these methods, with the name originating from the effective renormalisation in low-order terms.<sup>74,244</sup> Many other related self-energies can be found, for example those reported in e.g. Ref. 99. An additional perspective on effective renormalisation of the propagator is to perform EP calculations in a basis of Brueckner orbitals, which can have significant effect on those terms in the self-energy that are vanishing.<sup>73,225,245,246</sup> Table 2.1 shows the computational scaling for the various EP self-energies discussed in this section in terms of the number of occupied orbitals  $n_{\text{occ}}$  and virtual orbitals  $n_{\text{vir}}$ .<sup>74,99,233,240,247</sup> The iterative bottleneck represents the scaling of the steps that must be recomputed at each iteration of either an iterative eigensolver or a self-consistent eigenvalue formulation, whilst the non-iterative bottleneck represents the scaling of steps that only need to be calculated once. In most scenarios, this can be separated into the frequency independent parts (non-iterative) and frequency dependent parts (iterative). The CPU bottlenecks are listed in terms of the calculation of a single IP or EA, where  $n_{\text{vir}} \gg n_{\text{occ}}$  is assumed.

## 2.7 Coupled cluster

The coupled cluster (CC) method considers an exponential ansatz for the ground state, which is explicitly size-extensive.<sup>248–255</sup> With respect to a HF reference state we can write this as

$$\left| \Psi_{\text{CC}}^{\text{R}} \right\rangle = e^{\hat{T}} \left| \Psi_{\text{HF}} \right\rangle, \quad (2.131)$$

where we have introduced a cluster operator  $\hat{T}$  that can be expanded in terms of consecutive orders of particle-hole excitations

$$\hat{T} = \hat{T}_1 + \hat{T}_2 + \dots \quad (2.132a)$$

$$= \sum_i^{\text{occ}} \sum_a^{\text{vir}} t_i^a \hat{a}_a \hat{a}_i^\dagger + \sum_{i < j}^{\text{occ}} \sum_{a < b}^{\text{vir}} t_{ij}^{ab} \hat{a}_a \hat{a}_b \hat{a}_j^\dagger \hat{a}_i^\dagger + \dots \quad (2.132b)$$

The operator  $e^{\hat{T}}$  is non-unitary, and therefore the corresponding bra cannot be expressed simply as the adjoint of the ket. Instead, introduce a pair of biorthogonal wavefunctions<sup>68,256</sup>

$$\left\langle \Psi_{\text{CC}}^{\text{L}} \left| \Psi_{\text{CC}}^{\text{R}} \right\rangle = 1, \quad (2.133)$$

where the bra is typically defined as

$$\left\langle \Psi_{\text{CC}}^{\text{L}} \left| = \left\langle \Psi_{\text{HF}} \left| (1 + \hat{\Lambda}) e^{-\hat{T}}, \quad (2.134)$$

where  $\hat{\Lambda}$  is a linear de-excitation operator defined similarly to Equation 2.132

$$\hat{\Lambda} = \hat{\Lambda}_1 + \hat{\Lambda}_2 + \dots \quad (2.135a)$$

$$= \sum_i^{\text{occ}} \sum_a^{\text{vir}} l_a^i \hat{a}_i \hat{a}_a^\dagger + \sum_{i < j}^{\text{occ}} \sum_{a < b}^{\text{vir}} l_{ab}^{ij} \hat{a}_i \hat{a}_j \hat{a}_b^\dagger \hat{a}_a^\dagger + \dots \quad (2.135b)$$

The energy of a CC model can be evaluated by projection against the reference state

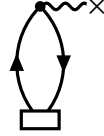
$$E_{\text{CC}} = \left\langle \Psi_{\text{HF}} \left| \hat{H} \left| \Psi_{\text{CC}}^{\text{R}} \right\rangle, \quad (2.136)$$

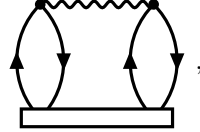
where cluster operators of greater than second-order do not contribute,  $\hat{H}$  being a two-particle operator. Additionally, Brillouin's theorem tells us that  $\left\langle \Psi_{\text{HF}} \left| \hat{H} \hat{T}_1 \left| \Psi_{\text{HF}} \right\rangle = 0$  and therefore we can expand Equation 2.136 to get

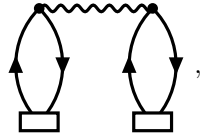
$$E_{\text{CC}} = \left\langle \Psi_{\text{HF}} \left| \left[ \hat{H}, \left( 1 + \hat{T}_2 + \frac{1}{2} \hat{T}_1^2 \right) \right] \left| \Psi_{\text{HF}} \right\rangle \quad (2.137a)$$

$$= \sum_i^{\text{occ}} \sum_a^{\text{vir}} F_{ia} t_i^a + \frac{1}{4} \sum_{ij}^{\text{occ}} \sum_{ab}^{\text{vir}} \langle ij || ab \rangle t_{ij}^{ab} + \frac{1}{2} \sum_{ij}^{\text{occ}} \sum_{ab}^{\text{vir}} \langle ij || ab \rangle t_i^a t_j^b. \quad (2.137b)$$

The corresponding diagrams for these terms are

$$\sum_i^{\text{occ}} \sum_a^{\text{vir}} F_{ia} t_i^a = \text{Diagram (2.138a)}, \quad (2.138a)$$


$$\frac{1}{4} \sum_{ij}^{\text{occ}} \sum_{ab}^{\text{vir}} \langle ij || ab \rangle t_{ij}^{ab} = \text{Diagram (2.138b)}, \quad (2.138b)$$


$$\frac{1}{2} \sum_{ij}^{\text{occ}} \sum_{ab}^{\text{vir}} \langle ij || ab \rangle t_i^a t_j^b = \text{Diagram (2.138c)}, \quad (2.138c)$$


which is the subset of diagrams responsible for the energy in any CC ansatz including at least singly and doubly excited cluster amplitudes. The notation  $\square$  indicates a cluster operator  $\hat{T}$ , with its rank indicated by the number of hole and particle lines entering and exiting it. Projection onto excited wavefunctions produces sets of non-linear equations that can be used to update the cluster amplitudes  $t$  self-consistently, and can be written generally as

$$0 = \langle \Psi_{ij\dots}^{ab\dots} | \hat{H}_N | \Psi_{CC}^R \rangle, \quad (2.139)$$

where the normal-ordered Hamiltonian  $\hat{H}_N$  is defined as

$$\hat{H}_N = \hat{H} - \langle \Psi_{HF} | \hat{H} | \Psi_{HF} \rangle = \hat{H} - E_0. \quad (2.140)$$

This results in a set of equations to be converged, not necessarily variationally, although it is both size-consistent and size-extensive. Whilst the diagrams corresponding to the energy are the same for any ansatz including at least singly and doubly excited cluster operators, the  $\hat{T}_1$  and  $\hat{T}_2$  operators contain different subsets of diagrams for higher-order ansatzes via Equation 2.139. There exist many in-depth discussions of the diagrams contained in Equation 2.139 for different CC ansatzes, which we will not show here.<sup>68,252,257–265</sup> The condition under which the  $\hat{\Lambda}$  amplitudes are optimised can be written in a similar fashion

$$0 = \langle \Psi_{CC}^L | \hat{H}_N | \Psi_{ij\dots}^{ab\dots} \rangle. \quad (2.141)$$

Density matrices can be computed at the level of CC using familiar second quantised expressions, i.e. for the one-body reduced density matrix

$$\gamma_{pq} = \langle \Psi_{CC}^L | \hat{a}_q^\dagger \hat{a}_p | \Psi_{CC}^R \rangle, \quad (2.142a)$$

$$= \langle \Psi_{HF} | (1 + \hat{\Lambda}) e^{-\hat{T}} \hat{a}_q^\dagger \hat{a}_p e^{\hat{T}} | \Psi_{HF} \rangle, \quad (2.142b)$$

$$= \langle \Psi_{HF} | (1 + \hat{\Lambda}) \bar{a}_q^\dagger \bar{a}_p | \Psi_{HF} \rangle, \quad (2.142c)$$

where we have introduced the compact notations  $\bar{a}_p = e^{-\hat{T}} \hat{a}_p e^{\hat{T}}$  and  $\bar{a}_p^\dagger = e^{-\hat{T}} \hat{a}_p^\dagger e^{\hat{T}}$ , noting that  $e^{\hat{T}} e^{-\hat{T}} = 1$ . Equivalent expressions can be written for higher-order density matrices such as the second-order reduced density matrix  $\Gamma_{pqrs}$ , and these expressions can be evaluated algebraically and diagrammatically. By default, the density matrices are non-Hermitian as a result of the non-Hermitian CC ansatz.

### 2.7.1 Equation-of-motion coupled cluster

The equation-of-motion coupled cluster (EOM-CC) method can be used to target a state in a linear operation starting from a CC ground state wavefunction.<sup>68,256,266–270</sup> This concept can be readily applied to probe the IP, EA, and electron excitation (EE) at the level of a particular CC ansatz. Considering a target state  $\Psi_k$  in addition to the ground state  $\Psi_{CC}$ , we seek to determine the difference in energies  $\omega_k = E_k - E_{HF}$ . This can be expressed considering a pair of Schrödinger equations

$$\hat{H} |\Psi_{CC}\rangle = E_{CC} |\Psi_{CC}\rangle, \quad (2.143a)$$

$$\hat{H} |\Psi_k\rangle = E_k |\Psi_k\rangle. \quad (2.143b)$$

where the target excited state is related to the ground state wavefunctions by linear operators  $\hat{R}$  and  $\hat{L}$ , whose form depends on the character of the desired target state. The expressions can be manipulated to arrive at the EOM-CC expressions

$$\left[ \bar{H}, \hat{R}_k \right] |\Psi_{HF}\rangle = (E_k - E_{CC}) \hat{R}_k |\Psi_{HF}\rangle = \omega_k \hat{R}_k |\Psi_{HF}\rangle, \quad (2.144)$$

which can be interpreted as the (manifestly non-Hermitian) matrix eigenvalue problem  $\bar{\mathbf{H}}\mathbf{R} = \mathbf{R}\omega$ , with the left-handed analogue possessing the same energy, i.e.  $\mathbf{L}^\dagger \bar{\mathbf{H}} = \mathbf{L}^\dagger \omega$ . The right-hand excitation operators for EE-EOM-CC, IP-EOM-CC and EA-EOM-CC can be written

$$\hat{R}_k^{EE} = \sum_i^{\text{occ}} \sum_a^{\text{vir}} r_i^a \hat{a}_a^\dagger \hat{a}_i + \sum_{i<j}^{\text{occ}} \sum_{a<b}^{\text{vir}} r_{ij}^{ab} \hat{a}_a^\dagger \hat{a}_b^\dagger \hat{a}_j \hat{a}_i + \dots, \quad (2.145a)$$

$$\hat{R}_k^{IP} = \sum_i^{\text{occ}} r_i \hat{a}_i + \sum_{i<j}^{\text{occ}} \sum_a^{\text{vir}} r_{ij}^a \hat{a}_a^\dagger \hat{a}_j \hat{a}_i + \dots, \quad (2.145b)$$

$$\hat{R}_k^{EA} = \sum_a^{\text{vir}} r^a \hat{a}_a^\dagger + \sum_i^{\text{occ}} \sum_{a<b}^{\text{vir}} r_i^{ab} \hat{a}_a^\dagger \hat{a}_b^\dagger \hat{a}_i + \dots \quad (2.145c)$$

The left-handed excitation operators have the same form and can be read from Equation 2.145 with the substitutions  $\hat{R} \leftrightarrow \hat{L}$  and  $r \leftrightarrow l$ . Typically, one expands  $\hat{R}$  (or  $\hat{L}$ ) to the same truncation as the ground state CC cluster operator  $\hat{T}$ . The eigenfunctions are biorthogonal and when appropriately normalised satisfy

$$\left\langle \Psi_{HF} \left| \hat{L}_k \hat{R}_m \right| \Psi_{HF} \right\rangle = \delta_{km}, \quad (2.146)$$

and give a resolution of the identity

$$1 = \sum_k \hat{R}_k |\Psi_{\text{HF}}\rangle \langle \Psi_{\text{HF}}| \hat{L}_k. \quad (2.147)$$

This relationship allows us to connect to Green's function theory with the Lehmann representation for a non-Hermitian single-particle Green's function<sup>270</sup>

$$G_{pq}(\omega + i0^+) = \sum_k \frac{u_{pk}^L u_{qk}^R}{\omega - \omega_k + i0^+}, \quad (2.148)$$

where the Dyson orbitals are defined as

$$u_{pk}^L = \langle \Psi_{\text{HF}} | \hat{L}_k \bar{a}_p | \Psi_{\text{HF}} \rangle, \quad (2.149a)$$

$$u_{qk}^R = \langle \Psi_{\text{HF}} | (1 + \hat{\Lambda}) \bar{a}_q^\dagger \hat{R}_k | \Psi_{\text{HF}} \rangle, \quad (2.149b)$$

which are fully separable into occupied and virtual components since they only depend on either the  $\hat{R}$  and  $\hat{L}$  corresponding to IPs or EAs.

The eigenvalue problem of Equation 2.144 can be considered that of an effective self-energy upfolded into its configuration space as detailed in Section 2.4.2. This effective self-energy is not equal to the *true* CC self-energy (the identity of which will be discussed in Section 2.7.2) by virtue of the EOM-CC formalism. A principal difference between these self-energies manifests in the same fashion as the 'non-Dyson' approximation to ADC discussed in Section 2.5.2. To recap, the small space of  $\bar{\mathbf{H}}$  spans only occupied (virtual) MOs in the case of  $\hat{R}^{\text{IP}}$  ( $\hat{R}^{\text{EA}}$ ), and the virtual (occupied) self-energy does not contribute to the dynamic part of the self-energy when folded down into those spanned MOs. For a detailed discussion of these differences in terms of diagrams and time orderings, the reader should refer to Ref. 270.

## 2.7.2 Green's function coupled cluster

Recalling the expressions for the single-particle Green's function in frequency space shown in Equation 2.67, the Green's function in the case of a CC ground state, defining the Green's function coupled cluster (GF-CC) method, can be written as<sup>128,130,131,271–282</sup>

$$\begin{aligned} G_{pq}(\omega + i0^+) &= \left\langle \Psi_{\text{CC}}^L \left| \hat{a}_q^\dagger \left[ \omega + \hat{H}_N + i0^+ \right]^{-1} \hat{a}_p \right| \Psi_{\text{CC}}^R \right\rangle \\ &+ \left\langle \Psi_{\text{CC}}^L \left| \hat{a}_p \left[ \omega - \hat{H}_N + i0^+ \right]^{-1} \hat{a}_q^\dagger \right| \Psi_{\text{CC}}^R \right\rangle, \end{aligned} \quad (2.150a)$$

$$\begin{aligned} &= \left\langle \Psi_{\text{HF}} \left| (1 + \hat{\Lambda}) \bar{a}_q^\dagger \left[ \omega + \bar{H}_N + i0^+ \right]^{-1} \bar{a}_p \right| \Psi_{\text{HF}} \right\rangle \\ &+ \left\langle \Psi_{\text{HF}} \left| (1 + \hat{\Lambda}) \bar{a}_p \left[ \omega - \bar{H}_N + i0^+ \right]^{-1} \bar{a}_q^\dagger \right| \Psi_{\text{HF}} \right\rangle, \end{aligned} \quad (2.150b)$$

where the signs in front of the respective  $\bar{H}_N$  correct the sign of the poles of the Green's function in the case of IPs. It is then necessary to introduce a pair of frequency-dependent many-body

operators that can be expanded perturbatively

$$\begin{aligned}\hat{X}_p(\omega) &= \hat{X}_{p,1}(\omega) + \hat{X}_{p,2}(\omega) + \dots \\ &= \sum_i^{\text{occ}} [x^i(\omega)]_p \hat{a}_i + \sum_{i<j}^{\text{occ}} \sum_a^{\text{vir}} [x_a^{ij}(\omega)]_p \hat{a}_a^\dagger \hat{a}_j \hat{a}_i + \dots,\end{aligned}\quad (2.151)$$

$$\begin{aligned}\hat{Y}_p(\omega) &= \hat{Y}_{p,1}(\omega) + \hat{Y}_{p,2}(\omega) + \dots \\ &= \sum_a^{\text{vir}} [y^a(\omega)]_p \hat{a}_a^\dagger + \sum_i^{\text{occ}} \sum_{a<b}^{\text{vir}} [y_i^{ab}(\omega)]_p \hat{a}_a^\dagger \hat{a}_b^\dagger \hat{a}_i + \dots,\end{aligned}\quad (2.152)$$

yielding a system of linear equations in frequency space

$$P_X (\omega + \bar{H}_N + i0^+) X_p |\Psi_{\text{HF}}\rangle = P_X \bar{a}_p |\Psi_{\text{HF}}\rangle, \quad (2.153a)$$

$$P_Y (\omega - \bar{H}_N + i0^+) Y_p |\Psi_{\text{HF}}\rangle = P_Y \bar{a}_p^\dagger |\Psi_{\text{HF}}\rangle. \quad (2.153b)$$

The projectors  $P_X$  and  $P_Y$  project onto appropriate excited configurations

$$\begin{aligned}P_X &= P_{X,1} + P_{X,2} + \dots \\ &= \sum_i^{\text{occ}} \hat{a}_i |\Psi_{\text{HF}}\rangle \langle \Psi_{\text{HF}} | \hat{a}_i^\dagger + \sum_{i<j}^{\text{occ}} \sum_a^{\text{vir}} \hat{a}_a^\dagger \hat{a}_j \hat{a}_i |\Psi_{\text{HF}}\rangle \langle \Psi_{\text{HF}} | \hat{a}_i^\dagger \hat{a}_j^\dagger \hat{a}_a,\end{aligned}\quad (2.154a)$$

$$\begin{aligned}P_Y &= P_{Y,1} + P_{Y,2} + \dots \\ &= \sum_a^{\text{vir}} \hat{a}_a^\dagger |\Psi_{\text{HF}}\rangle \langle \Psi_{\text{HF}} | \hat{a}_a + \sum_i^{\text{occ}} \sum_{a<b}^{\text{vir}} \hat{a}_a^\dagger \hat{a}_b^\dagger \hat{a}_i |\Psi_{\text{HF}}\rangle \langle \Psi_{\text{HF}} | \hat{a}_i^\dagger \hat{a}_b \hat{a}_a.\end{aligned}\quad (2.154b)$$

These equations allow the construction of Equation 2.150 using the  $X$  and  $Y$  operators determined at a given frequency

$$\begin{aligned}G_{pq}(\omega) &= \left\langle \Psi_{\text{HF}} \left| (1 + \hat{\Lambda}) \bar{a}_q^\dagger X_p(\omega) \right| \Psi_{\text{HF}} \right\rangle \\ &\quad + \left\langle \Psi_{\text{HF}} \left| (1 + \hat{\Lambda}) \bar{a}_p Y_q(\omega) \right| \Psi_{\text{HF}} \right\rangle.\end{aligned}\quad (2.155)$$

Typically, one truncates the  $\hat{X}$ ,  $\hat{Y}$ , and respective  $P$  to the same order as the  $\hat{T}$  and  $\hat{\Lambda}$  operators. For example, at the level of coupled cluster singles and doubles (CCSD) the operators are truncated to  $1h$  and  $2h1p$  spaces for the IP, and  $1p$  and  $1h2p$  spaces for the EA. This ensures that the fluctuation space describing singly-charged excitations is not complete, but consistent in its description of both the ground state and the excited state. As a result, applying the Galitskii–Migdal formula using the Green’s function obtained in the Green’s function coupled cluster singles and doubles (GF-CCSD) method does not yield an energy that agrees with the CCSD energy calculated in the canonical fashion, which requires dynamical fluctuations into the  $3h2p$  space.<sup>270–272</sup>

## 2.8 *GW* approximation

Hedin's equations present a self-consistent formalism for the single-particle Green's function in the case of a screened Coulomb interaction  $W$ , rather than the bare interaction  $V$  given by the ERIs.<sup>76,283–296</sup> The *GW* approximation seeks to solve these equations with the so-called vertex corrections  $\Gamma$  equal to identity. The screened interaction can be understood by its own Dyson-like equation

$$W = V + V\chi V, \quad (2.156)$$

which can be interpreted diagrammatically as

$$W = \text{~~~~~}, \quad (2.157a)$$

$$V + V\chi V = \text{~~~~~} + \text{~~~~~}, \quad (2.157b)$$

where  $\chi$  is the reducible polarisation propagator. In *GW*, the self-energy is defined by the integral

$$\Sigma^{GW}(\mathbf{x}_1, \mathbf{x}_2; \omega_1) = \frac{i}{2\pi} \int d\omega_2 e^{i0^+ \omega_2} G(\mathbf{x}_1, \mathbf{x}_2; \omega_1 + \omega_2) W_{\text{corr}}(\mathbf{x}_2, \mathbf{x}_1; \omega_2), \quad (2.158)$$

where  $W_{\text{corr}} = W - V$  indicates the correlation part of  $W$ , and  $\chi$  can be written as a sum over its poles

$$\chi(\mathbf{x}_1, \mathbf{x}_2; \omega) = \sum_n \frac{\rho_n(\mathbf{x}_1)\rho_n^*(\mathbf{x}_2)}{\omega - \Omega_n + i0^+} + \sum_n \frac{\rho_n(\mathbf{x}_1)\rho_n^*(\mathbf{x}_2)}{\omega + \Omega_n - i0^+}, \quad (2.159)$$

where the neutral excitations  $\Omega$  possess transition densities  $\rho$ , and  $n$  enumerates the excitations. These equations lead to an analytic expression for the self-energy

$$\Sigma_{pq}^{GW}(\omega) = \sum_n \sum_i^{\text{occ}} \frac{(pi|n)(n|qi)}{\omega - (\epsilon_i - \Omega_n) - i0^+} + \sum_n \sum_a^{\text{vir}} \frac{(pa|n)(n|qa)}{\omega - (\epsilon_a + \Omega_n) + i0^+}, \quad (2.160)$$

where  $\epsilon$  are the pole energies of  $G$  entering Equation 2.158, and the three-centre integrals  $(n|pq)$  are defined by

$$(n|pq) = \int d\mathbf{x}_1 d\mathbf{x}_2 \rho_n(\mathbf{x}_1) \frac{1}{|\mathbf{r}_1 - \mathbf{r}_2|} \psi_p^*(\mathbf{x}_1) \psi_q(\mathbf{x}_2). \quad (2.161)$$

The transition densities can be defined as

$$\rho_n(\mathbf{x}) = \langle \Psi_{\text{HF}} | \hat{n}(\mathbf{x}) | \Psi_n \rangle = \sum_{pq} \psi_p^*(\mathbf{x}) \psi_q(\mathbf{x}) \langle \Psi_{\text{HF}} | \hat{a}_p^\dagger \hat{a}_q | \Psi_n \rangle, \quad (2.162)$$



and as such one must construct the set of  $\Omega_n$  and  $\Psi_n$  in order to determine the self-energy. The two parts of the self-energy can be interpreted diagrammatically as

$$\sum_n \sum_i^{\text{occ}} \frac{(pi|n)(n|qi)}{\omega - (\epsilon_i - \Omega_n)} = \text{Diagram (2.163a)}, \quad (2.163a)$$

$$\sum_n \sum_a^{\text{vir}} \frac{(pa|n)(n|qa)}{\omega - (\epsilon_a + \Omega_n)} = \text{Diagram (2.163b)}, \quad (2.163b)$$

where the infinitesimals used to regularise Equation 2.158 have been omitted. The polarisability is typically determined using the (direct) RPA approximation starting from the eigenproblem<sup>297–301</sup>

$$\begin{bmatrix} \mathbf{A} & \mathbf{B} \\ -\mathbf{B}^* & -\mathbf{A}^* \end{bmatrix} \begin{bmatrix} \mathbf{X}^n \\ \mathbf{Y}^n \end{bmatrix} = \Omega_n \begin{bmatrix} \mathbf{X}^n \\ \mathbf{Y}^n \end{bmatrix}, \quad (2.164)$$

where the eigenvectors  $\mathbf{X}$  and  $\mathbf{Y}$  define the amplitudes  $\rho$  of the polarisation propagator. The transition amplitudes can then be computed as

$$(n|pq) = \sum_i^{\text{occ}} \sum_a^{\text{vir}} [X_{ia}^n \langle ip|aq \rangle + Y_{ia}^n \langle ap|i q \rangle]. \quad (2.165)$$

In the case of the time-dependent Hartree dielectric function, the matrix elements of Equation 2.164 can be written

$$A_{ia,jb} = (\epsilon_a - \epsilon_i) \delta_{ab} \delta_{ij} + \langle aj|ib \rangle, \quad (2.166a)$$

$$B_{ia,jb} = \langle ij|ab \rangle. \quad (2.166b)$$

The TDA can be defined by setting  $\mathbf{B} = \mathbf{0}$ , effectively decoupling the excitation and de-excitation spaces.<sup>302</sup> Whilst RPA constitutes a correlated ground state, without this coupling the de-excitation is symmetric with respect to excitation and therefore cannot induce correlation into the ground state.<sup>303,304</sup> RPA is closely connected to CC theory.<sup>270,304–306</sup>

By inspection of Equations 2.160 to 2.162 one can infer that in the case of  $\Psi_n = \Psi_{\text{HF}}$ ,  $\Omega_n = \epsilon_a - \epsilon_i$ , and  $\epsilon_k = \epsilon_k$ , the self-energy in Equation 2.160 can be summarised by the diagrams that are topologically identical to those in Equation 2.126. The first two of these conditions can be interpreted as approximating the polarisability to be equal to its value at the level of HF, and the third condition the assumption that  $G = G_0$ . The conclusion of this observation is that  $GW$  is simply second-order perturbation theory in the case of a screened Coulomb interaction and neglect of second-order exchange. The bare second-order exchange term can be reintroduced to the self-energy by instead employing the RPax, within which ERIs of the  $GW$  self-energy are antisymmetrised as they are in the standard second-order self-energy. This is known to suffer from complex solutions in the case of unstable reference states.<sup>307</sup> The so-called second-order screened

exchange (SOSEX) extension to *GW* can be used to introduce a screened exchange interaction that remedies these instabilities and includes additional diagrams.<sup>308–311</sup>

Ref. 312 details parameters for the self-energies in the case of both TDA and RPA screening, for TDA these are

$$V_{p,ija} = \langle pa|ij \rangle, \quad (2.167a)$$

$$V_{p,iab} = \langle pi|ba \rangle, \quad (2.167b)$$

$$K_{ija,klb} = \delta_{ik}\delta_{jl}\delta_{ab}(\varepsilon_i + \varepsilon_j - \varepsilon_a), \quad (2.167c)$$

$$K_{iab,jcd} = \delta_{ij}\delta_{ac}\delta_{bd}(\varepsilon_a + \varepsilon_b - \varepsilon_i), \quad (2.167d)$$

$$C_{ija,klb} = -\langle jb|al \rangle \delta_{ik}, \quad (2.167e)$$

$$C_{iab,jcd} = \langle aj|ic \rangle \delta_{bd}. \quad (2.167f)$$

This is closely related to the *2p1h*-TDA method discussed in Section 2.6. In the case of RPA, Ref. 312 details the operations contributing to the dot-product of the self-energy matrix with a vector. It is important to note that the dot-product of the self-energy matrix and a vector in the case of TDA can be performed as  $\mathcal{O}(n_{\text{MO}}^4)$  if one employs a density fitting (DF) scheme, leading to an efficient route to perform non-self-consistent *GW* in the case of TDA.

The most common form of *GW* neglects self-consistency in both *G* and *W* and is called  $G_0W_0$ , and is known to be accurate and efficient.<sup>215,295,296,313–318</sup> This can be seen from the additional bare interaction terms in the **C** blocks compared to the second-order self-energy, corresponding to the insertion of the bare form of Equation 2.157b into the second-order diagrams. Further approximations ignore just one of the self-consistencies leading to  $GW_0$  and  $G_0W$ , with other partial self-consistencies existing.<sup>215,285,319–333</sup> Unless explicitly referred to as self-consistent, the name *GW* will be used for the non-self-consistent variant.

## 2.9 Configuration interaction

FCI expands the wavefunction in all possible excited state determinants<sup>57,334</sup>

$$\begin{aligned}
 |\Phi\rangle = & c_0 |\Psi_{\text{HF}}\rangle + \sum_i^{\text{occ}} \sum_a^{\text{vir}} c_i^a |\Psi_i^a\rangle + \sum_{i<j}^{\text{occ}} \sum_{a<b}^{\text{vir}} c_{ij}^{ab} |\Psi_{ij}^{ab}\rangle \\
 & + \sum_{i<j<k}^{\text{occ}} \sum_{a<b<c}^{\text{vir}} c_{ijk}^{abc} |\Psi_{ijk}^{abc}\rangle + \dots
 \end{aligned} \tag{2.168}$$

For a system of  $n_{\text{MO}}$  spin orbitals of which  $n_{\text{occ}}$  are occupied and  $n_{\text{vir}}$  unoccupied, the number of determinants entering the  $n$ th term of Equation 2.168 (where we consider the  $c_0$  term to be the zeroth term) equals

$$\binom{n_{\text{occ}}}{n} \binom{n_{\text{MO}} - n_{\text{occ}}}{n}, \tag{2.169}$$

which even for modest system sizes is a prohibitively large number. The FCI matrix can be written

$$\begin{bmatrix}
 \langle 0|\hat{H}|0\rangle & 0 & \langle 0|\hat{H}|D\rangle & 0 & 0 & \dots \\
 0 & \langle S|\hat{H}|S\rangle & \langle S|\hat{H}|D\rangle & \langle S|\hat{H}|T\rangle & 0 & \dots \\
 \langle D|\hat{H}|0\rangle & \langle D|\hat{H}|S\rangle & \langle D|\hat{H}|D\rangle & \langle D|\hat{H}|T\rangle & \langle D|\hat{H}|Q\rangle & \dots \\
 0 & \langle T|\hat{H}|S\rangle & \langle T|\hat{H}|D\rangle & \langle T|\hat{H}|T\rangle & \langle T|\hat{H}|Q\rangle & \dots \\
 0 & 0 & \langle Q|\hat{H}|D\rangle & \langle Q|\hat{H}|T\rangle & \langle Q|\hat{H}|Q\rangle & \dots \\
 \vdots & \vdots & \vdots & \vdots & \vdots & \ddots
 \end{bmatrix}, \tag{2.170}$$

where a compact notation has been used such that  $|0\rangle = |\Psi_{\text{HF}}\rangle$ ,  $|S\rangle = |\Psi_i^a\rangle$ , and so forth. Some observations can be made from the structure of Equation 2.170:

- As a consequence of Brillouin's theorem (see Appendix B),  $\langle 0|\hat{H}|S\rangle = 0$ . This manifests in no *direct* coupling with singly excited determinants and the ground state wavefunction, and therefore, little effect on the ground state energy. In contrast, the doubly excited configurations are the only ones that couple *directly* with the ground state and therefore are typically of the greatest importance in describing the ground state energy.
- Matrix elements of the Hamiltonian between determinants who differ in more than two spin orbitals are zero. This results in  $\langle 0|\hat{H}|T\rangle = 0$ ,  $\langle S|\hat{H}|Q\rangle = 0$ , etc., but also in sparsity of the blocks away from the diagonal such as  $\langle D|\hat{H}|Q\rangle$  for which most of the possible configurations do not satisfy this condition.

The  $n$ th eigenvalue of Equation 2.170 gives an upper bound to the energy of the  $n$ -tuply excited state of the system, and is exact in the limit of a complete basis and within the Born–Oppenheimer approximation. As such, the difference between  $E_{\text{HF}}$  and the lowest eigenvalue gives the exact correlation energy within that basis. As a result of Equation 2.169, the size of Equation 2.170 grows exponentially with system size. This makes FCI only computationally feasible for the smallest systems, where one employs typically the Davidson algorithm to avoid storage of Equation 2.170 on

memory. A considerable number of approximations, numerical techniques, and simple truncations exist to reduce the computational effort required to perform CI calculations, none of which will be discussed in the present work.<sup>90,335-337</sup> One feature of truncated CI that we note is that it is not, in the trivial case, size-extensive; this in part affords CC the supremacy it has amassed in the field of quantum chemistry. The single-particle Green's function can be defined according to the (appropriately normalised) excited state determinants using Equation 2.67, where  $\Psi_0^N$  and  $E_0^N$  are the ground state wavefunction and energy calculated at the level of FCI. This represents a summation over all possible Goldstone diagrams for an  $N$ -electron system to infinite order.



## Chapter 3

# Block Lanczos

### 3.1 Introduction

This Chapter will begin by introducing the Lanczos algorithm, followed by the subsequent extension to the block Lanczos algorithm. The Lanczos algorithm is an iterative approach to solving the eigenproblem, named after Cornelius Lanczos who formulated the original idea in a 1950 publication.<sup>93</sup> Subsequent improvements in the numerical stability have resulted in a popular method, particularly when applied to the calculation of extremal eigenvalues, and which is very effective when applied to sparse matrices. The block Lanczos algorithm extends the Lanczos procedure to allow the account of multiplicity in eigenvalues. Whilst the single-vector Lanczos algorithm considers the orthogonal projection of the particular matrix onto a *tridiagonal* matrix within a subspace, the block Lanczos algorithm considers block vectors and the projection onto a *block tridiagonal* matrix, and this procedure will also be outlined in this Chapter. Therein, the utility of block Lanczos will be described in the context of solving the Dyson equation in Green's function perturbation theories. Much of this is based on the work of Refs. 44,45. Several works have applied the block Lanczos procedure to many-body problems, and more specifically problems of determining the Green's function, however in many cases the requirement of vectors spanning the entire configuration space of the particular self-energy do not offer particularly great applicability to larger problems.

We then shift our focus to reformulating the block Lanczos algorithm within the context of solving the Dyson equation, leveraging the spectral moments introduced in Section 2.4.4. The reformulation in Section 3.5 was introduced in the simplest example in Ref. 51, and was therein extended to arbitrary numbers of Lanczos iterations for applications in work yet to be published. The second reformulation from the perspective of moments of the Green's function in Section 3.6 was originally developed by P. V. Sriluckshmy for the work discussed in Ref. 338, and therein extended to the case of non-Hermitian Green's functions by the author for Ref. 339. These two algorithms permit an efficient approach to applying block Lanczos to the solution of the Dyson equation, exploiting similar benefits to other existing solvers, and permitting tractable self-consistency in an upfolded representation. They are not without downsides, mostly originating in the exponentiation of the spectral parameters in the calculation of the moments, which will also be discussed.

## 3.2 Lanczos algorithm

The Lanczos algorithm is an iterative eigensolver originally formulated by Cornelius Lanczos, and later by Ojalvo and Newman to improve the numerical stability.<sup>93,94</sup> The input to the algorithm is the function

$$\mathbf{q} \mapsto \mathbf{M}\mathbf{q}, \quad (3.1)$$

where  $\mathbf{M}$  is a Hermitian matrix of dimension  $n$ ,<sup>a</sup> that can act upon an arbitrary state vector  $\mathbf{q}$ . The algorithm seeks to construct a vector space called a Krylov subspace  $\mathcal{K}$

$$\mathcal{K}_i(\mathbf{M}, \mathbf{q}) = \text{span}(\mathbf{q}, \mathbf{M}\mathbf{q}, \mathbf{M}^2\mathbf{q}, \dots, \mathbf{M}^{i-1}\mathbf{q}), \quad (3.2)$$

into which  $\mathbf{M}$  can then be projected, yielding a new matrix whose eigenvalues are approximations to those of  $\mathbf{M}$ . For an arbitrary initial unit vector  $\mathbf{q}_1 \in \mathbb{C}^n$  the algorithm proceeds as

$$\mathbf{r}_i = \mathbf{M}\mathbf{q}_i, \quad (3.3a)$$

$$\alpha_i = \mathbf{v}_i^\dagger \mathbf{r}_i, \quad (3.3b)$$

$$\mathbf{r}_i = \mathbf{r}_i - \beta_{i-1}\mathbf{q}_{i-1} - \alpha_i\mathbf{q}_i, \quad (3.3c)$$

$$\beta_i = \|\mathbf{r}_i\|, \quad (3.3d)$$

$$\mathbf{q}_{i+1} = \mathbf{r}_i/\beta_i, \quad (3.3e)$$

with  $\beta_0 = 0$  and  $\mathbf{q}_0$  a zero vector. This can be summarised by the three-term recurrence

$$\mathbf{M}\mathbf{q}_i = \beta_{i-1}\mathbf{q}_{i-1} + \alpha_i\mathbf{q}_i + \beta_i\mathbf{q}_{i+1}. \quad (3.4)$$

The values  $\alpha$  and  $\beta$  then define a tridiagonal matrix

$$\mathbf{T} = \begin{bmatrix} \alpha_1 & \beta_1 & & & 0 \\ \beta_1 & \alpha_2 & \beta_2 & & \\ & \beta_2 & \alpha_3 & \ddots & \\ & & \ddots & \ddots & \beta_{i-1} \\ 0 & & & \beta_{i-1} & \alpha_i \end{bmatrix}, \quad (3.5)$$

which can then be diagonalised. In the case of  $i = n$  and exact arithmetic, the eigenvalues of  $\mathbf{T}$  are those of  $\mathbf{M}$ , and the eigenvectors of  $\mathbf{T}$  can be transformed into those of  $\mathbf{M}$  using the Lanczos vectors  $\mathbf{q}$ . In the case of  $i \ll n$ , the eigenspectrum of  $\mathbf{T}$  can be viewed as a compression of that of  $\mathbf{M}$ , with particular emphasis on the preservation of extremal eigenvalues at the upper and lower regions of the eigenspectrum. Under floating point arithmetic, the Lanczos vectors  $\mathbf{q}$  quickly suffer from a loss in orthogonality, whereas they should in principle form an orthonormal basis. This can also result in a linearly dependent  $\mathbf{q}$  and hence spurious eigenvalues, and the problem is propagated through successive iterations. Computer implementations of the Lanczos algorithm must typically employ methods to remedy this loss in orthogonality, which have presented a large



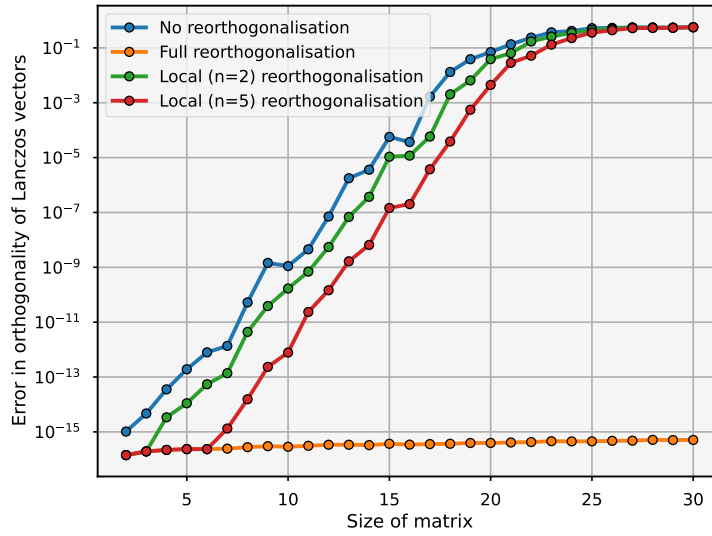


Figure 3.1: Loss in orthogonality for the fully converged Lanczos algorithm for a number of matrix sizes, with four different reorthogonalisation schemes. No reorthogonalisation does not change the vectors, full reorthogonalisation enforces orthogonality of each new vector with *every* previous vector, whilst the local schemes enforce it with the previous  $n$  vectors. Random Hermitian matrices were generated, and each point is the mean over 100 of such matrices, where elements are double precision (64 bit) floating point values.

area of research in the past.<sup>341</sup> Whilst we will not review the details of these schemes, Figure 3.1 shows the difference in the loss of orthogonality with some naive reorthogonalisation schemes, which are not optimal in practice. The full reorthogonalisation with every previous vector predictably results in a constantly (numerically) zero error in the orthogonality of the Lanczos vectors, whereas the lack of reorthogonalisation quickly results in very large errors. Reorthogonalisation with the previous  $n$  vectors is not sufficient for the single-vector Lanczos method, only having an effect in extremely small matrices close to  $n$  in size.

Consider the matrix of Lanczos vectors  $\mathbf{q}^{(j)} = [\mathbf{q}_1, \mathbf{q}_2, \dots, \mathbf{q}_j]$  that satisfies the basis  $\mathcal{K}_j(\mathbf{M}, \mathbf{q})$ , i.e. transforms  $\mathbf{M}$  into the matrix  $\mathbf{T}^{(j)}$  denoting the truncation of  $\mathbf{T}$  up to  $\alpha_j$ . We can define a truncation of  $\mathbf{M}$  as its projection into this space

$$\begin{aligned} \mathbf{M}^{(j)} &= \mathbf{q}^{(j)} \mathbf{T}^{(j)} \mathbf{q}^{(j)\dagger} \\ &= \mathbf{q}^{(j)} \mathbf{q}^{(j)\dagger} \mathbf{M} \mathbf{q}^{(j)} \mathbf{q}^{(j)\dagger}, \end{aligned} \quad (3.6)$$

where for the sake of the following arguments we will assume  $j < n$  and exact arithmetic. Considering also the residual  $\mathbf{W}^{(j)}$  such that  $\mathbf{M} = \mathbf{M}^{(j)} + \mathbf{W}^{(j)}$ , we obviously have  $\mathbf{M}^{(n)} = \mathbf{M}$  and  $\mathbf{W}^{(n)} = \mathbf{0}$  at full convergence of the Lanczos algorithm. One can then use Equation 3.4 to

<sup>341</sup>The Lanczos method can be considered as a special case of the Arnoldi method in the case of a Hermitian matrix.<sup>340</sup>

show that<sup>44</sup>

$$\mathbf{q}_{l'}^\dagger \mathbf{M}^k \mathbf{q}_l = 0 \quad \forall l' > l + k, \quad (3.7a)$$

$$\mathbf{W}^{(j)} \mathbf{q}_l = 0 \quad \forall l \leq j - 1, \quad (3.7b)$$

$$\mathbf{q}_{l'}^\dagger \mathbf{W}^{(j)} \mathbf{q}_l = 0 \quad \forall l, l' \leq j, \quad (3.7c)$$

which leads to

$$\mathbf{W}^{(j)} \mathbf{M}^k \mathbf{q}_1 = 0 \quad \forall 0 \leq k \leq j - 2, \quad (3.8a)$$

$$\mathbf{q}_1^\dagger \mathbf{M}^{k'} \mathbf{W}^{(j)} \mathbf{M}^k \mathbf{q}_1 = 0 \quad \forall 0 \leq k, k' \leq j - 1, \quad (3.8b)$$

and finally to the relationships with which we are concerned

$$\left( \mathbf{M}^{(j)} \right)^k \mathbf{q}_1 = \mathbf{M}^k \mathbf{q}_1 \quad \forall 0 \leq k \leq j - 1, \quad (3.9a)$$

$$\mathbf{q}_1^\dagger \left( \mathbf{M}^{(j)} \right)^k \mathbf{q}_1 = \mathbf{q}_1^\dagger \mathbf{M}^k \mathbf{q}_1 \quad \forall 0 \leq k \leq 2j - 1. \quad (3.9b)$$

The result in Equation 3.9b indicates an important relationship in the present work. It tells us that a truncated Lanczos algorithm exactly preserves the first  $2j - 2$  (up to order  $2j - 1$ ) moments of  $\mathbf{M}$ , with respect to starting vector  $\mathbf{q}_1$ , and  $\mathbf{M}^{(j)}$  can be considered an optimal approximation to  $\mathbf{M}$  in the context of Equations 3.9a and 3.9b. In fact, there is no Hermitian rank  $j$  approximation that exactly preserves moment orders higher than does  $\mathbf{M}^{(j)}$ .<sup>44</sup>

### 3.3 Block Lanczos algorithm

Instead of a single initial vector  $\mathbf{q}$ , consider the action of a matrix  $\mathbf{M}$  upon a block vector  $\mathbf{Q} = [\mathbf{q}_1, \mathbf{q}_2, \dots, \mathbf{q}_b]$ <sup>43,341–345</sup>

$$\mathbf{Q} \mapsto \mathbf{M}\mathbf{Q}. \quad (3.10)$$

The subspace we seek to construct is

$$\mathcal{K}_i(\mathbf{M}, \mathbf{Q}) = \text{span}(\mathbf{Q}, \mathbf{M}\mathbf{Q}, \mathbf{M}^2\mathbf{Q}, \dots, \mathbf{M}^{i-1}\mathbf{Q}), \quad (3.11)$$

the projection of  $\mathbf{M}$  into which results in a matrix that is block tridiagonal rather than tridiagonal. For an initial block of vectors with orthonormal columns  $\mathbf{Q}_1 \in \mathbb{C}^n$  the algorithm proceeds as

$$\mathbf{R}_i = \mathbf{M}\mathbf{Q}_i, \quad (3.12a)$$

$$\mathbf{A}_i = \mathbf{Q}_i^\dagger \mathbf{R}_i, \quad (3.12b)$$

$$\mathbf{R}_i = \mathbf{R}_i - \mathbf{Q}_i \mathbf{A}_i - \mathbf{Q}_{i-1} \mathbf{B}_{i-1}, \quad (3.12c)$$

$$\mathbf{Q}_{i+1} \mathbf{B}_i^\dagger = \mathbf{R}_i, \quad (3.12d)$$

where Equation 3.12d is a QR factorisation of  $\mathbf{R}_i$ . We can again summarise this using a three-term recurrence

$$\mathbf{M}\mathbf{Q}_i = \mathbf{Q}_{i-1} \mathbf{B}_{i-1} + \mathbf{Q}_i \mathbf{A}_i + \mathbf{Q}_{i+1} \mathbf{B}_i^\dagger, \quad (3.13)$$

and the resulting block tridiagonal matrix has the form

$$\mathbf{T} = \begin{bmatrix} \mathbf{A}_1 & \mathbf{B}_1 & & & \mathbf{0} \\ \mathbf{B}_1^\dagger & \mathbf{A}_2 & \mathbf{B}_2 & & \\ & \mathbf{B}_2^\dagger & \mathbf{A}_3 & \ddots & \\ & & \ddots & \ddots & \mathbf{B}_{i-1} \\ \mathbf{0} & & & \mathbf{B}_{i-1}^\dagger & \mathbf{A}_i \end{bmatrix}. \quad (3.14)$$

We note that there is an additional variant known as ‘banded’ Lanczos, which is identical to block Lanczos in exact arithmetic but exhibits some operational differences in non-exact arithmetic.<sup>346,347</sup> We will only consider block Lanczos here as it is a more convenient formulation of the algorithm in the context of the present work. The block variant was originally formulated to identify the multiplicity of degenerate eigenvalues, not accounted for in the Lanczos algorithm.

We can proceed with a similar analysis of the conserving properties of the block Lanczos algorithm as in Section 3.2 by defining again a matrix of (block) Lanczos vectors  $\mathbf{Q}^{(j)} = [\mathbf{Q}_1, \mathbf{Q}_2, \dots, \mathbf{Q}_j]$  satisfying the basis  $\mathcal{K}_j(\mathbf{M}, \mathbf{Q})$ . The analogue of Equation 3.6 is

$$\begin{aligned} \mathbf{M}^{(j)} &= \mathbf{Q}^{(j)} \mathbf{T}^{(j)} \mathbf{Q}^{(j)\dagger} \\ &= \mathbf{Q}^{(j)} \mathbf{Q}^{(j)\dagger} \mathbf{M} \mathbf{Q}^{(j)} \mathbf{Q}^{(j)\dagger}, \end{aligned} \quad (3.15)$$

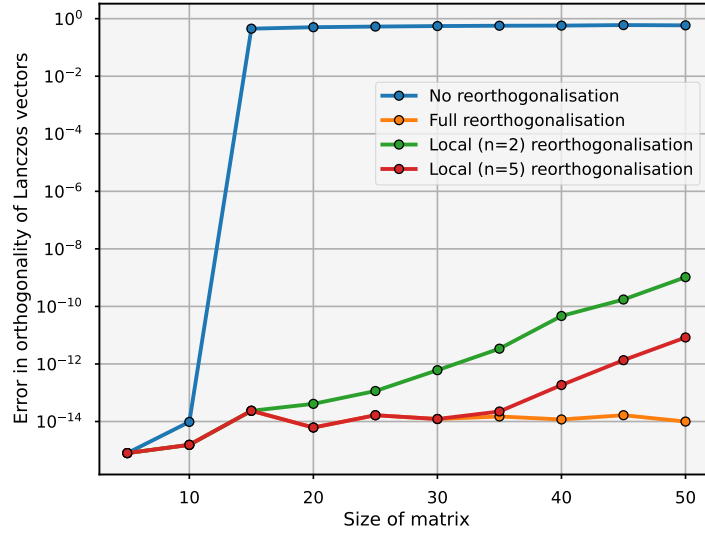


Figure 3.2: Loss in orthogonality for the fully converged block Lanczos algorithm for a number of matrix sizes, with block sizes of 5, and with four different reorthogonalisation schemes. No reorthogonalisation does not change the vectors, full reorthogonalisation enforces orthogonality of each new vector with *every* previous vector, whilst the local schemes enforce it with the previous  $n$  vectors. Random Hermitian matrices were generated, and each point is the mean over 100 of such matrices, and elements are double precision (64 bit) floating point values.

and an equivalent analysis to Equations 3.7 to 3.9 leads to the expressions<sup>44</sup>

$$\left(\mathbf{M}^{(j)}\right)^k \mathbf{Q}_m = \mathbf{M}^k \mathbf{Q}_m \quad \forall 0 \leq m \leq n \quad \forall 0 \leq k \leq j-1, \quad (3.16a)$$

$$\mathbf{Q}_{m'}^\dagger \left(\mathbf{M}^{(j)}\right)^k \mathbf{Q}_m = \mathbf{Q}_{m'}^\dagger \mathbf{M}^k \mathbf{Q}_m \quad \forall 0 \leq m, m' \leq n \quad \forall 0 \leq k \leq 2j-1, \quad (3.16b)$$

where  $n$  is the block size (number of vectors in each block vector). In contrast to Equation 3.9, this preserves on- and off-diagonal moments equally. This provides convergence in the global eigenspectrum rather than only in extremal parts. For the operator functional  $f(\hat{O})$  it offers an efficient route to compute matrix elements  $\langle \psi_p | f(\hat{O}) | \psi_q \rangle$  where one observes exponential convergence to the true matrix elements with the number of iterations.

As a result of the QR factorisation in Equation 3.12d, The block Lanczos vectors are orthogonal within their block, but they still suffer from loss of orthogonality with respect to other blocks between vectors. As such, similar considerations of reorthogonalisation must be taken. Figure 3.2 shows the loss of orthogonality with some naive reorthogonalisation schemes, equivalent to that shown in Figure 3.1. Comparing these figures, we can conclude that in the case of block Lanczos the local (partial) reorthogonalisation schemes are more effective at restoring the orthogonality of the Lanczos vectors, which is likely aided by the existing orthogonality within blocks.

### 3.4 Application to the Dyson equation

It can be concluded from Section 3.3 that the block Lanczos algorithm offers a method to obtain truncated solutions to the eigenproblem in Equation 2.84, with the truncation systematically and exponentially converging to the true Green's function. This involves projecting the  $(\mathbf{K}+\mathbf{C})$  matrix block, along with the columns of  $\mathbf{V}$ , into the Krylov subspace spanned by the Lanczos vectors. This has the effect of projecting the full self-energy matrix into a block tridiagonal representation, and a truncation to a non-complete subspace is sufficient to preserve particular properties as shown in the previous Section. In the context of the Dyson equation, this can be considered a compression of the configuration space of the self-energy in a fashion that preserves its spectral moments. This configuration space consists of static auxiliary functions whose downfolding is responsible for the dynamic nature of the self-energy, and the application of the algorithm equally represents a compression of this coupling to an auxiliary space.

A convenient choice of starting vectors are the couplings of the small and large parts of the self-energy matrix  $\mathbf{V}$ . Since the starting vectors must be orthonormal, the algorithm begins with a QR factorisation of the transposed couplings<sup>45</sup>

$$\mathbf{V}^\dagger = \mathbf{Q}_1 \mathbf{X}^\dagger, \quad (3.17)$$

where  $\mathbf{X}$  is a lower triangular matrix of the same dimension as the static  $\Sigma(\infty)$  in Equation 2.84. The block Lanczos algorithm is then applied to  $(\mathbf{K}+\mathbf{C})$  as outlined in Section 3.3, yielding the block tridiagonal matrix  $\mathbf{T}^{(j)}$

$$\mathbf{T}^{(j)} = \mathbf{Q}^{(j)\dagger} (\mathbf{K}+\mathbf{C}) \mathbf{Q}^{(j)}, \quad (3.18)$$

where  $j$  indicates the number of iterations. By applying identity in the physical space (i.e. the small space of the self-energy matrix) we can write the full transformation vectors for the self-energy matrix into this reduced representation

$$\tilde{\mathbf{Q}}^{(j)} = \begin{bmatrix} \mathbf{I} & \mathbf{0} \\ \mathbf{0} & \mathbf{Q}^{(j)} \end{bmatrix}, \quad (3.19)$$

which is sufficient to transform Equation 2.80 as

$$\begin{aligned} \tilde{\Sigma}^{(j)} &= \tilde{\mathbf{Q}}^{(j)\dagger} \Sigma \tilde{\mathbf{Q}}^{(j)} = \tilde{\mathbf{Q}}^{(j)\dagger} \begin{bmatrix} \Sigma(\infty) & \mathbf{V} \\ \mathbf{V}^\dagger & (\mathbf{K}+\mathbf{C}) \end{bmatrix} \tilde{\mathbf{Q}}^{(j)} \\ &= \begin{bmatrix} \Sigma(\infty) & \mathbf{X} & & & \mathbf{0} \\ \mathbf{X}^\dagger & \mathbf{A}_1 & \mathbf{B}_1 & & & \\ & \mathbf{B}_1^\dagger & \mathbf{A}_2 & \mathbf{B}_2 & & \\ & & \mathbf{B}_2^\dagger & \mathbf{A}_3 & \ddots & \\ & & & \ddots & \ddots & \mathbf{B}_{j-1} \\ \mathbf{0} & & & & \mathbf{B}_{j-1}^\dagger & \mathbf{A}_j \end{bmatrix}. \end{aligned} \quad (3.20)$$

Since  $\mathbf{X}$  and  $\mathbf{B}$  are the lower-triangular matrices resulting from QR factorisations, one can see how  $\tilde{\Sigma}$  exhibits a banded structure in practice. The matrices  $\mathbf{X}$  represent couplings between the frequency-independent physical space  $\Sigma(\infty)$  and the first on-diagonal block  $\mathbf{A}_1$ . The matrix  $\tilde{\Sigma}$  is a compressed self-energy, conserving the first  $2j$  moments of the dynamic part of the self-energy as defined in Section 2.4.4. The eigenvalues of  $\tilde{\Sigma}$  are approximate energies of the Dyson states, numbering  $n_{\text{orb}}(j+1)$ , whereas the Dyson orbitals can be obtained by projecting onto the space of the MOs and back-transforming the eigenvectors using  $\mathbf{X}$

$$\mathbf{u} = \mathbf{X}\mathbf{P}_{\text{MOs}}\tilde{\mathbf{u}}, \quad (3.21)$$

where  $\tilde{\mathbf{u}}$  are the eigenvectors of  $\tilde{\Sigma}$  and  $\mathbf{P}_{\text{MOs}}$  corresponds to a projector into the space of MOs. Equation 3.20 can easily be rotated into a representation in which the large subspace is diagonal by first diagonalising  $\mathbf{T}^{(j)}$ , and then rotating the large subspace of Equation 3.20 into this diagonal representation, including the coupling terms  $\mathbf{X}$ .

For a self-energy with a matrix-vector operation scaling with the number of MOs as  $\mathcal{O}(n_{\text{MO}}^p)$ , the block Lanczos algorithm scales as  $\mathcal{O}(n_{\text{MO}}^{p+1})$ , with this increase reflecting the need to compute the product between the self-energy matrix and a block vector whose block size enumerates the MOs. Whilst this may at first appearance reduce its efficacy as a drop-in replacement for single-vector iterative solvers in many-body methods involving Green's functions, in many cases this is remedied by the fact that methods often have iterative costs (those originating from the matrix-vector product) that are less expensive than the one-shot cost. Some electron propagator methods exhibiting this feature are listed in Table 2.1, with the second-order self-energies also falling into this category due to the necessity to transform the ERIs at a cost of  $\mathcal{O}(n_{\text{MO}}^5)$ . Additionally, the equation-of-motion coupled cluster singles and doubles (EOM-CCSD) method requires a  $\mathcal{O}(n_{\text{MO}}^6)$  ground state calculation despite exhibiting a matrix-vector operation scaling as  $\mathcal{O}(n_{\text{MO}}^5)$ .

### 3.5 Self-energy recurrence relations

A significant drawback of the block Lanczos algorithm in the context of its application to the Dyson equation as outlined in Section 3.4 is the necessity to store vectors spanning the large space of  $(\mathbf{K}+\mathbf{C})$ . Even with no reorthogonalisation the algorithm requires the storage of two matrices of dimension  $n_{\text{orb}} \times n_{\mathbf{K}+\mathbf{C}}$ , which can become prohibitively large with  $n_{\mathbf{K}+\mathbf{C}}$  scaling cubically in  $n_{\text{orb}}$  even at the level of second-order perturbation theory. Figure 3.2 clearly shows that this is not an option, and at least very local reorthogonalisation is required, which further increases this storage overhead. To solve this problem, the present work will derive recurrence relations in terms of the moments of the self-energy that permit a modified block Lanczos algorithm, which operates purely within the inner space of the block vectors.

Rearranging Equation 3.13 in the case of the application to the Dyson equation, we can write an expression for the  $(i+1)$ th Lanczos vector  $\mathbf{Q}_{i+1}$

$$\mathbf{Q}_{i+1} = [(\mathbf{K}+\mathbf{C}) \mathbf{Q}_i - \mathbf{Q}_i \mathbf{A}_i - \mathbf{Q}_{i-1} \mathbf{B}_{i-1}] \mathbf{B}_i^{-1,\dagger} \quad (3.22)$$

$$= \mathbf{R}_i \mathbf{B}_i^{-1,\dagger}. \quad (3.23)$$

We can use this expression along with the  $i$ th Lanczos vector  $\mathbf{Q}_i$  to define the recurrence relations

$$\begin{aligned} \mathbf{S}_{i+1,i}^{(n)} &= \mathbf{Q}_{i+1}^\dagger (\mathbf{K}+\mathbf{C})^n \mathbf{Q}_i \\ &= \mathbf{B}_i^{-1} [(\mathbf{K}+\mathbf{C}) \mathbf{Q}_i - \mathbf{Q}_i \mathbf{A}_i - \mathbf{Q}_{i-1} \mathbf{B}_{i-1}]^\dagger (\mathbf{K}+\mathbf{C})^n \mathbf{Q}_i \\ &= \mathbf{B}_i^{-1} \left[ \mathbf{Q}_i^\dagger (\mathbf{K}+\mathbf{C})^{n+1} \mathbf{Q}_i - \mathbf{A}_i \mathbf{Q}_i^\dagger (\mathbf{K}+\mathbf{C})^n \mathbf{Q}_i - \mathbf{B}_{i-1}^\dagger \mathbf{Q}_{i-1}^\dagger (\mathbf{K}+\mathbf{C})^n \mathbf{Q}_i \right] \\ &= \mathbf{B}_i^{-1} \left[ \mathbf{S}_{i,i}^{(n+1)} - \mathbf{A}_i \mathbf{S}_{i,i}^{(n)} - \mathbf{B}_{i-1}^\dagger \mathbf{S}_{i-1,i}^{(n)} \right], \end{aligned} \quad (3.24a)$$

$$\begin{aligned} \mathbf{S}_{i+1,i+1}^{(n)} &= \mathbf{Q}_{i+1}^\dagger (\mathbf{K}+\mathbf{C})^n \mathbf{Q}_{i+1} \\ &= \mathbf{B}_i^{-1} [(\mathbf{K}+\mathbf{C}) \mathbf{Q}_i - \mathbf{Q}_i \mathbf{A}_i - \mathbf{Q}_{i-1} \mathbf{B}_{i-1}]^\dagger (\mathbf{K}+\mathbf{C})^n [(\mathbf{K}+\mathbf{C}) \mathbf{Q}_i - \mathbf{Q}_i \mathbf{A}_i - \mathbf{Q}_{i-1} \mathbf{B}_{i-1}] \mathbf{B}_i^{-1,\dagger} \\ &= \mathbf{B}_i^{-1} \left[ \mathbf{Q}_i^\dagger (\mathbf{K}+\mathbf{C})^{n+2} \mathbf{Q}_i + \mathbf{A}_i \mathbf{Q}_i^\dagger (\mathbf{K}+\mathbf{C})^n \mathbf{Q}_i \mathbf{A}_i + \mathbf{B}_{i-1}^\dagger \mathbf{Q}_{i-1}^\dagger (\mathbf{K}+\mathbf{C})^n \mathbf{Q}_{i-1} \mathbf{B}_{i-1} \right. \\ &\quad \left. - P \left( \mathbf{Q}_i^\dagger (\mathbf{K}+\mathbf{C})^{n+1} \mathbf{Q}_i \mathbf{A}_i \right) - P \left( \mathbf{Q}_i^\dagger (\mathbf{K}+\mathbf{C})^{n+1} \mathbf{Q}_{i-1} \mathbf{B}_{i-1} \right) \right. \\ &\quad \left. + P \left( \mathbf{A}_i \mathbf{Q}_i^\dagger (\mathbf{K}+\mathbf{C})^n \mathbf{Q}_{i-1} \mathbf{B}_{i-1} \right) \right] \mathbf{B}_i^{-1,\dagger} \\ &= \mathbf{B}_i^{-1} \left[ \mathbf{S}_{i,i}^{(n+2)} + \mathbf{A}_i \mathbf{S}_{i,i}^{(n)} \mathbf{A}_i + \mathbf{B}_{i-1}^\dagger \mathbf{S}_{i-1,i-1}^{(n)} \mathbf{B}_{i-1} - P \left( \mathbf{S}_{i,i}^{(n+1)} \mathbf{A}_i \right) \right. \\ &\quad \left. - P \left( \mathbf{S}_{i,i-1}^{(n+1)} \mathbf{B}_{i-1} \right) + P \left( \mathbf{A}_i \mathbf{S}_{i,i-1}^{(n)} \mathbf{B}_{i-1} \right) \right] \mathbf{B}_i^{-1,\dagger}, \end{aligned} \quad (3.24b)$$

where the permutation operator  $P$  is defined as

$$P(\mathbf{Z}) = \mathbf{Z} + \mathbf{Z}^\dagger. \quad (3.25)$$

Due to the symmetry in the target matrix, we note that

$$\mathbf{S}_{i,j}^{(n)} = \mathbf{S}_{j,i}^{(n),\dagger}, \quad (3.26)$$

$$\mathbf{A}_i = \mathbf{A}_i^\dagger. \quad (3.27)$$

The zeroth-order Lanczos vectors are zero and therefore

$$\mathbf{S}_{i,0}^{(n)} = \mathbf{S}_{0,i}^{(n)} = \mathbf{S}_{0,0}^{(n)} = \mathbf{0}, \quad (3.28)$$

and since we desire the vectors to be orthogonal, we can also say

$$\mathbf{S}_{i,j}^{(0)} = \delta_{ij} \mathbf{I} \quad \forall i, j > 0. \quad (3.29)$$

Observing from Equation 3.17 that  $\mathbf{Q}_1$  can be written as  $\mathbf{Q}_1 = \mathbf{V}\mathbf{X}^{-1,\dagger}$ , we can initialise the recurrence coefficients as

$$\begin{aligned} \mathbf{S}_{1,1}^{(n)} &= \mathbf{Q}_1^\dagger (\mathbf{K} + \mathbf{C})^n \mathbf{Q}_1 \\ &= \mathbf{X}^{-1} \mathbf{V} (\mathbf{K} + \mathbf{C})^n \mathbf{V}^\dagger \mathbf{X}^{-1,\dagger} \\ &= \mathbf{X}^{-1} \boldsymbol{\Xi}^{(\Sigma,n)} \mathbf{X}^{-1,\dagger}, \end{aligned} \quad (3.30)$$

which are simply the moments of the self-energy orthogonalised under the metric of  $\mathbf{X}^{-1}$ . Whilst intuitively Equation 3.17 seems to require that  $\mathbf{V}$  is stored in memory, we can get around this by employing the *Cholesky QR* algorithm that proceeds as<sup>348,349</sup>

$$\begin{aligned} \mathbf{X}^\dagger &= (\mathbf{V}\mathbf{V}^\dagger)^{\frac{1}{2}} \\ &= \left( \boldsymbol{\Xi}^{(\Sigma,0)} \right)^{\frac{1}{2}}, \end{aligned} \quad (3.31a)$$

$$\mathbf{Q}_1 = \mathbf{V}^\dagger \mathbf{X}^{-1,\dagger}. \quad (3.31b)$$

This algorithm can be unstable in the case of a badly conditioned  $\mathbf{V}$ , which can be remedied with an iterative approach. We find that in typical self-energies the coupling is not badly conditioned, which likely reflects the regularisation of the coupling value due to both the basis set and decay of the Coulomb interaction. Furthermore, if one computes the square root of the matrix not by CD but instead via the eigendecomposition,  $\mathbf{X}$  and therefore the  $\mathbf{B}$  matrices become Hermitian. Whilst this means that  $\mathbf{T}$  is no longer banded but truly block tridiagonal, it simplifies the equations and their subsequent implementation as conjugate transposition does not need to be of concern.

The  $\mathbf{B}$  matrices can be evaluated by expanding the expressions for  $\mathbf{R}$

$$\begin{aligned} \mathbf{B}_i^2 &= \mathbf{R}_i^\dagger \mathbf{R}_i \\ &= \left[ \mathbf{S}_{i,i}^{(2)} + \mathbf{A}_i^2 + \mathbf{B}_{i-1}^\dagger \mathbf{B}_{i-1} - P \left( \mathbf{S}_{i,i}^{(1)} \mathbf{A}_i \right) - P \left( \mathbf{S}_{i,i-1}^{(1)} \mathbf{B}_{i-1} \right) \right], \end{aligned} \quad (3.32)$$

which is equivalent to the squared-bracketed term of Equation 3.24b in the case of  $n = 0$ , and by removing terms that are necessarily zero. From Equations 3.12a and 3.12b we can also derive an expression for  $\mathbf{A}$

$$\begin{aligned} \mathbf{A}_i &= \mathbf{Q}_i^\dagger (\mathbf{K} + \mathbf{C}) \mathbf{Q}_i \\ &= \mathbf{S}_{i,i}^{(1)}. \end{aligned} \quad (3.33)$$



This can be seen from the projection of Equation 3.17 onto the space spanned by the Lanczos vectors of a single iteration. This observation also leads to a second definition for  $\mathbf{B}$  terms, corresponding to a similar projection

$$\begin{aligned}\mathbf{B}_i &= \mathbf{Q}_i^\dagger (\mathbf{K} + \mathbf{C}) \mathbf{Q}_{i+1} \\ &= \mathbf{S}_{i,i+1}^{(1)},\end{aligned}\tag{3.34}$$

though in practice, the use of this definition leads to infinite recursion. As such, the  $\mathbf{S}_{i,j}^{(1)}$  terms can be understood to be blocks of the block tridiagonal matrix  $\mathbf{T}$ .

These expressions are sufficient to perform the recursive calculation of the coefficients and then extract the relevant  $\mathbf{A}$  and  $\mathbf{B}$  terms to construct  $\mathbf{T}$ , with a storage overhead scaling as  $\mathcal{O}(n_{\text{orb}}^3)$ , regardless of the size of the self-energy configuration space. Instead, the algorithm requires *a priori* knowledge of the moments of the self-energy being diagonalised. With respect to the notation in Equation 3.20, this process requires the first  $2j$  moments as an input, i.e. up to and including the  $n = 2j - 1$  moment. Similarly, the resulting compression conserves the first  $2j$  moments. As described in Section 3.4 this matrix can easily be rotated into a representation where the large subspace is diagonal, and therein moments can easily be computed to check the correctness of the process. The eigenpairs can be interpreted in the same fashion as those of Section 3.4, with the eigenvalues giving energies and the eigenvectors simple to rotate into Dyson orbitals.

The inclusion of reorthogonalisation terms in the Lanczos vectors cancels out when transformed into the inner space in the derivation above. That is not to say however that loss of orthogonality is not a factor in the present reformulation, but that it symbolically cancels out when infinite precision is assumed. Despite this, the loss of orthogonality of subsequent block vectors is exceptionally simple to diagnose and cure in the case of the present algorithm, as it can be tracked directly from the error in the left- and right-hand side of Equation 3.29, and the  $\mathbf{S}_{i,j}^{(0)}$  can be forcefully stored to satisfy this equality in order to maintain a good amount of orthogonality throughout. This method still observes significant numerical instability due to the exponentiation of energies in the moments of the self-energy. Since the moments involve powers of  $(\mathbf{K} + \mathbf{C})$ , they exponentially grow in value with order  $n$ , as does the range of values the moments take. As such, the scale of values upon which arithmetic operations are applied in the recurrence relations grows beyond the precision of a 64 bit floating point value, and numerical noise becomes significant. The point at which this becomes worrisome depends on the self-energy being used, and therefore on the system, but for the studied self-energies sufficient iterations to render the algorithm useful can be performed before overwhelming numerical instability.

We have therefore presented a method to diagonalise an arbitrary self-energy and obtain an approximate Green's function that treats the entire eigenspectrum rather than targeting an extremal part of it, and whose approximation systematically converges to the exact diagonalisation in the limit of infinite moments and exact arithmetic. Furthermore, this is done in a fashion that is computationally efficient with the limiting step performed ahead of time, and with a manageable storage overhead. As a final comment on notation, we note that in the context of the application of this algorithm to moments at different levels of theory, we will

---

consider number of iterations  $n_{\text{iter}}$  to refer to the number of  $\mathbf{B}$  blocks in the block tridiagonal matrix—that is to say, a calculation using these recurrences at the level of  $n_{\text{iter}} = 0$  represents the block tridiagonal matrix as the coupling between the static self-energy and the  $\mathbf{A}_1$  block via coupling  $\mathbf{X}$ . This diagonalisation therefore conserves the first two (zeroth- and first-order) moments.

### 3.6 Green's function recurrence relations

We now turn to the problem of reconstructing a self-energy, and therefore computing the resulting Green's function, according to the conservation in moments of the Green's function rather than those of the self-energy.<sup>338,350,351</sup> We wish to find a different set of Lanczos vectors  $\mathbf{Q}^{(j)}$  that similarly rotate the self-energy matrix into a block tridiagonal form, but rather than doing so in a way that conserves the moments of the self-energy, the representation conserves moments of the Green's function following diagonalisation. Whilst the orthonormality of the Dyson orbitals requires that the zeroth central moment of the Green's function is identity, this may not be satisfied if i.e. one separates hole and particle moments, which is convenient or necessary in many applications. Generally speaking, the moments must therefore be orthogonalised under the metric of the zeroth moment in a fashion similar to that of Section 3.5

$$\tilde{\Xi}^{(\mathbf{G},n)} = \left[ \Xi^{(\mathbf{G},0)} \right]^{-\frac{1}{2}} \Xi^{(\mathbf{G},n)} \left[ \Xi^{(\mathbf{G},0)} \right]^{-\frac{1}{2}}. \quad (3.35)$$

It is instructive to write the trivial example, where in the notation of Equation 3.20 we wish to construct a compressed self-energy that conserves the first two (zeroth- and first-order) moments of the Green's function

$$\tilde{\Sigma}^{(j=1)} = \mathbf{A}_1 = \tilde{\Xi}^{(\mathbf{G},1)}, \quad (3.36)$$

which can be intuited simply as the diagonalisation of the Fock matrix with possible correlation-induced changes through the static self-energy, the correspondence of which to the first moment of the Green's function was shown in Equation 2.105b. In the case of a Green's function completely defined by  $\mathbf{G}^0$ , that is to say there is no *dynamic* self-energy contribution, this eigenproblem fully determines the poles of the Green's function.

We also note that the moments of the Green's function can be written as powers of the self-energy matrix they originate from, projected down onto the space of the Green's function

$$\tilde{\Xi}^{(\mathbf{G},n)} = \tilde{\mathbf{Q}}_1^\dagger \Sigma^n \tilde{\mathbf{Q}}_1, \quad (3.37)$$

where the first element of the expanded Lanczos vectors in Equation 3.19 have been used to indicate the projection. Let the recurrence coefficients  $\mathbf{S}$  now satisfy

$$\tilde{\mathbf{Q}}_i = \sum_{j=1}^{i+1} \Sigma^{j-1} \tilde{\mathbf{Q}}_1 \mathbf{S}_{i,j}, \quad (3.38)$$

which implies the conditions

$$\mathbf{S}_{1,1} = \mathbf{I}, \quad (3.39)$$

$$\mathbf{S}_{i,j} = \mathbf{0} \quad \forall i < 1, j < 1, i < j. \quad (3.40)$$

By inserting Equation 3.38 into the expression for the  $\mathbf{A}$  blocks in terms of the Lanczos vectors in Equation 3.33, we can write expressions for the  $\mathbf{A}$  blocks in the case of conservation of moments

of the Green's function

$$\begin{aligned}
\mathbf{A}_i &= \tilde{\mathbf{Q}}_i^\dagger \Sigma \tilde{\mathbf{Q}}_i \\
&= \sum_{j=1}^{i+1} \sum_{k=1}^{i+1} \mathbf{S}_{i,j}^\dagger \tilde{\mathbf{Q}}_1^\dagger \Sigma^{j+k-1} \tilde{\mathbf{Q}}_1 \mathbf{S}_{i,k} \\
&= \sum_{j=1}^{i+1} \sum_{k=1}^{i+1} \mathbf{S}_{i,j}^\dagger \tilde{\Xi}^{(\mathbf{G},j+k-1)} \mathbf{S}_{i,k}.
\end{aligned} \tag{3.41}$$

Similarly, by inserting Equation 3.38 into the expression for the  $\mathbf{B}$  blocks in terms of the Lanczos vectors in Equation 3.34, we can write expressions for the  $\mathbf{B}$  blocks

$$\begin{aligned}
\mathbf{B}_i &= \tilde{\mathbf{Q}}_i^\dagger \Sigma \tilde{\mathbf{Q}}_{i+1} \\
&= \sum_{j=1}^{i+1} \sum_{k=1}^{i+2} \mathbf{S}_{i,j}^\dagger \tilde{\mathbf{Q}}_1^\dagger \Sigma^{j+k-1} \tilde{\mathbf{Q}}_1 \mathbf{S}_{i+1,k} \\
&= \sum_{j=1}^{i+1} \sum_{k=1}^{i+2} \mathbf{S}_{i,j}^\dagger \tilde{\Xi}^{(\mathbf{G},j+k-1)} \mathbf{S}_{i+1,k}.
\end{aligned} \tag{3.42}$$

By replacing the Lanczos vectors in Equation 3.13 with their respective coefficients, we can also obtain a recurrence relation for the coefficients

$$\mathbf{S}_{i,j-1} = \mathbf{S}_{i-1,j} \mathbf{B}_{i-1}^\dagger + \mathbf{S}_{i,j} \mathbf{A}_i + \mathbf{S}_{i+1,j} \mathbf{B}_i. \tag{3.43}$$

These expressions must be rearranged to yield useful recursion relations, which are<sup>338</sup>

$$\mathbf{A}_{i+1} = \sum_{j=1}^{i+2} \sum_{k=1}^{i+2} \mathbf{S}_{i+1,j}^\dagger \tilde{\Xi}^{(\mathbf{G},j+k-1)} \mathbf{S}_{i+1,k}, \tag{3.44a}$$

$$\mathbf{B}_{i+1}^2 = \sum_{j=1}^{i+1} \sum_{k=1}^{i+2} \mathbf{S}_{i+1,j}^\dagger \tilde{\Xi}^{(\mathbf{G},j+k-1)} \mathbf{S}_{i+1,k-1} - \mathbf{A}_{i+1}^2 - \mathbf{B}_i^{2\dagger}, \tag{3.44b}$$

$$\mathbf{S}_{i+1,j} = \left[ \mathbf{S}_{i,j-1} - \mathbf{S}_{i,j} \mathbf{A}_i - \mathbf{S}_{i-1,j} \mathbf{B}_{i-1}^\dagger \right] \mathbf{B}_i^{-1}. \tag{3.44c}$$

One can then write the compressed self-energy matrix whose eigenvalues yield the moment conserving Dyson orbitals and energies, which in the form of Equation 3.20 is

$$\begin{aligned}
\tilde{\Sigma}^{(j)} &= \tilde{\mathbf{Q}}^{(j)\dagger} \Sigma \tilde{\mathbf{Q}}^{(j)} = \tilde{\mathbf{Q}}^{(j)\dagger} \begin{bmatrix} \Sigma^{(\infty)} & \mathbf{V} \\ \mathbf{V}^\dagger & (\mathbf{K}+\mathbf{C}) \end{bmatrix} \tilde{\mathbf{Q}}^{(j)} \\
&= \begin{bmatrix} \mathbf{A}_1 & \mathbf{B}_1 & & & \mathbf{0} \\ \mathbf{B}_1^\dagger & \mathbf{A}_2 & \mathbf{B}_2 & & \\ & \mathbf{B}_2^\dagger & \mathbf{A}_3 & \ddots & \\ & & \ddots & \ddots & \mathbf{B}_{j-1} \\ \mathbf{0} & & & \mathbf{B}_{j-1}^\dagger & \mathbf{A}_j \end{bmatrix}.
\end{aligned} \tag{3.45}$$

As previously, the eigenvalues give energies of the Dyson states (Green's function poles), and the eigenvectors can be projected and back-transformed to obtain Dyson orbitals are

$$\mathbf{u} = \left[ \tilde{\Xi}^{(\mathbf{G},0)} \right]^{\frac{1}{2}} \mathbf{P}_{\text{MOS}} \tilde{\mathbf{u}}, \quad (3.46)$$

where  $\tilde{\mathbf{u}}$  are the eigenvectors of  $\tilde{\Sigma}$  and  $\mathbf{P}_{\text{MOS}}$  is a projector onto the space of MOs.

This algorithm has been extended to the case of non-Hermitian Green's function moments to facilitate its application to the CC Green's function. The resulting expressions are

$$\mathbf{A}_{i+1} = \sum_{j=1}^{i+2} \sum_{k=1}^{i+2} \mathbf{S}_{i+1,j}^{\text{L}} \tilde{\Xi}^{(\mathbf{G},j+k-1)} \mathbf{S}_{i+1,k}^{\text{R}}, \quad (3.47a)$$

$$\mathbf{B}_{i+1}^2 = \sum_{j=1}^{i+1} \sum_{k=1}^{i+2} \mathbf{S}_{i+1,j}^{\text{L}} \tilde{\Xi}^{(\mathbf{G},j+k-1)} \mathbf{S}_{i+1,k-1}^{\text{R}} - \mathbf{A}_{i+1}^2 - \mathbf{C}_i^2, \quad (3.47b)$$

$$\mathbf{C}_{i+1}^2 = \sum_{j=1}^{i+1} \sum_{k=1}^{i+2} \mathbf{S}_{i+1,j-1}^{\text{L}} \tilde{\Xi}^{(\mathbf{G},j+k-1)} \mathbf{S}_{i+1,j}^{\text{R}} - \mathbf{A}_{i+1}^2 - \mathbf{B}_i^2, \quad (3.47c)$$

$$\mathbf{S}_{i+1,j}^{\text{L}} = [\mathbf{S}_{i,j-1}^{\text{L}} - \mathbf{S}_{i,j}^{\text{L}} \mathbf{A}_i - \mathbf{S}_{i-1,j}^{\text{L}} \mathbf{B}_{i-1}] \mathbf{C}_i^{-1}, \quad (3.47d)$$

$$\mathbf{S}_{i+1,j}^{\text{R}} = \mathbf{B}_i^{-1} [\mathbf{S}_{i,j-1}^{\text{R}} - \mathbf{A}_i \mathbf{S}_{i,j}^{\text{R}} - \mathbf{C}_{i-1} \mathbf{S}_{i-1,j}^{\text{R}}], \quad (3.47e)$$

where the coefficients now satisfy

$$\tilde{\mathbf{Q}}_i^{\text{R}} = \sum_{j=1}^{i+1} \Sigma^{j-1} \tilde{\mathbf{Q}}_1^{\text{R}} \mathbf{S}_{i,j}^{\text{R}}, \quad (3.48a)$$

$$\tilde{\mathbf{Q}}_i^{\text{L}} = \sum_{j=1}^{i+1} \mathbf{S}_{i,j}^{\text{L}} \tilde{\mathbf{Q}}_1^{\text{L}} \Sigma^{j-1}, \quad (3.48b)$$

and the subsequent rotation is

$$\begin{aligned} \tilde{\Sigma}^{(j)} &= \tilde{\mathbf{Q}}^{(\text{L},j)} \Sigma \tilde{\mathbf{Q}}^{(\text{R},j)} = \tilde{\mathbf{Q}}^{(\text{L},j)} \begin{bmatrix} \Sigma^{(\infty)} & \mathbf{V}^{\text{L}} \\ \mathbf{V}^{\text{R}} & (\mathbf{K}+\mathbf{C}) \end{bmatrix} \tilde{\mathbf{Q}}^{(\text{R},j)} \\ &= \begin{bmatrix} \mathbf{A}_1 & \mathbf{B}_1 & & & \mathbf{0} \\ \mathbf{C}_1 & \mathbf{A}_2 & \mathbf{B}_2 & & \\ & \mathbf{C}_2 & \mathbf{A}_3 & \ddots & \\ & & \ddots & \ddots & \mathbf{B}_{j-1} \\ \mathbf{0} & & & \mathbf{C}_{j-1} & \mathbf{A}_j \end{bmatrix}. \end{aligned} \quad (3.49)$$

$\tilde{\Sigma}$  now permits a non-symmetric eigenproblem, of which the eigenvalues give energies of the Dyson states, and the eigenvectors can be transformed to admit left- and right-hand Dyson orbitals as

$$\mathbf{u}^{\text{L}} = \left[ \tilde{\Xi}^{(\mathbf{G},0)} \right]^{\frac{1}{2}} \mathbf{P}_{\text{MOS}} \tilde{\mathbf{u}}, \quad (3.50a)$$

$$\mathbf{u}^{\text{R}} = \left( \tilde{\mathbf{u}}^{-1} \mathbf{P}_{\text{MOS}} \left[ \tilde{\Xi}^{(\mathbf{G},0)} \right]^{\frac{1}{2}} \right)^{\dagger}, \quad (3.50b)$$

where  $\tilde{\mathbf{u}}$  are the eigenvectors of  $\tilde{\mathbf{\Sigma}}$ . This therefore defines a non-Hermitian system of Dyson orbitals sufficient to recover the non-Hermitian moments of the Green's function as

$$\Xi^{(\mathbf{G},n)} = \mathbf{u}^L \boldsymbol{\lambda}^n \mathbf{u}^{\mathbf{R},\dagger}, \quad (3.51)$$

where  $\boldsymbol{\lambda}$  is a diagonal matrix of the eigenvalues of  $\tilde{\mathbf{\Sigma}}$ . The dynamic Green's function and therefore the spectral function can also be obtained with the non-Hermitian system of Dyson orbitals.

The notation we shall use for methods employing this algorithm are similar to those of Section 3.5 in that a calculation using  $n_{\text{iter}} = 0$  still incorporates a single  $\mathbf{A}_1$  block in the block tridiagonal Hamiltonian, and which conserves the first two (zeroth- and first-order) moments.

	Input	No. of Dyson orbitals	Cost (CPU)	Cost (RAM)
$\Xi^{(\Sigma, n)}$	$\forall 0 \leq n \leq 2n_{\text{iter}} + 1$	$n_{\text{MO}}(n_{\text{iter}} + 2)$	$\mathcal{O}(n_{\text{iter}}^2 n_{\text{MO}}^3)^\dagger$	$\mathcal{O}(n_{\text{iter}}^2 n_{\text{MO}}^2)$
$\Xi^{(G, n)}$	$\forall 0 \leq n \leq 2n_{\text{iter}} + 1$	$n_{\text{MO}}(n_{\text{iter}} + 1)$	$\mathcal{O}(n_{\text{iter}}^3 n_{\text{MO}}^3)$	$\mathcal{O}(n_{\text{iter}}^2 n_{\text{MO}}^2)$

Table 3.1: Required input moments and corresponding number of output states for the self-energy and Green’s function block Lanczos recurrence schemes, along with the scaling of the cost in terms of both CPU and RAM for each algorithm. <sup>†</sup>This scaling represents the cost to perform the block Lanczos recurrence, however the diagonalisation of the resulting compressed self-energy will scale as  $\mathcal{O}(n_{\text{iter}}^3 n_{\text{MO}}^3)$ .

### 3.7 Comparison

In summary, the two schemes for performing the Dyson equation under the metric of the conservation of moments of the self-energy or Green’s function can be compared using Table 3.1. Both schemes require *a priori* the moments of either the self-energy or Green’s function, for all  $n$  in  $0 \leq n \leq 2n + 1$  (i.e. the first  $2n + 2$  moments). In the case of the self-energy recurrence, these moments result in  $n_{\text{MO}}$  more Dyson states due to the inclusion of the static self-energy. Table 3.1 considers a self-energy without a non-Dyson approximation, hence the number of states and costs depend on  $n_{\text{MO}}$ . These numbers do not depend on whether one uses the central, hole, or particle parts of the distributions, however if one separately performs the recursion on the hole and particle moments before combining the Dyson orbitals, the total number will be doubled. In the case of a non-Dyson approximation  $n_{\text{MO}}$  in Table 3.1 is replaced by  $n_{\text{occ}}$  or  $n_{\text{vir}}$  depending on whether one is considering hole or particle moments, respectively—more generally,  $n_{\text{MO}}$  represents the size of whichever basis the input moments are in.

Whilst the self-energy recurrence has a CPU bottleneck scaling less than the Green’s function recurrence by a factor  $n_{\text{iter}}$ , the subsequent diagonalisation of the compressed block tridiagonal matrix scales as  $n_{\text{iter}}^3 n_{\text{MO}}^3$  in both cases. Since  $n_{\text{iter}}$  scales in the large system limit with system size as  $\mathcal{O}(1)$ , this can be considered an  $\mathcal{O}(n_{\text{MO}}^3)$  algorithm—obviously, this is significantly lower than most canonical quantum chemistry algorithms that one may use to compute the moments, and therefore the moment computation is almost always the bottleneck for any calculation involving these algorithms. One drawback of this is the possible extension to two-particle Green’s function theories, in which one may wish to express moments in a pair basis of size  $n_{\text{occ}} n_{\text{vir}}$ , and therefore scaling would increase to  $\mathcal{O}(n_{\text{MO}}^6)$ .

In the Hermitian variants of the recurrence schemes, non-causality in the respective distributions can result in  $\mathbf{B}^2$  blocks that are not positive semi-definite. In order to produce a causal set of Dyson orbitals from the block Lanczos recurrence, the space of  $\mathbf{B}^2$  corresponding to negative eigenvalues must be removed in order to compute  $\mathbf{B}$ , which may discard information and result in a representation that does not conserve the desired moments. Furthermore, the calculation of  $\mathbf{B}^{-1}$  implies a non-singular  $\mathbf{B}$  and therefore  $\mathbf{B}^2$ , and any null space of  $\mathbf{B}$  must be removed. This is likely to occur closer to the limit of the number of blocks for a particular system. In the case of central moments, no positive or negative definiteness is required in the moments. By construction, particle

moments are positive semi-definite, and hole moments are positive semi-definite for even  $n$  and negative semi-definite for odd  $n$ . Deviation from this implies non-causality, however satisfaction of this rule does not necessarily imply causality.<sup>a</sup> Implementations of the block Lanczos recurrence should pay careful observation to the eigenspectrum of the  $\mathbf{B}^2$  at each iteration.

---

<sup>a</sup>For example, consider a spectrum in which two poles couple to a single physical orbital, with one pole causal and one non-causal, where  $e_1, v_1$  are the energy and coupling of the causal pole and  $e_2, v_2$  of the non-causal pole. Any moment  $n$  for which  $v_1 e_1^n v_1 > v_2 e_2^n v_2$  is positive definite.





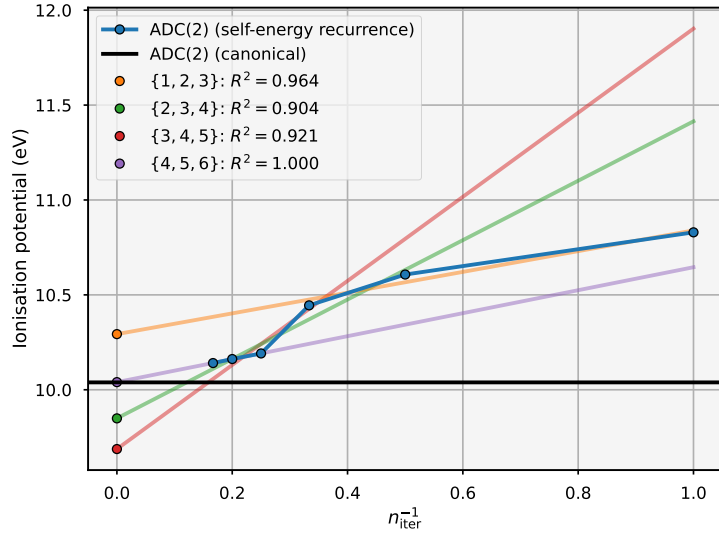


Figure 3.3: Example of the extrapolation scheme for excitations found using the block Lanczos recurrence algorithms. The example shown is for a hypochlorous acid (HOCl) molecule in a cc-pVDZ basis set, with iterations of the self-energy recurrence at the level of IP-ADC(2). The extrapolations each use three iterations, and these iteration numbers and the respective  $R^2$  value are shown in the legend.

and therefore the value of the excitations saturate. Since the vast majority of self-energies has significantly more poles than there are HF orbitals, the number of iterations required to reach this limit is high enough that  $\frac{1}{n_{\text{iter}}^{\text{max}}}$  is sufficiently close to 0 and therefore simply reading the intercept  $c$  is a good estimate of the extrapolated value. Additionally, it should be noted that despite  $n_{\text{iter}} = 0$  being used in the notation of this work, that value clearly cannot be used in the extrapolation—however one should aim to extrapolate with the largest accessible iteration calculations possible. Figure 3.3 shows an example of the extrapolation for a hypochlorous acid (HOCl) molecule in a cc-pVDZ basis set, with iterations of the self-energy recurrence at the level of IP-ADC(2). Despite the 1,2,3 extrapolation showing a good  $R^2$ , since it involves small iteration numbers it does not extrapolate a good IP. On the other hand, 2,3,4 and 3,4,5 have poorer  $R^2$  (depending on where one places their threshold for ‘poor’), indicating that they may poorly extrapolate the IP due to the erratic nature of convergence with iterations. The 4,5,6 result has an  $R^2$  of 1.000, indicating the very strong linearity of these points in the domain  $n_{\text{iter}}^{-1}$ . This example extrapolates an IP that is extremely close to that predicted by the canonical ADC(2) algorithm.<sup>a</sup>

<sup>a</sup>Note that this example is one that was chosen to best exemplify the extrapolation, and is not respective of the behaviour or  $R^2$  for other such systems.



## Chapter 4

# Second-order auxiliary Green's function perturbation theory

## 4.1 Introduction

As outlined in Section 2.5.3 a method exists to numerically iterate the Dyson equation in order to screen (renormalise) the propagators in the diagrams at  $n$ th-order. This method is algorithmically complicated, with a discretisation of the time and frequency variables introducing an often significant prefactor. Since a Fourier transform is required between these domains the use of non-uniform quadrature is non-trivial, and imaginary frequency (Matsubara) axes are typically required to ensure the Green's function is represented smoothly introducing a finite temperature.<sup>102,103</sup> This means that real frequency spectra require analytic continuation to the real frequency axis which is an ill-conditioned problem. Instead, we wish to exploit the techniques discussed in Chapters to perform the renormalisation without the use of these troublesome continuous variables.

The recurrences outlined in Chapter 3 afford a systematically improvable perspective to solving the Dyson equation without the need for any frequency or time grids. Whilst the most obvious application of these algorithms is simply as a drop-in block-box solver instead of other iterative eigensolvers, their property of allowing tractable iteration according to the Dyson equation result in the possibility for an efficient route to renormalised physics.

The second-order auxiliary Green's function perturbation theory (AGF2) method has been developed throughout the course of the present work, with significant improvements in efficiency and understanding of the parameterisation according to number of recurrence iterations. This has led to an efficient and readily applicable method for applying renormalised second-order perturbation theory to electronic structure calculations, and has featured in a number of publications,<sup>51–53,355</sup> as well as an implementation in the PySCF programming package.<sup>26,27</sup> Conceptually, AGF2 is similar to earlier work in Ref. 123, where the authors applied a block Lanczos procedure to the self-energy at second-order to achieve self-consistency in the Dyson equation, for which they apply a numerical procedure. Their method considers the Green's function and self-energy to be diagonal in their basis, which they note only has a minor effect in the atomic systems they study. The study however does not consider the effect of different numbers of iterations in the block Lanczos procedure, nor do they consider a generalisation to molecular systems. AGF2 seeks to extend this initial work to outline a practical method for the solution of the Dyson equation at the level of second-order perturbation theory.

In principle, the order of perturbation theory is not constrained to the second-order. Expressions for the moments of self-energies at different orders of perturbation theory, including the various EP self-energies discussed in Section 2.6, should be readily applicable to this scheme in order to find their respective solutions on the Dyson equation under the constraint of the conservation of their moments. Future work will seek to apply these concepts to other self-energies, including the  $GW$  moments to be introduced in Chapter 5, with the latter permitting self-consistent  $GW$  calculations.

## 4.2 Method

As presented in Equation 2.125, the hole and particle parts of the self-energy at second-order can be written as

$$\Sigma_{pq}^{(2)}(\omega) = \Sigma_{pq}^{(2),<}(\omega) + \Sigma_{pq}^{(2),>}(\omega) \quad (4.1a)$$

$$\Sigma_{pq}^{(2),<}(\omega) = \frac{1}{2} \sum_{ij}^{\text{occ}} \sum_a^{\text{vir}} \frac{\langle ij||ap \rangle \langle aq||ij \rangle}{\omega - (\varepsilon_i + \varepsilon_j - \varepsilon_a)} \quad (4.1b)$$

$$\Sigma_{pq}^{(2),>}(\omega) = \frac{1}{2} \sum_i^{\text{occ}} \sum_{ab}^{\text{vir}} \frac{\langle pi||ab \rangle \langle ab||qi \rangle}{\omega - (\varepsilon_a + \varepsilon_b - \varepsilon_i)}, \quad (4.1c)$$

which have been separated into their respective parts below and above the chemical potential. As discussed in Section 2.4.4, this separation corresponds to the constraint of the moment integrals to the intervals  $(-\infty, \mu)$  and  $(\mu, \infty)$  for the hole and particle moments, respectively. The parameters satisfying the upfolded self-energy take the form

$$V_{p,ija}^{<} = \frac{1}{\sqrt{2}} \langle ij||ap \rangle, \quad (4.2a)$$

$$V_{p,iab}^{>} = \frac{1}{\sqrt{2}} \langle pi||ab \rangle, \quad (4.2b)$$

$$K_{ija,klb}^{<} = \delta_{ik} \delta_{jl} \delta_{ab} (\varepsilon_i + \varepsilon_j - \varepsilon_a), \quad (4.2c)$$

$$K_{iab,jcd}^{>} = \delta_{ij} \delta_{ac} \delta_{bd} (\varepsilon_a + \varepsilon_b - \varepsilon_i), \quad (4.2d)$$

$$C_{ija,klb}^{<} = 0, \quad (4.2e)$$

$$C_{iab,jcd}^{>} = 0. \quad (4.2f)$$

The moments at second-order can be written in the case of AGF2 by inserting the parameters in Equation 4.2 into the expression for the moments in Equation 2.98. This results in the expressions

$$\Xi_{pq}^{(\Sigma^{(2),<},n)} = \frac{1}{2} \sum_{ij}^{\text{occ}} \sum_a^{\text{vir}} \langle ij||ap \rangle (\varepsilon_i + \varepsilon_j - \varepsilon_a)^n \langle aq||ij \rangle, \quad (4.3a)$$

$$\Xi_{pq}^{(\Sigma^{(2),>},n)} = \frac{1}{2} \sum_i^{\text{occ}} \sum_{ab}^{\text{vir}} \langle pi||ab \rangle (\varepsilon_a + \varepsilon_b - \varepsilon_i)^n \langle ab||qi \rangle. \quad (4.3b)$$

Performing the recursion outlined in Section 3.5 allows one to diagonalise the self-energy with a consistency in these moments up to a desired order  $n$ , yielding a Green's function expressed as a sum-over-states of its pole positions and associated Dyson orbitals. This can be considered to be a solution to the ADC(2) matrix in the absence of the usual non-Dyson approximation, approximated up to a given accuracy via the moment expansion. The separation of the hole and particle moments allows the resolution of the low-energy dynamics, whilst also ensuring that the high-energy expansion of the central moments is resolved.

In order to further iterate the Dyson equation one can reinsert these states into the self-energy, effectively replacing the occupied  $(i, j)$  and virtual  $(a, b)$  MO indices in Equation 4.3 with

occupied and virtual Dyson orbitals and energies, which are sometimes referred to as the quasi-molecular orbitals (QMOs). This extended space still represents an idempotent density when its density matrix is defined in the entire space of the Dyson orbitals, but its projection onto the MOs provides a non-idempotent (correlated) density matrix resulting from the pair correlation effects contained in the self-energy of choice. This space would usually span the entire  $1h$ ,  $1p$ ,  $2h1p$  and  $1h2p$  spaces in which the second-order self-energy matrix is defined, for example if one were to perform a full diagonalisation at the level of ADC(2), but the effective compression introduced by the moment expansion results in a compressed QMO space. Furthermore, we can perform an additional compression to this space by writing the moments of the Green's function using the compressed QMOs as the Dyson orbitals and energies, and applying the recurrence discussed in Section 3.6.

This compression allows one to iterate the Dyson equation without expressing the Green's function and self-energy on dynamically resolved quadrature, as the diagonalisation of the self-energy now results in a  $\mathcal{O}(n_{\text{MO}})$  number of QMOs, whereas the diagonalisation of the full self-energy results in  $\mathcal{O}(n_{\text{MO}}^3)$  roots. This method has been termed AGF2, referencing its connection to the many-body Green's function perturbation theory in the case of a self-energy expressed in terms of its explicitly static configuration (or 'auxiliary') space.

As well as the outermost iterations of the Dyson equation, there exists an additional SCF on the correlated density matrix resulting from the QMOs, and its associated Fock matrix. This can be considered a renormalisation of the propagators in the first-order diagrams (whilst the Dyson equation renormalises the propagators in the second-order diagrams), relaxing the density matrix and resulting in a Fock matrix that is no longer diagonal in the basis of MOs. This is equivalent to updating the static part of the self-energy using the updated Green's function according to Equation 2.79. The non-idempotent density matrix resulting from this update is not guaranteed to trace to the correct (physical) number of electrons, and so a shift in the poles of the self-energy must also be self-consistently determined such that the resulting relaxed density matrix is both a minimum with respect to the SCF, and also one which satisfies the correct number of electrons in the system.

The moniker AGF2 without specification of the number of moments in the self-energy and Green's function expansions will refer to the simplest such compression, that is, a conservation in only the first two (zeroth- and first-order) moments of the self-energy. Otherwise, the notation  $\text{AGF2}(n_{\text{iter}}^G, n_{\text{iter}}^\Sigma)$  is used. We will later show that increasing the number of moments and approaching the GF2 limit is detrimental to the accuracy.

### 4.3 Energy functionals

As discussed in Section 2.4.5 and Section 2.5.3, the energy in many-body Green's function perturbation theory is typically partitioned into contributions due to one- and two-body quantities. This differs from the partition into mean-field and correlation, since the first-order (HF) diagrams also change due to the renormalisation of their propagators through the intermediate SCF. The one-body energy can be trivially calculated using Equation 2.106, where the frequency-independent self-energy in AGF2 takes the form of the Fock matrix updated due to correlation

$$E_{1b} = \frac{1}{2} \sum_{pq}^{\text{MOS}} \gamma_{pq} [H_{pq} + F_{pq}]. \quad (4.4)$$

The two-body part of the energy can be calculated by analytically evaluating the Galitskii–Migdal formula for the two-body energy shown in Equation 2.107, using the explicit pole representation of the self-energy and Green's function afforded in AGF2. We can proceed by inserting the pole representations into the Galitskii–Migdal formula on the Matsubara axis

$$E_{2b} = \frac{1}{2} \frac{1}{2\pi} \sum_{pq}^{\text{MOS}} \int_{-\infty}^{\infty} d\omega \Sigma_{pq}(i\omega) G_{pq}(i\omega) \quad (4.5a)$$

$$= \frac{1}{2} \frac{1}{2\pi} \sum_{pq}^{\text{MOS}} \sum_{\alpha}^{\text{aux}} \sum_x^{\text{QMOS}} V_{p\alpha} V_{q\alpha}^* u_{px} u_{qx}^* \int_{-\infty}^{\infty} d\omega (i\omega - K_{\alpha})^{-1} (i\omega - \lambda_x)^{-1}, \quad (4.5b)$$

where  $\alpha$  enumerates the compressed configuration space (auxiliaries) of the self-energy, which is expressed in a basis in which  $(\mathbf{K}+\mathbf{C})$  is diagonal and hence  $\mathbf{C} = \mathbf{0}$ . The integral can be evaluated as (see Appendix C)

$$\int_{-\infty}^{\infty} d\omega (i\omega - K_{\alpha})^{-1} (i\omega - \lambda_x)^{-1} = \begin{cases} \frac{2\pi}{\lambda_x - K_{\alpha}} & \text{if } K_{\alpha} > 0, \lambda_x < 0, \\ \frac{2\pi}{K_{\alpha} - \lambda_x} & \text{if } K_{\alpha} < 0, \lambda_x > 0, \\ 0 & \text{otherwise,} \end{cases} \quad (4.6)$$

which restricts the energy expression to one that sums over separate occupied and virtual self-energy and Green's function poles, and we can exploit symmetry in the two permutations leading to

$$E_{2b} = \sum_{pq}^{\text{MOS}} \sum_{\alpha}^{\text{occ aux}} \sum_x^{\text{vir QMOS}} \frac{V_{p\alpha} V_{q\alpha}^* u_{px} u_{qx}^*}{K_{\alpha} - \lambda_x}. \quad (4.7)$$

If one replaces the self-energy poles with the explicit (uncompressed) parameters at second-order, expressed in a basis of QMOs as they are in an AGF2 calculation, this expression becomes

$$E_{2b} = \frac{1}{2} \sum_{pq}^{\text{MOS}} \sum_{yz}^{\text{occ QMOS}} \sum_{wx}^{\text{vir QMOS}} \frac{\langle yz || wp \rangle \langle wq || yz \rangle u_{px} u_{qx}^*}{\lambda_y + \lambda_z - \lambda_x - \lambda_w}. \quad (4.8)$$



We can then consume the Dyson orbitals along with the summation over MOs, by interpreting them as a rotation of the remaining MO indices into the QMO space

$$E_{2b} = \frac{1}{2} \sum_{yz}^{\text{occ QMOS}} \sum_{wx}^{\text{vir QMOS}} \frac{\langle yz || wx \rangle \langle wx || yz \rangle}{\lambda_y + \lambda_z - \lambda_x - \lambda_w}. \quad (4.9)$$

By comparing Equation 4.9 to Equation 2.114, one can easily see that in the case of  $\mathbf{G} = \mathbf{G}^0$  (i.e. when the QMO space is the original MO space), this equals twice the MP2 energy. We can also rationalise the two-body energy functional as the calculation of half the MP2 energy in a basis of QMOs, rather than the original MOs. The discrepancy in the partitioning of the energy is compensated by the changes to the one-body density matrix, such that in the limit of infinite moments the zeroth iteration AGF2 energy still yields the MP2 energy. This partitioning is discussed in detail in Ref. 143.

## 4.4 Density matrices

The one-particle density matrices are trivially computed by the projection of the inner space of the occupied Dyson orbitals onto the MO space

$$\gamma_{pq} = \sum_x^{\text{occ QMOS}} u_{px} u_{qx}^*, \quad (4.10)$$

where  $p$  and  $q$  run over the MOs. The cumulant part of the two-particle density matrix can be defined by an integral on the Matsubara axis at zero temperature<sup>356,357</sup>

$$\mathbf{\Gamma} = \frac{1}{2} \frac{1}{2\pi} \int_{-\infty}^{\infty} d\omega \text{Tr} \left( \frac{\partial \mathbf{\Sigma}(i\omega)}{\partial \lambda} \right)_{G,h} \mathbf{G}(i\omega), \quad (4.11a)$$

$$\Gamma_{pqrs} = \frac{1}{2} \frac{1}{2\pi} \int_{-\infty}^{\infty} d\omega I_{trpq}(i\omega) G_{ts}(i\omega), \quad (4.11b)$$

where the partial derivative is with respect to the perturbation  $\lambda$  (not to be confused with the Green's function energies), originating from the derivative of the self-energy in Equation 2.77. It can be interpreted diagrammatically as the cutting of an interaction line in the diagrams shown in Equation 2.128, and therefore can be written (on the Matsubara axis) in terms of the QMOs that enter the self-energy

$$I_{trpq}(i\omega) = \sum_{ij}^{\text{occ QMOS}} \sum_a^{\text{vir QMOS}} \frac{u_{ra} u_{pi}^* u_{qj}}{i\omega - (\lambda_i + \lambda_j - \lambda_a)} \langle at || ij \rangle + \sum_i^{\text{occ QMOS}} \sum_{ab}^{\text{vir QMOS}} \frac{u_{ri} u_{pa}^* u_{qb}}{i\omega - (\lambda_a + \lambda_b - \lambda_i)} \langle ti || ab \rangle. \quad (4.12)$$

where  $i, j, a, b$  run over QMOs and  $p, q, r, s, t$  run over MOs. These terms do not inherit the factor  $\frac{1}{2}$  of the second-order self-energy, not due to the diagrammatic topology (see Section 2.3), but rather because they gain an additional factor two since there are two symmetric ways to cut the interaction in the second-order diagrams. This is entirely equivalent to considering the symmetry in the terms resulting from the expansion of the derivative in Equation 4.11a under the product rule. Expanding Equation 4.11 in terms of Equation 4.12 and the explicit pole representation of the Green's function yields

$$\begin{aligned} \Gamma_{pqrs} = & \frac{1}{2} \frac{1}{2\pi} \sum_t^{\text{MOS}} \sum_x^{\text{QMOS}} \sum_{ij}^{\text{occ QMOS}} \sum_a^{\text{vir QMOS}} \int_{-\infty}^{\infty} d\omega \frac{u_{tx} u_{sx}^* u_{ra} u_{pi}^* u_{qj}}{(i\omega - \lambda_x) (i\omega - \lambda_i + \lambda_j - \lambda_a)} \\ & + \frac{1}{2} \frac{1}{2\pi} \sum_t^{\text{MOS}} \sum_x^{\text{QMOS}} \sum_i^{\text{occ QMOS}} \sum_{ab}^{\text{vir QMOS}} \int_{-\infty}^{\infty} d\omega \frac{u_{tx} u_{sx}^* u_{ri} u_{pa}^* u_{qb}}{(i\omega - \lambda_x) (i\omega - \lambda_a + \lambda_b - \lambda_i)}. \end{aligned} \quad (4.13)$$

We can again exploit the integral evaluation of Equation 4.6 (see Appendix C for the derivation), along with the orthogonality condition in the Dyson orbitals, to yield the expression

$$\begin{aligned} \Gamma_{pqrs} = & \frac{1}{2} \sum_t^{\text{MOS}} \sum_x^{\text{QMOS}} \sum_{ij}^{\text{occ QMOS}} \sum_a^{\text{vir QMOS}} N(\lambda_i, \lambda_j, \lambda_a; \lambda_x) \frac{u_{tx} u_{sx}^* u_{ra} u_{pi}^* u_{qj} \langle at || ij \rangle}{\lambda_i + \lambda_j - \lambda_a - \lambda_x} \\ & + \frac{1}{2} \sum_t^{\text{MOS}} \sum_x^{\text{QMOS}} \sum_i^{\text{occ QMOS}} \sum_{ab}^{\text{vir QMOS}} N(\lambda_a, \lambda_b, \lambda_i; \lambda_x) \frac{u_{tx} u_{sx}^* u_{ri} u_{pa}^* u_{qb} \langle ti || ab \rangle}{\lambda_a + \lambda_b - \lambda_i - \lambda_x}, \end{aligned} \quad (4.14)$$

where

$$N(i, j, k; l) = \begin{cases} 1 & \text{if } l > 0, i + j - k < 0, \\ -1 & \text{if } l < 0, i + j - k > 0, \\ 0 & \text{otherwise.} \end{cases} \quad (4.15)$$

Equation 4.14 can be simplified by inserting Equation 4.15

$$\begin{aligned} \Gamma_{pqrs} = & \frac{1}{2} \sum_{ij}^{\text{occ QMOS}} \sum_{ab}^{\text{vir QMOS}} \frac{u_{sb}^* u_{ra} u_{pi}^* u_{qj} \langle ab || ij \rangle}{\lambda_i + \lambda_j - \lambda_a - \lambda_b} - \frac{1}{2} \sum_{ij}^{\text{occ QMOS}} \sum_{ab}^{\text{vir QMOS}} \frac{u_{sj}^* u_{ri} u_{pa}^* u_{qb} \langle ji || ab \rangle}{\lambda_a + \lambda_b - \lambda_i - \lambda_j} \\ = & \sum_{ij}^{\text{occ QMOS}} \sum_{ab}^{\text{vir QMOS}} \frac{u_{pi}^* u_{qj} u_{ra}^* u_{sb} \langle ij || ab \rangle}{\lambda_i + \lambda_j - \lambda_a - \lambda_b}. \end{aligned} \quad (4.16)$$

This expression can be verified by observing that

$$E_{2b} = \frac{1}{2} \sum_{pqrs}^{\text{MOS}} \langle pq || rs \rangle \Gamma_{pqrs}, \quad (4.17)$$

satisfies Equation 4.9.

## 4.5 Algorithm

The described method results in a solution to the Dyson equation with an overall cost scaling as  $\mathcal{O}(n_{\text{MO}}^5)$ , i.e. the same as MP2 and ADC(2), and has no dependency on grid size. The number of moments used provides a parameterisation that systemically improves toward canonical GF2 in the limit of infinite moments. This limit is rigorously diagrammatic, whilst truncations of AGF2 at given numbers of moments are not.<sup>a</sup> Algorithm 4.1 can be used to construct the moments of

---

**Algorithm 4.1:** Calculation of the first  $n_{\text{mom}}$  moments of the hole and particle self-energy for AGF2.

---

**Data:** ERIs in the MO basis  $\langle pq||rs\rangle$ , Dyson orbitals  $\mathbf{u}$  and pole energies  $\boldsymbol{\lambda}$ .

**Result:** AGF2 self-energy moments for the hole  $\Xi^{(\Sigma^<,n)}$  and particle  $\Xi^{(\Sigma^>,n)}$  cases.

$$\begin{aligned} \langle ij||ap\rangle &\leftarrow \sum_{qrs}^{\text{MOS}} \langle qr||sp\rangle u_{qi}^* u_{rj} u_{sa}^* \\ \langle aq||ij\rangle &\leftarrow \sum_{prs}^{\text{MOS}} \langle pq||rs\rangle u_{pa}^* u_{ri}^* u_{sj} \\ \langle pi||ab\rangle &\leftarrow \sum_{qrs}^{\text{MOS}} \langle pq||rs\rangle u_{qi} u_{ra}^* u_{sb} \\ \langle ab||qi\rangle &\leftarrow \sum_{prs}^{\text{MOS}} \langle pr||qs\rangle u_{pa}^* u_{rb} u_{si} \\ \Xi_{pq}^{(\Sigma^<,n)} &\leftarrow 0 \\ \Xi_{pq}^{(\Sigma^>,n)} &\leftarrow 0 \end{aligned}$$

```

† for i ∈ occ do
  | xpja ← ⟨ij||ap⟩
  | yqja ← ⟨aq||ij⟩
  | for n = 0 → nmom do
  | | Ξpq(Σ<,n) ← Ξpq(Σ<,n) + ∑jocc ∑avir xpja yqja
  | | if n ≠ nmom then
  | | | xpja ← xpja (λi + λj - λa)
  | | end
  | end
end

† for a ∈ vir do
  | xpbi ← ⟨pi||ab⟩
  | yqbi ← ⟨ab||qi⟩
  | for n = 0 → nmom do
  | | Ξpq(Σ>,n) ← Ξpq(Σ>,n) + ∑bvir ∑iocc xpbi yqbi
  | | if n ≠ nmom then
  | | | xpbi ← xpbi (λa + λb - λi)
  | | end
  | end
end
end

```

---

<sup>a</sup>The dynamic quantities that *are* rigorously diagrammatic have been coarse-grained into a representation that is not exact in the diagrammatic sense.

---

**Algorithm 4.2:** Relaxation of the density matrix in AGF2 calculations.

---

**Data:** Dyson orbitals  $\mathbf{u}$  and pole energies  $\boldsymbol{\lambda}$ , the core Hamiltonian matrix elements  $\mathbf{H}$ , and the static part of the self-energy  $\boldsymbol{\Sigma}(\infty)$ .

**Result:** Updated Dyson orbitals  $\mathbf{u}$  and energies  $\boldsymbol{\lambda}$  satisfying the correct number of electrons and are a minimum with respect to the SCF.

```

 $\gamma_{pq} \leftarrow \sum_x^{\text{occ}} u_{px} u_{qx}^*$ 
while  $|\gamma_{pq}^{(i)} - \gamma_{pq}^{(i-1)}| > \text{threshold}$  do
‡   while  $|\sum_p^{\text{MOS}} \gamma_{pp} - n_{\text{elec}}| > \text{threshold}$  do
‡   |    $\boldsymbol{\Sigma} \leftarrow \text{shift}(\boldsymbol{\Sigma})$ 
‡   |    $\mathbf{u}, \boldsymbol{\lambda} \leftarrow \boldsymbol{\Sigma}, \boldsymbol{\Sigma}(\infty)$ 
‡   |    $\gamma_{pq} \leftarrow \sum_x^{\text{occ}} u_{px} u_{qx}^*$ 
   end
    $F_{pq} \leftarrow H_{pq} + \sum_{rs}^{\text{MOS}} \gamma_{rs} \langle pr || qs \rangle$ 
    $\boldsymbol{\Sigma}_{pq}(\infty) \leftarrow F_{pq}$ 
‡    $\mathbf{u}, \boldsymbol{\lambda} \leftarrow \boldsymbol{\Sigma}, \boldsymbol{\Sigma}(\infty)$ 
    $\gamma_{pq} \leftarrow \sum_x^{\text{occ}} u_{px} u_{qx}^*$ 
end

```

---

the self-energy required for an AGF2 calculation, where daggered ( $\dagger$ ) line indicate loops that are typically distributed across CPUs or nodes via the message passing interface (MPI) protocol, and double daggered ( $\ddagger$ ) lines are dispatched using general matrix-multiplication (GEMM) routine via a basic linear algebra subprogram (BLAS) interface and typically also leverage open multi-processing (OpenMP) parallelism. This permits the algorithm to be applicable on HPC environments, allowing AGF2 calculations on large systems. In practice, one would implement Algorithm 4.1 in a spatial-orbital representation by spin-integrating the required quantities, and this further allows the use of a DF scheme that reduces the storage requirements to scale with system size as  $\mathcal{O}(n_{\text{MO}}^3)$ . The SCF used to relax the density matrix in the presence of the updated self-energy follows an adapted SCF algorithm, outlined in Algorithm 4.2. The daggered ( $\dagger$ ) lines indicate the diagonalisation of the compressed self-energy matrix, and the double daggered ( $\ddagger$ ) correspond to optimising a shift in the energy of the poles of said self-energy, typically handled using Newton iterations. This step scales with system size as  $\mathcal{O}(n_{\text{mom}}^4)$  due to the construction of the Fock matrix, which can be parallelised according to either MPI or OpenMP protocols, or both. The present algorithm has been implemented in the open-source PySCF<sup>26,27</sup> including hybrid MPI and OpenMP parallelism. This should amount to an *embarrassingly parallel* task in the case of all  $\mathcal{O}(n_{\text{MO}}^5)$  parts of the algorithm.

To aid convergence, self-consistent quantum chemical methods often leverage direct inversion of the iterative subspace (DIIS) to accelerate convergence.<sup>358,359</sup> This can be readily applied to AGF2 by considering the convergence of the self-energy moments, which should be unchanging at a fixed point on the Dyson equation. The moments in the hole and particle sector can therefore

---

**Algorithm 4.3:** Full AGF2 calculation.

---

**Data:** Total energy  $E_{\text{HF}}$ , coefficients  $\mathbf{C}$  and orbital energies  $\boldsymbol{\varepsilon}$  from a HF calculation.

**Result:** Converged Dyson orbitals  $\mathbf{u}$  and energies  $\boldsymbol{\lambda}$ .

$E_{\text{tot}} \leftarrow E_{\text{HF}}$

$\mathbf{u}, \boldsymbol{\lambda} \leftarrow \mathbf{C}, \boldsymbol{\varepsilon}$

**while**  $\left| E_{\text{tot}}^{(i)} - E_{\text{tot}}^{(i-1)} \right| > \text{threshold}$  **do**

$\boldsymbol{\Xi} \leftarrow \mathbf{u}, \boldsymbol{\lambda}$

(Algorithm 4.1)

$\boldsymbol{\Sigma} \leftarrow \boldsymbol{\Xi}$

(Section 3.5)

$\mathbf{u}, \boldsymbol{\lambda} \leftarrow \boldsymbol{\Sigma}$

(Equation 2.84)

    Relax  $\mathbf{u}, \boldsymbol{\lambda}$  self-consistently.

(Algorithm 4.2)

    Calculate  $E_{1b}$ .

(Equation 4.4)

    Calculate  $E_{2b}$ .

(Equation 4.7)

$E_{\text{tot}} \leftarrow E_{1b} + E_{2b}$ .

**end**

---

be concatenated into a vector, with the corresponding error vector being the vector at the current iteration minus that of the previous iteration. This facilitates the solving of the linear equations for the DIIS coefficients, allowing the extrapolation of the moments in a linear combination. A simpler alternative is to damp the moments by taking a linear combination of the moments at the current iteration with those of the previous iteration, with the coefficients summing to one and their values provided as a parameter.

Shown in Figure 4.1 is a benchmark for the AGF2 algorithm as implemented in PySCF, detailing the parallel speedup and timings per-iteration for AGF2 calculations on a guanine molecule in an aug-cc-pVDZ basis set. This system consists of 298 AOs and 78 electrons, and a DF scheme was used with the aug-cc-pVTZ-RI auxiliary basis. The calculations were performed on nodes consisting of two 20-core Intel Xeon Gold 6248 2.5 GHz processors. The plot on the left shows the parallel speedup, with the ideal linear speedup indicated as the black line, of both the full timings and those due to the leading-order scaling ( $\mathcal{O}(n_{\text{MO}}^5)$ ) steps. The latter will dominate the cost of AGF2 calculations in the limit of large systems, and so the parallel speedup of these steps are of the most interest in benchmarking the method. The scaling of these steps can be seen to be almost completely linear in the plotted regime (up to 100 CPUs), indicating the scalability of the algorithm and suitability for application to large systems on HPCs. The full algorithm has slightly poorer parallel speedup, due to steps such as the SCF and Fock matrix construction that are not as well distributed to large numbers of cores. These steps however constitute a smaller fraction of the total runtime as the size of the system increases.

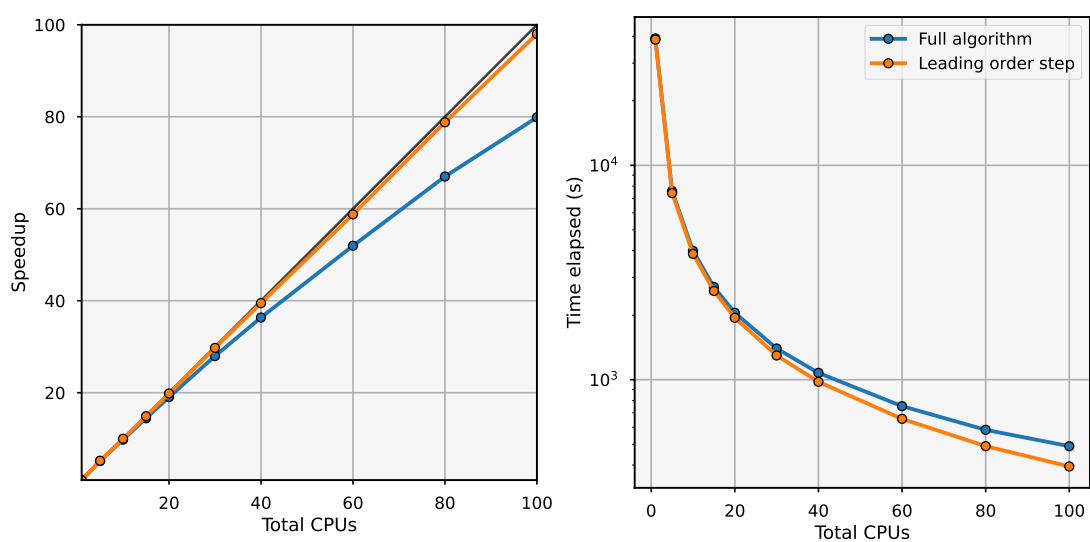


Figure 4.1: Benchmark of the AGF2 implementation in PySCF with calculations on a guanine molecule in an aug-cc-pVDZ basis set, with 298 AOs and 78 electrons. A DF scheme was used with the aug-cc-pVTZ-RI auxiliary basis. The times shown are for a single iteration of AGF2, on nodes consisting of two 20-core Intel Xeon Gold 6248 2.5 GHz processors. The left plot shows the speedup with respect to the single core timing, whilst the right plot shows the actual times. Shown are the timings for the entire AGF2 algorithm, along with timings only for the leading-order scaling ( $\mathcal{O}(n_{\text{MO}}^5)$ ) steps, which will dominate the cost in the limit of very large systems. The black line on the left plot indicates the ideal linear speedup.

## 4.6 Application to solids

The ideas presented thus far largely focus on real-space orbitals and the application to molecular systems. They are however readily applicable to orbitals resolved in momentum space, or  $k$ -space, exploiting the periodic symmetry in crystalline systems. To apply this to AGF2 we can simply rewrite Equation 4.3 in  $k$ -space

$$\Xi_{\mathbf{k}_p \mathbf{k}_q, pq}^{(\Sigma^{(2), <, n})} = \frac{1}{2} \sum_{ij}^{\text{occ}} \sum_a^{\text{vir}} \langle i_{\mathbf{k}_i} j_{\mathbf{k}_j} || a_{\mathbf{k}_a} p_{\mathbf{k}_p} \rangle (\varepsilon_{\mathbf{k}_i, i} + \varepsilon_{\mathbf{k}_j, j} - \varepsilon_{\mathbf{k}_a, a})^n \langle a_{\mathbf{k}_a} q_{\mathbf{k}_q} || i_{\mathbf{k}_i} j_{\mathbf{k}_j} \rangle, \quad (4.18a)$$

$$\Xi_{\mathbf{k}_p \mathbf{k}_q, pq}^{(\Sigma^{(2), >, n})} = \frac{1}{2} \sum_i^{\text{occ}} \sum_{ab}^{\text{vir}} \langle p_{\mathbf{k}_p} i_{\mathbf{k}_i} || a_{\mathbf{k}_a} b_{\mathbf{k}_b} \rangle (\varepsilon_{\mathbf{k}_a, a} + \varepsilon_{\mathbf{k}_b, b} - \varepsilon_{\mathbf{k}_i, i})^n \langle a_{\mathbf{k}_a} b_{\mathbf{k}_b} || q_{\mathbf{k}_q} i_{\mathbf{k}_i} \rangle. \quad (4.18b)$$

Whilst Equation 4.18 appears to formally scale with the fifth power of the number of  $k$ -space vectors, it can be simplified by noting that

$$\Xi_{\mathbf{k}_p \mathbf{k}_q, rs}^{(\dots, n)} = \delta_{pq} \Xi_{\mathbf{k}_p \mathbf{k}_q, rs}^{(\dots, n)}, \quad (4.19)$$

and also by considering the law of momentum conservation requiring

$$(\mathbf{k}_p - \mathbf{k}_q + \mathbf{k}_r - \mathbf{k}_s) \cdot \mathbf{a} = 2n\pi, \quad (4.20)$$

where  $\mathbf{a}$  are the lattice vectors of the unit cell. As a result the number of permutations of  $k$ -space vectors in Equation 4.18 scale only as the third power of the number of  $k$ -points, in order to calculate the moments at every  $k$ -point (where the moments are diagonal in  $k$ -space as a result of Equation 4.19). The overall scaling of AGF2 for periodic solids is therefore  $\mathcal{O}(n_{\text{kpts}}^3 n_{\text{MO}}^5)$  where  $n_{\text{kpts}}$  is the number of  $k$ -points and  $n_{\text{MO}}$  is the number of MOs in a single unit cell.

In non-self-consistent Green's function methods applied to *ab initio* solids such as EOM-CCSD, GW, and more recently ADC, one typically calculates the Green's function only at a single  $k$ -point, most often computing the direct band gap at the highest symmetry point  $\Gamma$  in the first Brillouin zone.<sup>205,296,360–364</sup> One then has the option to perform separate calculations with a shifted  $k$ -point mesh in order to trace out bands through high-symmetry points in the first Brillouin zone. AGF2 is different in this respect, since the self-consistent formalism requires one to build subsequent self-energies with sums over quantities in the basis of the Dyson orbitals at different  $k$ -points, as can be seen in Equation 4.18. This requires the calculation of the Green's function at *every* sampled  $k$ -point at each iteration, and has the effect of including some non-local correlation effects, with the self-energy incorporating diagrams whose configurations can consist of combinations of  $k$ -points, so long as momentum conservation is adhered to. A simple approximation can be made in periodic AGF2 to only perform self-consistency at the  $\Gamma$  point where one wishes to probe the direct band gap, with the propagator at all other sampled  $k$ -points remaining at the level of MP2. The non-self-consistent self-energy already provides sufficient long-range dispersion effects at the level of MP2 such that this approximation will be satisfactory for many systems, without the need for self-consistency away from the  $\Gamma$  point, with these self-consistencies likely to be small in effect. This reduces the iterative cost to  $\mathcal{O}(n_{\text{kpts}}^2 n_{\text{MO}}^5)$ , and whilst there still exists a  $\mathcal{O}(n_{\text{kpts}}^3 n_{\text{MO}}^5)$  non-iterative cost, the prefactor for this step is reduced significantly. This method is denoted  $\Gamma$ -AGF2.



## 4.7 Multiple solutions

The existence of multiple solutions at different levels (or absence) of self-consistency in Green's functions methods is well known and documented.<sup>145,216,357,365–374</sup> As discussed in Sections 2.4.2 and 2.4.3 the Dyson equation can be solved linearly when unfolded into its configuration space, despite the subsequent projection of the Dyson orbitals onto the space spanned by MOs (the physical space) still being non-linear. The equation however is commonly solved non-linearly i.e. downfolded into the frequency domain, leading to the fulfilment of the non-linear equations by multiple solutions.<sup>357</sup> Furthermore, the introduction of self-consistency necessarily results in additional non-linearities since in a linear form the number of configurations would grow intractably. The compression of these configurations, either by moment constraints or simply downfolding onto the physical space, affects the number of solutions. These non-linearities can manifest in discontinuous surfaces for many properties such as the IP and EA including within several flavours of *GW* and in GF2.<sup>370</sup> An example of this is with the quasiparticle equation, whose solution corresponds to that with the largest renormalisation factor as written in Equation 2.91. When the renormalisation factor of two such quasiparticle states cross over along the reaction coordinate of a particular energy surface, the character of the solution therefore changes to the dominant factor, and a discontinuity can be observed. This can become particularly erratic when spurious poles occur in the self-energy due to singularities, often resulting in a fragmented energy surface where the dominant solution changes multiple times in a short range of the reaction coordinate.<sup>370</sup>

Figure 4.2 shows the discontinuities in the quasiparticle energies  $\lambda_p$ , self-energy elements  $\Sigma_{pp}(\lambda_p)$ , and quasiparticle renormalisation factors  $Z_p$  with increasing atomic separation of  $\text{H}_2$  in a 6-31G basis set. The panels show results for single-shot *GW* with both a HF and Perdew–Burke–Ernzerhof (PBE) density functional, for ADC(2), and for two parameterisations of AGF2 with  $n_{\text{iter}} = 0$  and 5 in the self-energy recurrence algorithm, respectively. The canonical *GW* results employ the quasiparticle approximation. In the ADC(2) and AGF2 results, the quasiparticle solutions were determined by the roots in the Green's function with the largest overlap with each MO, whereas *GW* applies the quasiparticle equation to similar effect. Significant discontinuities can be observed for the *GW* results, whilst this manifests most intuitively in the quasiparticle energy surface in the first column its source can be understood best from the renormalisation factor in the third column; across the reaction coordinate the dominant renormalisation factor changes multiple times resulting in the selection of a different quasiparticle solution, in both the LUMO+1 and LUMO+2. Similar observations can be made for the ADC(2) results, where a clear crossover in renormalisation factor curves occurs for the LUMO+2 at around 0.6 Å. A similar feature can be seen at around 1.0 Å likely due to a spurious pole in the self-energy. At the level of AGF2, all three panels are completely continuous in this range of separations in the case of  $n_{\text{iter}} = 0$  in the self-energy recurrence, however the discontinuities are almost identical to those of ADC(2) with  $n_{\text{iter}} = 5$ . The latter method, termed AGF2(None, 5), is likely converged to the full-frequency GF2 result numerically exactly, with very few moments required to capture the dynamics of the self-energy in such a simple system.

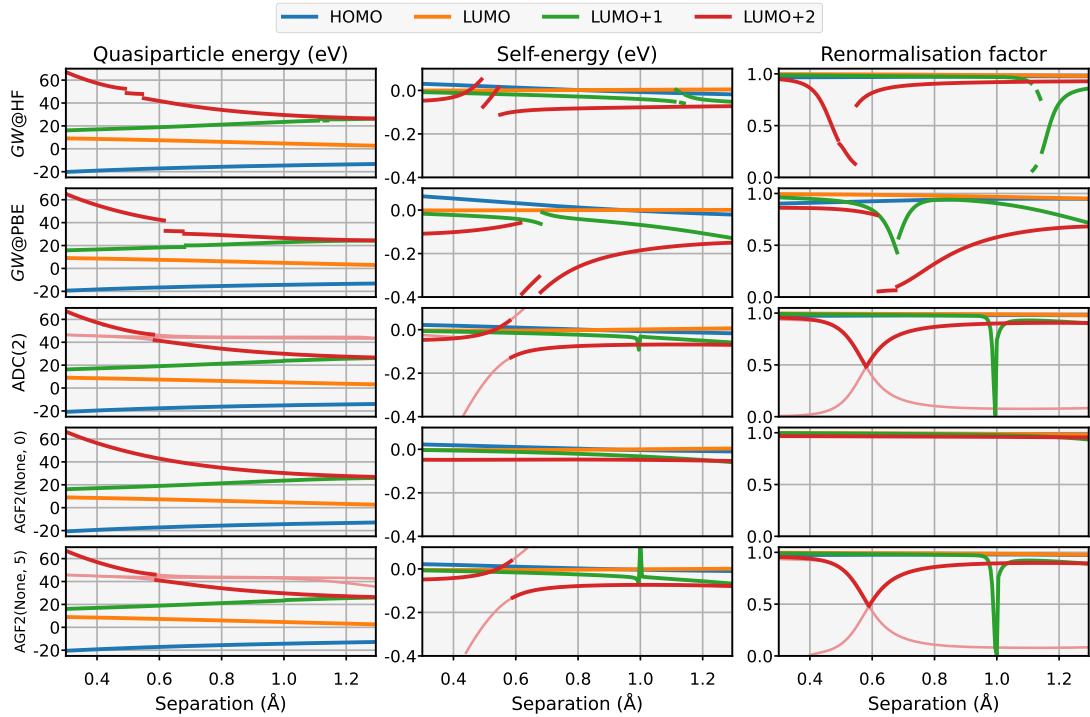


Figure 4.2: Discontinuities in the quasiparticle energies  $\lambda_p$ , self-energy elements  $\Sigma_{pp}(\lambda_p)$ , and quasiparticle renormalisation factors  $Z_p$  with increasing atomic separation of  $\text{H}_2$  in a 6-31G basis set. Plots are shown for single-shot  $GW$  with both a HF and Perdew–Burke–Ernzerhof (PBE) density functional, for ADC(2), and for two parameterisations of AGF2 with  $n_{\text{iter}} = 0$  and 5 in the self-energy recurrence algorithm, respectively. The canonical  $GW$  results employ the quasiparticle approximation. The orbitals  $p$  enumerate the HOMO, LUMO, LUMO+1, and LUMO+2, respectively. All results were computed with the PySCF programming package.<sup>26,27</sup> In the ADC(2) and AGF2 results, the quasiparticle solutions were determined by the roots in the Green’s function with the largest overlap with each MO, whereas  $GW$  applies the quasiparticle equation to similar effect. The transparent lines follow the alternate solutions where discontinuities occur in the case of the final three rows, which is more difficult to show in the case of the top two rows that rely on the quasiparticle equation.

The self-consistent renormalisation of the propagators according to the Dyson equation therefore does not remedy the unphysical discontinuities in this example, however the reduction of resolution in the self-energy offered by AGF2(None, 0) does. The reduced resolution means that spurious poles in the self-energy that do not contribute significantly to the zeroth or first moments do not appear, with their dynamics coarsely represented by more significant neighbouring poles such that the self-energy still reproduces the moments. This results in a Green's function with far fewer poles with non-quasiparticle-like behaviour. This is not a strict feature; the Green's function at the level of AGF2(None, 0) consists of  $3n_{\text{MO}}$  poles, which still obey sum rules, meaning that there must be some poles with small weights.





## Chapter 5

# Auxiliary $GW$ approximation

## 5.1 Introduction

Performing *GW* calculations in a numerically exact fashion using the RPA has a bottleneck scaling as  $\mathcal{O}(n_{\text{MO}}^6)$ . Whilst an exhausting number of approximations exist to make *GW* calculations practical, such approximations are often harsh and consequential. These include using quasiparticle equation formulations, diagonal approximations to the self-energy, or both. Many also employ numerical methods such as analytic continuation and Fourier transforms, with necessary resolutions on discrete grids and often a finite temperature. Ref. 333 recently reported a *GW* implementation scaling with system size as low as  $\mathcal{O}(n_{\text{MO}}^3)$ , without exploiting locality or sparsity. This leverages a susceptibility calculated in the time domain over real-space coordinates, leveraging an RI along with a modern analytical continuation approach applied directly to the screened Coulomb interaction.

The techniques outlined in Chapter 3 can be applied to *GW* calculations, and in combination with some recently developed numerical integration techniques an efficient and tractable moment-resolved *GW* solver can be formulated, the details of which shall be outlined in this Chapter. The developments leading to the evaluation of the RPA moments is largely the work of C. J. C. Scott building upon Ref. 375. The combination of this formulation with the self-energy recurrence of Section 3.5 results in this efficient *GW* solver, and is the topic of a paper currently in preparation.<sup>54</sup> In the spirit of the AGF2 nomenclature, we term this method auxiliary *GW* (*AGW*) and will often use  $\text{AGW}(n_{\text{iter}})$  to denote the number of iterations applied in the block Lanczos recurrence.

*GW* solvers aiming to bypass the numerical quadrature of typical implementations have been discussed previously in the literature, with a recent implementation offering a  $\mathcal{O}(n_{\text{MO}}^4)$  implementation in the case of TDA screening and DF outlined in Ref. 312, in which the *GW* is unfolded into its configuration space and solved using an iterative eigensolver. The authors discuss initial efforts to also formulate a similar scheme in the case of RPA screening. The present Chapter will outline a scheme scaling also with system size as  $\mathcal{O}(n_{\text{MO}}^4)$ , and naturally employing the RPA for screening.

The approach outlined here also offers a very simply extension to perform self-consistent *GW* calculations with moment constraints, in a fashion analogous to that of AGF2. This will also require some of the considerations of additional self-consistencies in the physical density matrix, as well as maintenance of the particle number, borrowing many ideas from Chapter 4. This will be the topic of future work.

## 5.2 Method

Recapping its definition in Equation 2.159, the reducible polarisation propagator can be written as a sum over its poles

$$\chi(\mathbf{x}_1, \mathbf{x}_2; \omega) = \sum_n \frac{\rho_n(\mathbf{x}_1)\rho_n^*(\mathbf{x}_2)}{\omega - \Omega_n + i0^+} + \sum_n \frac{\rho_n(\mathbf{x}_1)\rho_n^*(\mathbf{x}_2)}{\omega + \Omega_n - i0^+}. \quad (5.1)$$

The reducible polarisation propagator was previously discussed in the context of the RPA in Section 2.8. A more compact form of the polarisation propagator can be written in terms of the eigenpairs in Equation 2.164, by summing together  $1h1p$  and  $1p1h$  contributions

$$\eta_{ia,jb}(\omega) = \sum_m \frac{(X_{ia}^m + Y_{ia}^m)(X_{jb}^m + Y_{jb}^m)^*}{\omega - \Omega_m}, \quad (5.2)$$

which only needs to be defined in the positive frequency sector, owing to the boson-like symmetry in the RPA eigenproblem. It is clear that Equation 5.2 is of a form very appropriate to the present work, as its spectral moments read

$$\Xi_{ia,jb}^{(\eta,n)} = -\frac{1}{\pi} \int_0^\infty d\omega \operatorname{Im}[\eta_{ia,jb}(\omega)] \omega^n \quad (5.3a)$$

$$= \sum_m (X_{ia}^m + Y_{ia}^m) \Omega_m^n (X_{jb}^m + Y_{jb}^m), \quad (5.3b)$$

which is analogous to the moments of the single-particle Green's function shown in Section 2.4.4, here, for a two-particle Green's function. RPA can be reformulated entirely in terms of these moments with no loss of information, and recurrence relations can be defined to calculate higher-order moments from the zeroth moment and the  $\mathbf{A}$  and  $\mathbf{B}$  matrices entering the RPA problem

$$\Xi^{(\eta,n)} = (\mathbf{A} - \mathbf{B})(\mathbf{A} + \mathbf{B})\Xi^{(\eta,n-2)} \quad (5.4a)$$

$$= [\Xi^{(\eta,0)}(\mathbf{A} + \mathbf{B})]^n \Xi^{(\eta,0)}. \quad (5.4b)$$

The details leading to these recurrence relations are discussed in Ref. 375. Also of note is that in the case of the TDA, the moments become trivial

$$\Xi^{(\eta,n)} = \mathbf{A}^n, \quad (5.5)$$

and therefore identity in the case of the zeroth moment. This reflects the lack of correlation in the ground state.<sup>303,304</sup>



### 5.3 Efficient evaluation of moments

Whilst Equation 5.3b can be constructed naively with a bottleneck scaling as  $\mathcal{O}(n_{\text{MO}}^6)$ , we seek to find a low-scaling algorithm to construct these objects in order to obtain a practical  $GW$  algorithm. The algorithm requires a linear transformation from the  $1h1p$  space to a space scaling linearly with system size. This is achieved by the standard DF approximation in quantum chemistry, in which the RI basis has a linear scaling with system size but conserves well the ERIs on the rotation of two MO indices into it. Under a density fitting approximation, Equation 2.166 becomes

$$A_{ia,jb} = (\varepsilon_a - \varepsilon_i)\delta_{ab}\delta_{ij} + \sum_Q^{\text{aux}} (ia|Q)(Q|jb), \quad (5.6a)$$

$$B_{ia,jb} = \sum_Q^{\text{aux}} (ia|Q)(Q|jb), \quad (5.6b)$$

and the response can also be (partially) rotated using the interaction matrices

$$\tilde{\eta}_{ia,Q} = \sum_j^{\text{occ}} \sum_b^{\text{vir}} \eta_{ia,jb}(jb|Q), \quad (5.7)$$

along with the associated moments

$$\Xi_{ia,Q}^{(\tilde{\eta},n)} = \sum_j^{\text{occ}} \sum_b^{\text{vir}} \Xi_{ia,jb}^{(\eta,n)}(jb|Q). \quad (5.8)$$

To retain a bottleneck scaling with system size as  $\mathcal{O}(n_{\text{MO}}^4)$ , we wish to write the part of the recurrence of Equation 5.4a involving  $\mathbf{A}$  and  $\mathbf{B}$  as a diagonal matrix plus a low-rank correction. This is applicable to RPA since

$$A_{ia,jb} - B_{ia,jb} = (\varepsilon_a - \varepsilon_i)\delta_{ab}\delta_{ij} = D_{ia}, \quad (5.9)$$

is diagonal, and  $(\mathbf{A} + \mathbf{B})$  can be written as

$$A_{ia,jb} + B_{ia,jb} = D_{ia} + 2 \sum_Q^{\text{aux}} (ia|Q)(Q|jb). \quad (5.10)$$

These definitions allow us to express  $(\mathbf{A} - \mathbf{B})(\mathbf{A} + \mathbf{B})$  as a diagonal matrix plus low-rank correction

$$\begin{aligned} (\mathbf{A} - \mathbf{B})(\mathbf{A} + \mathbf{B}) &= \mathbf{D}^2 + (\mathbf{D}\mathbf{V})(2\mathbf{V})^\dagger \\ &= \mathbf{D}^2 + \mathbf{L}\mathbf{R}^\dagger, \end{aligned} \quad (5.11)$$

where the matrix  $\mathbf{V}$  has been introduced such that

$$\mathbf{V}_{ia}\mathbf{V}_{jb}^\dagger = \sum_Q (ia|Q)(Q|jb) = \langle ij|ab \rangle. \quad (5.12)$$

The first-order moments can be trivially extracted from these matrices as

$$\Xi^{(\tilde{\eta},1)} = \mathbf{D}\mathbf{V} = \mathbf{L}. \quad (5.13)$$

An expression for the zeroth moment without the DF approximation can be derived from Equation 5.4b

$$\Xi^{(\eta,0)} = [(\mathbf{A} - \mathbf{B})(\mathbf{A} + \mathbf{B})]^{\frac{1}{2}} (\mathbf{A} + \mathbf{B})^{-1}, \quad (5.14)$$

and can therefore be written in the low-rank format

$$\Xi^{(\tilde{\eta},0)} = (\mathbf{D}^2 + \mathbf{L}\mathbf{R}^\dagger)^{\frac{1}{2}} (\mathbf{D} + 2\mathbf{V}\mathbf{V}^\dagger)^{-1} \mathbf{V}. \quad (5.15)$$

This expression can be evaluated using integration over numerical quadrature, the details of which are to be discussed in Ref. 54. Higher-order moments can then be computed from the zeroth- and first-order moments according to the recurrence relations in Equation 5.4.

## 5.4 Calculation of self-energy moments

The moments of the polarisation propagator can be used to obtain the moments of the self-energy at the level of *GW*, from which one can apply the recurrence of Section 3.5 to obtain approximate quasiparticle excitation energies. This can be achieved via the binomial theorem, corresponding to the moments of a convolution

$$\Xi_{pq}^{(\Sigma^<,n)} = \sum_{ij}^{\text{occ}} \sum_{ab}^{\text{vir}} \sum_{PQ}^{\text{aux}} V_{ia}^{(Q)} V_{jb}^{(P)} \sum_k^{\text{occ}} V_{pk}^{(Q)} V_{qk}^{(P)} \sum_{t=0}^n \binom{n}{t} (-1)^t \varepsilon_k^{n-t} \Xi_{ia,jb}^{(\tilde{\eta},t)}, \quad (5.16a)$$

$$\Xi_{pq}^{(\Sigma^>,n)} = \sum_{ij}^{\text{occ}} \sum_{ab}^{\text{vir}} \sum_{PQ}^{\text{aux}} V_{ia}^{(Q)} V_{jb}^{(P)} \sum_c^{\text{vir}} V_{pc}^{(Q)} V_{qc}^{(P)} \sum_{t=0}^n \binom{n}{t} \varepsilon_c^{n-t} \Xi_{ia,jb}^{(\tilde{\eta},t)}. \quad (5.16b)$$

These operations can be ordered such that the scaling with system size does not exceed  $\mathcal{O}(n_{\text{MO}}^4)$ , for example in the case of the hole moment

$$\Xi_{pq}^{(\Sigma^<,n)} = \sum_k^{\text{occ}} \sum_{t=0}^n \binom{n}{t} (-1)^t \varepsilon_k^{n-t} \Xi_{pqk}^{(\tilde{\Sigma}^<,n)}, \quad (5.17a)$$

$$\Xi_{pqk}^{(\tilde{\Sigma}^<,n)} = \sum_Q^{\text{aux}} \left( V_{pk}^{(Q)} \sum_P^{\text{aux}} \left( V_{qk}^{(P)} \Xi_{QP}^{(\tilde{\eta},t)} \right) \right), \quad (5.17b)$$

$$\Xi_{QP}^{(\tilde{\eta},t)} = \sum_{ij}^{\text{occ}} \sum_{ab}^{\text{vir}} V_{ia}^{(Q)} V_{jb}^{(P)} \Xi_{ia,jb}^{(\eta,t)}, \quad (5.17c)$$

where Equation 5.17c represents the moments of the polarisation propagator in the basis of DF auxiliary functions. Finally, the moments can simply be passed to the self-energy recurrence relations of Section 3.5 in order to calculate approximate quasiparticle excitations at the level of *GW*. As discussed in Section 4.2, this is performed separately for the hole and particle moments in order to appropriately resolved the low-energy dynamics.

Additionally, this scheme offers a simple extension to self-consistent forms of *GW* in the future, where the Green's function obtained via the diagonalisation of the compressed self-energy matrix can be reinserted into the self-energy diagrams. This is identical to the ideas used to obtain self-consistency in AGF2, and may too require considerations of correlation-induced updates to the static self-energy, along with maintenance of the particle number via a chemical potential.

## 5.5 Multiple solutions

Section 4.7 showed that the coarse representation afforded by low numbers of iterations in the block Lanczos recursion relaxed many of the issues associated with multiple quasiparticle solutions resulting from calculations at (self-consistent) second-order perturbation theory. Figure 5.1 shows the discontinuities in the quasiparticle energies  $\lambda_p$ , self-energy elements  $\Sigma_{pp}(\lambda_p)$ , and quasiparticle renormalisation factors  $Z_p$  with increasing atomic separation of  $\text{H}_2$  in a 6-31G basis set. The panels show results for single-shot  $GW$  with both a HF and PBE density functional, for ADC(2), and for two parameterisations of AGW with  $n_{\text{iter}} = 0$  and 5 in the self-energy recurrence algorithm, respectively. The AGW calculations use a HF reference. The canonical  $GW$  results employ the quasiparticle approximation. The top three rows are identical to those of Figure 4.2, and are only repeated here for ease of comparison with the last two rows, which show the equivalent AGW results rather than the AGF2 ones of Figure 4.2. Like in AGF2, the results at  $n_{\text{iter}} = 0$  (conserving only the zeroth and first moment of the separate hole and particle  $GW$  self-energies) relax the discontinuities observed in the canonical  $GW$  results, and which also appear in the AGW results when one uses a greater number of iterations. At this level the renormalisation factors are all continuously close to unity with the only deviation occurring towards the maximum of the domain for the LUMO+1 state, where the crossover occurs with the LUMO+2. That being said, within the plotted domain no discontinuity is observed in the self-energy or in the quasiparticle energies, whilst the canonical  $GW@HF$  and indeed the  $n_{\text{iter}} = 5$  result both observe discontinuities in this regime. This is an advantage of low-iteration AGW calculations, which will be shown to rapidly converge the IP and EA to the full-frequency result in Chapter 7.

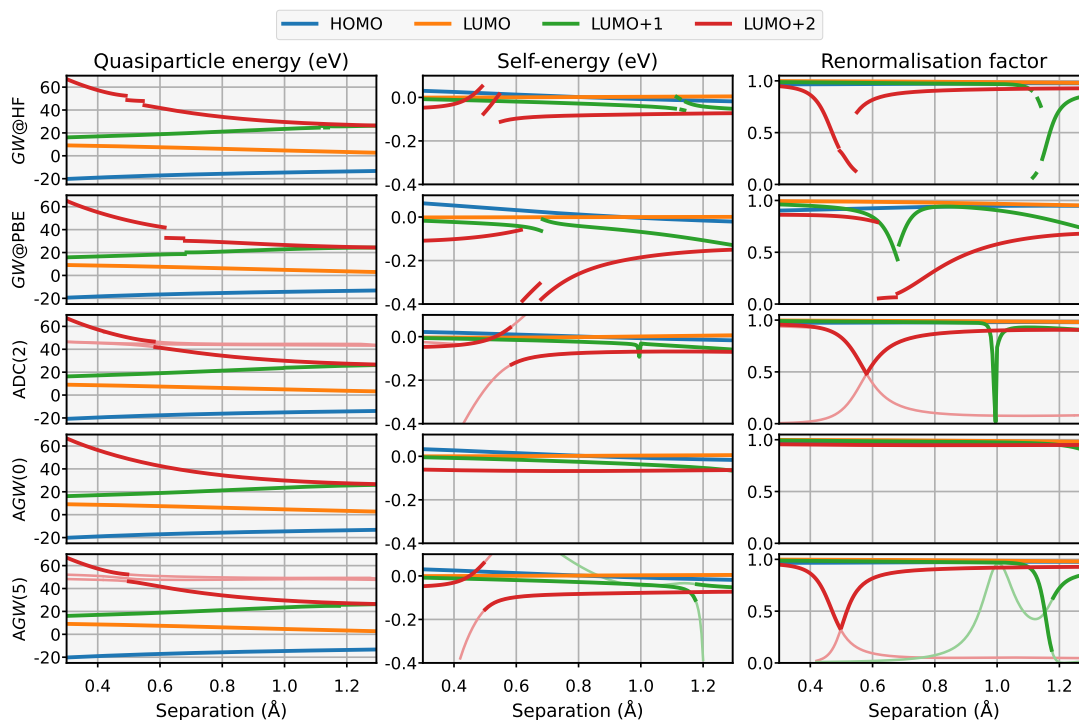


Figure 5.1: Discontinuities in the quasiparticle energies  $\lambda_p$ , self-energy elements  $\Sigma_{pp}(\lambda_p)$ , and quasiparticle renormalisation factors  $Z_p$  with increasing atomic separation of  $\text{H}_2$  in a 6-31G basis set. Plots are shown for single-shot *GW* with both a HF and PBE density functional, for ADC(2), and for two parameterisations of moment-resolved *GW* (AGW) with  $n_{\text{iter}} = 0$  and 5 in the self-energy recurrence algorithm, respectively. The AGW calculations use a HF reference. The canonical *GW* results employ the quasiparticle approximation. The orbitals  $p$  enumerate the HOMO, LUMO, LUMO+1, and LUMO+2, respectively. All results were computed with the PySCF programming package.<sup>26,27</sup> In the ADC(2) and AGW results, the quasiparticle solutions were determined by the roots in the Green’s function with the largest overlap with each MO, whereas *GW* applies the quasiparticle equation to similar effect. The transparent lines follow the alternate solutions where discontinuities occur in the case of the final three rows, which is more difficult to show in the case of the top two rows that rely on the quasiparticle equation.





## Chapter 6

# Moment-resolved coupled cluster Green's function



## 6.1 Introduction

Section 2.7.2 outlined a method by which one can construct the Green's function at the level of an arbitrary CC ansatz. This is a powerful tool for probing the spectrum of materials at the level of CC, and has seen recent popularity with efficient formulations, often based on projecting the problem onto a subspace that drastically reduces the number of FLOPs required.<sup>128,130</sup> Despite this, most of these formulations still retain either a formal scaling dependency on the size of the grid, or at least incorporate the grid and broadening parameter into the calculation requiring entirely separate calculations to alter such parameters. Instead, we can make use of the techniques outlined to obtain an explicit pole representation of the CC Green's function, which offers both an efficient construction and the ability to adjust dynamic parameters when plotting the spectrum without a separate calculation. This can be achieved by deriving expressions to calculate the moments of the Green's function, in a similar fashion to how one would compute the density matrix at the level of CC. Therein one can apply the recurrence relations on the Green's function moments—in contrast to the previous two Chapters where the recurrence was applied to moments of the self-energy—in order to obtain the effective Dyson orbitals and energies.

This method has been discussed in a recent publication,<sup>339</sup> and at the time of writing open-source code has been submitted to the PySCF programming package.<sup>26,27</sup> This publication and implementation concerns the application of the solver to the CCSD ansatz, however the discussion can be generalised to virtually any other ansatz, requiring the derivation of expressions for matrix elements at the particular level of CC. Future work will seek to derive such expressions for higher-order CC ansatzes, including less familiar ones that handle active spaces at higher levels of theory.

Other implementations of GF-CC methods similarly look to transform the problem according to projection into a smaller subspace. These include the implementations in the GFCCLib package based on the model-order reduction technique, where the iterative cost at each frequency is relaxed to avoid excessive computational resources being required to resolve the spectrum well.<sup>130,131</sup> This approach however still requires one to perform separate calculations in order to adjust the grid parameters. To combat this requirement, Ref. 128 seeks to project the similarity-transformed Hamiltonian into a Krylov subspace using a single-vector biorthogonal Lanczos algorithm, corresponding to a conservation of elements of the moments of the effective self-energy of the system. Their method however has a cost with system size scaling as  $\mathcal{O}(n_{\text{MO}}^7)$  in order to access off-diagonal elements of the Green's function, which is of little impact in their application which is based on embedding problems and therefore scaling of some contractions is relaxed to  $\mathcal{O}(1)$ . The benefit of this method is that it does not require the separate solution of a linear equation at each frequency point. The method described in this Chapter will seek to combine the benefits of subspace projection with the lack of a frequency dependence in the working equations.

## 6.2 Method

Recalling the expressions for the Green's function at the level of a given CC ansatz in Equation 2.150

$$G_{pq}(\omega + i0^+) = \left\langle \Psi_{\text{HF}} \left| (1 + \hat{\Lambda}) \bar{a}_q^\dagger [\omega + \bar{H}_N + i0^+]^{-1} \bar{a}_p \right| \Psi_{\text{HF}} \right\rangle + \left\langle \Psi_{\text{HF}} \left| (1 + \hat{\Lambda}) \bar{a}_p [\omega - \bar{H}_N + i0^+]^{-1} \bar{a}_q^\dagger \right| \Psi_{\text{HF}} \right\rangle, \quad (6.1)$$

the moments of the Green's function can be written

$$\Xi_{pq}^{(G^<,n)} = \left\langle \Psi_{\text{HF}} \left| (1 + \hat{\Lambda}) \bar{a}_q^\dagger [-P_Y \bar{H}_N P_Y]^n \bar{a}_p \right| \Psi_{\text{HF}} \right\rangle, \quad (6.2a)$$

$$\Xi_{pq}^{(G^>,n)} = \left\langle \Psi_{\text{HF}} \left| (1 + \hat{\Lambda}) \bar{a}_p [P_X \bar{H}_N P_X]^n \bar{a}_q^\dagger \right| \Psi_{\text{HF}} \right\rangle, \quad (6.2b)$$

where the projectors  $P_X$  and  $P_Y$  as given in Equation 2.154 ensure projection onto the correct set of excitations. We note that these are moments of the hole and particle Green's function, i.e. the hole energies are below the Fermi energy, whereas previous derivations such as that of Ref. 339 take the hole moment in the context of IPs where the sign of the energies is flipped and therefore the minus sign in Equation 6.2a is missing. One can see that the expression for  $\Xi^{(G^<,0)}$

$$\begin{aligned} \Xi_{pq}^{(G^<,0)} &= \left\langle \Psi_{\text{HF}} \left| (1 + \hat{\Lambda}) \bar{a}_q^\dagger \bar{a}_p \right| \Psi_{\text{HF}} \right\rangle \\ &= \gamma_{pq}^{\text{CC}}, \end{aligned} \quad (6.3)$$

is equal to the one-particle CC density matrix. Whereas higher-order moments are defined simply by powers of the  $n = 1$  moment in a mean-field picture, in this correlated picture additional order moments provide more information resulting in additional spectral features, resulting from the existence of a dynamic self-energy.

As discussed in Section 2.7.1,  $\bar{H}$  is only referred to as an *effective* self-energy upfolded into its configuration space, rather than a proper self-energy. This can be seen by the fact that the Green's function moments are not simply equal to powers of  $\bar{H}$  projected down onto the physical space, but rather they must be acted upon by similarity transformed operators in the bra and ket. These are defined as

$$\mathbf{x}_p^< = \bar{a}_p^\dagger | \Psi_{\text{HF}} \rangle, \quad (6.4a)$$

$$\mathbf{x}_p^> = \bar{a}_p | \Psi_{\text{HF}} \rangle, \quad (6.4b)$$

$$\mathbf{y}_p^< = \langle \Psi_{\text{HF}} | (1 + \hat{\Lambda}) \bar{a}_p, \quad (6.4c)$$

$$\mathbf{y}_p^> = \langle \Psi_{\text{HF}} | (1 + \hat{\Lambda}) \bar{a}_p^\dagger, \quad (6.4d)$$

which must be evaluated within a given ansatz to obtain tensorial expressions. Unlike the EOM-CC similarity transformed Hamiltonian, these vectors (specifically the bra) depend on the de-excitation amplitudes  $\hat{\Lambda}$ . This reflects the biorthogonal correlated ground state at the level of CC, rather than simply the HF ground state. The most common choice of ansatz is to truncate the excitation and de-excitation operators to span only singles and doubles, leading to the ubiquitous CCSD method.

At this level, in the case of the hole Green's function, the bra and ket span the  $1h$  and  $2h1p$  spaces and are defined according to the character of the index of the second-quantised operator<sup>128</sup>

$$x_{i,j}^< = \delta_{ij}, \quad (6.5a)$$

$$x_{a,j}^< = t_j^a, \quad (6.5b)$$

$$x_{i,klb}^< = 0, \quad (6.5c)$$

$$x_{a,klb}^< = t_{kl}^{ab}, \quad (6.5d)$$

$$y_{i,j}^< = \delta_{ij} - \sum_e^{\text{vir}} l_e^j t_i^e - \frac{1}{2} \sum_k^{\text{occ}} \sum_{ab}^{\text{vir}} l_{ab}^k t_{ik}^{ab}, \quad (6.5e)$$

$$y_{a,j}^< = l_a^j, \quad (6.5f)$$

$$y_{i,klb}^< = \sum_a^{\text{vir}} t_i^a l_{ab}^{lk} + \delta_{ik} l_b^l - \delta_{il} l_b^k, \quad (6.5g)$$

$$y_{a,klb}^< = l_{ba}^{lk}. \quad (6.5h)$$

In the case of the particle Green's function, the bra and ket span the  $1p$  and  $1h2p$  spaces and are defined as

$$x_{i,b}^> = -t_i^b, \quad (6.6a)$$

$$x_{a,b}^> = \delta_{ab}, \quad (6.6b)$$

$$x_{i,cdj}^> = t_{ij}^{dc}, \quad (6.6c)$$

$$x_{a,cdj}^> = 0, \quad (6.6d)$$

$$y_{i,b}^> = -l_b^i, \quad (6.6e)$$

$$y_{a,b}^> = \delta_{ab} - \sum_i^{\text{occ}} l_b^i t_i^a - \frac{1}{2} \sum_{ij}^{\text{occ}} \sum_c^{\text{vir}} l_{bc}^{ij} t_{ij}^{ac}, \quad (6.6f)$$

$$y_{i,cdj}^> = l_{cd}^{ji}, \quad (6.6g)$$

$$y_{a,cdj}^> = \sum_i^{\text{vir}} t_i^a l_{cd}^{ji} + \delta_{ac} l_d^j - \delta_{ad} l_c^j. \quad (6.6h)$$

These expressions can be generated for arbitrary CC ansatzes using Wick's theorem, which is implemented in many symbolic algebra packages allowing computer generation of the expressions.<sup>376–381</sup> The product between the similarity transformed Hamiltonian projected into the particular configurations can also be generated diagrammatically, and is implemented in many modern quantum chemistry packages, allowing the dot-product with an arbitrary state vector.<sup>26,27,267,273</sup>

One can then perform the recursion outlined in Section 3.6 for each set of moments, obtaining a set of Dyson orbitals and pole energies that conserve the separate hole and particle Green's function moments. This must be done using the non-Hermitian variant of the algorithm as the non-unitary CC exponential parameterisation results in non-Hermitian moments. These moments can be forcefully Hermitised in order to use the Hermitian recursion, though this is *ad hoc* approach

---

introduces additional errors and does not guarantee the necessary definiteness of the moments. The non-Hermitian nature of these moments can also result in complex Dyson orbitals and pole energies, even in the case of a real self-energy.<sup>382</sup> This results in the possibility of non-causal parts of the resulting spectrum.

### 6.3 Explicit self-energy construction

Chapter 3 briefly discussed the possibility of rotating the block tridiagonal Hamiltonian into a familiar ‘arrowhead’ representation, from which one can read off auxiliary self-energy parameters. We now turn to discussion of this technique in the general case of a non-Hermitian Green’s function (and therefore self-energy). This is of particular interest within the application of the moment-resolved solvers to GF-CC theory, because obtaining the EOM-CC self-energy is difficult otherwise. Note that as discussed previously, the matrix  $\bar{\mathbf{H}}$  is not equal to the EOM-CC self-energy upfolded into its configuration space, but rather is an *effective* self-energy.

The diagonalisation of the non-Hermitian approximate self-energy as defined in Equation 3.49 yields left- and right-hand Dyson amplitudes  $\mathbf{u}^L$  and  $\mathbf{u}^R$ , as per the projection onto the space of MOs and back-transformation according to the orthogonalisation metric outlined in Equation 3.50. The separation of the hole and particle moments results in separate orbitals for each sector which can be concatenated

$$\mathbf{u}^L = \begin{bmatrix} \mathbf{u}^{L,<} & \mathbf{u}^{L,>} \end{bmatrix}, \quad (6.7a)$$

$$\mathbf{u}^R = \begin{bmatrix} \mathbf{u}^{R,<} & \mathbf{u}^{R,>} \end{bmatrix}, \quad (6.7b)$$

which have dimension  $n_{\text{MO}} \times (L + M)$ , where  $L$  and  $M$  are the sizes of the hole and particle Dyson orbital spaces, respectively. These orbitals can be transformed into full-rank square matrices maintaining the projection onto MOs by constructing additional  $(L + M) - n_{\text{MO}}$  rows, using any complete biorthogonal basis that does not change the existing vectors. A simple and efficient choice is a two-sided Gram–Schmidt, however one could also use the eigenvectors corresponding to the non-null-space of  $\mathbf{I} - \mathbf{u}^{L,\dagger} \mathbf{u}^R$ . We define a biorthogonal eigenbasis spanning the MOs and an additional external space, which conserves the spectrum exactly

$$\bar{\mathbf{H}}_{\text{comb}} = \mathbf{u}^L \begin{bmatrix} \lambda^< & \mathbf{0} \\ \mathbf{0} & \lambda^> \end{bmatrix} \mathbf{u}^{R,\dagger}, \quad (6.8)$$

where  $\lambda^<$  and  $\lambda^>$  are the eigenvalues associated with the Dyson orbitals in the hole and particle sector, respectively. We now wish to rotate the ‘external’ (auxiliary) subspace of Equation 6.8 into a diagonal representation such that we can read off a set of non-interacting self-energy parameters (where  $\mathbf{C} = \mathbf{0}$ ) thus defining a sum-over-states of self-energy pole positions and amplitudes. Taking the projector  $\mathbf{P}_{\text{ext}} = \mathbf{I} - \mathbf{P}_{\text{MOS}}$ , the eigenvalues of the subspace matrix are computed as

$$\mathbf{P}_{\text{ext}} \bar{\mathbf{H}}_{\text{comb}} \mathbf{P}_{\text{ext}} \mathbf{c} = \mathbf{c} \mathbf{K}, \quad (6.9)$$

and the self-energy parameters can therein be defined as

$$\Sigma(\infty) = \mathbf{P}_{\text{MOS}} \bar{\mathbf{H}}_{\text{comb}} \mathbf{P}_{\text{MOS}}, \quad (6.10)$$

$$\mathbf{V}^L = \mathbf{P}_{\text{MOS}} \bar{\mathbf{H}}_{\text{comb}} \mathbf{P}_{\text{ext}} \mathbf{c}, \quad (6.11)$$

$$\mathbf{V}^{R,\dagger} = \mathbf{c}^{-1} \mathbf{P}_{\text{ext}} \bar{\mathbf{H}}_{\text{comb}} \mathbf{P}_{\text{MOS}}, \quad (6.12)$$

$$\mathbf{K} = \mathbf{c}^{-1} \mathbf{P}_{\text{ext}} \bar{\mathbf{H}}_{\text{comb}} \mathbf{P}_{\text{ext}} \mathbf{c}, \quad (6.13)$$

$$\mathbf{C} = \mathbf{0}. \quad (6.14)$$

These parameters therefore define a self-energy either in its configuration space according to Equation 2.80, or folded into frequency space according to Equation 2.78, with the only modification being that in this non-Hermitian case the couplings  $\mathbf{V}$  and  $\mathbf{V}^\dagger$  are replaced by  $\mathbf{V}^L$  and  $\mathbf{V}^{R,\dagger}$ , respectively. The Green's function can then be written according to the Dyson equation

$$\mathbf{G}(\omega) = \left( \omega - \Sigma(\infty) - \mathbf{V}^{R,\dagger} [\omega - (\mathbf{K} + \mathbf{C})]^{-1} \mathbf{V}^L \right)^{-1}. \quad (6.15)$$

One particular advantage of this approach is that it permits the analytical evaluation of Fermi liquid parameters, as well as the quasiparticle renormalisation factors as per Equation 2.91. In condensed matter they can quantify phase transitions due to correlation, and in finite systems as previously discussed they can be used as a proxy to quantify correlation on a particular MO.

## 6.4 Algorithm

---

**Algorithm 6.1:** Calculation of the first  $n_{\text{mom}}$  moments of the hole and particle Green's function for a given CC ansatz.

---

**Data:** Excitation operator tensors  $\mathbf{T}$  and de-excitation operators  $\mathbf{A}$  converged for the given CC ansatz.

**Result:** CC Green's function moments for the hole  $\Xi^{(G^<,n)}$  and particle  $\Xi^{(G^>,n)}$  cases.

```

 $\Xi_{pq}^{(G^<,n)} \leftarrow 0$ 
 $\Xi_{pq}^{(G^>,n)} \leftarrow 0$ 
 $\mathbf{x}_q^< \leftarrow \bar{a}_q |\Psi_{\text{HF}}\rangle$ 
 $\mathbf{x}_q^> \leftarrow \bar{a}_q^\dagger |\Psi_{\text{HF}}\rangle$ 
† for  $p \in \text{MOS}$  do
     $\mathbf{y}_p^< \leftarrow \langle \Psi_{\text{HF}} | (1 + \hat{\Lambda}) \bar{a}_p^\dagger$ 
     $\mathbf{y}_p^> \leftarrow \langle \Psi_{\text{HF}} | (1 + \hat{\Lambda}) \bar{a}_p$ 
    for  $n = 0 \rightarrow n_{\text{mom}}$  do
    ‡    $\Xi_{qp}^{(G^<,n)} \leftarrow \Xi_{qp}^{(G^<,n)} + \mathbf{y}_p^< \mathbf{x}_q^<$ 
    ‡    $\Xi_{pq}^{(G^>,n)} \leftarrow \Xi_{pq}^{(G^>,n)} + \mathbf{y}_p^> \mathbf{x}_q^>$ 
        if  $n \neq n_{\text{mom}}$  then
        IP    $\mathbf{y}_p^< \leftarrow -\mathbf{y}_p^< [P_X \bar{H}_N P_X]$ 
        EA    $\mathbf{y}_p^> \leftarrow \mathbf{y}_p^> [P_Y \bar{H}_N P_Y]$ 
        end
    end
end
end

```

---

Algorithm 6.1 summarises the algorithm to build the moments of the Green's function for a given CC ansatz. The daggered ( $\dagger$ ) lines indicate those which can be distributed using MPI parallelism, and the double daggered ( $\ddagger$ ) lines indicates those which are dispatched efficiently and with OpenMP parallelism via a GEMM routine in a BLAS interface. The lines marked **IP** and **EA** represent standard EOM-CC matrix-vector product routines for the IP and EA, respectively. In this case, the left-sided matrix-vector product is used, which reduces the distribution overhead in the case of MPI due to the relative structural simplicity of the ket compared to the bra. As can be seen in Equations 6.5 and 6.6, the ket  $\mathbf{x}$  only depends on  $\hat{T}$  and the delta functions, and as such the dot-product  $\mathbf{y} \cdot \mathbf{x}$  can be computed without explicit storage of  $\mathbf{x}$  by instead considering the contractions with the individual components. On the other hand, it would be more difficult to compute these contractions directly (without storage of the full vector) if one were to use the more standard right-hand matrix-vector product of the similarity transformed Hamiltonian. The details of the construction of the bra and ket vectors and the matrix-vector product routines vary depending on the chosen ansatz in the ground state, with the example of CCSD shown in Equations 6.5 and 6.6. It is also important to note that the dot-product  $\mathbf{y} \cdot \mathbf{x}$  assumes that the vectors span only

non-repeated index pairs with respect to the indistinguishability of antisymmetric dummy indices, for example in the hole case

$$\mathbf{y}_p \cdot \mathbf{x}_q = \sum_i^{\text{occ}} y_{p,i} x_{q,i} + \frac{1}{2} \sum_{i < j}^{\text{occ}} \sum_a^{\text{vir}} y_{p,ija} x_{p,ija}, \quad (6.16)$$

which is entirely equivalent to including a factor  $\frac{1}{2}$  in the doubles ( $2h1p$  or  $1h2p$ ) part of the contraction with the vector spanning the entire doubles space. In the case of non-antisymmetric restricted expressions resulting from a spin adaptation of the spin orbital expressions, this consideration is not required.

The present algorithm requires only  $n_{\text{mom}} n_{\text{MO}}$  evaluations of each of the IP- and EA-EOM-CC matrix-vector product routines, which is familiar with regard to discussions in Chapter 3, where we observed that the cost of using the block Lanczos solver is typically a factor  $n_{\text{MO}}$  greater than the cost with the single-vector iterative eigensolver. This is an improvement on naive algorithms that may require one to converge an iterative process at each frequency point, increasing the number of evaluations to  $n_{\text{iter}} n_{\text{MO}} n_{\text{freq}}$ , where  $n_{\text{iter}}$  is the average number of iterations required and  $n_{\text{freq}}$  the number of frequency points one wishes to plot. This may also present further numerical challenges such as increased difficulty to converge around a pole, which is not a feature of the present algorithm, and also the need to increase the grid size if one wishes to probe larger energy scales at the same resolution.





## Chapter 7

# Results

## 7.1 Introduction

In this Chapter, the performance of the block Lanczos recurrence for the self-energy and Green's function will be benchmarked in the context of a number of quantum chemical methods. This includes benchmark sets, along with several isolated systems, in order to stimulate a diverse discussion of the performance of the recurrences and the schemes presented in Chapters 4 to 6. In the discussion of errors aggregated over benchmark sets, the convention for the sign of signed errors is

$$\Delta_{\text{method}}^{\text{system}} = E_{\text{reference}}^{\text{system}} - E_{\text{method}}^{\text{system}}, \quad (7.1)$$

such that a positive error indicates an underestimated quantity, and a negative error indicates an overestimated quantity. Discussion of the aggregate errors within benchmark sets will leverage a number of error measures in order to more simply quantify the distribution of error. The mean absolute error (MAE) is a measure of the mean deviation from the true values with no consideration of sign in the error

$$\text{MAE}_{\text{method}} = \frac{1}{n_{\text{system}}} \sum_{\text{system}} |\Delta_{\text{method}}^{\text{system}}|, \quad (7.2)$$

whilst the mean signed error (MSE) gives a measure of the true mean error

$$\text{MSE}_{\text{method}} = \frac{1}{n_{\text{system}}} \sum_{\text{system}} \Delta_{\text{method}}^{\text{system}}, \quad (7.3)$$

and in the case of a completely biased (one-sided) prediction will be identical (within a sign) to the MAE, however for a completely unbiased prediction may approach zero. The maximum deviation from the reference values can be measured using the greatest absolute error (GAE)

$$\text{GAE}_{\text{method}} = \max_{\text{system}} |\Delta_{\text{method}}^{\text{system}}|, \quad (7.4)$$

and the distribution of the error can be quantified using the standard deviation (STD)

$$\text{STD}_{\text{method}} = \left( \frac{1}{n_{\text{system}}} \sum_{\text{system}} |\Delta_{\text{method}}^{\text{system}}|^2 \right)^{\frac{1}{2}}. \quad (7.5)$$

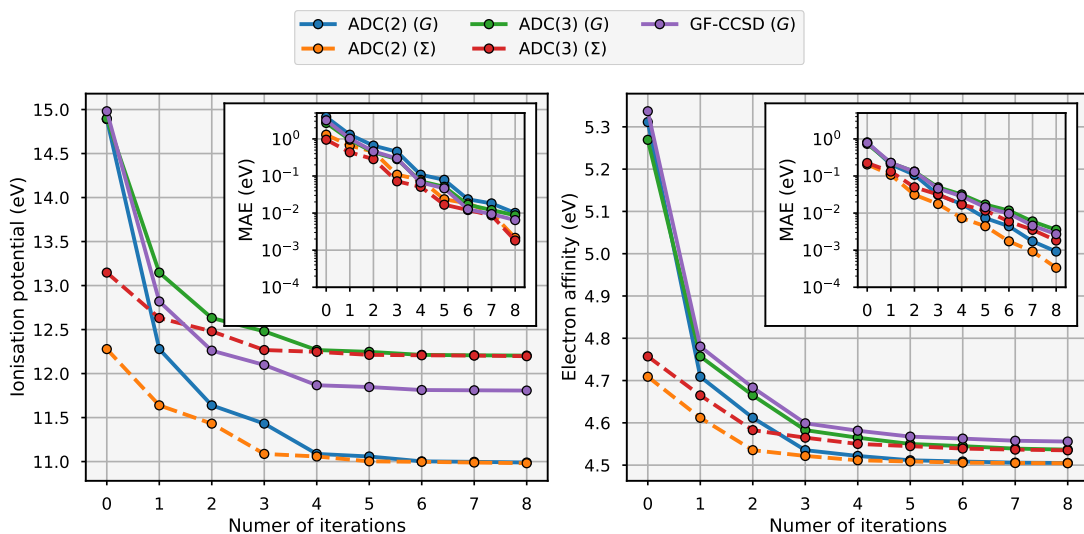


Figure 7.1: Convergence of the first IP (left) and EA (right) for the H<sub>2</sub>O molecule in a cc-pVDZ basis with number of iterations in the moment recurrence algorithms. Results for ADC(2) and ADC(3) are shown for both the self-energy moment recurrence, marked  $\Sigma$ , and the Green's function moment recurrence, marked  $G$ . Results for GF-CCSD are shown for the Green's function moment recurrence. The inset shows the same data as MAE with respect to the exact eigenvalues at each level of theory. The moments and exact eigensolutions were found using via brute-force calculation of the full Hamiltonians.

## 7.2 Water

To facilitate a more in-depth discussion of the results using detailed benchmarks, we begin with a prototypical system to illustrate the techniques discussed thus far. By using a very small system we allow the brute-force computation of moments from existing quantum chemistry programs, and will therefore proceed with a simple water molecule with an O–H bond length of 0.9579 Å and H–O–H bond angle of 104.12°. We use a cc-pVDZ basis, resulting in 23 orbitals and 10 electrons. The RHF ground-state energy for this system calculated using the PySCF programming package is  $-76.016\,789\,472 E_h$ .

### 7.2.1 Ionisation potential and electron affinity

The convergence of the moment-resolved block Lanczos solvers is shown for the ADC(2), ADC(3), and GF-CCSD Hamiltonians in Figure 7.1 for the first IP and EA of the H<sub>2</sub>O molecule in a cc-pVDZ basis set. Both the self-energy and Green's function recurrence are shown for the ADC methods, whilst only the Green's function recurrence is shown for GF-CCSD since explicit self-energy moment expressions are unavailable, and a non-Hermitian variant of the self-energy recurrence has not yet been derived. The inset plots show the error taken with respect to the separate converged value for each level of theory, obtained using the eigenvalues of the

Hamiltonians with a dense eigensolver. Convergence to chemical accuracy<sup>a</sup> is rapid for both the IP and EA, typically requiring around six iterations for the IPs and around five for the EAs. Only a small number of moments of the respective distributions are therefore required in order to faithfully recover the frontier excitations of the system, and the introduction of additional moments systematically improves the accuracy in such excitations. The moment representation offers an extremely compact representation of the dynamics of the self-energy and Green's function.

For both the IP and EA the accuracy with zero iterations is much better in the case of the self-energy recurrence. Subsequent iterations of the Green's function recurrence can be seen to give equal results to the previous number of iterations in the self-energy recurrence. This fact reflects the relationship between the moments of the self-energy and Green's function in the case of a non-Dyson theory, as outlined in Equation 2.105. The Green's function recurrence at zero iterations simply represents a diagonalisation of the static self-energy, which can be seen to give similar results for each of the three theories.

There are no particularly evident differences in the rate of convergence for the IPs, however the ADC(2) results for the EA can be seen to converge slightly faster than those of the higher order theories. This likely reflects the fact that there are significantly more diagrams in third-order perturbation theory and CCSD, as discussed throughout Chapter 2. The configuration space in the case of ADC(3) and CCSD formally has non-zero coupling between configurations, i.e.  $\mathbf{C} \neq \mathbf{0}$ , whereas ADC(2) does not. This results in significantly more information being contracted over when constructing the moments, whereas the algorithm does not produce a greater number of poles in the resulting spectrum in proportion to this, and as such is a (relatively) more coarse representation. This reflects the more diagrammatically complete self-energy in these levels of theory. This is less pronounced in the case of the IP, since in any good quality basis the  $1h2p$  states will far outnumber of the  $2h1p$  states.

### 7.2.2 Spectral functions

Figures 7.2 to 7.4 show the convergence of the spectral functions resolved on the real frequency axis for these calculations. The spectral functions allow us to consider also the global convergence properties of the moment recurrence approaches. For all of the examples one can observe a general trend of convergence from mean-field (HF) to the correlated spectrum with increasing numbers of iterations, resulting from the increase in resolution of the dynamics. The convergence is faster in regimes where the HF spectrum is more representative of the correlated spectrum, such as the low-energy regimes around the Fermi energy, whilst the higher energy regimes are more slowly converging. This reflects the need for higher-order moments to resolve more complicated features in the spectrum.

Once again, the equivalence between the Green's function and self-energy recurrences for non-Dyson theories can be observed in these results, with the spectra for Green's function recurrence

---

<sup>a</sup>'chemical accuracy' is considered to be  $1 \text{ kcal mol}^{-1}$ , or approximately  $0.04 \text{ eV}$  for a single molecule.

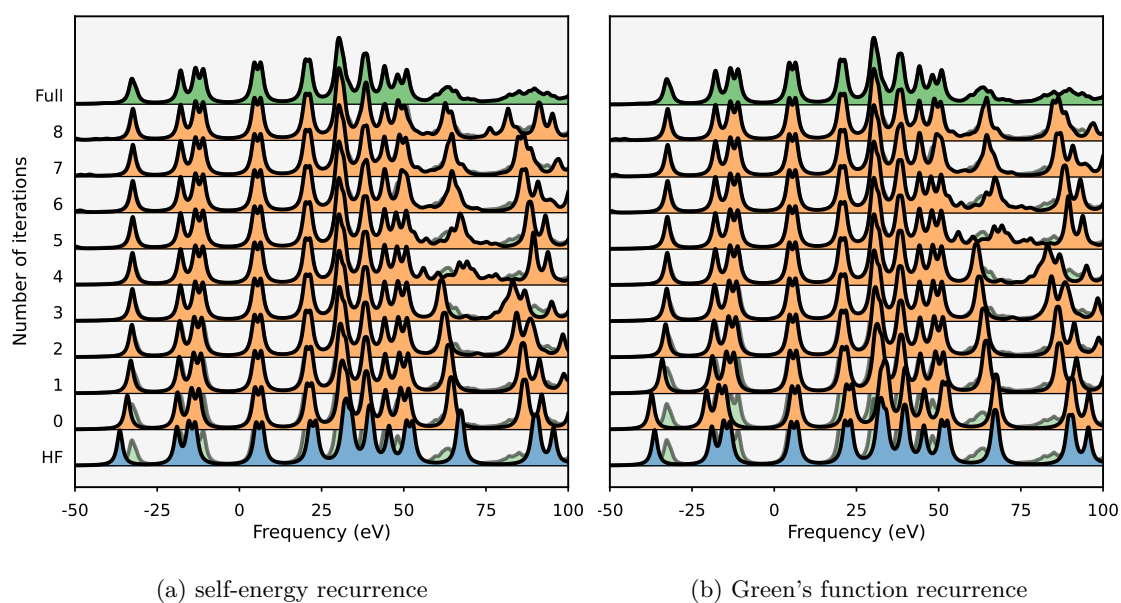


Figure 7.2: Convergence of the spectral functions for the  $\text{H}_2\text{O}$  molecule in a cc-pVDZ basis with number of iterations in the moment recurrence algorithms, for the ADC(2) Hamiltonian using the self-energy recurrence (a) and the Green's function recurrence (b). A broadening factor of  $\eta = 1.0 \text{ eV}$  was applied. The HF result is shown at the bottom, and the 'full' result is rendered faintly behind each of the other spectra.

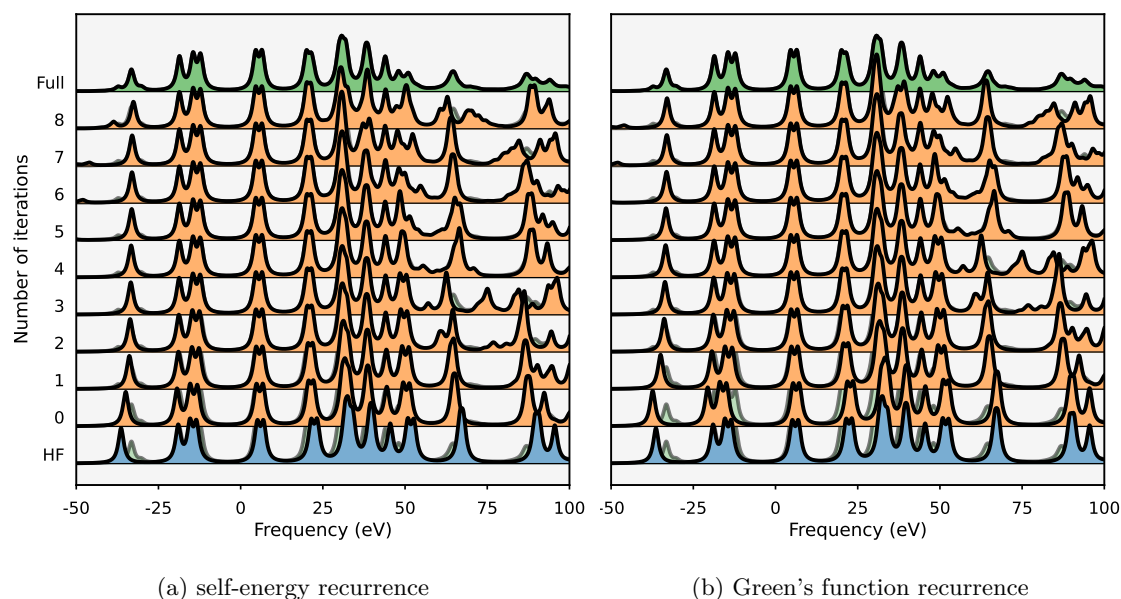


Figure 7.3: Convergence of the spectral functions for the  $\text{H}_2\text{O}$  molecule in a cc-pVDZ basis with number of iterations in the moment recurrence algorithms, for the ADC(3) Hamiltonian using the self-energy recurrence (a) and the Green's function recurrence (b). A broadening factor of  $\eta = 1.0\text{eV}$  was applied. The HF result is shown at the bottom, and the 'full' result is rendered faintly behind each of the other spectra.

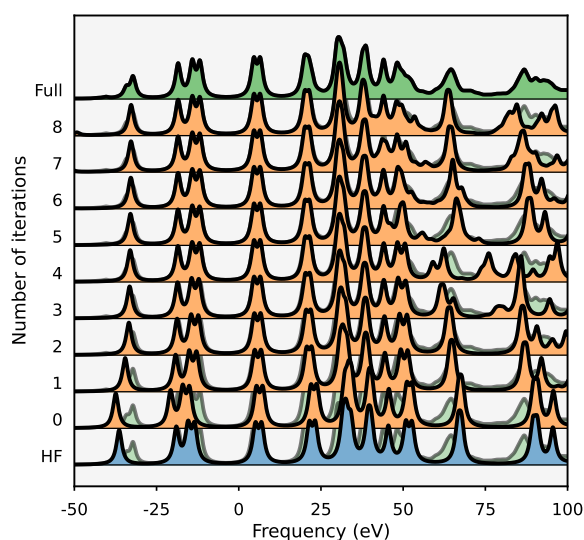


Figure 7.4: Convergence of the spectral functions for the  $\text{H}_2\text{O}$  molecule in a cc-pVDZ basis with number of iterations in the moment recurrence algorithms, for the GF-CCSD Hamiltonian using the Green's function recurrence. A broadening factor of  $\eta = 1.0\text{eV}$  was applied. The HF result is shown at the bottom, and the 'full' result is rendered faintly behind each of the other spectra.

iterations being equal to those of the previous self-energy recurrence iteration. This is accompanied by the zero iteration Green's function recurrence result being much closer to the HF spectrum than the zero iteration self-energy recurrence, the latter representing the full correlated spectrum particularly well.

The convergence of the high-lying particle states can often be seen to be quite erratic and not particularly systematic. These peaks in the spectrum are due to a significant number of  $1h2p$  states that, except for in ADC(2), have non-zero interaction with each other, and are mixed upon solving the Dyson equation. These peaks are not however of significant interest much of the time, with excitations close to the Fermi energy along with core hole states being those with the most utility; and it is unlikely both practically and numerically that one would resolve these peaks well using a traditional iterative eigensolver.

The larger relative errors in GF-CCSD are once again reflected in the spectra qualitatively. Despite this, the convergence of the spectra even in the high frequency regime appears to be suitably systematic and robust, and with very few moments one can still very accurately depict the spectrum around the Fermi energy. Since GF-CCSD requires that the Green's function recurrence is performed using a non-Hermitian Green's function, there is the possibility for non-causal poles to appear in the spectrum. These may have formally complex energies and negative weight in the spectrum, however we find that in broadened spectra at the GF-CCSD these poles cancel, and the traced spectral function is positive over the domain plotted. Ref. 382 provides a detailed discussion of complex roots in CC theory.



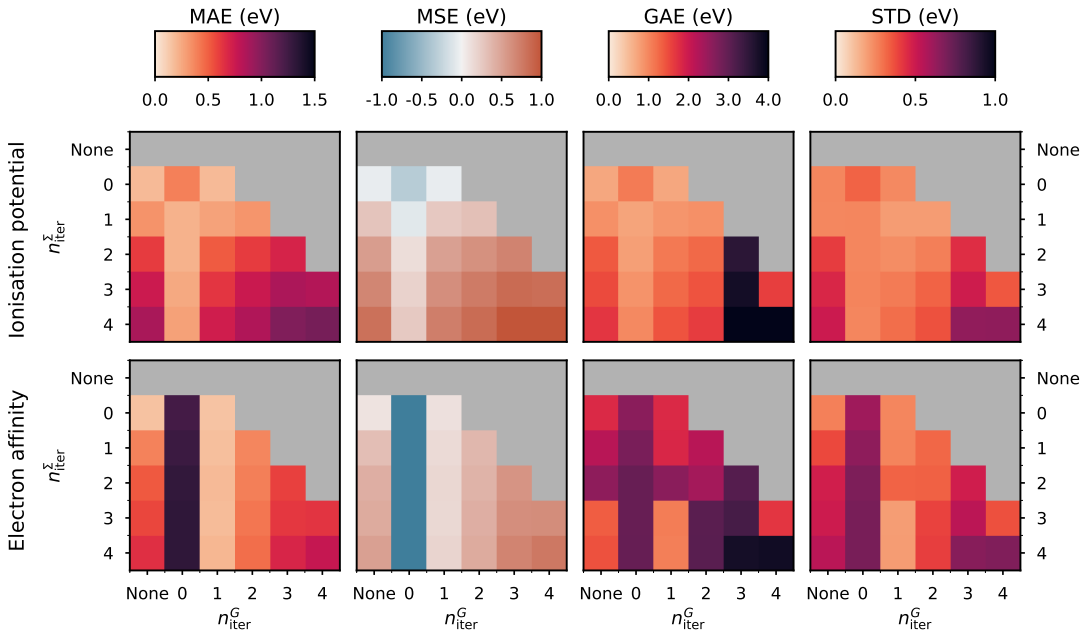


Figure 7.5: Heatmaps for MAE, MSE, GAE, and STD values for different numbers of iterations in the self-energy recurrence  $n_{\text{iter}}^{\Sigma}$  and Green’s function recurrence  $n_{\text{iter}}^G$  in AGF2 calculations for the W4-11 benchmark in a cc-pVDZ basis set. ‘None’ indicates that no compression according to the particular algorithm was applied. Errors are taken with respect to  $\Delta\text{CCSD(T)}$ . The first row shows errors for the IPs, and the second row for the EAs. The columns correspond to each aggregated statistical measure, indicated by the labelled colour bar at the top of each column, which provides the colour key for both the IP and EA heatmap.

### 7.3 W4-11

In order to quantify the accuracy of AGF2 with respect to different numbers of iterations  $n_{\text{iter}}$  in the self-energy and Green’s function recurrence, a subset of the W4-11 benchmark set will be used.<sup>383–385</sup> This benchmark set consists of small molecules, typically for the purpose of benchmarking thermochemistry, however in our case it offers a sufficiently sized set of molecules that are not prohibitively large when one moves to large  $n_{\text{iter}}$ . The set is constrained to all systems with no more than fifty orbitals in a cc-pVDZ basis set, and with an equal number of  $\alpha$  and  $\beta$  electrons to permit the use of restricted spin symmetry in the calculations.

Figure 7.5 shows heatmaps for the MAEs, MSEs, GAEs, and STDs in the IPs and EAs for the W4-11 set at different levels of moment conservation in AGF2. Results are shown for different numbers of iterations in the two-step compression scheme conserving first the moments of the self-energy by applying  $n_{\text{iter}}^{\Sigma}$  recurrence iterations, followed by conservation of the moments of the Green’s function by applying  $n_{\text{iter}}^G$  recurrence iterations. Table 7.1 tabulates this data. The limit in the accuracy of the subsequent Green’s function recurrence is bound by that of the initial self-energy recurrence, which is necessary to obtain a tractable number of Green’s function poles with

$n_{\text{iter}}^{\Sigma}$	$n_{\text{iter}}^G$	IP					EA				
		$N$	MAE	MSE	GAE	STD	$N$	MAE	MSE	GAE	STD
	ADC(2)	72	0.522	0.494	1.975	0.452	72	0.354	0.352	1.685	0.293
	CCSD	72	0.100	-0.007	0.641	0.148	72	0.072	0.064	0.808	0.123
0	None	72	0.192	-0.040	0.700	0.254	72	0.162	0.093	1.799	0.265
0	0	72	0.398	-0.324	1.108	0.325	72	1.227	-1.226	2.600	0.605
0	1	72	0.188	-0.044	0.700	0.246	72	0.156	0.105	1.799	0.252
1	None	72	0.328	0.287	0.920	0.246	72	0.387	0.326	2.179	0.381
1	0	72	0.217	-0.080	0.723	0.253	72	1.263	-1.263	2.758	0.644
1	1	72	0.277	0.262	0.866	0.203	72	0.173	0.145	1.833	0.255
1	2	72	0.326	0.316	0.920	0.202	72	0.376	0.371	2.179	0.319
2	None	72	0.610	0.536	1.376	0.406	72	0.520	0.426	2.571	0.481
2	0	72	0.221	0.132	0.766	0.250	72	1.299	-1.299	2.923	0.683
2	1	72	0.515	0.515	1.111	0.236	72	0.189	0.164	2.609	0.327
2	2	72	0.613	0.613	1.263	0.267	72	0.399	0.396	2.366	0.329
2	3	72	0.699	0.699	3.541	0.441	72	0.592	0.592	3.096	0.486
3	None	72	0.747	0.684	1.504	0.460	72	0.577	0.446	1.346	0.496
3	0	72	0.254	0.201	0.878	0.255	72	1.307	-1.307	2.933	0.692
3	1	72	0.627	0.627	1.260	0.275	72	0.186	0.162	1.082	0.196
3	2	72	0.754	0.754	1.426	0.325	72	0.431	0.428	3.053	0.393
3	3	72	0.856	0.856	3.791	0.491	72	0.626	0.626	3.263	0.537
3	4	72	0.834	0.834	1.597	0.350	72	0.638	0.638	1.679	0.366
4	None	72	0.868	0.816	1.687	0.499	72	0.651	0.512	1.449	0.541
4	0	72	0.285	0.257	0.976	0.254	72	1.309	-1.309	2.944	0.695
4	1	72	0.731	0.731	1.432	0.303	72	0.202	0.182	1.077	0.202
4	2	72	0.849	0.849	1.611	0.361	72	0.453	0.450	3.077	0.400
4	3	72	1.009	1.009	4.026	0.634	72	0.694	0.694	3.775	0.658
4	4	72	1.047	1.047	4.125	0.640	72	0.771	0.771	3.823	0.674

Table 7.1: MAE, MSE, GAE, and STD values for different numbers of iterations in the self-energy recurrence  $n_{\text{iter}}^{\Sigma}$  and Green's function recurrence  $n_{\text{iter}}^G$  in AGF2 calculations for the W4-11 benchmark in a cc-pVDZ basis set. 'None' indicates that no compression according to the particular algorithm was applied. Errors are taken with respect to CCSD(T).  $N$  indicates the number of data points available for a particular method.

which one can compute their moments. The errors are taken with respect to  $\Delta\text{CCSD(T)}$  results, which calculate the IP and EA using the differences between the  $N$ -electron and  $(N \mp 1)$ -electron CCSD(T) wavefunctions, respectively, calculated using the ORCA programming package.<sup>20,21</sup>

The second truncation to  $n_{\text{iter}}^G = n_{\text{iter}}^\Sigma + 1$  provides a representation of similar quality to not applying any Green’s function recurrence whatsoever; this reflects the fact that the conservation of the  $n_{\text{mom}}$  central moments of the Green’s function also conserves  $n_{\text{mom}} - 2$  central moments of the self-energy by virtue of Equation 2.105. Applying this truncation is likely to be slightly worse than not applying it, as the latter already conserves the same number of moments of the separate hole and particle self-energy by virtue of the self-energy recurrence applied beforehand, which is relaxed to only a conservation of the *central* moments if one does apply the  $n_{\text{iter}}^G = n_{\text{iter}}^\Sigma + 1$  recurrence iterations. The difference between applying this step and not applying any Green’s function recurrence iterations becomes more pronounced as the number of iterations increases.

The most significant conclusion from this data is that AGF2(None, 0) and AGF2(1, 0) offer the smallest errors, with their respective MAEs just 0.192 and 0.188 eV for the IPs and 0.162 and 0.156 eV for the EAs, despite these schemes being the *most* coarse-grained. The significance of this owes to the fact that these schemes are by far the most computationally efficient AGF2 models. At this level, the MAEs in both the IP and EA improve on those of ADC(2) by at least a factor of two.<sup>a</sup> AGF2(None, 0) corresponds to a conservation of only the first two (zeroth- and first-order) moments of the separate hole and particle moments, and is the most simple form of self-consistency that the block Lanczos recurrence schemes offer.

For  $n_{\text{iter}}^G > 0$ , there is a systematic increase in the MAE and MSE with increasing resolution through additional iterations in both recurrences. The most complete method consisting of  $n_{\text{iter}} = 4$  in both the self-energy and Green’s function recurrence exhibits very poor results, with the MAEs of both the IP and EA being approximately a factor of two worse than those of ADC(2). Ref. 109 similarly shows that self-consistency of the Dyson equation with a second-order self-energy is not necessarily beneficial to the accuracy of the IPs and EAs in the context of the EKT. They also show that GF2 systematically underestimates both the IP and EA, reflected by the positive MSE in the high  $n_{\text{iter}}$  AGF2 models. This underestimation exists at second-order without self-consistency, and is exacerbated by the self-consistency. The models AGF2(0, None), AGF2(0, 0), AGF2(0, 1), and AGF2(1, 0) however overestimate the IP, and similarly the models with  $n_{\text{iter}}^G = 0$  overestimate the EA. This suggests that the extremely reduced resolution offered by the truncation in these cases offers a cancellation in the error, with the cancellation not only balancing the error induced by the self-consistency, but also achieving some cancellation in the error that already exists in the non-self-consistent second-order self-energy.

The results at the level of  $n_{\text{iter}}^G = 0$  are particularly anomalous. In the case of the IP the errors tend to be anomalously good, with smaller MAEs than one would expect observing the trend at  $n_{\text{iter}}^G > 0$ , and MSEs slightly negative for  $n_{\text{iter}}^\Sigma = 0$  and 1, and slightly positive for  $n_{\text{iter}}^\Sigma > 1$ . For the EA the errors are anomalously poor, with the MSE being very negative for all  $n_{\text{iter}}^\Sigma$  and the

<sup>a</sup>This benchmark only uses a relatively small basis set and a restricted set of molecules, and Section 7.4 will offer a more systematic comparison between the accuracies of AGF2(None, 0) and ADC(2).

respective MAEs being extremely high, indicating a very large overestimation of the EAs. The  $n_{\text{iter}}^G = 0$  approximation conserves the first two (zeroth and first-order) moments of the separate hole and particle Green's functions, and was seen to be a very poor approximation in the case of the H<sub>2</sub>O example in Section 7.2 even for the frontier excitations close to the Fermi energy. The zeroth-order central moment of the Green's function is implicitly conserved so long as one obtains any orthonormal set of Dyson orbitals, and offers little information whatsoever, whilst the conservation of the first-order central moment corresponds to a conservation of the static part of the self-energy  $\Sigma(\infty)$ ; as such recurrence to  $n_{\text{iter}}^G = 0$  does not directly conserve any dynamics of the self-energy.

The observation of the trends with respect to numbers of iterations in each recurrence scheme in AGF2 has led to the use of the simple AGF2 acronym to refer to the AGF2(None, 0) approximation. Apart from AGF2(1, 0) this level of self-consistency is the most accurate, but is however incredibly simple and efficient to implement. At each iteration, one is only required to evaluate the zeroth and first moments of the second-order self-energy in the basis of the Dyson orbitals from the previous iteration, which can be efficiently calculated according to Algorithm 4.1. The block tridiagonal matrix one must diagonalise to obtain said Dyson orbitals consists of Equation 3.20 with only a single on-diagonal block  $\mathbf{A}_1$ , coupling to the static part of the self-energy via  $\mathbf{X}$ , which as shown in Equation 3.31 is equal to the square root of the zeroth moment. The block  $\mathbf{A}_1$  can then be simply computed within the self-energy recurrence scheme from the first moment as

$$\mathbf{A}_1 = \mathbf{X}^{-1} \Xi^{(\Sigma, 1)} \mathbf{X}^{-1, \dagger}. \quad (7.6)$$

Such a simple scheme and the requirement for only the first two (zeroth- and first-order) moments also means that the numerical instability observed at large numbers of iterations is not an issue. AGF2 calculations will herein refer to the AGF2(None, 0) approximation, with any other approximation explicitly specified in the brackets.

## 7.4 *GW*100 dataset

The implementation details of methods under the name *GW* vary wildly, with many different approximations existing, codes varying in their type of basis functions, and the most common non-iterative *GW* calculations exhibiting a starting point dependence. This unfortunate reality in part motivated the creation of the *GW*100 benchmark, which is a diverse set of small molecules possessing a wide range of early periodic species and chemical bonding types.<sup>270,294,386</sup> As an example, the IP of the molecules in the set ranges from  $\sim 4$  eV to  $\sim 25$  eV, including molecules with bound metal atoms, strongly ionic bonding, and molecules with a strongly delocalised electronic structure. The molecules range in size from simple atomic systems to the five canonical nucleobases, offering a diversity in size without being particularly restrictive in terms of computational effort required. Additionally, all systems are closed-shell (even number of electrons), meaning that the entire benchmark set can be treated using a restricted reference and those who wish to benchmark their methods are not required to adapt their code to unrestricted references. The benchmark is therefore useful to pronounce differences in *GW* implementations and allow both a quantitative and qualitative platform for understanding and benchmarking approximations and computational methods.

In the Dyson-orbital-based methods, i.e. those that are not computed as the difference between two independent determinants, we limit reported excitations to those with a quasiparticle weight of at least 0.1, meaning that at least 10% of its character is physical. This excludes completely non-physical excitations that have all their weight on the configurations of the particular self-energy, but does not only limit the excitations to be Koopmans'-like. The latter would imply non-black-box results that require a per-system treatment and consideration, and may encounter issues in cases where Koopmans' theorem is known to break down such as  $N_2$ .<sup>387</sup> Furthermore, the EOM-CC eigenvectors are not proportional to the  $\Lambda$  amplitudes and therefore the squared norm of the eigenvector projected onto single excitations only offers an approximation to the quasiparticle weight, which is often inaccurate.

### 7.4.1 System details

As pointed out in Ref. 317, two of the structures in the original 100 systems of the benchmark were originally provided with incorrect structures. Whilst this is problematic for the comparison to experimental data, since we will be concerned with a comparison to computational methods performed on the same set of geometries both versions of these systems will be included. These systems are vinyl bromide ( $CH_2=CHBr$ ) and phenol ( $C_6H_5OH$ ). Therefore, the *GW*100 in the context of the present work consists of 102 systems.

Features of the set include, but are not limited to

- Hydrocarbons (both aliphatic and aromatic) such as ethane ( $C_2H_6$ ), ethylene ( $C_2H_4$ ), acetylene ( $C_2H_2$ ), and benzene ( $C_6H_6$ ).
- Halogenated hydrocarbons.
- Many oxides and sulfides, and a selenide.

- The five canonical nucleobases adenine, cytosine, guanine, thymine, and uracil, which are some of the largest molecules in the set.
- Dimers of metallic atoms such as copper ( $\text{Cu}_2$ ), silver ( $\text{Ag}_2$ ), lithium ( $\text{Li}_2$ ), sodium ( $\text{Na}_2$ ), and rubidium ( $\text{Rb}_2$ ).
- Dimers of most of the non-metallic atoms.
- Small metallic clusters for sodium ( $\text{Na}_4$ ,  $\text{Na}_6$ ),
- The atoms helium (He), neon (Ne), argon (Ar) and krypton (Kr).
- The hydrosilicons silane ( $\text{SiH}_4$ ), disilane ( $\text{Si}_2\text{H}_6$ ), and pentasilane ( $\text{Si}_5\text{H}_{12}$ ), along with germane ( $\text{GeH}_4$ ).
- Alkaline metal hydrides with both extremely ionic bonding such as lithium fluoride ( $\text{LiF}$ ), and more moderate ones such as potassium bromide ( $\text{KBr}$ ).
- Periodic series, such as  $\text{F}_2 \rightarrow \text{Cl}_2 \rightarrow \text{Br}_2 \rightarrow \text{I}_2$ , allowing trends to be studied.

All calculations in this work using the GW100 set do so using the def2-TZVPP basis set as implemented in the PySCF programming package, and in the case of DF the RI basis of the same name.<sup>26,27,388,389</sup> Additionally, the atoms Rb, Ag, I, Cs, Au, and Xe are treated by an effective core potential (ECP) specified as def2-TZVPP in PySCF. This uses an ECP that is the same for all def2 basis sets in PySCF.<sup>390–394</sup> There are a total of 7 systems containing at least one such atom.

### 7.4.2 ADC(2) moments

Figure 7.6 shows the convergence of the IP and EA with increasing numbers of iterations of the self-energy moment recurrence for ADC(2), for the GW100 benchmark set in a def2-TZVPP basis set. The extrapolated results are indicated by  $\infty$  and extrapolate values at the three largest iteration numbers, with extrapolations exhibiting an  $R^2$  of less than 0.95 being rejected. Table 7.2 shows aggregated error values for this same data, including the number of systems involved in the extrapolation. The majority of the systems, 90 for the IP and 86 for the EA, which suggests that the convergence is robust in the vast majority of cases. In both the IP and the EA there is a monotonic decrease in the MAE with increasing numbers of iterations. The extrapolations both offer MAEs that improve on the highest iteration studied, at 0.279 and 0.108 eV for the IP and EA respectively, but overshoot the true value such that the MSEs have the opposite sign to those calculated data. The STDs improve with each iteration, and the extrapolated STDs are of similar quality to those at 5 iterations.

The IPs are recovered better than the EAs by approximately a factor of two, a somewhat surprising result considering that there are significantly more configurations one must contract over when calculating the moments for the EA case in any good quality basis set. This result is similar to that observed for the simple example of a  $\text{H}_2\text{O}$  molecule in Figure 7.1 in which the convergence of the EA at the level of ADC(2) is faster than the IP or the EA for the other levels of theory.

There are several clear outliers in the case of the IP; whilst one may initially conclude that the moment extrapolation fails to converge robustly in these cases, study of the IPs compared to

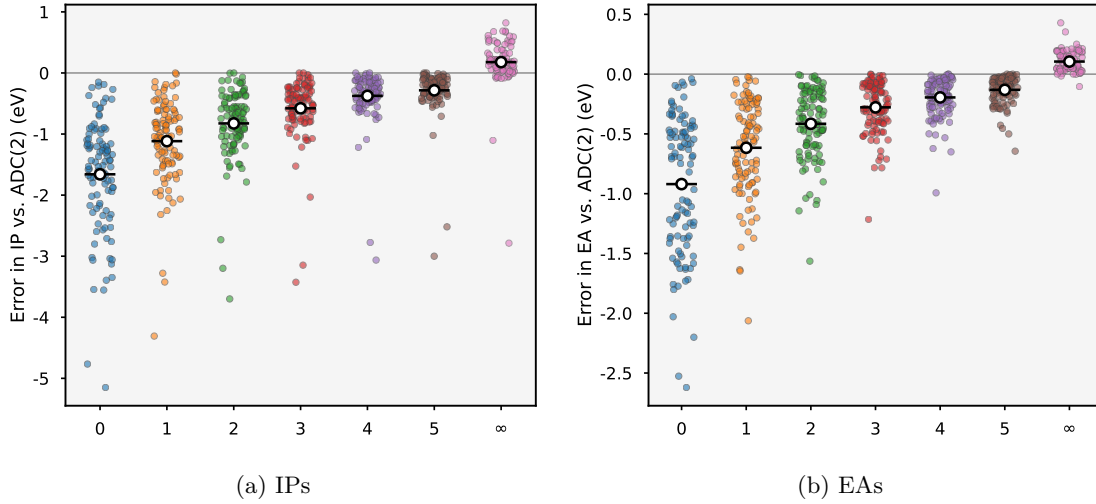


Figure 7.6: Distribution of errors in the moment-resolved ADC(2) calculations for IPs (a) and EAs (b) for the *GW*100 benchmark in a def2-TZVPP basis set. Errors are taken with respect to canonical ADC(2), and the central points show the MSEs. The number of iterations of the self-energy recurrence is indicated by the second bracketed number, with  $\infty$  indicating the extrapolation using the results corresponding to the three most complete moment expansions. Extrapolations with an  $R^2$  of less than 0.95 are removed.

$n_{\text{iter}}$	IP					EA				
	$N$	MAE	MSE	GAE	STD	$N$	MAE	MSE	GAE	STD
0	102	1.659	-1.659	5.150	0.930	102	0.920	-0.920	2.621	0.576
1	102	1.116	-1.116	4.308	0.698	102	0.616	-0.616	2.063	0.404
2	102	0.826	-0.826	3.700	0.584	102	0.415	-0.415	1.564	0.294
3	102	0.579	-0.579	3.427	0.503	102	0.278	-0.278	1.215	0.212
4	102	0.375	-0.375	3.064	0.420	102	0.195	-0.195	0.993	0.162
5	102	0.284	-0.284	3.001	0.388	102	0.131	-0.131	0.644	0.115
$\infty$	90	0.279	0.178	2.786	0.407	86	0.108	0.105	0.429	0.086

Table 7.2: MAE, MSE, GAE and STD values for the moment-resolved ADC(2) calculations for the *GW*100 benchmark in a def2-TZVPP basis set. Errors are taken with respect to canonical ADC(2).  $N$  indicates the number of data points available for a particular method, and  $\infty$  indicates the extrapolation using the results corresponding to the three most complete moment expansions. Extrapolations with an  $R^2$  of less than 0.95 are removed.

high levels of theory indicates that the canonical ADC(2) is actually performing poorly for these systems. The three extremely problematic systems are copper ( $\text{Cu}_2$ ), copper cyanide ( $\text{CuCN}$ ), and magnesium oxide ( $\text{MgO}$ ). These systems are examples of stronger correlation in the benchmark. Ref. 294 observe significant quasiparticle renormalisation for these systems, indicated by large values in  $\frac{\partial \Sigma(\omega)}{\partial \omega}$ , and note that non-self-consistent  $GW$  calculations also find non-unique solutions and convergence difficulties. The EA for titanium fluoride ( $\text{TiF}_4$ ) is an outlier, which is another system exhibiting relatively strong correlation.

### 7.4.3 $GW$ moments

Figure 7.7 shows the convergence of the IP and EA with increasing numbers of iterations of the self-energy moment recurrence for AGW, for the GW100 benchmark set in a def2-TZVPP basis set. Table 7.3 shows the aggregated error values for this data. The extrapolation is much less robust for the IP, with only 41 systems being valid under the  $R^2$  threshold of 0.95, compared with 84 systems for the EA.

In both the IP and EA the extrapolation produces error distributions with larger MAEs and STDs than the non-extrapolated data at high iteration numbers, giving a less successful extrapolation than ADC(2). The IP and EA are predicted with roughly equal quality at this level of theory, in contrast to the poorer IPs for ADC(2) and the poorer EAs in GF-CCSD as will be shown in Section 7.4.4. The MAEs are however significantly better for the coarse-grained  $GW$  calculations than those at the ADC(2) level, indicating that the  $GW$  self-energy is more effectively compressed by the block Lanczos recurrence scheme. The self-energy at the level of  $GW$  lacks the second-order exchange term existing in the bare second-order self-energy of ADC(2), perhaps simplifying the information lost in the contraction to the moments, however the remaining (direct) second-order diagram has interactions screened at the level of RPA. The MAEs of the IP and EA for AGW at  $n_{\text{iter}} = 5$  are 0.284 and 0.131 eV respectively, compared to 0.035 and 0.041 eV when applying the same number of iterations to the  $GW$  self-energy. This extremely small error means that the use of extrapolative schemes to access the high  $n_{\text{iter}}$  limit is considerably less important.

As discussed in Section 7.4.2, the outliers for the IP generally belong to the systems that have a large quasiparticle renormalisation, or more generally are systems exhibiting stronger correlation. This indicates that the AGW IPs agree more faithfully than those of ADC(2), between the moment-conserving solver and the quasiparticle equation used to solve the canonical  $GW$  quasiparticle energies. The single significant outlier in the EA data is titanium fluoride ( $\text{TiF}_4$ ).



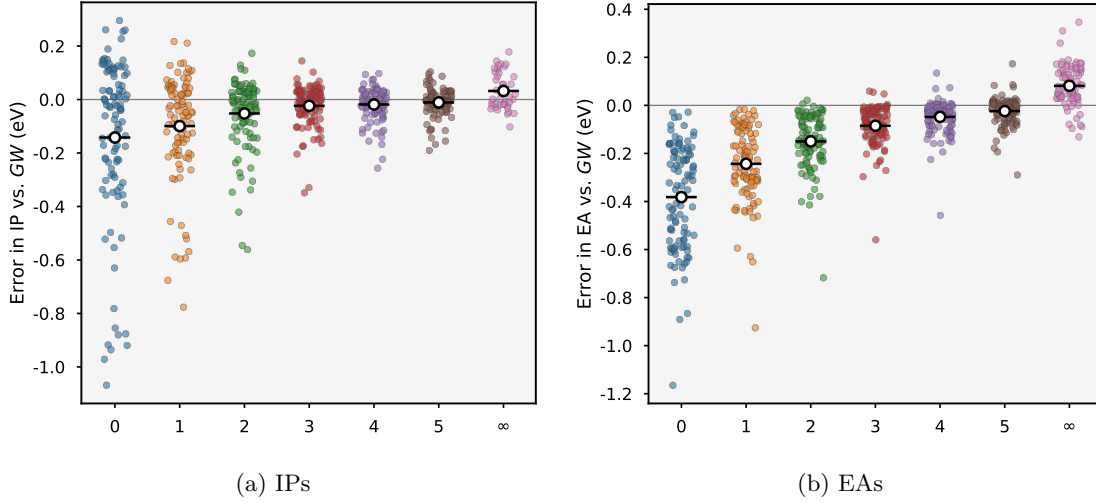


Figure 7.7: Distribution of errors in the moment-resolved AGW calculations for IPs (a) and EAs (b) for the *GW100* benchmark in a def2-TZVPP basis set. Errors are taken with respect to canonical (single-shot) *GW*, and the central points show the MSEs. The number of iterations of the self-energy recurrence is indicated by the second bracketed number, with  $\infty$  indicating the extrapolation using the results corresponding to the three most complete moment expansions. Extrapolations with an  $R^2$  of less than 0.95 are removed.

$n_{\text{iter}}$	IP					EA				
	$N$	MAE	MSE	GAE	STD	$N$	MAE	MSE	GAE	STD
0	102	0.230	-0.142	1.068	0.310	102	0.382	-0.382	1.165	0.219
1	102	0.149	-0.099	0.777	0.195	102	0.243	-0.243	0.926	0.157
2	102	0.088	-0.052	0.561	0.129	102	0.150	-0.150	0.718	0.113
3	102	0.053	-0.024	0.349	0.077	102	0.088	-0.085	0.560	0.083
4	102	0.042	-0.019	0.257	0.060	102	0.055	-0.048	0.458	0.069
5	102	0.035	-0.011	0.190	0.052	102	0.041	-0.024	0.290	0.059
$\infty$	41	0.059	0.032	0.178	0.069	84	0.096	0.081	0.346	0.084

Table 7.3: MAE, MSE, GAE and STD values for the moment-resolved AGW calculations for the *GW100* benchmark in a def2-TZVPP basis set. Errors are taken with respect to canonical (single-shot) *GW*.  $N$  indicates the number of data points available for a particular method, and  $\infty$  indicates the extrapolation using the results corresponding to the three most complete moment expansions. Extrapolations with an  $R^2$  of less than 0.95 are removed.

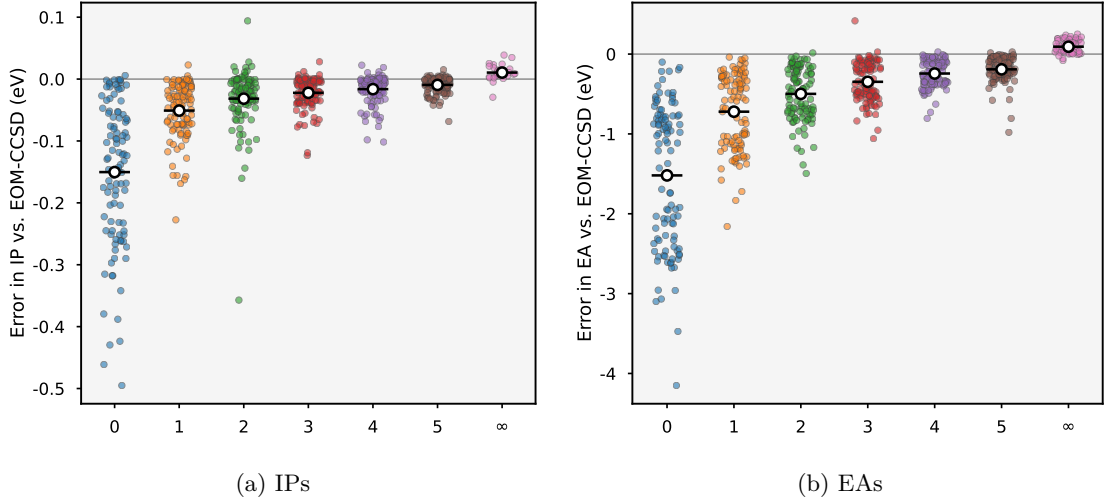


Figure 7.8: Distribution of errors in the moment-resolved GF-CCSD calculations for IPs (a) and EAs (b) for the GW100 benchmark in a def2-TZVPP basis set. Errors are taken with respect to EOM-CCSD, and the central points show the MSEs. The number of iterations of the self-energy recurrence is indicated by the second bracketed number, with  $\infty$  indicating the extrapolation using the results corresponding to the three most complete moment expansions. Extrapolations with an  $R^2$  of less than 0.95 are removed.

$n_{\text{iter}}$	IP					EA				
	$N$	MAE	MSE	GAE	STD	$N$	MAE	MSE	GAE	STD
0	102	0.150	-0.150	0.495	0.117	102	1.519	-1.519	4.151	0.900
1	102	0.051	-0.051	0.227	0.046	102	0.721	-0.721	2.159	0.476
2	102	0.036	-0.032	0.357	0.049	102	0.499	-0.498	1.495	0.333
3	102	0.024	-0.022	0.124	0.025	102	0.356	-0.347	1.059	0.247
4	102	0.018	-0.016	0.102	0.023	102	0.244	-0.243	0.806	0.170
5	102	0.011	-0.009	0.069	0.013	102	0.192	-0.191	0.980	0.160
$\infty$	32	0.013	0.011	0.039	0.012	76	0.097	0.093	0.250	0.077

Table 7.4: MAE, MSE, GAE and STD values for the moment-resolved GF-CCSD calculations for the GW100 benchmark in a def2-TZVPP basis set. Errors are taken with respect to canonical GF-CCSD.  $N$  indicates the number of data points available for a particular method, and  $\infty$  indicates the extrapolation using the results corresponding to the three most complete moment expansions. Extrapolations with an  $R^2$  of less than 0.95 are removed.

System	$n_{\text{iter}}$					
	0	1	2	3	4	5
H <sub>2</sub> O	0.9229	0.9206	0.8642	0.9182	0.9178	0.9175
HCN	0.8858	0.9178	0.9041	0.9165	0.9161	0.9160

Table 7.5: GF-CCSD quasiparticle weights of the IPs of H<sub>2</sub>O and HCN with increasing number of iterations of the Green’s function recurrence. A discontinuity in the convergent behaviour can be seen at  $n_{\text{iter}} = 2$ .

#### 7.4.4 GF-CCSD moments

Figure 7.8 shows the convergence of the IP and EA with increasing numbers of iterations of the self-energy moment recurrence for GF-CCSD, for the *GW100* benchmark set in a def2-TZVPP basis set. Table 7.4 shows the aggregated error values for this data. As seen in Section 7.4.3, the extrapolation is much less robust for the IP, with only 32 systems being valid under the  $R^2$  threshold of 0.95 compared with 76 systems for the EA.

The convergence of the EA with number of iterations is significantly poorer than that of the IP by approximately an order of magnitude, perhaps a reflection of the fact that the configuration space is significantly larger for the particle self-energy since the basis is reasonably large. This results in a particle spectrum with a more detailed pole structure, and the representation at a given number of moments is therefore coarser than the hole spectrum with an equivalent number of moments. This is in contrast to the results for ADC(2) where the EA is better recovered than the IP, with CCSD containing many more diagrams compared to ADC(2), however it must be noted that these two results are not directly comparable since the former conserves the Green’s function moments and the latter those of the self-energy. That being said, the extrapolation performs particularly well for the EA, with roughly a factor 2 improvement on the aggregated errors. Once again, the extrapolation largely overshoots the converged value, flipping the sign of the MSE. The errors in the IP converge extremely quickly, even faster than those of the self-energy recurrence with the *GW* self-energy, with  $n_{\text{iter}} = 5$  giving a MAE of just 0.011 eV and even  $n_{\text{iter}} = 1$  exhibit just 0.051 eV.

In the case of the IP at  $n_{\text{iter}} = 2$  there are two very anomalous results identified as water (H<sub>2</sub>O) and hydrogen cyanide (HCN). In both cases, the quasiparticle weight of the IP is convergent with respect to the number of iterations, yet experiences a jump in the weight at the  $n_{\text{iter}} = 2$  result, as detailed in Table 7.5. This is a drawback of the moment-conserving approach, since the algorithms simply produce a spectral distribution that best reproduces the input moments, rather than directly targeting a physically appropriate representation. In most cases the reproduction of these moments results in a good representation of the converged spectrum around the Fermi energy, and therefore gives a good IP and EA, but outliers of this sort remain a possibility.

### 7.4.5 $\Delta$ CCSD(T) benchmark

Thus far, we have considered benchmarks of methods under moment-conserving solvers with the canonical algorithms as a point of comparison. Whilst this quantifies the error of such solvers in the case of each of these methods, it does not make reference to the implicit error of the methods themselves, and how they perform when compared to an accurate quantum chemical benchmark. To this end, CCSD(T) calculations have been performed for the *GW*100 benchmark for the  $N$ ,  $N - 1$ , and  $N + 1$  electron variants of each molecule, allowing accurate  $\Delta$ CCSD(T) reference energies for both the IP and EA.<sup>51</sup> The CCSD(T) calculations were performed using the *ORCA* programming package, and unlike the other methods employed a frozen core approximation to reduce computational difficulty due to their expense.<sup>20,21</sup> The number of electrons frozen in this way correspond to the default values introduced in the 4.0 version of *ORCA*. Whilst this approach does not allow Dyson orbitals to be computed, it includes orbital relaxation through the independent mean-field calculations, and provides extremely accurate IP and EA values.

As discussed in Ref. 99, there is some discrepancy between reported CCSD(T) values for the *GW*100 benchmark set. Major differences are noted between the work of Ref. 318 and Ref. 395 which can be explained by the preference of the latter for stable HF solutions, whereas the former ignore HF instabilities completely. The use of stability analysis on the mean-field results in lower total energies which may have broken symmetries, accounting more fully for orbital relaxation. In the present data, we prefer the stable HF solution, allowing the more accurate account of orbital relaxation. In systems with large orbital relaxation effects in their single particle excitations, this may provide IPs or EAs that are less similar to those calculated using EOM-CC or other single reference approaches. We consider this to be the more appropriate target benchmark for arbitrary quantum chemical methods.

Figure 7.9 and Table 7.6 summarise the errors across the *GW*100 benchmark for some selected quantum chemical methods, with errors taken with respect to  $\Delta$ CCSD(T). The sets are complete for all methods shown except for AGF2, which experienced convergence problems in the case of xenon (Xe) and hexafluorobenzene ( $C_6F_6$ ). ADC(2) underestimates the IP with nearly perfect consistency, with only very small errors in cases where it is overestimated. Despite this fact, the errors are only slightly improved with respect to HF, with MAEs of 0.589 and 0.689 eV for ADC(2) and HF, respectively. In the case of EAs ADC(2) offers a much greater improvement, exhibiting an MAE of 0.297 eV compared to 1.003 eV at the level of HF, and again underestimates more often than not. AGF2 offers small improvements in both the IP and EA at the level of ADC(2), with MAEs of 0.437 and 0.222 eV for the IPs and EAs, respectively. In both cases, the general trend in the sign of the errors flips with respect to that of ADC(2), likely indicating an overcorrection due to the renormalisation of the propagators in second-order diagrams. Section 7.3 previously discussed this cancellation of error in more detail. AGF2 similarly offers good improvements in the GAE and STD for both excitations compared to ADC(2) and even ADC(3), which may benefit from the fact that AGF2 does not have to leverage iterative eigensolvers which can be numerically unstable and may be influenced by preconditioning and choice of initial guess. Despite this improvement, *GW* offers even greater improvements in errors, indicating that a simple one-shot screening of the

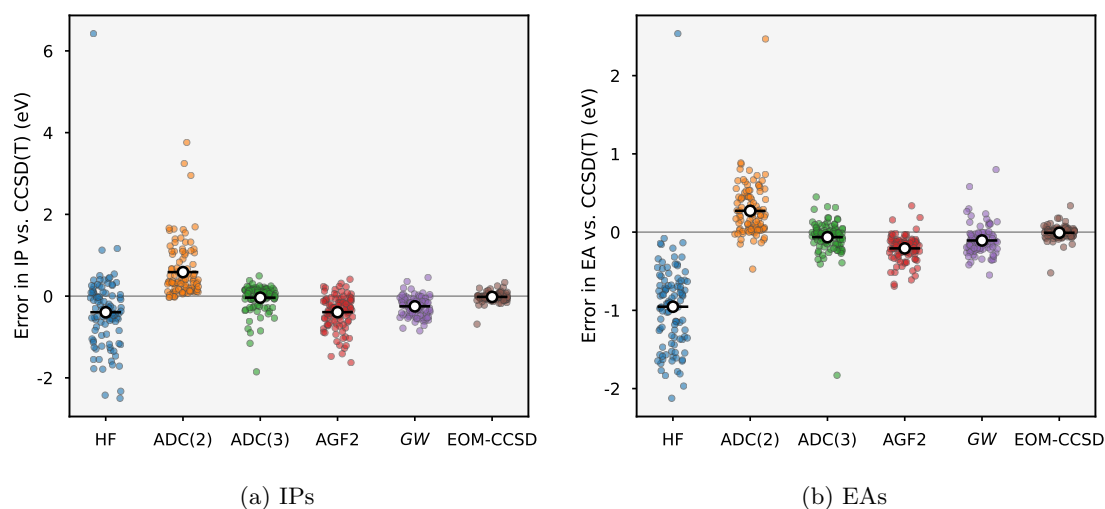


Figure 7.9: Distribution of errors in various quantum chemical methods for IPs (a) and EAs (b) for the *GW*100 benchmark in a def2-TZVPP basis set. Errors are taken with respect to  $\Delta\text{CCSD(T)}$ , and the central points show the MSEs.

Method	IP					EA				
	<i>N</i>	MAE	MSE	GAE	STD	<i>N</i>	MAE	MSE	GAE	STD
HF	102	0.689	-0.395	6.422	0.980	102	1.003	-0.954	2.536	0.581
ADC(2)	102	0.589	0.587	3.760	0.672	102	0.297	0.272	2.468	0.344
ADC(3)	102	0.209	-0.038	1.852	0.327	102	0.134	-0.065	1.830	0.231
<i>GW</i>	102	0.278	-0.250	0.851	0.230	102	0.172	-0.107	0.799	0.184
EOM-CCSD	102	0.067	-0.019	0.686	0.109	102	0.051	-0.008	0.521	0.084
AGF2	100	0.437	-0.392	1.627	0.407	100	0.222	-0.208	0.692	0.160

Table 7.6: MAE, MSE, GAE and STD values for selected quantum chemical methods applied to the *GW*100 benchmark in a def2-TZVPP basis set. Errors are taken with respect to  $\Delta\text{CCSD(T)}$ . *N* indicates the number of data points available for a particular method. In the case of AGF2, xenon (Xe) and hexafluorobenzene ( $\text{C}_6\text{F}_6$ ) suffer from convergence problems and are removed.

Coulomb potential perhaps more effectively captures correlation than a self-consistent screening of the propagators in both second-order diagrams. The MAEs at the level of  $GW$  are only bettered by those of ADC(3) and EOM-CCSD, which is to be expected since both scale with system size as  $\mathcal{O}(n_{\text{MO}}^6)$ . Unsurprisingly, EOM-CCSD has extremely small aggregated errors for both IPs and EAs along with very few outliers. Increasing the order of perturbation theory in ADC to the third-order ADC(3) improves on both excitations and offers particularly unbiased errors, however does not boast quality near to that of EOM-CCSD.

By combining the information afforded by Tables 7.2 to 7.4 with Table 7.6, we can observe when the error due to the moment-conserving solver becomes less than, or of a similar magnitude to, the implicit error in the method without a moment approximation. This is useful to measure, as it gives an estimate as to when one can consider the moment-conserving solvers to be ‘converged’, with additional iterations possibly being futile since they improve the excitations on scales that are smaller than the implicit error in such excitation. For ADC(2), this threshold is met at  $n_{\text{iter}} = 3$  for both the IP and EA. In the case of AGW, convergence is more rapid with the threshold met at  $n_{\text{iter}} = 1$  for the IP and  $n_{\text{iter}} = 2$  for the EA. For GF-CCSD the threshold is also met at  $n_{\text{iter}} = 1$  for the IP, however the error due to the moment approximation in the EA never meets values less than those due to the CC ansatz, with the extrapolated MAE still being approximately twice as large as the MAE for EA-EOM-CCSD. By virtue of most of these methods converging the frontier excitations extremely quickly and with the requirement of very few moments, the moment-conserving solvers can be considered to be very practical in the context of calculating IPs and EAs. The issue of numerical instability at large numbers of iterations is balanced by this observation since at some point any subsequent iterations are improving the accuracy of the solver on scales smaller than the accuracy of the method itself, and in some cases such as AGF2, more iterations may even deteriorate results.

Table 7.7 shows errors in the moment-resolved data reviewed in Sections 7.4.2 to 7.4.4 with respect to the  $\Delta\text{CCSD(T)}$  benchmark, rather than with respect to the converged moment limit. Therefore, whilst the errors in the previous Section 7.4.5 have ignored the implicit error of the methods, this data includes that error. One of the most significant observations from the data in this format is how poorly the EA is recovered by the moment-conserving GF-CCSD method; at all iterations the MAEs at the level of ADC(2) and AGW are smaller than that of GF-CCSD, however the GF-CCSD excitations extrapolate better and outperform ADC(2) and AGW in the limit of infinite moments. It should be noted that comparison at the same number of iterations between these methods is somewhat *ad hoc*, since in the case of ADC(2) and AGW the moments of the self-energy are conserved whereas moments of the Green’s function are conserved for the GF-CCSD application. For ADC(2), there is an equivalence in the two recurrences, as discussed in Section 7.2, however AGW does not employ a non-Dyson approximation and therefore the recurrences are not equivalent. The rapid saturation of the improvement in the MAEs for the IPs further shows how the error due to the moment approximation quickly becomes smaller than the implicit error in these methods. In the case of ADC(2) the MSE experiences significant changes with increasing numbers of iterations, whilst the MAE is controlled by the implicit error. This

$n_{\text{iter}}$	IP					EA				
	$N$	MAE	MSE	GAE	STD	$N$	MAE	MSE	GAE	STD
ADC(2)										
0	102	1.072	-1.072	2.125	0.457	102	0.648	-0.648	2.225	0.374
1	102	0.536	-0.530	1.625	0.378	102	0.352	-0.344	1.346	0.252
2	102	0.316	-0.239	1.009	0.351	102	0.178	-0.144	0.904	0.211
3	102	0.282	0.008	0.921	0.343	102	0.135	-0.006	1.254	0.217
4	102	0.379	0.212	1.735	0.458	102	0.159	0.077	1.476	0.239
5	102	0.396	0.303	1.931	0.473	102	0.194	0.140	1.824	0.268
$\infty$	90	0.790	0.787	3.566	0.752	86	0.397	0.383	1.079	0.305
AGW										
0	102	0.456	-0.392	1.613	0.423	102	0.491	-0.489	1.415	0.245
1	102	0.394	-0.349	1.221	0.320	102	0.357	-0.350	1.177	0.197
2	102	0.339	-0.302	1.106	0.270	102	0.267	-0.257	0.964	0.175
3	102	0.304	-0.273	0.874	0.239	102	0.213	-0.192	0.846	0.164
4	102	0.300	-0.269	0.802	0.234	102	0.188	-0.155	0.707	0.163
5	102	0.293	-0.261	0.802	0.231	102	0.176	-0.131	0.623	0.170
$\infty$	41	0.314	-0.248	0.953	0.264	84	0.144	-0.035	0.627	0.186
GF-CCSD										
0	102	0.187	-0.170	0.837	0.165	102	1.528	-1.528	4.271	0.889
1	102	0.100	-0.070	0.760	0.122	102	0.730	-0.730	2.280	0.467
2	102	0.084	-0.051	0.711	0.114	102	0.507	-0.507	1.616	0.326
3	102	0.079	-0.042	0.722	0.113	102	0.365	-0.356	1.179	0.245
4	102	0.078	-0.036	0.707	0.114	102	0.254	-0.252	0.926	0.174
5	102	0.072	-0.029	0.698	0.111	102	0.202	-0.200	0.961	0.169
$\infty$	32	0.081	-0.042	0.663	0.135	76	0.103	0.095	0.314	0.096

Table 7.7: MAE, MSE, GAE and STD values for the moment-resolved calculations for the *GW*100 benchmark in a def2-TZVPP basis set. Errors are taken with respect to  $\Delta\text{CCSD(T)}$ ,  $N$  indicates the number of data points available for a particular method, and  $\infty$  indicates the extrapolation using the results corresponding to the three most complete moment expansions. Extrapolations with an  $R^2$  of less than 0.95 are removed.

shows that a low-moment approximation to ADC(2) overestimates the IP, whilst a more converged representation underestimates the IP, which is also observed in the canonical ADC(2) results. This helps to rationalise why AGF2 has MSEs of the opposite sign to ADC(2), since loosely speaking it is based on an  $n_{\text{iter}}^{\Sigma} = 0$  representation of ADC(2). The same features are observed for the EA in ADC(2). On the other hand, the error in the EAs for GF-CCSD at high numbers of iterations is dominated by the error in the moment approximation.

From this we can conclude that (with the exception of the EA in GF-CCSD) the block Lanczos solvers are very effective methods to solve the respective self-energies for the purpose of obtaining quasiparticle energies. This is in combination with the other benefits of the solvers such as their efficiency and provision of a full eigenspectrum, rather than just targeting specific quasiparticle energies, and also the ease and convenience of self-consistency thereafter.

The data comprising the GW100 benchmark in this Section (with respect to the accurate CCSD(T) benchmark) is shown as a series of scatter plots in Appendix D. These scatter plots are also coloured according to the quasiparticle weight of the excitations in appropriate methods. Additionally, the value for the IP and EA of every system in the set are listed in Appendix E. This large repository of data includes the first report of CCSD(T) results in the case of the EA, with values only for the IP previously reported in the literature.<sup>395</sup> Also included are results for HF, GW (single-shot with a HF reference), ADC(2), ADC(3), AGF2, and EOM-CCSD. It is hoped that this data contributes to the field by assisting other benchmark studies, and promotes reproducibility of the present conclusions.

#### 7.4.6 Multiple solutions

As previously mentioned, several examples within the GW100 dataset present large derivatives of the self-energy, and therefore renormalisation factors (Equation 2.91) that are noticeably smaller than one. This can result in problems due to multiple physical solutions when applying a quasiparticle approximation, or when attempting to converge on a particular pole with e.g. the Davidson algorithm. Sections 4.7 and 5.5 showed that in the simple example of the stretching of H<sub>2</sub> in a small basis set, some issues associated with multiple solutions can be significantly relaxed when one uses a very coarse resolution offered by lower  $n_{\text{iter}}$  approximations in the block Lanczos recurrence schemes. Ref. 294 observes that magnesium oxide (MgO), ozone (O<sub>3</sub>), boron nitride (BN), and beryllium oxide (BeO) exhibit multiple solutions in the IP emerging where the intersection corresponding to solutions of the quasiparticle equation are close to poles in the self-energy. For the systems potassium bromide (BrK), lithium hydride (LiH), potassium hydride (KH), copper cyanide (CuCN), and the copper dimer (Cu<sub>2</sub>), the self-energy around the IP has a large derivative and therefore the solution has a renormalisation factor noticeably less than one. For typical methods of solution this does not result in multiple solutions since despite the self-energy having a large derivative, the derivative is typically fairly constant between the mean-field and quasiparticle IPs.<sup>294</sup> Since the IP is close in energy to poles of the self-energy however, the value of the IPs in these systems can be extremely sensitive to changes in the self-energy using different methodologies, resulting in inconsistencies. Figure 7.10 shows the



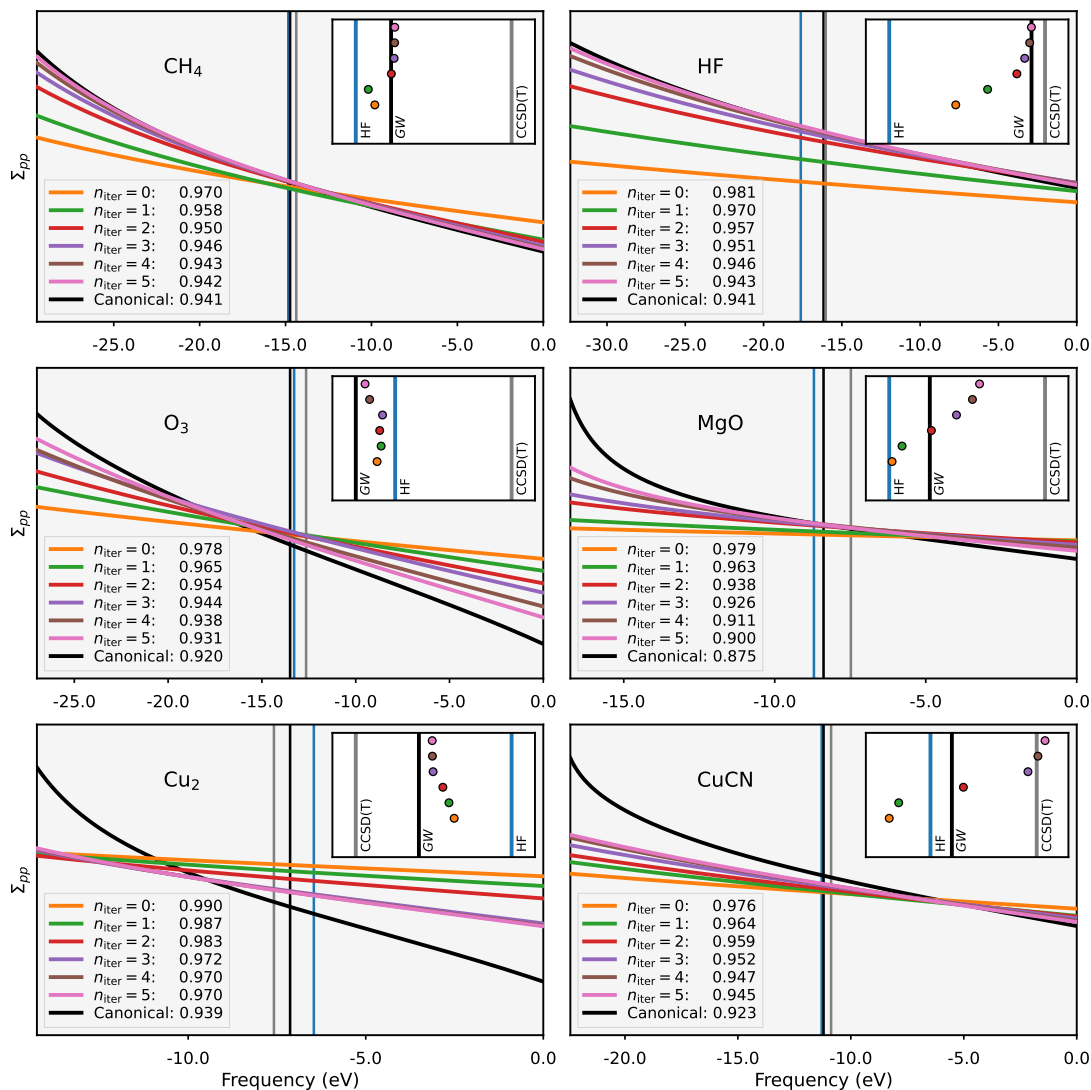


Figure 7.10: Structure of the self-energy about the IP for six systems in the GW100 dataset. Shown are methane (CH<sub>4</sub>), hydrogen fluoride (HF), ozone (O<sub>3</sub>), magnesium oxide (MgO), copper (Cu<sub>2</sub>), and copper cyanide (CuCN), all in a def2-TZVPP basis set. Each plot shows a comparison in the relative gradients of the AGW self-energies around the energy of the IPs for different numbers of iterations  $n_{iter}$  in the self-energy recurrence, with the renormalisation factor (Equation 2.91) shown in the legend, along with the canonical single-shot GW self-energy calculated using the quasiparticle equation. The vertical lines show the GW, HF, and CCSD(T) IPs, where the inset zooms in on this domain including labels, showing also the convergence of the IPs at each  $n_{iter}$ .

self-energies of several of the GW100 systems; the first row shows two non-problematic systems—methane (CH<sub>4</sub>) and hydrogen fluoride (HF)—for reference, the second row shows two of the second class of problematic systems (O<sub>3</sub> and MgO), and the third row shows two of the first class of problematic systems (Cu<sub>2</sub> and CuCN). Each plot compares the relative gradient in the self-energies of each  $n_{\text{iter}}$  of AGW with the canonical GW result for the regime immediately around the energy of the IPs. The canonical GW calculation employs the quasiparticle equation to find a solution, and is therefore sensitive to the issues related to multiple solutions. The vertical lines indicate the positions of the IPs at the levels of HF, GW, and CCSD(T), with the lines labelled in the inset, which zooms into this regime. The inset also indicates the convergence of the IPs with increasing  $n_{\text{iter}}$  in AGW, where units have been omitted since once again the convergence *relative* to the positions of the HF, GW, and CCSD(T) values is the important observation. The legend of each plot indicates the quasiparticle renormalisation factors according to Equation 2.91, i.e. a smaller factor indicates a larger self-energy derivative about the IP.

In the non-problematic examples of the first row, the self-energy within the moment-conserving solvers systematically converges to that obtained with the canonical GW calculation, indicated graphically by the curves in the plot and quantitatively by the convergence of the renormalisation factors in the legend. The renormalisation factors remain high, indicating that the derivative of the self-energies are low and that there are not particularly pronounced correlation-induced changes to the IP in these regimes. Cu<sub>2</sub> does not exhibit a particularly large derivative indicated by the reasonably large renormalisation factor of the full GW self-energy, with O<sub>3</sub> and CuCN observing slightly smaller factors, and MgO having a very small factor of 0.875. In all four cases, the convergence of the renormalisation factors with increasing  $n_{\text{iter}}$  is less systematic than the two non-problematic systems, with this accompanied by a stark inability of the AGW IP to converge to the canonical GW result in MgO and CuCN. In both of these cases, however, the IP converges to a value closer to the CCSD(T) result. This difference is caused by the more coarse representation of the self-energy resulting in fewer poles, thereby causing the derivative of the self-energy to be smaller around the IP, and relaxing the possibility of multiple solutions.

Despite ‘decluttering’ the self-energy, the block Lanczos solvers can of course still result in a solution with several Dyson orbitals close in energy that can be interpreted as multiple solutions, however an intrinsic feature of these solvers is that one always obtains solutions spanning the full eigenspectrum, and it is therefore easier to identify these multiple solutions without requiring any tricky numerical analysis. One can conclude that reduced-resolution solvers controlled by the moments of the Green’s function or self-energy have promise in handling convergence of conventional methodology in systems exhibiting stronger correlation.

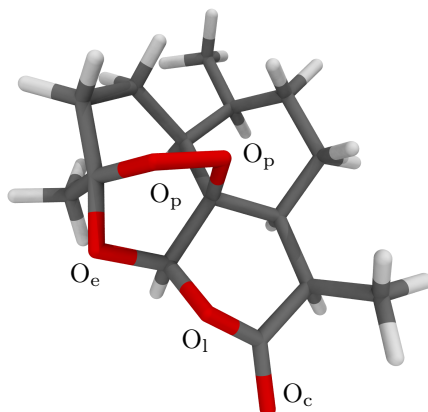


Figure 7.11: Artemisinin ( $C_{15}H_{22}O_5$ ) molecular structure with the different oxygen types labelled as  $O_p$  (peroxidic),  $O_e$  (etheric),  $O_l$  (inner-ring lactonic), and  $O_c$  (carbonyl lactonic).

## 7.5 Artemisinin

Earning a share of the Nobel Prize in Medicine in 2015, the 1972 discovery of artemisinin proved an important advance in the area of antimalarial combination therapy. Essential in its activity is the site of removal and addition of an electron, with a reactive endoperoxide bond facilitating an electrophilic attack, and the subsequent radicals affording antiparasitic properties.<sup>396,397</sup> Figure 7.11 shows the molecular structure of the molecule, with labels assigned to the different types of oxygen atom to ease discussion of excitation character. These types are  $O_p$  (peroxidic),  $O_e$  (etheric),  $O_l$  (inner-ring lactonic), and  $O_c$  (carbonyl lactonic). The IP of artemisinin has been identified in Ref. 398 as 9.40 eV using ultraviolet PES, who use density functional theory (DFT) calculations with the B3LYP functional to assign the bands in a Koopmans' fashion. This characterisation considered the ionisation as having  $n(O_p)^-$  character, corresponding to lone pairs on the endoperoxidic oxygen atoms. Ref. 399 corroborates the IP at a value of 9.75 eV, but assign it to two energetically close states with  $n(O_c, O_l)$  and  $n(O_p, O_c, O_e, O_l)$  character. Their assignment leveraged OVGf calculations and so their differences with respect to the characterisation of Ref. 398 may be due to the incorporation of correlation through the electron propagator, and is significantly more delocalised. Ref. 399 similarly study the EA using electron transmission spectroscopy, and assign a value of 1.76 eV. Using OVGf calculations, they attribute it to primarily  $\sigma^*(O_p O_p)$  with contributions also from  $\pi^*(CO_c)$ . This results in an experimental band gap of 7.69 eV whereas the OVGf calculations significantly underestimate it at 5.4 eV.

Given that it is capable of producing Dyson orbitals renormalised under the effects of correlation, and considering the appropriate system size of artemisinin, AGF2 may be a suitable method to elucidate the character going beyond DFT or OVGf assignment. The single-particle spectrum of artemisinin at the level of AGF2 was produced in an aug-cc-pVDZ basis, totalling 658 orbitals and 152 correlated electrons, which converged in around 2,500 CPU hours. The

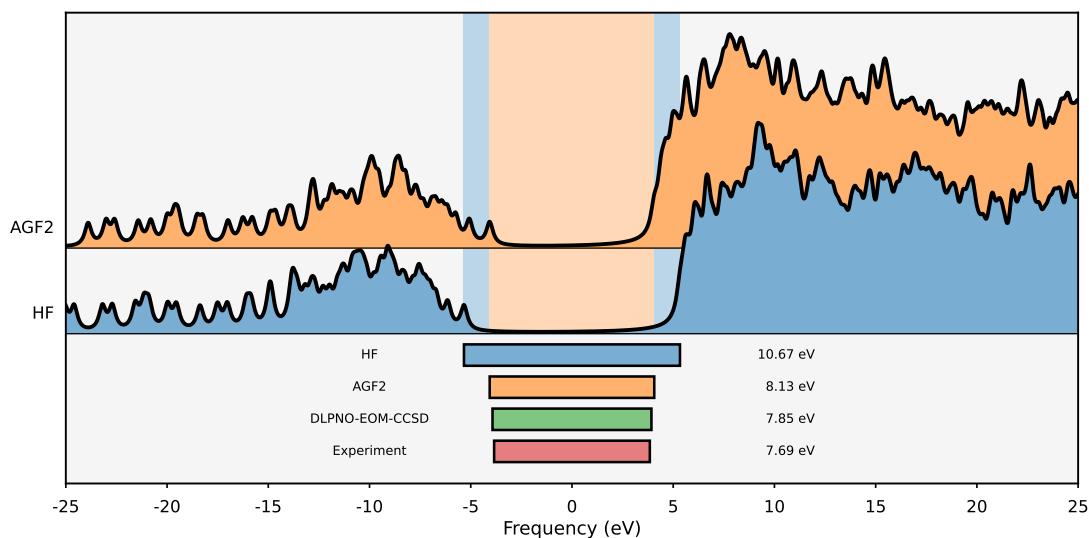


Figure 7.12: Spectral functions for the artemisinin molecule in an aug-cc-pVDZ basis set, at the levels of HF and AGF2. The bars below the spectra indicate the gap size at the plotted levels, and also at the level of domain-based local pair natural orbital (DLPNO)-EOM-CCSD and from the experimental data in Ref. 399. The HF and AGF2 band gaps are also indicated with vertical stripes behind the spectra. The spectra are centred about zero frequency by applying a chemical potential.

geometry was obtained from The Cambridge Crystallographic Data Centre, with identifier QNGHSU03.<sup>400</sup> Figure 7.12 shows a comparison between the spectra at the levels of HF and AGF2 for this calculation. The bars below the spectra additionally indicate the size of the band gaps, including the experimental data from Ref. 399 and data obtained from the domain-based local pair natural orbital (DLPNO)-EOM-CCSD method using the ORCA program,<sup>20,21,401,402</sup> at a value of 7.69 eV. This method is expected to be a good approximation to the accurate EOM-CCSD method, but is applicable in this larger system, and has a discrepancy of just 0.16 eV. In comparison, the gap at the level of AGF2 has a discrepancy of 0.28 eV, which is less than double that of the DLPNO-EOM-CCSD calculation. This provides evidence that the conclusions made about the accuracy of AGF2 for calculating charged excitations in the *GW*100 benchmark translates to this larger application.

Figure 7.13 shows the AGF2 spectrum projected onto Löwdin orthogonalised AOs on each type of oxygen. This allows one to visualise the contribution to the spectra, and more specifically the IP and EA, originating from each type of oxygen atom. The vertical stripe shows the band gap, centred about zero frequency. The spatial realisation of the Dyson orbitals corresponding to the IP and EA is also shown in Figure 7.14. The ionisation peak possesses a quasiparticle weight of 0.947 and can be seen to be dominated by contributions due to both the peroxidic ( $O_p$ ) and etheric ( $O_e$ ) oxygen atoms, corroborated by both the spatial localisation and the projected spectra. Smaller contributions can be observed on the inner-ring lactonic ( $O_l$ ) atoms. This is in agreement with the assignment made in Ref. 398, whereas the assignment made in Ref. 399 highlighted the

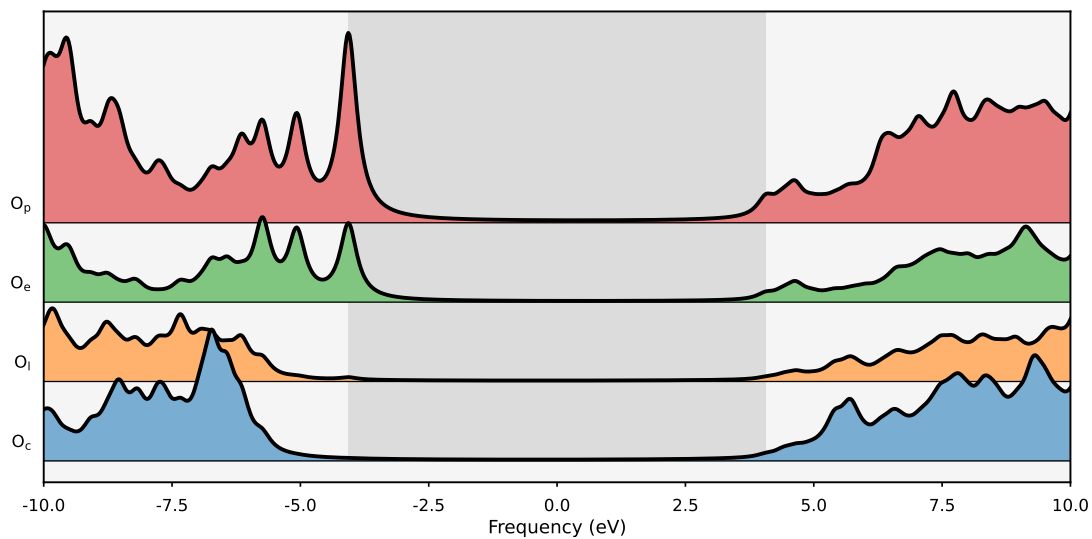


Figure 7.13: Projected spectral functions for the artemisinin molecule in an aug-cc-pVDZ basis set at the level of AGF2. The AGF2 band gap is indicated with a vertical stripe behind the spectra. The spectra are centred about zero frequency by applying a chemical potential. The spectra are projected onto AOs of each oxygen type, using Löwdin orthogonalised AOs.

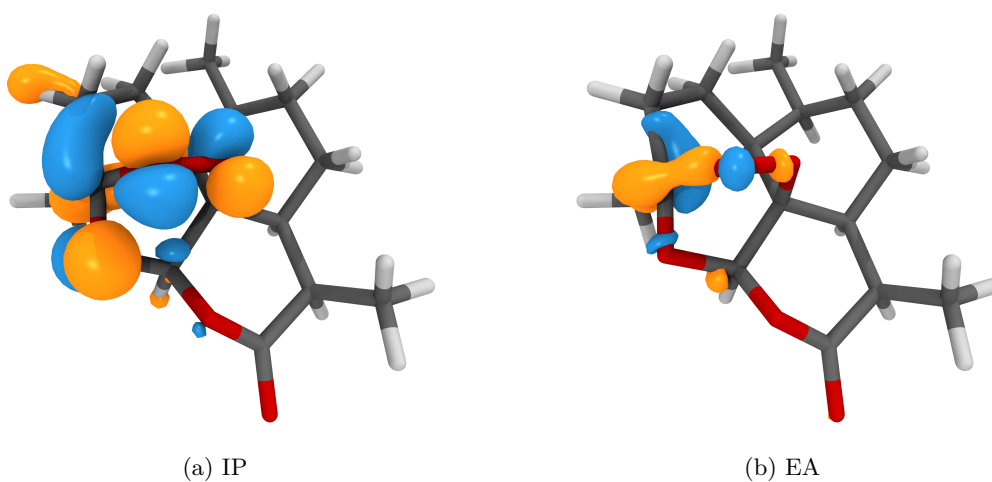


Figure 7.14: Dyson orbitals calculated at the level of AGF2 for the artemisinin molecule in an aug-cc-pVDZ basis set.

lactone group as the primary site of ionisation, which makes an insignificant contribution at the level of AGF2. The EA is represented by a dense manifold of relatively low-weighted excitations at the level of AGF2, and therefore the projection of Figure 7.13 gives a better visualisation of the character than the state-specific Dyson orbital of Figure 7.14b. All of the oxygen atoms have some degree of contribution to this manifold, with the peroxidic ( $O_p$ ) ones being the most dominant, with additional contributions due to the etheric ( $O_e$ ) atoms. This is in agreement with the assignment to  $\sigma^*$  antibonding orbitals in Ref. 399.

Systems							
AlAs	AIP	AlSb	BP	BaO	BaS	BaSe	BeSe
C	CaO	CaS	CaSe	KBr	KCl	LiBr	LiCl
LiF	Mg2Ge	Mg2Si	MgO	NaBr	NaCl	NaF	NaI
RbBr	RbCl	RbF	RbI	Si	SrO	SrS	SrSe

Table 7.8: List of systems included in the solids benchmark set. The details of the unit cells corresponding to each crystal can be found in Ref. 403.

## 7.6 Solids

In the solid state, the fundamental band gap is of great importance in describing and classifying materials. Principally, it can be used to classify the electrical conductivity of a solid, quantifying the energy gap between the valence band and the conduction band. The valence band corresponds to the continua of occupied states, whereas the conduction band to the unoccupied states, and therefore the band gap can be calculated according to the sum of the IP and EA of the material. The band gap can be further classified into direct and indirect band gaps. Direct band gaps occur in the case where the highest energy state in the valence band and the lowest energy state in the conduction band have the same momentum, whilst indirect band gaps are between states differing in momentum. Electronic transitions across an indirect gap must therefore also undergo a transfer in momentum.

As outlined in Section 4.6, AGF2 can be simply extended to periodic solids by resolving the expression for the moments in  $k$ -space. This Section will seek to benchmark the AGF2 in this setting, and compare the conclusions to those made for molecular systems. Application of perturbation theories to gapped systems in the solid state is a field of great importance, with  $GW$  calculations being perhaps the most common correlated level of theory used.

### 7.6.1 Benchmark

In order to benchmark AGF2 in the case of a  $k$ -space resolution, we select a subset of the systems presented in Ref. 403 and use a **GTH-DZVP-MOLOPT-SR** basis set with the **GTH-PADE ECP**.<sup>404</sup> This subset does not include systems with significantly heavy atoms requiring relativistic treatment, and ignores the noble gas crystals. This leaves a total of 32 systems, which are listed in Table 7.8.

Figure 7.15 shows distributions for the errors in the direct band gaps for the benchmark set for three different  $k$ -point meshes. The aggregated error values for this data are summarised in Table 7.9. For comparison, we include both mean-field and  $GW$  data using HF and DFT calculations using the PBE functional.<sup>405</sup> Since AGF2 has no dependency on the reference due to it reaching a fixed point on the Dyson equation, we need only show it for a single arbitrary mean-field reference.  $GW$  on the other hand exhibits a significant dependency on the reference. HF typically overestimates the band gap in solids, consistently so in this subset for  $k$ -point meshes of  $3\times 3\times 3$  or larger. On the other hand, PBE tends to underestimate the band gap, with the underestimation

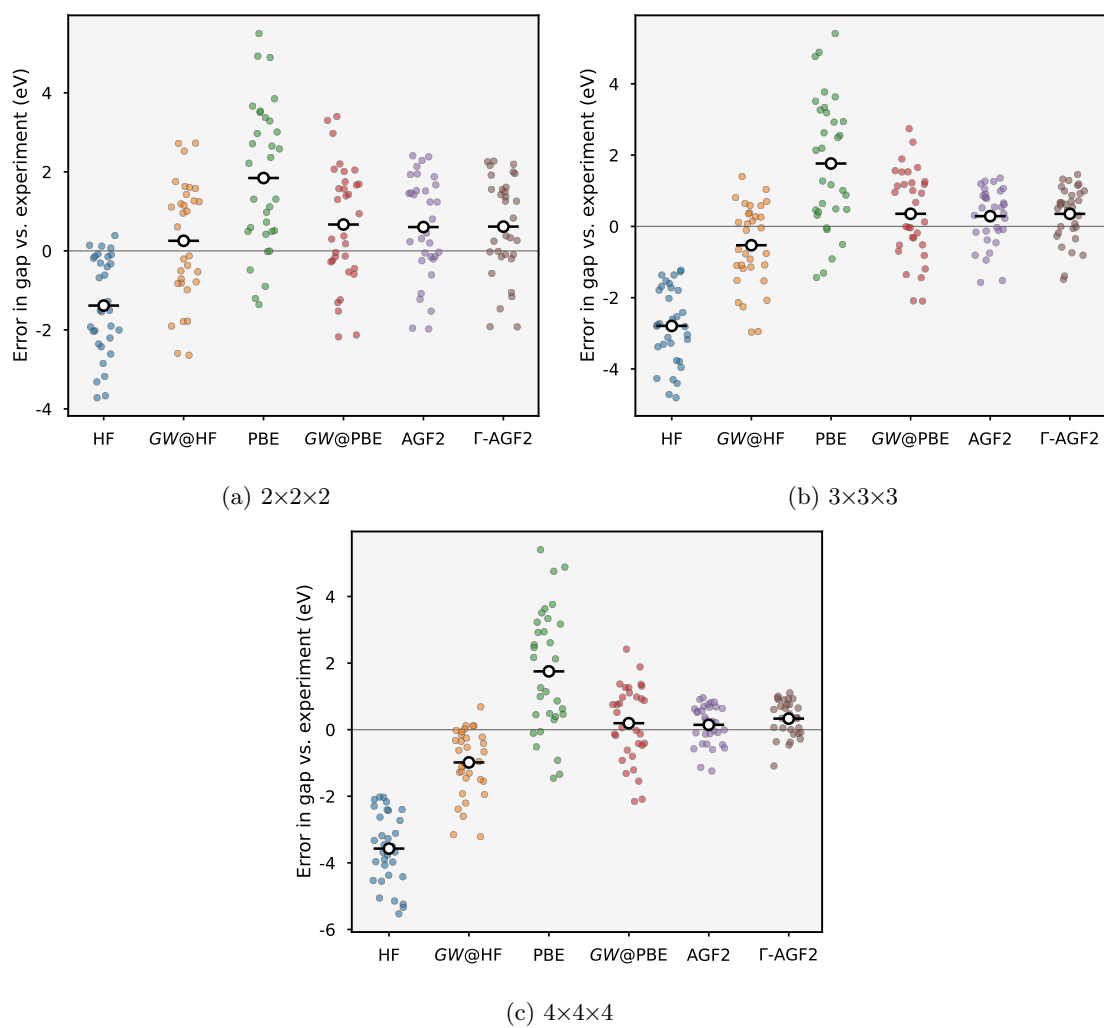


Figure 7.15: Distribution of errors in the direct band gap from AGF2 calculations on *ab initio* solids in a GTH-DZVP-MOLOPT-SR basis set and the GTH-PADE ECP. Errors are taken with respect to experiment, and the central points show the MSEs. Shown are results for three different  $k$ -point meshes,  $2 \times 2 \times 2$  (a),  $3 \times 3 \times 3$  (b), and  $4 \times 4 \times 4$  (c). Both GW and mean-field data is shown for HF as well as the DFT data using the PBE functional.



Method	$N$	MAE	MSE	GAE	STD
$2\times 2\times 2$					
HF	32	1.430	-1.384	3.716	1.223
$GW@HF$	32	1.291	0.255	2.727	1.472
PBE	32	2.093	1.844	5.500	1.821
$GW@PBE$	32	1.343	0.667	3.400	1.486
AGF2	32	1.178	0.603	2.409	1.272
$\Gamma$ -AGF2	32	1.156	0.614	2.271	1.242
$3\times 3\times 3$					
HF	32	2.791	-2.791	4.806	1.065
$GW@HF$	32	0.988	-0.528	2.967	1.140
PBE	32	2.033	1.764	5.410	1.813
$GW@PBE$	32	1.079	0.354	2.741	1.236
AGF2	32	0.722	0.287	1.571	0.787
$\Gamma$ -AGF2	32	0.720	0.352	1.483	0.761
$4\times 4\times 4$					
HF	32	3.572	-3.572	5.532	1.048
$GW@HF$	32	1.050	-0.984	3.214	0.989
PBE	32	2.026	1.751	5.405	1.816
$GW@PBE$	32	0.969	0.194	2.417	1.128
AGF2	32	0.513	0.145	1.242	0.583
$\Gamma$ -AGF2	29	0.532	0.332	1.104	0.542

Table 7.9: MAE, MSE, GAE and STD values for AGF2 calculations on *ab initio* solids in a GTH-DZVP-MOLOPT-SR basis set and the GTH-PADE ECP. Errors are taken with respect to experiment, and the central points show the MSEs. Shown are results for three different  $k$ -point meshes,  $2\times 2\times 2$  (a),  $3\times 3\times 3$  (b), and  $4\times 4\times 4$  (c). Both  $GW$  and mean-field data is shown for HF as well as the DFT data using the PBE functional.  $N$  indicates the number of systems available for each method.

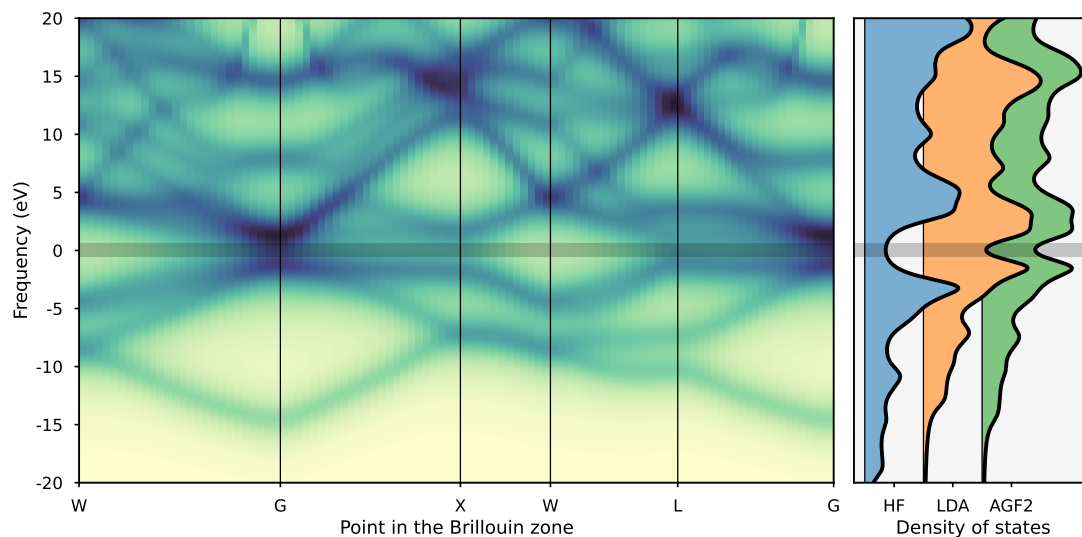
increasing in proportion to the magnitude of the gap and therefore becoming consistent at even moderately large values. This is a result of the unphysical self-Coulomb repulsion.<sup>406–410</sup> In both cases one-shot *GW* corrections offer an improvement on the band gap prediction, with *GW@HF* still overestimating the gap as one approaches the thermodynamic limit, and *GW@PBE* offering fairly unbiased errors at this limit.

AGF2 offers direct band gaps that are slightly improved on those of *GW@PBE*, with a smaller MAE and MSE, along with a smaller STD and GAE indicating fewer outliers. For the  $4\times 4\times 4$  mesh, AGF2 offers extremely unbiased errors with a MSE of just 0.145 eV, with similar observations for *GW@PBE* which has a MSE of 0.194 eV. The  $\Gamma$ -AGF2 calculations incorporating self-consistency only at the  $\Gamma$  point offer MAEs that are barely worse than those of AGF2, with the MAE actually being lower for the smallest  $2\times 2\times 2$  mesh. This is reflected by the extremely similar distribution of errors in Figure 7.15, showing that the  $\Gamma$ -only self-consistency introduces extremely small errors and is a very promising approximation to full AGF2 in *ab initio* solids. The only limit to this conclusion is that as the resolution of the  $k$ -point mesh increases, the robustness of the convergence of the Dyson equation in  $\Gamma$ -AGF2 tends to be worse than that of AGF2, culminating in three systems failing to converge for  $\Gamma$ -AGF2 in a  $4\times 4\times 4$   $k$ -point mesh that successfully converged for AGF2. This may be due to the unbalanced description of correlation at neighbouring  $k$ -points having more effect when those  $k$ -points are closer in  $k$ -space, resulting in inconsistencies in the curvature of bands, which has significant physical consequences relating to the effective mass of electrons. AGF2 can therefore be considered a promising method for studying *ab initio* solids, however more in-depth benchmarking including basis set dependency and behaviour at the thermodynamic limit is required to make a more reliable conclusion.

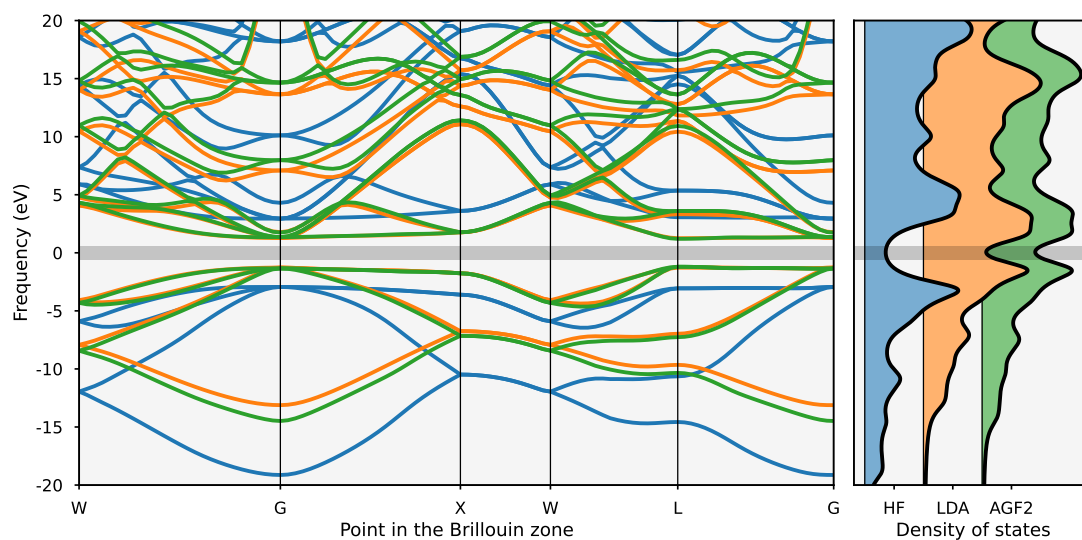
The MAE of AGF2 is similar to the quality observed for the molecular benchmark in Section 7.4. In the molecular benchmark of AGF2 in Section 7.4, the IP had a MAE of 0.437 eV and the EA of 0.222 eV. For both excitations this reflects a negative MSE, i.e. an overestimation compared to the reference. An overestimation in both excitations indicates that the resulting band gap calculated using the IP and EA are also overestimated, with the errors compounding. The combined error in the gap for the solid benchmark is 0.513 eV, which is of similar magnitude to the sum of the errors in the molecular benchmark. The gaps in the solids benchmark are fairly unbiased, with a reasonably even spread of overestimated and underestimated values, however the overall MSE indicates that those errors are slightly biased towards an underestimation.

### 7.6.2 Silicon bands

The AGF2 calculations on *ab initio* solids allow one to resolve the spectra in both frequency and  $k$ -space, which can be simply achieved by performing multiple AGF2 calculations with a  $k$ -point mesh shifted along a given path through the first Brillouin zone. This is shown in Figure 7.16 for a silicon crystal in a  $3\times 3\times 3$   $k$ -point mesh and the GTH-DZVP-MOLOPT-SR basis set with the GTH-PADE ECP.<sup>404</sup> The uppermost plot shows the broadened spectrum giving an indication of the differences in quasiparticle weight in different regions of frequency-momentum space, whereas the lower plot shows the path of each excitation through the first Brillouin zone regardless of



(a) Broadened



(b) State-specific

Figure 7.16: Band structure of silicon with a  $3 \times 3 \times 3$   $k$ -point mesh in a GTH-DZVP-MOLOPT-SR basis set and the GTH-PADE ECP. Plot (a) shows the AGF2 bands broadened with a broadening parameter  $\eta$  of 1.5 eV, and plot (b) shows each excitation in the spectrum as lines through the path in  $k$ -space, with the high-symmetry points in the first Brillouin zone labelled on the  $x$ -axis. The horizontal stripe indicates the experimental band gap. The density-of-states on the right-hand side indicates the spectrum summed over  $k$ -space, and uses a broadening  $\eta$  of 1.0 eV.

weight. The experimental gap, indicated by the horizontal stripe about zero frequency, has a value of 1.17 eV.<sup>403,411</sup> In comparison HF predicts a direct gap of 5.89 eV, whilst local density approximation (LDA) gives 2.52 eV and AGF2 gives 2.40 eV. LDA is particularly accurate for calculating the silicon band gap, and AGF2 successfully relaxes the inaccurate HF gap to a value closer to the experimental data.

Another solution to producing detailed spectra tracing the first Brillouin zone would be to employ interpolation between the sampled  $k$ -points, thereby avoiding the need to perform many calculations on shifted  $k$ -meshes, or relaxing the number of them necessary to produce smooth band structures. This has been successfully employed in Ref. 412 using Wannier orbitals where interpolation of the self-energy is shown to be more successful than interpolation of the Green's function. This is not a surprising result, given that interpolation of the Green's function means one must also interpolate the mean-field effects in the spectrum, whereas doing so with the self-energy only requires one to interpolate the correlation effects on top of the mean-field. These ideas should be readily applicable to AGF2, and in fact will be made more convenient by the moment representation of the self-energy, where the GTOs will behave in the same fashion as the Wannier orbitals used in Ref. 412. This presents an avenue for future research that could yield significant improvements in the capabilities of studying band structures at the level of many-body perturbation theories.



## Chapter 8

# Conclusion

The previous Chapters have described the state of the art within the field of quantum chemistry, and presented efficient reformulations of the block Lanczos algorithms in the context of solving the Dyson equation in Green's function perturbation theories. Using these reformulations, three methods have been outlined that leverage the efficient and compact moment representation, offering new perspectives on existing quantum chemical methods with a focus on the systematic improvability of the representation. The algorithms associated with these reformulations have been shown to converge quickly, and provide very good estimates to IPs and EAs in diverse benchmarks of small molecules. These approximate excitations have been shown to rapidly reach accuracies surpassing that of their respective methods, and as such very few iterations are required to use the solvers in place of existing ones.

The study of the behaviour of AGF2 with increasing numbers of iterations in the block Lanczos recurrences showed that such increases were detrimental to the accuracy of the calculated IPs and EAs. This led to the efficient and competitively accurate AGF2 model, with applicability to systems larger than just the small molecule benchmarks, exemplified using a study on the artemisinin molecule. Resulting also from this study was an insight into a debate over the character of excitations in the important drug molecule, giving some credence to the practical use of AGF2. Finally, a benchmark of *ab initio* solids was used to show that AGF2 shows much promise when formulated for extended systems, where it is capable of producing detailed correlated band diagrams. In the molecular case, AGF2 has been implemented within the PySCF programming package,<sup>26,27</sup> supporting both OpenMP and MPI parallel architectures, with applicable system sizes likely to surpass the 1000 orbital point depending on available resources.

The approximate AGW calculations leveraging the RPA moments show much promise, and will feature in a future publication and open-source implementation. The convergence of the IP and EA are particularly systematic and the implicit accuracy of *GW* is rapidly achieved. Whilst there are many existing *GW* implementations achieving very low scaling with system size, many of them make very harsh approximations not required in the scheme introduced in Chapter 5. There are

opportunities within this formulation to reduce the scaling with system size to  $\mathcal{O}(n_{\text{MO}}^3)$ , which will result in a very attractive *GW* solver. Furthermore, *GW* methods are utilised frequently in the field of solid state physics, and a *k*-space resolution of this framework will be an extremely worthwhile endeavour in the future. As discussed in Chapter 5 there exists many natural extensions of this framework to a diverse range of self-consistencies, which we also plan to implement.

The GF-CC work in this thesis only considered the Green's function at the level of GF-CCSD, which is perhaps the most popular and most frequently used CC ansatz. Recent work in the Booth group has applied algorithmic code generation to CC theory, and this can also be applied to generating the contributions to the vectors required to compute the GF-CC moments, as discussed in Chapter 6. These techniques have been implemented in the open-source package `ebcc` which is planned to include less straightforward ansatzes, such as those that treat active spaces at higher levels of theory within a cheaper CC calculation of the frozen space. Future work will look to applying the moment-resolved GF-CC techniques to some of these less traditional ansatzes, offering a route to quantifying the effect on the single-particle spectrum due to strongly correlated orbital fragments.

The limiting factors in the block Lanczos recurrences originate from the numerical instability associated with the moment formulation. The need to take increasingly large powers of the energies associated with the distributions results in instability under finite precision arithmetic. Future work related to this project should seek to remedy these numerical instabilities, which may be possible with an alternative polynomial expansion of the moments that constrains their values within a manageable interval, rather than the unconstrained monomial representation. The Green's function recurrence may also suffer from a loss in orthogonality of the Lanczos vectors, which is much easier to diagnose and cure in the self-energy recurrence, and may offer another possible area of improvement in the numerical stability. Improvements of this kind would allow the recurrence to proceed to much higher numbers of iterations, thereby better converging high-lying unoccupied or core states, and increasing the applicability of the algorithms. Extension of the self-energy recurrence to the case of non-Hermitian self-energies is also an important future development, and will complete the set of algorithms, allowing the compression of non-causal self-energies for example those found in CC theory.

The block Lanczos recurrences have pertinence in the field of EP theory, where a significant number of diagrammatically justified self-energies have been formulated beyond the simple examples shown at second and third order. As these diagrammatic expansions increase in complexity, as do the algebraic expressions for the blocks contributing to the self-energies, and therefore expressions for the moments become very involved, particularly when many contributions to the **C** block exist. Producing expressions to compute the moments of these self-energies may breathe new life into EP theory, particularly since in some cases the coarser representations have been shown to produce more accurate results than in the limit of infinite moments. Future work will seek to collect functions for producing moments at a diverse range of levels of theory. Obtaining such expressions for the moments of various self-energies also seamlessly permits the application of the AGF2 solver with very few modifications except for the

---

function computing the moments, easily offering renormalised physics at the level of many existing EP methods. Since many of the EPs implicitly include diagrams corresponding to partial renormalisation of lower-order ones, they may constitute different starting points leading to identical fixed points on the Dyson equation.

The moment matrices may also be opportune for interpolation, both in  $k$ -space such as the techniques discussed in Ref. 412, and also in the space of molecular geometry or basis functions employing a machine learning approach such as that of Refs. 413,414. We are also exploring avenues for collaboration with work on quantum Gaussian process states, according to the work in Ref. 415, and in relation to the computation of Green's functions on quantum devices according to Ref. 416. An important consideration in these approaches is that the definiteness of the moments must be conserved by any interpolative or predictive scheme.

Application of embedding theory to self-energies is an area of modern interest, with many papers detailing developments allowing the study of strongly correlated fragments embedded within self-energies computed at the level of perturbation theories.<sup>136,417–424</sup> In addition, work within the group has recently been focused largely on embedding problems, specifically in developing methods and algorithms for such calculations in the open-source project *Vayesta*.<sup>425–428</sup> This builds upon previous embedding work in the group that eventually led to the Green's function recurrence schemes of Section 3.6.<sup>338,350,351</sup> The moments of the self-energy are likely to be amenable to similar embedding approaches as the fully dynamic function, since the moment expansion can be roughly considered as a coarse-graining of the frequency dependency. This may permit more efficient self-energy embedding calculations which do not have to rely on poorly conditioned numerical algorithms. Additionally, the Green's function moments can be related to familiar objects in quantum chemistry, with the zeroth moment of the hole Green's function interpretable as the density matrix and the first moments as effective Fock matrices. As such, many of the techniques already developed in quantum embedding are applicable in combination with the Green's function recurrence. Work within the group is currently investigating the applicability of the approaches in Ref. 427 in the context of moments of the Green's function at the level of CC, as discussed in Chapter 6. These developments will permit high-level correlated calculations for the purpose of computing charged excitations and spectral functions in much larger systems, and in a way that is seamlessly extended to *ab initio* solids.

The application of AGF2 to solids is deserving of more investigation, particularly in order to obtain data at both the thermodynamic limit and the complete basis limit. These limits are particularly hard to reach and require significant overheads in terms of computational resources, and therefore may benefit from some partial self-consistent scheme along the lines of the  $\Gamma$ -AGF2 approach outlined in Chapter 4 and quantified in Section 7.6. As discussed in Section 7.6, there are concerns over the convergence properties in this method, likely due to inconsistencies in the bands at closely neighbouring  $k$ -points. Finding a middle ground in terms of completeness of the self-consistency and consistent treatment of neighbouring  $k$ -points may lead to an efficient and highly applicable approach for computing band structures in the solid state. The combination



therein with embedding approaches to exploit locality may result in an approach that can surpass *GW* accuracy with similar cost.

In conclusion, the moment representation offers an extremely compact and physically informed perspective to many existing theories, and opens up a wealth of avenues for less conventional approaches. In contrast to the resolution of the functions on explicit dynamic quadrature, the moments are interconvertible with the static pole representation offered by the Lehmann representation, where the efficient block Lanczos recurrence schemes allow the conversion of moments into this representation. Given the ubiquity of Green's functions throughout the wider field, we ultimately hope that this will provide a constructive impact to other pertinent areas.





## Chapter 9

# Appendices

## A Slater–Condon rules

The Slater–Condon rules allow the expression of one- and two-body integrals involving fermionic wavefunctions (as Slater determinants) in terms of the constituent orthonormal orbitals. These rules are of great utility in the derivation of quantum chemical theory.

Consider the decomposition of a one-body operator in an  $N$ -body system

$$\hat{F} = \sum_i^N \hat{f}(i). \quad (\text{A.1})$$

The Slater–Condon rules can be written<sup>56,429</sup>

$$\langle \Psi_{\text{HF}} | \hat{F} | \Psi_{\text{HF}} \rangle = \sum_p^N \langle p | \hat{F} | p \rangle, \quad (\text{A.2a})$$

$$\langle \Psi_{\text{HF}} | \hat{F} | \Psi_i^a \rangle = \langle i | \hat{F} | a \rangle, \quad (\text{A.2b})$$

$$\langle \Psi_{\text{HF}} | \hat{F} | \Psi_{ij}^{ab} \rangle = 0. \quad (\text{A.2c})$$

Similarly, two-body operators in an  $N$ -body system decompose as

$$\hat{V} = \sum_{p < q} \hat{v}(p, q), \quad (\text{A.3})$$

and the associated Slater–Condon rules are

$$\langle \Psi_{\text{HF}} | \hat{V} | \Psi_{\text{HF}} \rangle = \sum_{p < q}^N (\langle pq | \hat{v} | pq \rangle - \langle pq | \hat{v} | qp \rangle), \quad (\text{A.4a})$$

$$\langle \Psi_{\text{HF}} | \hat{V} | \Psi_i^a \rangle = \sum_p^N (\langle ip | \hat{v} | ap \rangle - \langle ip | \hat{v} | pa \rangle), \quad (\text{A.4b})$$

$$\langle \Psi_{\text{HF}} | \hat{V} | \Psi_{ij}^{ab} \rangle = \langle ij | \hat{v} | ab \rangle - \langle ij | \hat{v} | ba \rangle. \quad (\text{A.4c})$$

## B Brillouin's theorem

Consider the leading correction to the HF wavefunction in a multideterminantal representation considering the singly excited determinants

$$|\Phi\rangle = c_0 |\Psi_{\text{HF}}\rangle + \sum_i^{\text{occ}} \sum_a^{\text{vir}} c_i^a |\Psi_i^a\rangle. \quad (\text{B.5})$$

The coefficients  $c_a^i$  can be found according to the variational principle by diagonalising the Hamiltonian in the basis of the HF and singly-excited wavefunctions

$$\begin{bmatrix} \langle \Psi_{\text{HF}} | \hat{H} | \Psi_{\text{HF}} \rangle & \langle \Psi_{\text{HF}} | \hat{H} | \Psi_i^a \rangle \\ \langle \Psi_i^a | \hat{H} | \Psi_{\text{HF}} \rangle & \langle \Psi_i^a | \hat{H} | \Psi_i^a \rangle \end{bmatrix} \begin{bmatrix} c_0 \\ c_i^a \end{bmatrix} = E_0 \begin{bmatrix} c_0 \\ c_i^a \end{bmatrix}. \quad (\text{B.6})$$

Using the Slater–Condon rules (see Appendix A) we can evaluate the off-diagonal elements as

$$\begin{aligned} \langle \Psi_{\text{HF}} | \hat{H} | \Psi_i^a \rangle &= \langle i | \hat{h}_{\text{core}} | a \rangle + \sum_j \langle ij || aj \rangle \\ &= \langle i | \hat{f} | a \rangle. \end{aligned} \quad (\text{B.7})$$

Since  $i$  and  $a$  correspond to indices in occupied and virtual sectors respectively, they cannot be equal, and therefore Equation B.7 will always evaluate to zero since the Fock matrix is required to be diagonal by the HF eigenproblem. The HF ground-state can not be improved by mixing with singly excited determinants, which only couple indirectly via coupling with higher-order determinants in the exact ground state. Equation B.6 can be written for the lowest solution

$$\begin{bmatrix} E_0 & 0 \\ 0 & \langle \Psi_i^a | \hat{H} | \Psi_i^a \rangle \end{bmatrix} \begin{bmatrix} 1 \\ 0 \end{bmatrix} = E_0 \begin{bmatrix} 1 \\ 0 \end{bmatrix}. \quad (\text{B.8})$$

This fact is referred to as Brillouin's theorem.

## C Spectral product integral

Consider two functions written as spectral forms on an imaginary frequency (Matsubara) domain

$$f(i\omega) = \frac{1}{i\omega - x}, \quad (\text{C.9a})$$

$$g(i\omega) = \frac{1}{i\omega - y}, \quad (\text{C.9b})$$

which in this case simply contain unit poles at  $x$  and  $y$ , respectively. We wish to evaluate the integral

$$\int_{-\infty}^{\infty} d\omega f(i\omega)g(i\omega), \quad (\text{C.10})$$

By multiplying the numerator and denominator of  $f(\omega)$  and  $g(\omega)$  by  $i$ , Equation C.10 can be transformed as

$$\begin{aligned} \int_{-\infty}^{\infty} d\omega f(i\omega)g(i\omega) &= \int_{-\infty}^{\infty} d\omega \left( \frac{1}{i\omega - x} \right) \left( \frac{1}{i\omega - y} \right) \\ &= - \int_{-\infty}^{\infty} d\omega \left( \frac{1}{\omega + ix} \right) \left( \frac{1}{\omega + iy} \right). \end{aligned} \quad (\text{C.11})$$

Equation C.11 now has simple poles at complex values  $-ix$  and  $-iy$ .

Applying contour integration, the integral of Equation C.11 is therefore equal to the sum of the residues of poles contained in the contour. The contour can be closed in the upper half-plane if  $x$  and  $y$  are positive, in which case the poles  $-ix$  and  $-iy$  are clearly in the lower half-plane. Similarly, if  $x$  and  $y$  are negative then the poles are in the upper half-plane and the contour can be closed in to lower half-plane. In both of these cases the integral is zero. When  $x$  and  $y$  differ in sign, the contour in either half-plane must enclose one of the poles and therefore the integral is non-zero, more specifically equal to the residue of the enclosed pole. In the case of  $x > 0$  and  $y < 0$ , the pole at  $-iy$  is enclosed, and the residue is equal to  $\frac{i}{x-y}$ . For the case of  $x < 0$  and  $y > 0$ , the pole at  $-ix$  is enclosed, and the residue is equal to  $\frac{i}{y-x}$ . Incorporating the factor  $2\pi i$  from the residue theorem, we can collect the cases and evaluate the integral as

$$\int_{-\infty}^{\infty} d\omega f(i\omega)g(i\omega) = \begin{cases} \frac{2\pi}{x-y} & \text{if } x > 0, y < 0, \\ \frac{2\pi}{y-x} & \text{if } x < 0, y > 0, \\ 0 & \text{otherwise.} \end{cases} \quad (\text{C.12})$$

## D GW100 scatter plots

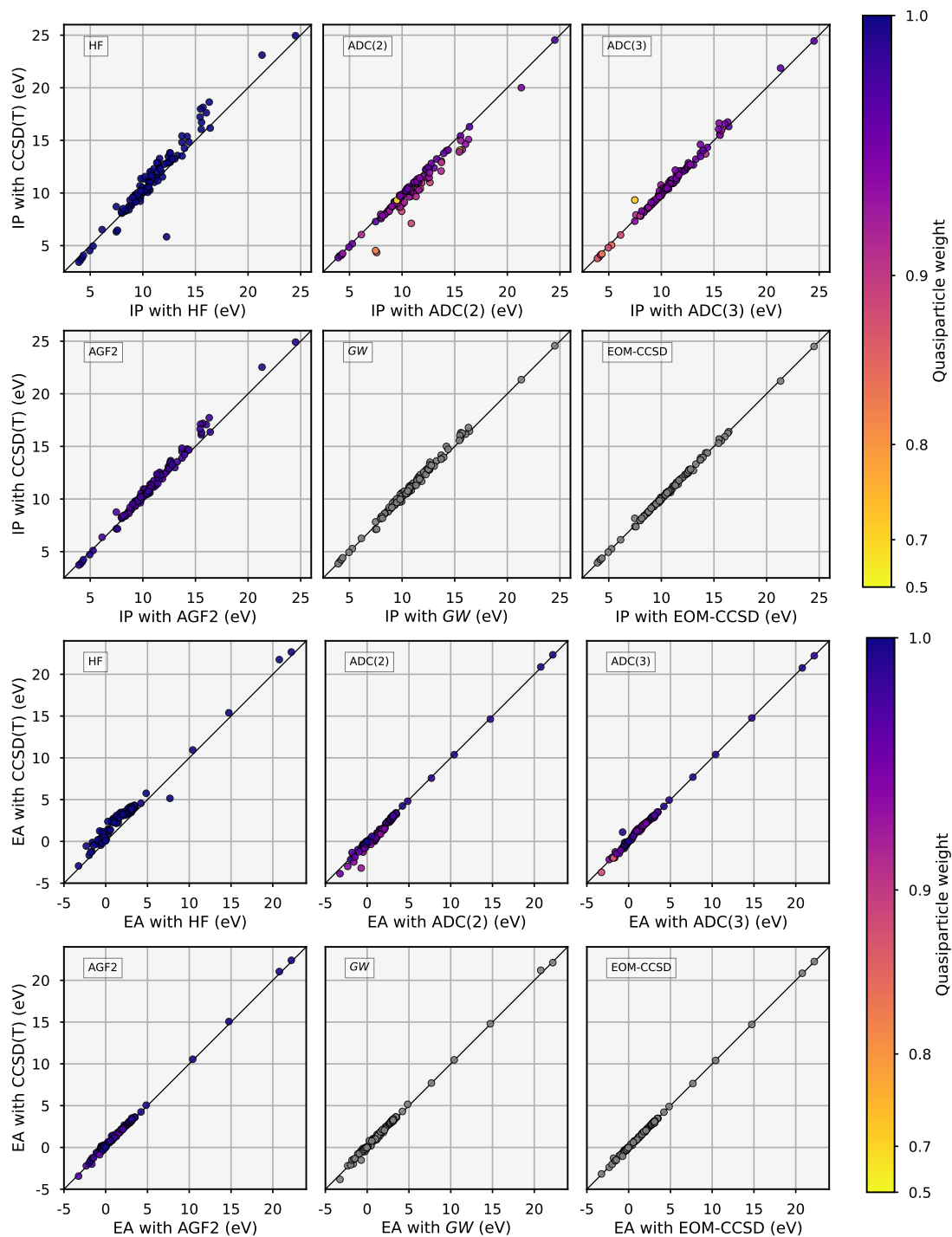


Figure D.1: Comparison between CCSD(T) values and several quantum chemical methods for the IPs (first two rows) and EAs (final two rows) of the GW100 dataset in a def2-TZVPP basis set. The colour of the points indicates the quasiparticle weight of the excitation.



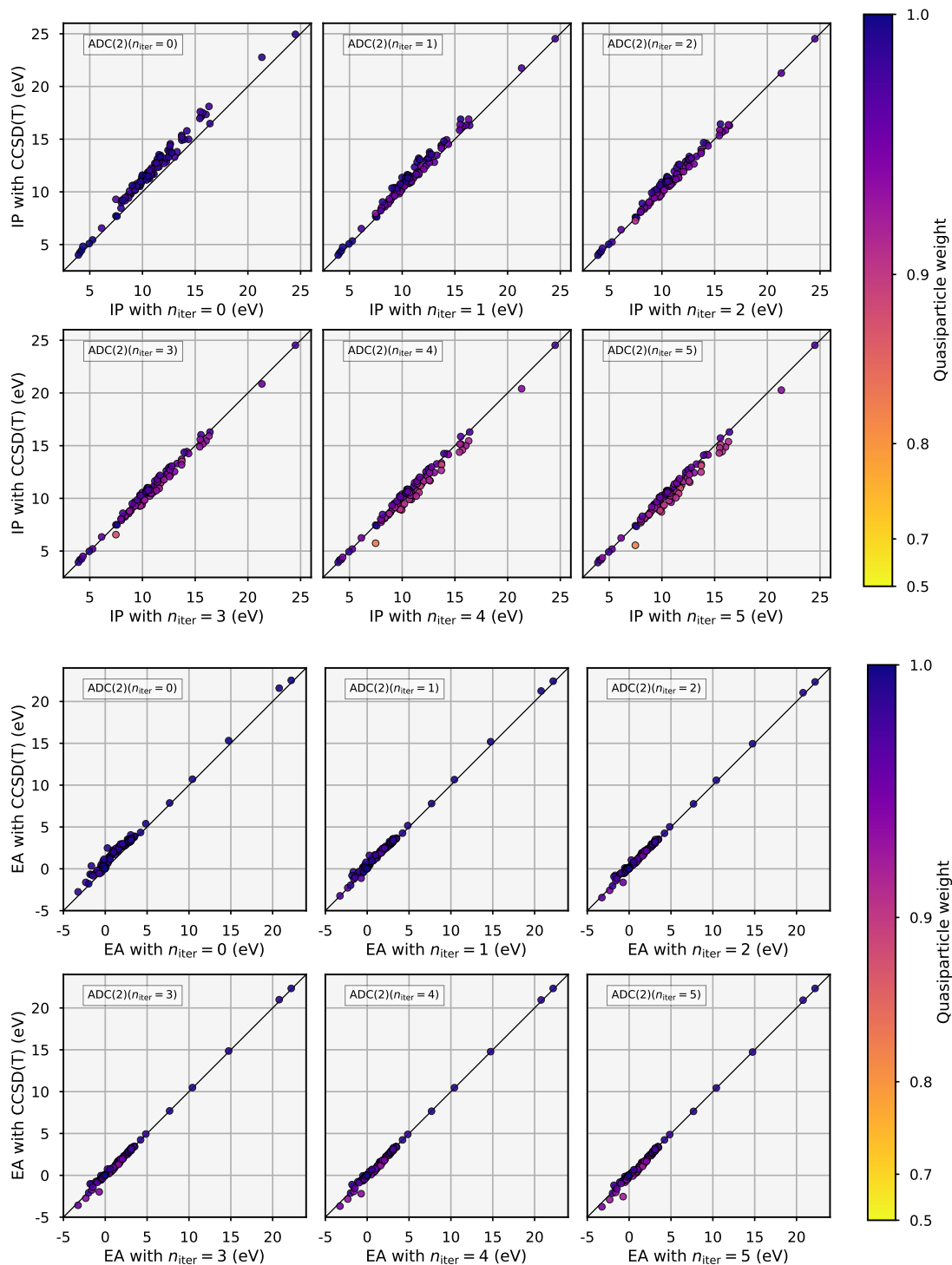


Figure D.2: Comparison between CCSD(T) values and moment-resolved ADC(2) calculations for the IPs (first two rows) and EAs (final two rows) of the GW100 dataset in a def2-TZVPP basis set. The number of iterations of the self-energy recurrence is indicated by the  $n_{\text{iter}}$  value. The colour of the points indicates the quasiparticle weight of the excitation.

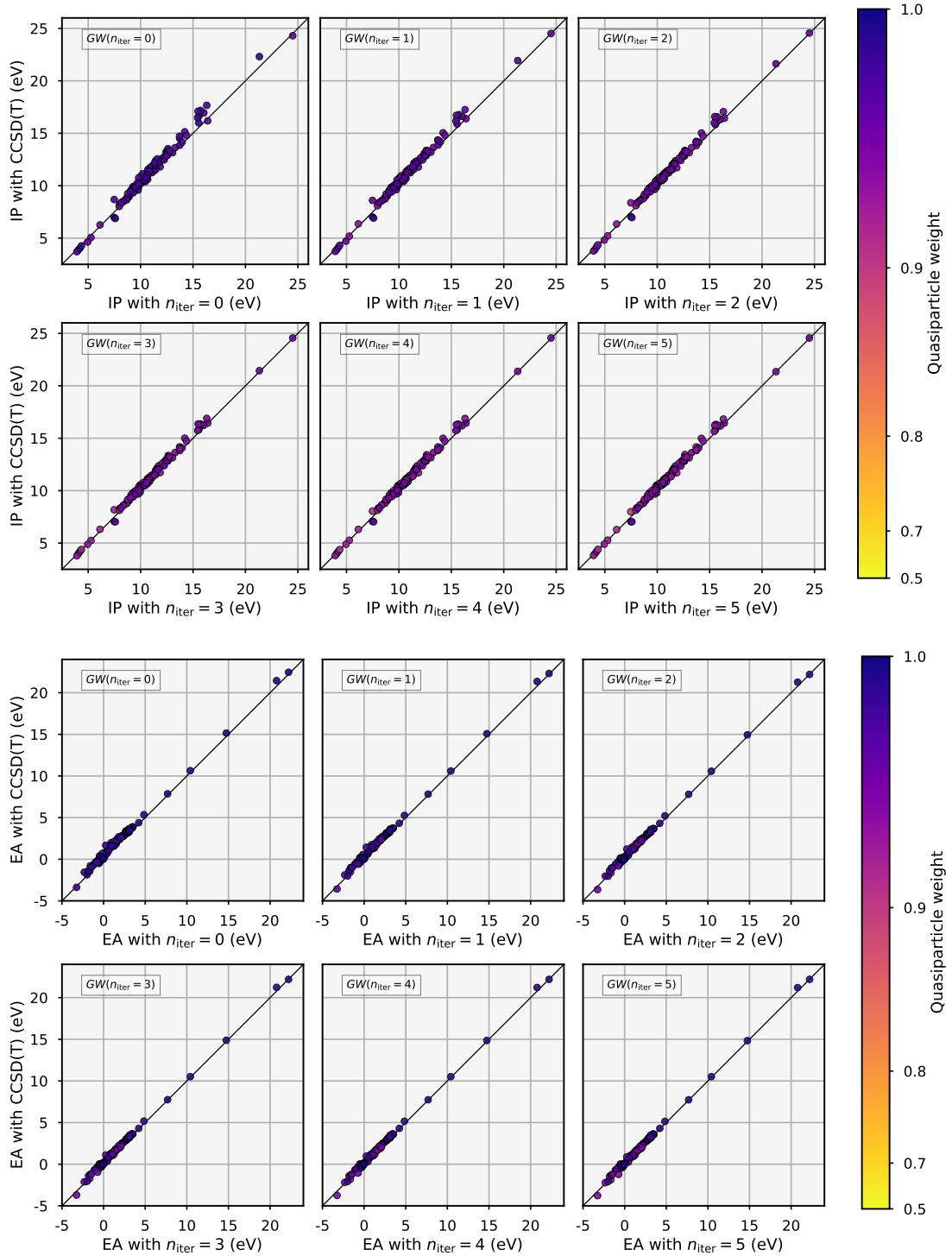


Figure D.3: Comparison between CCSD(T) values and moment-resolved GW calculations for the IPs (first two rows) and EAs (final two rows) of the GW100 dataset in a def2-TZVPP basis set. The number of iterations of the self-energy recurrence is indicated by the  $n_{\text{iter}}$  value. The colour of the points indicates the quasiparticle weight of the excitation.

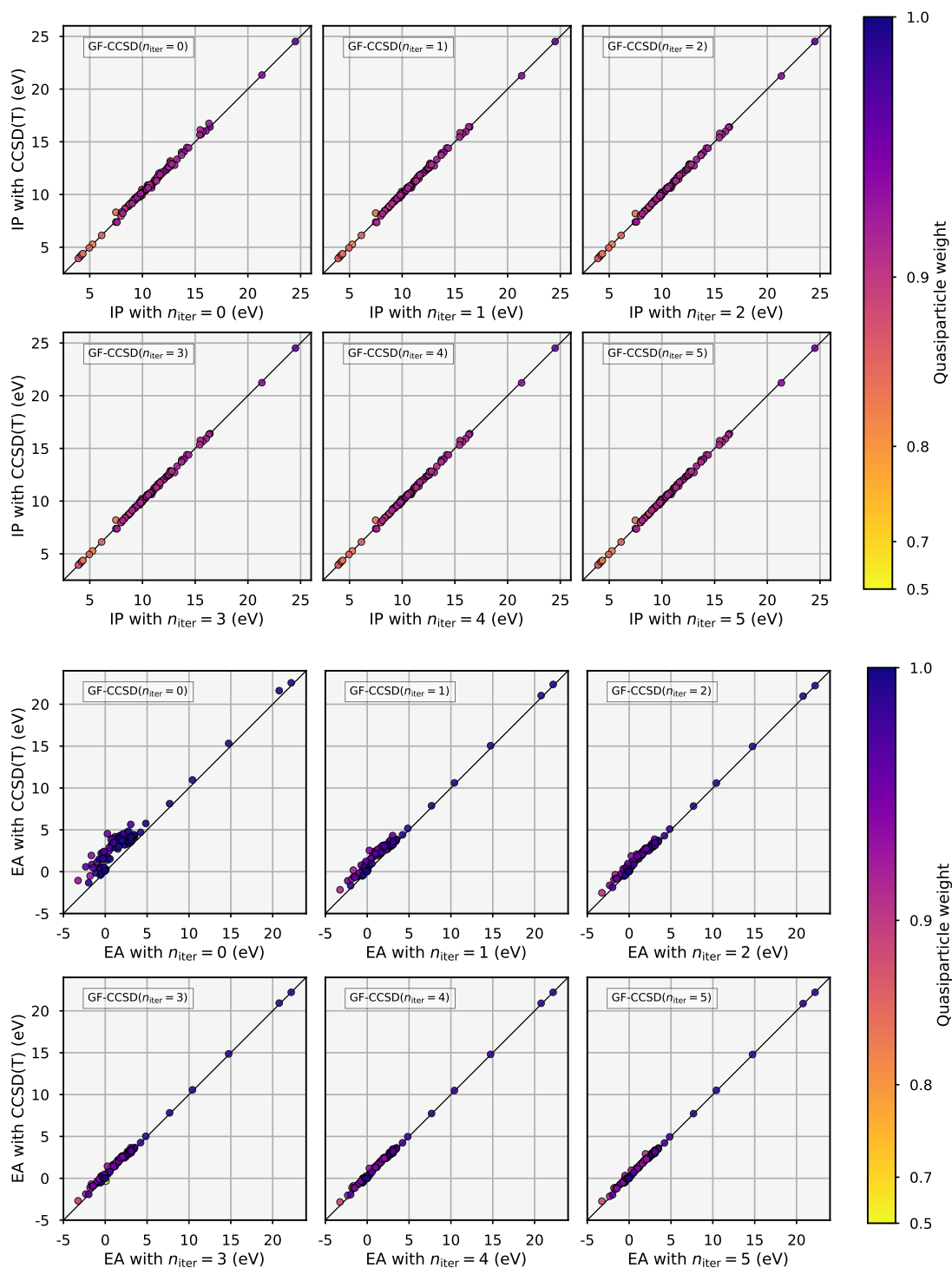


Figure D.4: Comparison between CCSD(T) values and moment-resolved GF-CCSD calculations for the IPs (first two rows) and EAs (final two rows) of the *GW100* dataset in a def2-TZVPP basis set. The number of iterations of the Green's function recurrence is indicated by the  $n_{\text{iter}}$  value. The colour of the points indicates the quasiparticle weight of the excitation.



E *GW*100 data

CAS	Name	HF	ADC(2)	ADC(3)	AGF2	<i>GW</i>	EOM-CCSD	CCSD(T)
100-41-4	ethylbenzene	8.787	8.529	8.698	8.964	9.051	8.873	8.859
10028-15-6	ozone	13.282	11.004	12.708	13.644	13.495	12.801	12.645
10043-11-5	boron nitride	11.531	10.956	12.113	11.929	11.690	11.939	11.863
106-97-8	butane	12.418	11.019	11.578	11.926	12.130	11.576	11.573
108-88-3	toluene	8.800	8.583	8.737	9.001	9.084	8.917	8.905
108-95-2	phenol	8.749	8.264	8.590	8.882	8.956	8.707	8.709
108-95-2v2	phenol v2	8.606	8.187	8.465	8.754	8.834	8.602	8.597
110-86-1	pyridine	9.448	8.647	9.550	9.772	9.843	9.729	9.709
12184-80-4	tetracarbone	11.483	10.911	11.102	11.331	11.554	11.281	11.263
12185-09-0	phosphorus dimer	10.064	10.431	10.310	10.458	10.505	10.592	10.458
12187-06-3	silver dimer	6.316	7.278	7.321	7.168	7.122	7.387	7.481
12190-70-4	copper dimer	6.461	4.340	7.917	7.173	7.130	7.370	7.585
124-38-9	carbon dioxide	14.807	13.050	13.796	14.519	14.161	13.743	13.718
1304-56-9	beryllium oxide	10.517	8.264	10.758	10.468	9.759	9.892	9.958
1309-48-4	magnesium oxide	8.703	4.526	9.331	8.756	7.826	8.165	7.479
13283-31-3	borane	13.562	13.232	13.215	13.550	13.624	13.318	13.281
1333-74-0	hydrogen	16.170	16.291	16.313	16.367	16.445	16.397	16.403
13768-60-0	boron fluoride	11.018	10.986	10.907	11.158	11.262	11.205	11.090
14452-59-6	lithium dimer	4.951	5.174	5.050	5.101	5.285	5.270	5.266
14868-53-2	pentasilane	9.821	9.177	9.248	9.792	9.760	9.361	9.261
1590-87-0	disilane	11.067	10.583	10.593	11.072	11.053	10.706	10.638
1603-84-5	carbonyl selenide	10.564	10.335	10.306	10.678	10.652	10.499	10.461
17108-85-9	gallium monochloride	9.513	9.538	9.832	9.832	9.864	9.767	9.765
17739-47-8	phosphorus mononitride	12.030	10.415	12.088	12.417	12.320	11.807	11.734
19287-45-7	borane	12.842	12.185	12.198	12.609	12.766	12.295	12.266
23878-46-8	arsenic dimer	9.219	9.785	9.717	9.644	9.706	9.874	9.760
25681-79-2	disodium	4.522	4.850	4.801	4.713	4.927	4.947	4.952
25681-80-5	dipotassium	3.605	4.023	3.891	3.828	4.026	4.081	4.062
25681-81-6	dirubidium	3.423	3.858	3.780	3.723	3.849	3.933	3.925
302-01-2	hydrazine	10.683	8.946	9.761	10.198	10.110	9.630	9.722
392-56-3	hexafluorobenzene	10.473	9.788	9.743		10.554	10.162	9.942
39297-86-4	sodium tetramer	3.824	4.083	4.103	3.996	4.238	4.257	4.225
39297-88-6	sodium hexamer	4.068	4.253	4.208	4.231	4.410	4.375	4.352
463-58-1	carbonyl sulfide	11.442	11.046	10.956	11.534	11.502	11.253	11.175
50-00-0	formaldehyde	12.032	9.694	11.130	11.480	11.308	10.786	10.845
507-25-5	tetraiodomethane	9.790	9.049	9.096	9.654	9.499	9.287	9.261
542-92-7	1,3-cyclopentadiene	8.396	8.318	8.528	8.633	8.793	8.707	8.684
544-92-3	copper cyanide	11.293	7.115	11.212	11.466	10.826	10.627	10.875
558-13-4	carbon tetrabromide	11.235	10.125	10.494	10.990	10.726	10.470	10.484
56-23-5	carbon tetrachloride	12.497	11.264	11.508	12.343	11.956	11.623	11.564
57-13-6	urea	11.354	8.965	10.339	10.942	10.614	10.089	10.059
593-60-2	vinyl bromide	9.183	8.975	9.186	9.317	9.408	9.290	9.252
593-60-2v2	vinyl bromide v2	9.895	9.521	9.765	9.982	10.008	9.856	9.856
593-66-8	iodoethane	9.362	9.128	9.179	9.492	9.463	9.358	9.329
60-29-7	ethyl ether	11.370	8.666	10.199	10.543	10.424	9.757	9.819
62-53-3	aniline	8.082	7.567	7.873	8.167	8.275	7.989	8.000
629-20-9	1,3,5,7-cyclooctatetraene	8.278	7.983	8.210	8.372	8.606	8.418	8.356
630-08-0	carbon monoxide	15.374	14.020	13.719	14.746	15.000	14.384	14.214
64-17-5	ethanol	12.016	9.634	10.970	11.390	11.225	10.622	10.689
64-18-6	formic acid	12.892	10.317	11.801	12.299	11.888	11.433	11.427
65-71-4	thymine	9.591	8.744	8.897	9.440	9.611	9.164	9.088
66-22-8	uracil	10.022	8.988	9.306	9.907	10.021	9.579	9.490
67-56-1	methyl alcohol	12.305	10.024	11.300	11.748	11.507	10.969	11.046
71-30-7	cytosine	9.323	8.269	8.654	9.207	9.209	8.797	8.777
71-43-2	benzene	9.142	9.019	9.140	9.396	9.452	9.329	9.299
73-24-5	adenine	8.358	7.934	8.163	8.518	8.633	8.345	8.339
73-40-5	guanine	8.124	7.678	7.806	8.244	8.362	8.057	8.042
74-82-8	methane	14.842	14.077	14.327	14.661	14.724	14.390	14.377
74-84-0	ethane	13.244	12.380	12.666	12.988	13.130	12.713	13.048
74-85-1	ethylene	10.283	10.346	10.485	10.595	10.709	10.698	10.674
74-86-2	acetylene	11.175	11.321	11.220	11.479	11.539	11.570	11.433
74-90-8	hydrogen cyanide	13.514	12.904	13.485	13.898	13.823	13.917	13.734
74-98-6	propane	12.740	11.544	12.048	12.395	12.569	12.060	12.054
7439-90-9	krypton	14.251	13.766	14.046	14.206	13.968	13.962	13.956
7440-01-9	neon	23.105	20.007	21.868	22.531	21.341	21.217	21.329
7440-37-1	argon	16.053	15.423	15.556	16.100	15.726	15.637	15.550
7440-59-7	helium	24.949	24.529	24.444	24.915	24.560	24.500	24.512
7440-63-3	xenon	5.835	12.260	12.170	12.325	12.314	12.314	12.257
7446-09-5	sulfur dioxide	13.471	11.413	12.419	13.077	12.889	12.388	12.422
75-01-4	chloroethene	10.093	9.796	9.957	10.256	10.311	10.142	10.100
75-02-5	fluoroethene	10.477	10.167	10.423	10.657	10.767	10.611	10.563
75-07-0	acetaldehyde	11.560	9.112	10.494	10.915	10.748	10.193	10.213
75-15-0	carbon disulfide	10.118	9.875	9.736	10.262	10.275	10.027	9.982
75-19-4	cyclopropane	11.362	10.329	10.856	11.102	11.233	10.869	10.874
75-73-0	tetrafluoromethane	18.637	15.083	16.741	17.719	16.785	16.249	16.308
7553-56-2	iodine	9.804	9.307	9.422	9.787	9.672	9.534	9.505
7580-67-8	lithium hydride	8.209	7.972	7.835	8.260	8.133	7.961	7.962
7647-01-0	hydrogen chloride	12.929	12.426	12.568	13.033	12.766	12.657	12.597
7647-14-5	sodium chloride	9.577	8.728	9.101	9.541	9.192	9.132	9.029
7664-39-3	hydrogen fluoride	17.624	14.634	16.563	17.067	16.163	15.910	16.032
7664-41-7	ammonia	11.648	10.146	10.875	11.289	11.141	10.777	10.811
7693-26-7	potassium hydride	6.525	6.044	6.007	6.368	6.255	6.126	6.128
7722-84-1	hydrogen peroxide	13.275	10.281	11.721	12.530	12.002	11.400	11.593
7726-95-6	bromine	11.021	10.182	10.634	10.900	10.712	10.534	10.554
7727-37-9	nitrogen	16.708	14.982	15.494	16.311	16.300	15.611	15.577
7732-18-5	water	8.823	11.475	12.865	13.353	12.814	12.485	12.571
7758-02-3	potassium bromide	8.518	7.842	8.284	8.412	8.176	8.168	8.138
7782-41-4	fluorine	18.141	14.109	15.944	17.190	16.257	15.540	15.717
7782-50-5	chlorine	12.038	11.107	11.410	12.024	11.728	11.473	11.415
7782-65-2	germane	12.904	12.460	12.510	12.883	12.835	12.515	12.490
7782-79-8	hydrogen azide	10.974	10.354	10.383	11.023	11.038	10.731	10.684
7783-06-4	hydrogen sulfide	10.443	10.174	10.250	10.596	10.479	10.368	10.314
7783-40-6	magnesium fluoride	15.427	12.083	14.610	14.827	13.785	13.712	13.713
7783-60-0	sulfur tetrafluoride	13.785	11.924	12.656	13.506	13.247	12.721	12.609
7783-63-3	titanium tetrafluoride	17.984	14.063	16.638	17.111	16.028	15.702	15.483
7784-18-1	aluminum fluoride	17.234	13.897	16.062	16.657	15.566	15.306	15.444
7784-23-8	aluminum iodide	10.176	9.696	9.661	10.190	9.969	9.824	9.807
7784-42-1	arsine	10.355	10.233	10.413	10.517	10.537	10.393	10.392
7786-30-3	magnesium chloride	12.263	11.436	11.716	12.274	11.887	11.770	11.667
7789-24-4	lithium fluoride	12.876	9.664	12.176	12.360	11.302	11.284	11.326
7803-51-2	phosphine	10.572	10.413	10.445	10.730	10.762	10.587	10.540
7803-62-5	silane	13.243	12.818	12.720	13.254	13.196	12.838	12.784

Table E.1: List of IPs (in units of eV) calculated for the *GW*100 dataset in a def2-TZVPP basis set.

CAS	Name	HF	ADC(2)	ADC(3)	AGF2	GW	EOM-CCSD	CCSD(T)
100-41-4	ethylbenzene	3.361	1.235	1.932	1.903	1.863	1.750	1.681
10028-15-6	ozone	-1.206	-1.681	-1.950	-1.995	-1.956	-1.535	-1.659
10043-11-5	boron nitride	-2.931	-3.858	-3.700	-3.436	-3.832	-3.175	-3.250
106-97-8	butane	3.777	2.787	2.928	3.023	3.095	2.883	2.860
108-88-3	toluene	3.272	1.224	1.891	1.855	1.810	1.703	1.643
108-95-2	phenol	3.126	1.143	1.814	1.729	1.681	1.612	1.601
108-95-2v2	phenol v2	3.186	1.192	1.876	1.790	1.739	1.666	1.641
110-86-1	pyridine	2.772	0.759	1.379	1.393	1.312	1.223	1.177
12184-80-4	tetracarbon	-0.554	-2.992	-2.173	-2.200	-2.194	-2.375	-2.324
12185-09-0	phosphorus dimer	0.629	-0.443	-0.174	0.141	-0.230	-0.114	-0.110
12187-06-3	silver dimer	0.252	-0.873	-0.803	-0.391	-0.457	-0.689	-0.773
12190-70-4	copper dimer	0.451	-0.363	-0.841	0.175	-0.130	-0.323	-0.516
124-38-9	carbon dioxide	3.644	2.605	2.966	2.926	2.981	2.799	2.828
1304-56-9	beryllium oxide	-1.661	-2.166	-1.917	-1.857	-2.087	-2.022	-1.979
1309-48-4	magnesium oxide	-1.305	-1.339	-1.983	-1.532	-1.519	-1.291	-1.812
13283-31-3	borane	1.473	0.266	0.374	0.598	0.676	0.324	0.322
1333-74-0	hydrogen	4.565	4.234	4.187	4.246	4.306	4.220	4.223
13768-60-0	boron fluoride	2.245	1.459	1.403	1.707	1.642	1.506	1.502
14452-59-6	lithium dimer	0.368	-0.099	-0.239	0.241	-0.036	-0.118	-0.198
14868-53-2	pentasilane	2.310	0.485	0.838	1.368	1.052	0.763	0.701
1590-87-0	disilane	3.226	2.111	2.262	2.670	2.471	2.244	2.208
1603-84-5	carbonyl selenide	2.656	0.844	1.676	1.750	1.369	1.427	1.501
17108-85-9	gallium monochloride	0.964	0.132	0.155	0.576	0.330	0.281	0.282
17739-47-8	phosphorus mononitride	1.222	0.169	0.339	0.609	0.341	0.453	0.454
19287-45-7	diborane	2.548	1.017	1.284	1.434	1.532	1.192	1.174
23878-46-8	arsenic dimer	0.327	-0.490	-0.473	-0.174	-0.364	-0.234	-0.289
25681-79-2	disodium	0.140	-0.303	-0.400	0.068	-0.233	-0.264	-0.328
25681-80-5	dipotassium	0.046	-0.422	-0.417	-0.104	-0.310	-0.323	-0.364
25681-81-6	dirubidium	0.014	-0.455	-0.479	-0.178	-0.346	-0.367	-0.415
302-01-2	hydrazine	3.210	2.440	2.517	2.612	2.679	2.508	2.488
392-56-3	hexafluorobenzene	2.562	0.383	1.529	0.912	0.912	1.056	1.121
39297-86-4	sodium tetramer	0.013	-0.649	-0.689	-0.087	-0.471	-0.537	-0.603
39297-88-6	sodium hexamer	0.165	-0.709	-0.583	0.057	-0.422	-0.494	-0.554
463-58-1	carbonyl sulfide	3.057	1.339	2.044	2.106	1.778	1.834	1.945
50-00-0	formaldehyde	2.958	1.396	1.636	1.858	1.865	1.655	1.621
507-25-5	tetraiodomethane	-0.125	-2.465	-1.258	-1.247	-1.407	-1.607	-1.596
542-92-7	1,3-cyclopentadiene	3.256	1.263	1.898	1.851	1.866	1.761	1.717
544-92-3	copper cyanide	-0.314	-0.981	-1.432	-0.621	-0.771	-0.962	-1.117
558-13-4	carbon tetrabromide	1.162	-1.276	-0.137	-0.137	-0.255	-0.477	-0.486
56-23-5	carbon tetrachloride	2.736	0.018	1.295	1.463	1.090	0.859	0.902
57-13-6	urea	3.124	2.219	2.409	2.484	2.509	2.332	2.312
593-60-2	vinyl bromide	3.385	1.537	2.185	2.254	2.157	2.016	2.039
593-60-2v2	vinyl bromide v2	3.378	1.403	2.142	2.216	2.085	1.935	1.954
593-66-8	iodoethene	2.747	0.945	1.526	1.753	1.660	1.399	1.393
60-29-7	ethyl ether	3.834	2.879	2.994	3.126	3.173	2.962	2.930
62-53-3	aniline	3.358	1.345	2.016	1.954	1.910	1.820	1.791
629-20-9	1,3,5,7-cyclooctatetraene	2.474	0.158	0.959	0.854	0.911	0.782	0.692
630-08-0	carbon monoxide	2.153	1.001	1.175	1.307	1.151	1.203	1.277
64-17-5	ethanol	3.637	2.796	2.861	3.014	3.056	2.859	2.821
64-18-6	formic acid	3.800	2.388	2.730	2.878	2.879	2.686	2.660
65-71-4	thymine	2.429	0.126	1.076	0.875	0.822	0.755	0.782
66-22-8	uracil	2.296	0.086	0.991	0.805	0.743	0.685	0.729
67-56-1	methyl alcohol	3.731	2.975	3.030	3.162	3.213	3.026	2.999
71-30-7	cytosine	2.587	0.281	1.224	1.067	0.985	0.907	0.952
71-43-2	benzene	3.315	1.294	1.964	1.932	1.861	1.771	1.728
73-24-5	adenine	3.090	0.707	1.427	1.450	1.420	1.270	1.278
73-40-5	guanine	2.848	0.887	1.830	1.768	1.868	1.564	1.611
74-82-8	methane	4.079	3.422	3.470	3.570	3.617	3.454	3.448
74-84-0	ethane	3.855	3.054	3.143	3.237	3.296	3.114	3.102
74-85-1	ethylene	3.892	2.283	2.717	2.793	2.796	2.624	2.634
74-86-2	acetylene	4.225	3.258	3.525	3.629	3.580	3.486	3.513
74-90-8	hydrogen cyanide	4.094	3.000	3.192	3.350	3.277	3.197	3.211
74-98-6	propane	3.774	2.873	2.986	3.084	3.149	2.950	2.931
7439-90-9	krypton	10.946	10.376	10.398	10.555	10.479	10.407	10.419
7440-01-9	neon	21.757	20.878	20.762	21.047	21.200	20.844	20.781
7440-37-1	argon	15.393	14.636	14.771	15.063	14.799	14.717	14.744
7440-59-7	helium	22.667	22.331	22.222	22.392	22.115	22.244	22.217
7440-63-3	xenon	5.153	7.574	7.691	7.707	7.707	7.646	7.689
7446-09-5	sulfur dioxide	0.436	-0.634	-0.389	-0.298	-0.494	-0.357	-0.260
75-01-4	chloroethene	3.512	1.619	2.294	2.328	2.249	2.112	2.145
75-02-5	fluoroethene	4.054	2.432	2.894	2.930	2.910	2.784	2.802
75-07-0	acetaldehyde	3.474	1.548	1.940	2.162	2.138	1.901	1.828
75-15-0	carbon disulfide	1.412	-0.351	0.608	0.567	0.191	0.277	0.454
75-19-4	cyclopropane	4.336	3.345	3.498	3.596	3.657	3.455	3.437
75-73-0	tetrafluoromethane	5.760	4.804	4.941	5.053	5.157	4.892	4.844
7553-56-2	iodine	-0.451	-1.875	-1.460	-1.262	-1.336	-1.490	-1.459
7580-67-8	lithium hydride	0.245	0.104	0.068	0.177	0.103	0.089	0.086
7647-01-0	hydrogen chloride	3.459	2.549	2.725	2.962	2.836	2.692	2.719
7647-14-5	sodium chloride	-0.449	-0.594	-0.589	-0.529	-0.560	-0.587	-0.584
7664-39-3	hydrogen fluoride	3.473	3.060	3.053	3.110	3.163	3.072	3.064
7664-41-7	ammonia	3.416	2.802	2.849	2.931	2.993	2.841	2.827
7693-26-7	potassium hydride	0.117	-0.053	-0.048	-0.011	-0.024	-0.036	-0.028
7722-84-1	hydrogen peroxide	3.646	2.646	3.004	3.106	3.174	3.009	2.963
7726-95-6	bromine	0.171	-1.245	-1.062	-0.742	-0.753	-0.937	-0.955
7727-37-9	nitrogen	4.185	2.848	2.996	3.239	3.074	3.035	3.043
7732-18-5	water	3.413	2.855	2.868	2.953	3.022	2.882	2.865
7758-02-3	potassium bromide	-0.232	-0.455	-0.434	-0.404	-0.382	-0.445	-0.438
7782-41-4	fluorine	2.385	-0.040	0.166	0.643	0.810	0.381	0.261
7782-50-5	chlorine	1.175	-0.666	-0.134	0.299	-0.031	-0.210	-0.148
7782-65-2	germane	4.084	3.149	3.073	3.513	3.421	3.177	3.126
7782-79-8	hydrogen azide	3.251	1.473	2.189	2.177	2.062	2.015	2.068
7783-06-4	hydrogen sulfide	3.573	2.660	2.811	3.080	2.965	2.779	2.795
7783-40-6	magnesium fluoride	0.303	-0.007	-0.072	0.073	0.046	-0.033	-0.081
7783-60-0	sulfur tetrafluoride	2.252	0.445	1.246	1.166	1.004	0.920	1.001
7783-63-3	titanium tetrafluoride	1.247	-3.190	1.109	-0.877	-1.520	-1.058	-0.721
7784-18-1	aluminum fluoride	1.369	0.604	0.604	0.812	0.772	0.619	0.565
7784-23-8	aluminum iodide	0.912	-0.837	-0.097	0.213	-0.223	-0.335	-0.304
7784-42-1	arsine	3.708	2.792	2.828	3.148	3.089	2.871	3.008
7786-30-3	magnesium chloride	0.494	-0.291	-0.155	0.161	-0.056	-0.187	-0.184
7789-24-4	lithium fluoride	0.057	-0.021	-0.009	0.011	-0.012	-0.022	-0.022
7803-51-2	phosphine	3.737	2.859	2.954	3.261	3.150	2.938	3.115
7803-62-5	silane	3.894	3.059	3.103	3.399	3.283	3.095	3.093

Table E.2: List of EAs (in units of eV) calculated for the GW100 dataset in a def2-TZVPP basis set.



---

# Bibliography

- [1] Heitler, W.; London, F. *Z. Phys.* **1927**, *44*, 455–472.
- [2] Pauling, L. *Chem. Rev.* **1928**, *5*, 173–213.
- [3] Schrödinger, E. *Phys. Rev.* **1926**, *28*, 1049–1070.
- [4] Schrödinger, E. *Ann. Phys.* **1926**, *385*, 437–490.
- [5] Mulliken, R. S. *Science* **1967**, *157*, 13–24.
- [6] Pauling, L. *J. Am. Chem. Soc.* **1931**, *53*, 1367–1400.
- [7] Pauling, L. *The Nature of the Chemical Bond and the Structure of Molecules and Crystals*; 1960.
- [8] Hückel, E. *Z. Phys.* **1930**, *60*, 423–456.
- [9] Hückel, E. *Z. Phys.* **1931**, *70*, 204–286.
- [10] Hückel, E. *Z. Phys.* **1932**, *76*, 628–648.
- [11] Dirac, P. *Proc. R. Soc. A* **1929**, *123*, 714–733.
- [12] *The IUPAC Compendium of Chemical Terminology*; International Union of Pure and Applied Chemistry (IUPAC), 2014.
- [13] Autumn, K.; Sitti, M.; Liang, Y. A.; Peattie, A. M.; Hansen, W. R.; Sponberg, S.; Kenny, T. W.; Fearing, R.; Israelachvili, J. N.; Full, R. J. *Proc. Natl. Acad. Sci.* **2002**, *99*, 12252–12256.
- [14] Russell, A. P.; Higham, T. E. *Proc. R. Soc. B* **2009**, *276*, 3705–3709.
- [15] Löwdin, P.-O. *Phys. Rev.* **1955**, *97*, 1509–1520.
- [16] Wigner, E. *Phys. Rev.* **1934**, *46*, 1002–1011.
- [17] Talirz, L.; Ghiringhelli, L. M.; Smit, B. *Living J. Comp. Mol. Sci.* **2021**, *3*.
- [18] Talirz, L.; Aprà, E.; Poncé, S. Italirz/atomistic-software: v2022.2.3. 2022; <https://zenodo.org/record/4639414>.
- [19] Ahlrichs, R.; Bär, M.; Häser, M.; Horn, H.; Kölmel, C. *Chem. Phys. Lett.* **1989**, *162*, 165–169.



- [20] Neese, F. *Wiley Interdiscip. Rev. Comput. Mol. Sci.* **2012**, *2*, 73–78.
- [21] Neese, F.; Wennmohs, F.; Becker, U.; Riplinger, C. *J. Chem. Phys.* **2020**, *152*, 224108.
- [22] Shao, Y.; Gan, Z.; Epifanovsky, E.; Gilbert, A. T.; Wormit, M.; Kussmann, J.; Lange, A. W.; Behn, A.; Deng, J.; Feng, X.; Ghosh, D.; Goldey, M.; Horn, P. R.; Jacobson, L. D.; Kaliman, I.; Khaliullin, R. Z.; Kuś, T.; Landau, A.; Liu, J.; Proynov, E. I.; Rhee, Y. M.; Richard, R. M.; Rohrdanz, M. A.; Steele, R. P.; Sundstrom, E. J.; III, H. L. W.; Zimmerman, P. M.; Zuev, D.; Albrecht, B.; Alguire, E.; Austin, B.; Beran, G. J. O.; Bernard, Y. A.; Berquist, E.; Brandhorst, K.; Bravaya, K. B.; Brown, S. T.; Casanova, D.; Chang, C.-M.; Chen, Y.; Chien, S. H.; Closser, K. D.; Crittenden, D. L.; Diedenhofen, M.; Jr., R. A. D.; Do, H.; Dutoi, A. D.; Edgar, R. G.; Fatehi, S.; Fusti-Molnar, L.; Ghysels, A.; Golubeva-Zadorozhnaya, A.; Gomes, J.; Hanson-Heine, M. W.; Harbach, P. H.; Hauser, A. W.; Hohenstein, E. G.; Holden, Z. C.; Jagau, T.-C.; Ji, H.; Kaduk, B.; Khistyayev, K.; Kim, J.; Kim, J.; King, R. A.; Klunzinger, P.; Kosenkov, D.; Kowalczyk, T.; Krauter, C. M.; Lao, K. U.; Laurent, A. D.; Lawler, K. V.; Levchenko, S. V.; Lin, C. Y.; Liu, F.; Livshits, E.; Lochan, R. C.; Luenser, A.; Manohar, P.; Manzer, S. F.; Mao, S.-P.; Mardirossian, N.; Marenich, A. V.; Maurer, S. A.; Mayhall, N. J.; Neuscammann, E.; Oana, C. M.; Olivares-Amaya, R.; O'Neill, D. P.; Parkhill, J. A.; Perrine, T. M.; Peverati, R.; Prociuk, A.; Rehn, D. R.; Rosta, E.; Russ, N. J.; Sharada, S. M.; Sharma, S.; Small, D. W.; Sodt, A.; Stein, T.; Stück, D.; Su, Y.-C.; Thom, A. J.; Tsuchimochi, T.; Vanovschi, V.; Vogt, L.; Vydrov, O.; Wang, T.; Watson, M. A.; Wenzel, J.; White, A.; Williams, C. F.; Yang, J.; Yeganeh, S.; Yost, S. R.; You, Z.-Q.; Zhang, I. Y.; Zhang, X.; Zhao, Y.; Brooks, B. R.; Chan, G. K.; Chipman, D. M.; Cramer, C. J.; III, W. A. G.; Gordon, M. S.; Hehre, W. J.; Klamt, A.; III, H. F. S.; Schmidt, M. W.; Sherrill, C. D.; Truhlar, D. G.; Warshel, A.; Xu, X.; Aspuru-Guzik, A.; Baer, R.; Bell, A. T.; Besley, N. A.; Chai, J.-D.; Dreuw, A.; Dunietz, B. D.; Furlani, T. R.; Gwaltney, S. R.; Hsu, C.-P.; Jung, Y.; Kong, J.; Lambrecht, D. S.; Liang, W.; Ochsenfeld, C.; Rassolov, V. A.; Slipchenko, L. V.; Subotnik, J. E.; van Voorhis, T.; Herbert, J. M.; Krylov, A. I.; Gill, P. M.; Head-Gordon, M. *Mol. Phys.* **2015**, *113*, 184–215.
- [23] Peng, C.; Lewis, C. A.; Wang, X.; Clement, M. C.; Pierce, K.; Rishi, V.; Pavošević, F.; Slattery, S.; Zhang, J.; Teke, N.; Kumar, A.; Masteran, C.; Asadchev, A.; Calvin, J. A.; Valeev, E. F. *J. Chem. Phys.* **2020**, *153*, 044120.
- [24] Epifanovsky, E.; Gilbert, A. T. B.; Feng, X.; Lee, J.; Mao, Y.; Mardirossian, N.; Pokhilko, P.; White, A. F.; Coons, M. P.; Dempwolff, A. L.; Gan, Z.; Hait, D.; Horn, P. R.; Jacobson, L. D.; Kaliman, I.; Kussmann, J.; Lange, A. W.; Lao, K. U.; Levine, D. S.; Liu, J.; McKenzie, S. C.; Morrison, A. F.; Nanda, K. D.; Plasser, F.; Rehn, D. R.; Vidal, M. L.; You, Z.-Q.; Zhu, Y.; Alam, B.; Albrecht, B. J.; Aldossary, A.; Alguire, E.; Andersen, J. H.; Athavale, V.; Barton, D.; Begam, K.; Behn, A.; Bellonzi, N.; Bernard, Y. A.; Berquist, E. J.; Burton, H. G. A.; Carreras, A.; Carter-Fenk, K.; Chakraborty, R.; Chien, A. D.; Closser, K. D.; Cofer-Shabica, V.; Dasgupta, S.; de Wergifosse, M.; Deng, J.; Diedenhofen, M.; Do, H.; Ehlert, S.; Fang, P.-T.; Fatehi, S.; Feng, Q.; Friedhoff, T.; Gayvert, J.; Ge, Q.; Gidofalvi, G.; Goldey, M.; Gomes, J.; González-Espinoza, C. E.; Gulania, S.; Gunina, A. O.; Hanson-Heine, M. W. D.; Harbach, P. H. P.; Hauser, A.; Herbst, M. F.; Hernández Vera, M.; Hodecker, M.; Holden, Z. C.; Houck, S.; Huang, X.; Hui, K.; Huynh, B. C.; Ivanov, M.; Jász, A.; Ji, H.; Jiang, H.; Kaduk, B.; Kähler, S.; Khistyayev, K.; Kim, J.; Kis, G.; Klunzinger, P.; Koczor-Benda, Z.; Koh, J. H.; Kosenkov, D.; Koulias, L.; Kowalczyk, T.; Krauter, C. M.; Kue, K.; Kunitsa, A.; Kus, T.; Ladjánszki, I.; Landau, A.;

- Lawler, K. V.; Lefrancois, D.; Lehtola, S.; Li, R. R.; Li, Y.-P.; Liang, J.; Liebenthal, M.; Lin, H.-H.; Lin, Y.-S.; Liu, F.; Liu, K.-Y.; Loipersberger, M.; Luenser, A.; Manjanath, A.; Manohar, P.; Mansoor, E.; Manzer, S. F.; Mao, S.-P.; Marenich, A. V.; Markovich, T.; Mason, S.; Maurer, S. A.; McLaughlin, P. F.; Menger, M. F. S. J.; Mewes, J.-M.; Mewes, S. A.; Morgante, P.; Mullinax, J. W.; Oosterbaan, K. J.; Paran, G.; Paul, A. C.; Paul, S. K.; Pavošević, F.; Pei, Z.; Prager, S.; Proynov, E. I.; Rák, A.; Ramos-Cordoba, E.; Rana, B.; Rask, A. E.; Rettig, A.; Richard, R. M.; Rob, F.; Rossomme, E.; Scheele, T.; Scheurer, M.; Schneider, M.; Sergueev, N.; Sharada, S. M.; Skomorowski, W.; Small, D. W.; Stein, C. J.; Su, Y.-C.; Sundstrom, E. J.; Tao, Z.; Thirman, J.; Tornai, G. J.; Tsuchimochi, T.; Tubman, N. M.; Veccham, S. P.; Vydrov, O.; Wenzel, J.; Witte, J.; Yamada, A.; Yao, K.; Yeganeh, S.; Yost, S. R.; Zech, A.; Zhang, I. Y.; Zhang, X.; Zhang, Y.; Zuev, D.; Aspuru-Guzik, A.; Bell, A. T.; Besley, N. A.; Bravaya, K. B.; Brooks, B. R.; Casanova, D.; Chai, J.-D.; Coriani, S.; Cramer, C. J.; Cserey, G.; DePrince, A. E.; DiStasio, R. A.; Dreuw, A.; Dunietz, B. D.; Furlani, T. R.; Goddard, W. A.; Hammes-Schiffer, S.; Head-Gordon, T.; Hehre, W. J.; Hsu, C.-P.; Jagau, T.-C.; Jung, Y.; Klamt, A.; Kong, J.; Lambrecht, D. S.; Liang, W.; Mayhall, N. J.; McCurdy, C. W.; Neaton, J. B.; Ochsenfeld, C.; Parkhill, J. A.; Peverati, R.; Rassolov, V. A.; Shao, Y.; Slipchenko, L. V.; Stauch, T.; Steele, R. P.; Subotnik, J. E.; Thom, A. J. W.; Tkatchenko, A.; Truhlar, D. G.; van Voorhis, T.; Wesolowski, T. A.; Whaley, K. B.; Woodcock, H. L.; Zimmerman, P. M.; Faraji, S.; Gill, P. M. W.; Head-Gordon, M.; Herbert, J. M.; Krylov, A. I. *J. Chem. Phys.* **2021**, *155*, 084801.
- [25] van Rossum, G.; Drake Jr, F. L. *Python reference manual*; Centrum voor Wiskunde en Informatica Amsterdam, 1995.
- [26] Sun, Q.; Berkelbach, T. C.; Blunt, N. S.; Booth, G. H.; Guo, S.; Li, Z.; Liu, J.; McClain, J. D.; Sayfutyarova, E. R.; Sharma, S.; Wouters, S.; Chan, G. K.-L. *Wiley Interdiscip. Rev. Comput. Mol. Sci.* **2017**, *8*, e1340.
- [27] Sun, Q.; Zhang, X.; Banerjee, S.; Bao, P.; Barbry, M.; Blunt, N. S.; Bogdanov, N. A.; Booth, G. H.; Chen, J.; Cui, Z.-H.; Eriksen, J. J.; Gao, Y.; Guo, S.; Hermann, J.; Hermes, M. R.; Koh, K.; Koval, P.; Lehtola, S.; Li, Z.; Liu, J.; Mardirossian, N.; McClain, J. D.; Motta, M.; Mussard, B.; Pham, H. Q.; Pulkin, A.; Purwanto, W.; Robinson, P. J.; Ronca, E.; Sayfutyarova, E. R.; Scheurer, M.; Schurkus, H. F.; Smith, J. E. T.; Sun, C.; Sun, S.-N.; Upadhyay, S.; Wagner, L. K.; Wang, X.; White, A.; Whitfield, J. D.; Williamson, M. J.; Wouters, S.; Yang, J.; Yu, J. M.; Zhu, T.; Berkelbach, T. C.; Sharma, S.; Sokolov, A. Y.; Chan, G. K.-L. *J. Chem. Phys.* **2020**, *153*, 024109.
- [28] Parrish, R. M.; Burns, L. A.; Smith, D. G. A.; Simmonett, A. C.; DePrince, A. E.; Hohenstein, E. G.; Bozkaya, U.; Sokolov, A. Y.; Di Remigio, R.; Richard, R. M.; Gonthier, J. F.; James, A. M.; McAlexander, H. R.; Kumar, A.; Saitow, M.; Wang, X.; Pritchard, B. P.; Verma, P.; Schaefer, H. F.; Patkowski, K.; King, R. A.; Valeev, E. F.; Evangelista, F. A.; Turney, J. M.; Crawford, T. D.; Sherrill, C. D. *J. Chem. Theory Comput.* **2017**, *13*, 3185–3197.
- [29] Smith, D. G. A.; Burns, L. A.; Sirianni, D. A.; Nascimento, D. R.; Kumar, A.; James, A. M.; Schriber, J. B.; Zhang, T.; Zhang, B.; Abbott, A. S.; Berquist, E. J.; Lechner, M. H.; Cunha, L. A.; Heide, A. G.; Waldrop, J. M.; Takeshita, T. Y.; Alenaizan, A.; Neuhauser, D.; King, R. A.; Simmonett, A. C.; Turney, J. M.; Schaefer, H. F.; Evangelista, F. A.; III, A. E. D.; Crawford, T. D.; Patkowski, K.; Sherrill, C. D. *J. Chem. Theory Comput.* **2018**, *14*, 3504–3511.

- [30] Hanson-Heine, M. W. D.; Ashmore, A. P. *Int. J. Quantum Chem.* **2022**,
- [31] Wigner, E.; Seitz, F. *Phys. Rev.* **1933**, *43*, 804–810.
- [32] Marr, G. V. *Phys. Bull.* **1977**, *28*, 572–572.
- [33] Himpsel, F. *Advances in Physics* **1983**, *32*, 1–51.
- [34] Kevan, S. *Angle-Resolved Photoemission*; 1992.
- [35] Plummer, E. W.; Eberhardt, W. *Advances in Chemical Physics*; John Wiley & Sons, Inc., 2007; pp 533–656.
- [36] Dose, V. *Surf. Sci. Rep.* **1985**, *5*, 337–378.
- [37] Smith, N. V. *Rep. Prog. Phys.* **1988**, *51*, 1227–1294.
- [38] Mohnen, V. A. Formation, Nature, and Mobility of Ions of Atmospheric Importance. Electrical Processes in Atmospheres. Heidelberg, 1976; pp 1–17.
- [39] Eriksson, S. K.; Josefsson, I.; Ellis, H.; Amat, A.; Pastore, M.; Oscarsson, J.; Lindblad, R.; Eriksson, A. I. K.; Johansson, E. M. J.; Boschloo, G.; Hagfeldt, A.; Fantacci, S.; Odelius, M.; Rensmo, H. *Phys. Chem. Chem. Phys.* **2016**, *18*, 252–260.
- [40] Snook, J. H.; Samuelson, L. A.; Kumar, J.; Kim, Y.-G.; Whitten, J. E. *Org. Electron.* **2005**, *6*, 55–64.
- [41] Barr, T. L.; Liu, Y. L. *J. Phys. Chem. Solids* **1989**, *50*, 657–664.
- [42] Iskakov, S.; Rusakov, A. A.; Zgid, D.; Gull, E. *Phys. Rev. B* **2019**, *100*, 085112.
- [43] Kim, Y. J. Block Lanczos Algorithm. Ph.D. thesis, Naval Postgraduate School, Monterey, California, 1989.
- [44] Meyer, H.-D.; Pal, S. *J. Chem. Phys.* **1989**, *91*, 6195–6204.
- [45] Weikert, H.-G.; Meyer, H.-D.; Cederbaum, L. S.; Tarantelli, F. *J. Chem. Phys.* **1996**, *104*, 7122–7138.
- [46] Minehardt, T. J.; Adcock, J. D.; Wyatt, R. E. *Phys. Rev. E* **1997**, *56*, 4837–4853.
- [47] Golod, A.; Deleuze, M. S.; Cederbaum, L. S. *J. Chem. Phys.* **1999**, *110*, 6014–6024.
- [48] Walker, B.; Saitta, A. M.; Gebauer, R.; Baroni, S. *Phys. Rev. Lett.* **2006**, *96*.
- [49] Grüning, M.; Marini, A.; Gonze, X. *Comput. Mater. Sci.* **2011**, *50*, 2148–2156.
- [50] Skeidsvoll, A. S.; Moitra, T.; Balbi, A.; Paul, A. C.; Coriani, S.; Koch, H. *Phys. Rev. A* **2022**, *105*.
- [51] Backhouse, O. J.; Santana-Bonilla, A.; Booth, G. H. *J. Phys. Chem. Lett.* **2021**, *12*, 7650–7658.
- [52] Backhouse, O. J.; Nusspickel, M.; Booth, G. H. *J. Chem. Theory Comput.* **2020**, *16*, 1090–1104.
- [53] Backhouse, O. J.; Booth, G. H. *J. Chem. Theory Comput.* **2020**, *16*, 6294–6304.

- [54] Scott, C. J. C.; Backhouse, O. J.; Booth, G. H. Auxiliary *GW* approximation, in preparation. 2022.
- [55] Born, M.; Oppenheimer, R. *Ann. Phys.* **1927**, *389*, 457–484.
- [56] Slater, J. C. *Phys. Rev.* **1929**, *34*, 1293–1322.
- [57] Szabo, A.; Ostlund, N. S. *Modern Quantum Chemistry: Introduction to Advanced Electronic Structure Theory*, 1st ed.; Dover Publications, Inc.: Mineola, 1996.
- [58] Pauli, W. *Z. Phys.* **1925**, *31*, 765–783.
- [59] Roothaan, C. C. J. *Rev. Mod. Phys.* **1951**, *23*, 69–89.
- [60] Hall, G. G. *Proc. R. Soc. A* **1951**, *205*, 541–552.
- [61] Pople, J. A.; Nesbet, R. K. *J. Chem. Phys.* **1954**, *22*, 571–572.
- [62] Koopmans, T. *Physica* **1934**, *1*, 104–113.
- [63] Heinrich, N.; Koch, W.; Frenking, G. *Chem. Phys. Lett.* **1986**, *124*, 20–25.
- [64] Krylov, A. I. *J. Chem. Phys.* **2020**, *153*, 080901.
- [65] Ortiz, J. V. *J. Chem. Phys.* **2020**, *153*, 070902.
- [66] Hugenholtz, N. *Physica* **1957**, *23*, 481–532.
- [67] Goldstone, J. *Proc. R. Soc. A* **1957**, *239*, 267–279.
- [68] Shavitt, I.; Bartlett, R. J. *Many-Body Methods in Chemistry and Physics*; Cambridge University Press, 2009.
- [69] Brandow, B. H. *Rev. Mod. Phys.* **1967**, *39*, 771–828.
- [70] Green, G. *An essay on the application of mathematical analysis to the theories of electricity and magnetism*; 1828.
- [71] Martin, R. N.; Reining, L.; Ceperley, D. M. *Interacting Electrons*; Cambridge University Press: Cambridge, United Kingdom, 2016.
- [72] Melania Oana, C.; Krylov, A. I. *J. Chem. Phys.* **2007**, *127*, 234106.
- [73] Ortiz, J. V. *Int. J. Quantum Chem.* **2004**, *100*, 1131–1135.
- [74] Díaz-Tinoco, M.; Corzo, H. H.; Pawłowski, F.; Ortiz, J. V. *Mol. Phys.* **2018**, *117*, 2275–2283.
- [75] Almladh, C.; Hedin, L. *Handbook on Synchrotron Radiation*; 1983; Vol. 1; Chapter Beyond the one-electron model: Many-electron effects in atoms, molecules, and solids, p 607.
- [76] Onida, G.; Reining, L.; Rubio, A. *Rev. Mod. Phys.* **2002**, *74*, 601–659.
- [77] Walter, O.; Cederbaum, L. S.; Schirmer, J. *J. Math. Phys.* **1984**, *25*, 729–737.
- [78] Löwdin, P.-O. *J. Chem. Phys.* **1951**, *19*, 1396–1401.

- [79] Löwdin, P.-O. *Rev. Mod. Phys.* **1962**, *34*, 520–530.
- [80] Löwdin, P.-O. *J. Math. Phys.* **1962**, *3*, 969–982.
- [81] Löwdin, P.-O. *J. Mol. Spectrosc.* **1964**, *14*, 112–118.
- [82] Löwdin, P.-O. *Int. J. Quantum Chem.* **1968**, *2*, 867–931.
- [83] Davidson, E. R.; McMurchie, L. E.; Day, S. J. *J. Chem. Phys.* **1981**, *74*, 5491–5496.
- [84] Deleuze, M.; Delhalle, J.; Pickup, B. T. *Theor. Chim. Acta* **1992**, *82*, 309–319.
- [85] Aryasetiawan, F.; Tomczak, J. M.; Miyake, T.; Sakuma, R. *Phys. Rev. Lett.* **2009**, *102*.
- [86] Manni, G. L.; Aquilante, F.; Gagliardi, L. *J. Chem. Phys.* **2011**, *134*, 034114.
- [87] Manni, G. L.; Ma, D.; Aquilante, F.; Olsen, J.; Gagliardi, L. *J. Chem. Theory Comput.* **2013**, *9*, 3375–3384.
- [88] Dvorak, M.; Rinke, P. *Phys. Rev. B* **2019**, *99*.
- [89] Dvorak, M.; Golze, D.; Rinke, P. *Phys. Rev. Mater* **2019**, *3*.
- [90] Li, J.; Yang, J. *J. Phys. Chem. Lett.* **2022**, *13*, 10042–10047.
- [91] Schirmer, J.; Angonoa, G. *J. Chem. Phys.* **1989**, *91*, 1754–1761.
- [92] Deleuze, M.; Scheller, M. K.; Cederbaum, L. S. *J. Chem. Phys.* **1995**, *103*, 3578–3588.
- [93] Lanczos, C. *J. Res. Natl. Inst. Stand. Technol.* **1950**, *45*, 255.
- [94] Ojalvo, I. U.; Newman, M. *AIAA J.* **1970**, *8*, 1234–1239.
- [95] Davidson, E. R. *J. Comput. Phys* **1975**, *17*, 87–94.
- [96] Morgan, R. B.; Scott, D. S. *SIAM J. Sci. Stat. Comput.* **1986**, *7*, 817–825.
- [97] Sleijpen, G. L. G.; Booten, A. G. L.; Fokkema, D. R.; van der Vorst, H. A. *BIT Numer. Math.* **1996**, *36*, 595–633.
- [98] Ortiz, J. V. *Wiley Interdiscip. Rev. Comput. Mol. Sci.* **2012**, *3*, 123–142.
- [99] Opoku, E.; Pawłowski, F.; Ortiz, J. V. *J. Chem. Phys.* **2021**, *155*, 204107.
- [100] Kutepov, A. L.; Oudovenko, V. S.; Kotliar, G. *Comput. Phys. Commun.* **2017**, *219*, 407–414.
- [101] Dahlen, N. E.; van Leeuwen, R. *J. Chem. Phys.* **2005**, *122*, 164102.
- [102] Gull, E.; Iskakov, S.; Krivenko, I.; Rusakov, A. A.; Zgid, D. *Phys. Rev. B* **2018**, *98*.
- [103] Kananenka, A. A.; Welden, A. R.; Lan, T. N.; Gull, E.; Zgid, D. *J. Chem. Theory Comput.* **2016**, *12*, 2250–2259.
- [104] Dong, X.; Zgid, D.; Gull, E.; Strand, H. U. R. *J. Chem. Phys.* **2020**, *152*, 134107.

- [105] Abrikosov, A.; Gorkov, L.; Dzyaloshinski, I.; Silverman, R. *Methods of Quantum Field Theory in Statistical Physics*; Dover Books on Physics; Dover Publications, 2012.
- [106] Coleman, P. *Introduction to Many-Body Physics*; Cambridge University Press, 2015.
- [107] Kraberger, G. J.; Triebl, R.; Zingl, M.; Aichhorn, M. *Phys. Rev. B* **2017**, *96*, 155128.
- [108] Smith, D. W. *J. Chem. Phys.* **1975**, *62*, 113.
- [109] Welden, A. R.; Phillips, J. J.; Zgid, D. **2015**,
- [110] Schüler, M.; Pavlyukh, Y. *Phys. Rev. B* **2018**, *97*.
- [111] Lee, J.; Malone, F. D.; Morales, M. A.; Reichman, D. R. *J. Chem. Theory Comput.* **2021**, *17*, 3372–3387.
- [112] Di Sabatino, S.; Koskelo, J.; Prodhon, J.; Berger, J. A.; Caffarel, M.; Romaniello, P. *Front. Chem.* **2021**, *9*.
- [113] Ernzerhof, M. *J. Chem. Theory Comput.* **2009**, *5*, 793–797.
- [114] Baym, G.; Kadanoff, L. P. *Phys. Rev.* **1961**, *124*, 287–299.
- [115] Vacondio, S.; Varsano, D.; Ruini, A.; Ferretti, A. *J. Chem. Theory Comput.* **2022**, *18*, 3703–3717.
- [116] Luttinger, J. M.; Ward, J. C. *Phys. Rev.* **1960**, *118*, 1417–1427.
- [117] Müther, H.; Taigel, T.; Kuo, T. *Nucl. Phys. A* **1988**, *482*, 601–616.
- [118] Müther, H.; Skouras, L. *Phys. Lett. B* **1993**, *306*, 201–206.
- [119] Müther, H.; Skouras, L. *Nucl. Phys. A* **1993**, *555*, 541–562.
- [120] Müther, H.; Skouras, L. *Nucl. Phys. A* **1995**, *581*, 247–266.
- [121] Müther, H.; Polls, A.; Dickhoff, W. H. *Phys. Rev. C* **1995**, *51*, 3040–3051.
- [122] Dewulf, Y.; van Neck, D.; van Daele, L.; Waroquier, M. *Phys. Lett. B* **1997**, *396*, 7–14.
- [123] van Neck, D.; Peirs, K.; Waroquier, M. *J. Chem. Phys.* **2001**, *115*, 15–25.
- [124] Somà, V.; Barbieri, C.; Duguet, T. *Phys. Rev. C* **2014**, *89*, 024323.
- [125] Porro, A.; Somà, V.; Tichai, A.; Duguet, T. Importance truncation in non-perturbative many-body techniques. 2021.
- [126] van Neck, D.; Waroquier, M.; Ryckebusch, J. *Nucl. Phys. A* **1991**, *530*, 347–369.
- [127] van Neck, D.; Waroquier, M.; van der Sluys, V.; Heyde, K. *Nucl. Phys. A* **1993**, *563*, 1–20.
- [128] Shee, A.; Zgid, D. *J. Chem. Theory Comput.* **2019**, *15*, 6010–6024.
- [129] Schilders, W. *Mathematics in Industry*; Springer Berlin Heidelberg, 2008; pp 3–32.

- [130] Peng, B.; van Beeumen, R.; Williams-Young, D. B.; Kowalski, K.; Yang, C. *J. Chem. Theory Comput.* **2019**, *15*, 3185–3196.
- [131] Peng, B.; Panyala, A.; Kowalski, K.; Krishnamoorthy, S. *Comput. Phys. Commun.* **2021**, *265*, 108000.
- [132] Laughon, K.; Yu, J. M.; Zhu, T. *J. Phys. Chem. Lett.* **2022**, *13*, 9122–9128.
- [133] Vogt, M.; Zimmermann, R.; Needs, R. *J. Phys. Rev. B* **2004**, *69*.
- [134] Freericks, J. K.; Turkowski, V. *Phys. Rev. B* **2009**, *80*.
- [135] Freericks, J. K.; Turkowski, V.; Krishnamurthy, H. R.; Knap, M. *Phys. Rev. A* **2013**, *87*.
- [136] Rusakov, A. A.; Phillips, J. J.; Zgid, D. *J. Chem. Phys.* **2014**, *141*, 194105.
- [137] Stieltjes, T.-J. *Ann. Fac. Sci. Toulouse* **1894**, *8*, 1–122.
- [138] Derkach, V.; Kovalyov, I. *Methods Funct. Anal. Topol.* **2020**, *26*, 1–26.
- [139] Schmüdgen, K. *The Moment Problem*; Springer International Publishing, 2017.
- [140] Baym, G. *Phys. Rev.* **1962**, *127*, 1391–1401.
- [141] Dahlen, N. E.; van Leeuwen, R.; von Barth, U. *Phys. Rev. A* **2006**, *73*.
- [142] Galitskii, V. M.; Migdal, A. B. *J. Exptl. Theoret. Phys.* **1958**, *34*, 139.
- [143] Holleboom, L. J.; Snijders, J. G. *J. Chem. Phys.* **1990**, *93*, 5826–5837.
- [144] Bruneval, F. *J. Chem. Theory Comput.* **2019**, *15*, 4069–4078.
- [145] Loos, P.-F.; Romaniello, P.; Berger, J. A. *J. Chem. Theory Comput.* **2018**, *14*, 3071–3082.
- [146] Rayleigh, J.; Lindsay, R. *The Theory of Sound*; Dover Books on Physics Series v. 1; Dover Publications, 1945.
- [147] Møller, C.; Plesset, M. S. *Phys. Rev.* **1934**, *46*, 618–622.
- [148] Bartlett, R. J.; Silver, D. M. *Int. J. Quantum Chem.* **1947**, *8*, 271–276.
- [149] Binkley, J. S.; Pople, J. A. *Int. J. Quantum Chem.* **1975**, *9*, 229–236.
- [150] Grüneis, A.; Marsman, M.; Kresse, G. *J. Chem. Phys.* **2010**, *133*, 74107.
- [151] Doser, B.; Lambrecht, D. S.; Kussmann, J.; Ochsenfeld, C. *J. Chem. Phys.* **2009**, *130*, 64107.
- [152] Bozkaya, U. *J. Chem. Theory Comput.* **2014**, *10*, 2371–2378.
- [153] Baudin, P.; Ettenhuber, P.; Reine, S.; Kristensen, K.; Kjærgaard, T. *J. Chem. Phys.* **2016**, *144*, 54102.
- [154] Bozkaya, U. *J. Chem. Theory Comput.* **2019**, *15*, 4415–4429.
- [155] Pople, J. A.; Binkley, J. S.; Seeger, R. *Int. J. Quantum Chem.* **1976**, *10*, 1–19.

- [156] Raghavachari, K.; Pople, J. A. *Int. J. Quantum Chem.* **1978**, *14*, 91–100.
- [157] Raghavachari, K.; Frisch, M. J.; Pople, J. A. *J. Chem. Phys.* **1980**, *72*, 4244–4245.
- [158] Kucharski, S. A.; Bartlett, R. J. In *Fifth-Order Many-Body Perturbation Theory and Its Relationship to Various Coupled-Cluster Approaches*; Löwdin, P.-O., Ed.; Advances in Quantum Chemistry; Academic Press, 1986; Vol. 18; pp 281–344.
- [159] Kucharski, S. A.; Noga, J.; Bartlett, R. J. *J. Chem. Phys.* **1989**, *90*, 7282–7290.
- [160] Raghavachari, K.; Trucks, G. W.; Pople, J. A.; Head-Gordon, M. *Chem. Phys. Lett.* **1989**, *157*, 479–483.
- [161] Cremer, D.; He, Z. *J. Phys. Chem.* **1996**, *100*, 6173–6188.
- [162] He, Z.; Cremer, D. *Int. J. Quantum Chem.* **1996**, *59*, 15–29.
- [163] He, Z.; Cremer, D. *Int. J. Quantum Chem.* **1996**, *59*, 31–55.
- [164] He, Z.; Cremer, D. *Int. J. Quantum Chem.* **1996**, *59*, 57–69.
- [165] Stevenson, P. D. *Int. J. Mod. Phys. C* **2003**, *14*, 1135–1141.
- [166] Cremer, D. *Wiley Interdiscip. Rev. Comput. Mol. Sci.* **2011**, *1*, 509–530.
- [167] Raghavachari, K.; Trucks, G. W.; Pople, J. A.; Head-Gordon, M. *Chem. Phys. Lett.* **2013**, *589*, 37–40.
- [168] Kucharski, S. A.; Bartlett, R. J. *Chem. Phys. Lett.* **1995**, *237*, 264–272.
- [169] Olsen, J.; Christiansen, O.; Koch, H.; Jørgensen, P. *J. Chem. Phys.* **1996**, *105*, 5082–5090.
- [170] Leininger, M. L.; Allen, W. D.; Schaefer, H. F.; Sherrill, C. D. *J. Chem. Phys.* **2000**, *112*, 9213–9222.
- [171] Mukherjee, D. *Chem. Phys. Lett.* **1986**, *125*, 207–212.
- [172] Handy, N. C.; Knowles, P. J.; Somasundram, K. *Theor. Chim. Acta* **1985**, *68*, 87–100.
- [173] Gill, P. M.; Radom, L. *Chem. Phys. Lett.* **1986**, *132*, 16–22.
- [174] Christiansen, O.; Olsen, J.; Jørgensen, P.; Koch, H.; Malmqvist, P.-Å. *Chem. Phys. Lett.* **1996**, *261*, 369–378.
- [175] Olsen, J.; Jørgensen, P.; Helgaker, T.; Christiansen, O. *J. Chem. Phys.* **2000**, *112*, 9736–9748.
- [176] Larsen, H.; Halkier, A.; Olsen, J.; Jørgensen, P. *J. Chem. Phys.* **2000**, *112*, 1107–1112.
- [177] Sedlak, R.; Riley, K. E.; Řezáč, J.; Pitoňák, M.; Hobza, P. *ChemPhysChem* **2013**, *14*, 698–707.
- [178] Riley, K. E.; Řezáč, J.; Hobza, P. *Phys. Chem. Chem. Phys.* **2012**, *14*, 13187–13193.
- [179] Bozkaya, U.; Sherrill, C. D. *J. Chem. Phys.* **2014**, *141*, 204105.
- [180] Sun, J.-Q.; Bartlett, R. J. *J. Chem. Phys.* **1997**, *107*, 5058–5071.



- [181] Hirata, S.; Hermes, M. R.; Simons, J.; Ortiz, J. V. *J. Chem. Theory Comput.* **2015**, *11*, 1595–1606.
- [182] Hirata, S.; Doran, A. E.; Knowles, P. J.; Ortiz, J. V. *J. Chem. Phys.* **2017**, *147*, 044108.
- [183] Jørgensen, P. *Second Quantization-Based Methods in Quantum Chemistry*; Elsevier Science, 1981.
- [184] Linderberg, J.; Öhrn, Y. *Propagators in Quantum Chemistry*; 2004.
- [185] Banerjee, S.; Sokolov, A. Y. *J. Chem. Phys.* **2019**, *151*.
- [186] Schirmer, J.; Trofimov, A. B.; Stelter, G. *J. Chem. Phys.* **1998**, *109*, 4734–4744.
- [187] Schirmer, J.; Cederbaum, L. S.; Walter, O. *Phys. Rev. A* **1983**, *28*, 1237–1259.
- [188] von Niessen, W.; Schirmer, J.; Cederbaum, L. S. *Comput. Phys. Rep.* **1984**, *1*, 57–125.
- [189] Zakzhevskii, V. G. *Theor. Exp. Chem.* **1991**, *26*, 676–679.
- [190] Mertins, F.; Schirmer, J. *Phys. Rev. A* **1996**, *53*, 2140–2152.
- [191] Schirmer, J.; Trofimov, A. B. *J. Chem. Phys.* **2004**, *120*, 11449–11464.
- [192] Dempwolff, A. L.; Schneider, M.; Hodecker, M.; Dreuw, A. *J. Chem. Phys.* **2019**, *150*.
- [193] Dempwolff, A. L.; Paul, A. C.; Belogolova, A. M.; Trofimov, A. B.; Dreuw, A. *J. Chem. Phys.* **2020**, *152*.
- [194] Banerjee, S.; Sokolov, A. Y. *J. Chem. Phys.* **2021**, *154*, 074105.
- [195] Dempwolff, A. L.; Hodecker, M.; Dreuw, A. *J. Chem. Phys.* **2022**, *156*, 054114.
- [196] Jørgensen, P.; Oddershede, J.; Beebe, N. H. F. *J. Chem. Phys.* **1978**, *68*, 2527.
- [197] Trofimov, A. B.; Schirmer, J. *J. Phys. B* **1995**, *28*, 2299–2324.
- [198] Trofimov, A. B.; Stelter, G.; Schirmer, J. *J. Chem. Phys.* **1999**, *111*, 9982–9999.
- [199] Trofimov, A. B.; Stelter, G.; Schirmer, J. *J. Chem. Phys.* **2002**, *117*, 6402–6410.
- [200] Harbach, P. H. P.; Wormit, M.; Dreuw, A. *J. Chem. Phys.* **2014**, *141*, 064113.
- [201] Dreuw, A.; Wormit, M. *Wiley Interdiscip. Rev. Comput. Mol. Sci.* **2015**, *5*, 82–95.
- [202] Mester, D.; Nagy, P. R.; Kállay, M. *J. Chem. Phys.* **2018**, *148*.
- [203] Herbst, M. F.; Scheurer, M.; Fransson, T.; Rehn, D. R.; Dreuw, A. *Wiley Interdiscip. Rev. Comput. Mol. Sci.* **2020**, 1–16.
- [204] Leitner, J.; Dempwolff, A. L.; Dreuw, A. *J. Chem. Phys.* **2022**,
- [205] Banerjee, S.; Sokolov, A. Y. *J. Chem. Theory Comput.* **2022**, *18*, 5337–5348.
- [206] Trofimov, A. B.; Schirmer, J. *J. Chem. Phys.* **2005**, *123*, 144115.
- [207] Peirs, K.; van Neck, D.; Waroquier, M. *J. Chem. Phys.* **2002**, *117*, 4095–4105.

- [208] Phillips, J. J.; Zgid, D. *J. Chem. Phys.* **2014**, *140*, 241101.
- [209] Phillips, J. J.; Kananenka, A. A.; Zgid, D. *J. Chem. Phys.* **2015**, *142*, 194108.
- [210] Neuhauser, D.; Baer, R.; Zgid, D. **2016**, 1–5.
- [211] Neuhauser, D.; Baer, R.; Zgid, D. *J. Chem. Theory Comput.* **2017**, *13*, 5396–5403.
- [212] Rusakov, A. A.; Zgid, D. *J. Chem. Phys.* **2016**, *144*, 054106.
- [213] Barbieri, C.; Carbone, A. *Lecture Notes in Physics* **2017**, *936*, 571–644.
- [214] Barbieri, C.; Raimondi, F.; McIlroy, C. *J. Phys. Conf. Ser.* **2018**, *966*, 012015.
- [215] Stan, A.; Dahlen, N. E.; van Leeuwen, R. *J. Chem. Phys.* **2009**, *130*, 114105.
- [216] Kozik, E.; Ferrero, M.; Georges, A. *Phys. Rev. Lett.* **2015**, *114*.
- [217] Pickup, B.; Goscinski, O. *Mol. Phys.* **1973**, *26*, 1013–1035.
- [218] Cederbaum, L. S. *J. Phys. B* **1975**, *8*, 290–303.
- [219] Born, G.; Kurtz, H. A.; Öhrn, Y. *J. Chem. Phys.* **1978**, *68*, 74.
- [220] Kurtz, H. A.; Öhrn, Y. *J. Chem. Phys.* **1978**, *69*, 1162.
- [221] Öhrn, Y.; Born, G. *Advances in Quantum Chemistry*; Elsevier, 1981; pp 1–88.
- [222] Longo, R.; Champagne, B.; Öhrn, Y. *Theor. Chim. Acta* **1995**, *90*, 397–419.
- [223] Zakrzewski, V. G.; Ortiz, J. V. *Int. J. Quantum Chem.* **1995**, *53*, 583–590.
- [224] Ortiz, J. V. *Computational Chemistry: Reviews of Current Trends*; World Scientific, 1997; pp 1–61.
- [225] Ortiz, J. *Advances in Quantum Chemistry*; Elsevier, 1999; pp 33–52.
- [226] Simons, J. *Encyclopedia of Computational Chemistry*; John Wiley & Sons, Ltd, 2004.
- [227] Simons, J. *Collect. Czechoslov. Chem. Commun.* **2005**, *70*, 579–604.
- [228] Simons, J. *Response Theory and Molecular Properties (A Tribute to Jan Linderberg and Poul Jørgensen)*; Elsevier, 2005; pp 213–233.
- [229] Herman, M. F.; Freed, K. F.; Yeager, D. L. *Advances in Chemical Physics*; John Wiley & Sons, Inc., 2007; pp 1–69.
- [230] Cederbaum, L. S.; Domcke, W. *Advances in Chemical Physics*; John Wiley & Sons, Ltd, 1977; pp 205–344.
- [231] Flores-Moreno, R.; Melin, J.; Dolgounitcheva, O.; Zakrzewski, V. G.; Ortiz, J. V. *Int. J. Quantum Chem.* **2009**, *110*, 706–715.
- [232] Danovich, D. *Wiley Interdiscip. Rev. Comput. Mol. Sci.* **2011**, *1*, 377–387.
- [233] Corzo, H. H.; Ortiz, J. V. *Advances in Quantum Chemistry*; Elsevier, 2017; pp 267–298.

- [234] Grimme, S. *J. Chem. Phys.* **2003**, *118*, 9095–9102.
- [235] Jung, Y.; Lochan, R. C.; Dutoi, A. D.; Head-Gordon, M. *J. Chem. Phys.* **2004**, *121*, 9793–9802.
- [236] Romero, J.; Charry, J. A.; Nakai, H.; Reyes, A. *Chem. Phys. Lett.* **2014**, *591*, 82–87.
- [237] Lim, F.-H.; Nishida, M.; Hori, Y.; Ida, T.; Mizuno, M. *Chem. Phys. Lett.* **2017**, *678*, 159–166.
- [238] Śmiga, S.; Grabowski, I. *J. Chem. Theory Comput.* **2018**, *14*, 4780–4790.
- [239] Schirmer, J.; Cederbaum, L. S. *J. Phys. B* **1978**, *11*, 1889–1900.
- [240] Corzo, H. H.; Galano, A.; Dolgounitcheva, O.; Zakrzewski, V. G.; Ortiz, J. V. *J. Phys. Chem. A* **2015**, *119*, 8813–8821.
- [241] Ortiz, J. V. *J. Chem. Phys.* **1996**, *104*, 7599–7605.
- [242] Ferreira, A. M.; Seabra, G.; Dolgounitcheva, O.; Zakrzewski, V. G.; Ortiz, J. V. *Understanding Chemical Reactivity*; Kluwer Academic Publishers, 2001; pp 131–160.
- [243] Ortiz, J. V. *Int. J. Quantum Chem.* **2005**, *105*, 803–808.
- [244] Ortiz, J. V. *J. Chem. Phys.* **1998**, *108*, 1008–1014.
- [245] Chiles, R. A.; Dykstra, C. E. *J. Chem. Phys.* **1981**, *74*, 4544–4556.
- [246] Sherrill, C. D.; Krylov, A. I.; Byrd, E. F.; Head-Gordon, M. *J. Chem. Phys.* **1998**, *109*, 4171–4181.
- [247] Dolgounitcheva, O.; Díaz-Tinoco, M.; Zakrzewski, V. G.; Richard, R. M.; Marom, N.; Sherrill, C. D.; Ortiz, J. V. *J. Chem. Theory Comput.* **2016**, *12*, 627–637.
- [248] Čížek, J. *J. Chem. Phys.* **1966**, *45*, 4256–4266.
- [249] Čížek, J. *Advances in Chemical Physics*; John Wiley & Sons, Ltd, 1969; pp 35–89.
- [250] Čížek, J.; Paldus, J. *Int. J. Quantum Chem.* **1971**, *5*, 359–379.
- [251] Paldus, J.; Čížek, J.; Shavitt, I. *Phys. Rev. A* **1972**, *5*, 50–67.
- [252] Purvis, G. D.; Bartlett, R. J. *J. Chem. Phys.* **1982**, *76*, 1910–1918.
- [253] Crawford, T. D.; Schaefer III, H. F. *Reviews in Computational Chemistry*; John Wiley & Sons, Ltd, 2000; pp 33–136.
- [254] Hirata, S.; Podeszwa, R.; Tobita, M.; Bartlett, R. J. *J. Chem. Phys.* **2004**, *120*, 2581–2592.
- [255] Bartlett, R. J.; Musiał, M. *Rev. Mod. Phys.* **2007**, *79*, 291–352.
- [256] Stanton, J. F.; Bartlett, R. J. *J. Chem. Phys.* **1993**, *98*, 7029–7039.
- [257] Pople, J. A.; Head-Gordon, M.; Raghavachari, K. *J. Chem. Phys.* **1987**, *87*, 5968–5975.
- [258] Noga, J.; Bartlett, R. J. *J. Chem. Phys.* **1987**, *86*, 7041–7050.
- [259] Christiansen, O.; Koch, H.; Jørgensen, P. *Chem. Phys. Lett.* **1995**, *243*, 409–418.

- [260] Koch, H.; Christiansen, O.; Jørgensen, P.; de Merás, A. M. S.; Helgaker, T. *J. Chem. Phys.* **1997**, *106*, 1808–1818.
- [261] Stanton, J. F. *Chem. Phys. Lett.* **1997**, *281*, 130–134.
- [262] Krylov, A. I.; Sherrill, C. D.; Byrd, E. F. C.; Head-Gordon, M. *J. Chem. Phys.* **1998**, *109*, 10669–10678.
- [263] Piecuch, P.; Kucharski, S. A.; Bartlett, R. J. *J. Chem. Phys.* **1999**, *110*, 6103–6122.
- [264] Kowalski, K.; Piecuch, P. *J. Chem. Phys.* **2000**, *113*, 18–35.
- [265] van Voorhis, T.; Head-Gordon, M. *J. Chem. Phys.* **2001**, *115*, 5033–5040.
- [266] Stanton, J. F.; Gauss, J. *J. Chem. Phys.* **1994**, *101*, 8938–8944.
- [267] Nooijen, M.; Bartlett, R. J. *J. Chem. Phys.* **1995**, *102*, 3629–3647.
- [268] Hirata, S. *J. Chem. Phys.* **2004**, *121*, 51–59.
- [269] Matthews, D. A.; Stanton, J. F. *J. Chem. Phys.* **2016**, *145*, 124102.
- [270] Lange, M. F.; Berkelbach, T. C. *J. Chem. Theory Comput.* **2018**, *14*, 4224–4236.
- [271] Nooijen, M.; Snijders, J. G. *Int. J. Quantum Chem.* **1992**, *44*, 55–83.
- [272] Nooijen, M.; Snijders, J. G. *Int. J. Quantum Chem.* **1993**, *48*, 15–48.
- [273] Nooijen, M.; Snijders, J. G. *J. Chem. Phys.* **1995**, *102*, 1681–1688.
- [274] Bhaskaran-Nair, K.; Kowalski, K.; Shelton, W. A. *J. Chem. Phys.* **2016**, *144*, 144101.
- [275] Peng, B.; Kowalski, K. *Phys. Rev. A* **2016**, *94*, 1–10.
- [276] Peng, B.; Kowalski, K. *J. Chem. Phys.* **2018**, *149*.
- [277] Furukawa, Y.; Kosugi, T.; Nishi, H.; Matsushita, Y.-i. *J. Chem. Phys.* **2018**, *148*, 204109.
- [278] Zhu, T.; Jiménez-Hoyos, C. A.; McClain, J.; Berkelbach, T. C.; Chan, G. K.-L. *Phys. Rev. B* **2019**, *100*, 115154.
- [279] Bauman, N. P.; Peng, B.; Kowalski, K. *Mol. Phys.* **2020**, 1–8.
- [280] Peng, B.; Bauman, N. P.; Gulania, S.; Kowalski, K. *Annual Reports in Computational Chemistry*; 2021; Vol. 17; pp 23–53.
- [281] Shee, A.; Yeh, C.-N.; Zgid, D. *J. Chem. Theory Comput.* **2022**, *18*, 664–676.
- [282] Shee, A.; Yeh, C.-N.; Peng, B.; Kowalski, K.; Zgid, D. Triple excitations in Green’s function coupled cluster solver for studies of strongly correlated systems in the framework of self-energy embedding theory. 2022; <https://arxiv.org/abs/2211.12680>.
- [283] Hedin, L. *Phys. Rev.* **1965**, *139*, A796–A823.

- [284] Hedin, L.; Lundqvist, S. *Solid State Physics*; Elsevier, 1970; pp 1–181.
- [285] Hybertsen, M. S.; Louie, S. G. *Phys. Rev. Lett.* **1985**, *55*, 1418–1421.
- [286] Aryasetiawan, F.; Gunnarsson, O. *Rep. Prog. Phys.* **1998**, *61*, 237–312.
- [287] Hedin, L. *J. Phys. Condens. Matter* **1999**, *11*, R489–R528.
- [288] Aulbur, W. G.; Jönsson, L.; Wilkins, J. W. *Solid State Physics*; Elsevier, 2000; pp 1–218.
- [289] Friedrich, C.; Schindlmayr, A. *Computing* **2006**, *31*, 335–355.
- [290] Kutepov, A.; Savrasov, S. Y.; Kotliar, G. *Phys. Rev. B* **2009**, *80*, 1–4.
- [291] Ke, S. H. *Phys. Rev. B* **2011**, *84*, 1–6.
- [292] Bruneval, F. *J. Chem. Phys.* **2012**, *136*.
- [293] van Setten, M. J.; Weigend, F.; Evers, F. *J. Chem. Theory Comput.* **2013**, *9*, 232–246.
- [294] van Setten, M. J.; Caruso, F.; Sharifzadeh, S.; Ren, X.; Scheffler, M.; Liu, F.; Lischner, J.; Lin, L.; Deslippe, J. R.; Louie, S. G.; Yang, C.; Weigend, F.; Neaton, J. B.; Evers, F.; Rinke, P. *J. Chem. Theory Comput.* **2015**, *11*, 5665–5687.
- [295] Reining, L. *Wiley Interdiscip. Rev. Comput. Mol. Sci.* **2017**, *8*.
- [296] Golze, D.; Dvorak, M.; Rinke, P. *Front. Chem.* **2019**, *7*.
- [297] Langreth, D. C.; Perdew, J. P. *Phys. Rev. B* **1977**, *15*, 2884–2901.
- [298] Chong, D. P. *Recent Advances in Density Functional Methods*; World Scientific, 1995.
- [299] Heßelmann, A.; Görling, A. *Mol. Phys.* **2010**, *108*, 359–372.
- [300] Eshuis, H.; Bates, J. E.; Furche, F. *Theor. Chem. Acc.* **2012**, *131*.
- [301] Ren, X.; Rinke, P.; Joas, C.; Scheffler, M. *J. Mater. Sci.* **2012**, *47*, 7447–7471.
- [302] Hirata, S.; Head-Gordon, M. *Chem. Phys. Lett.* **1999**, *314*, 291–299.
- [303] Furche, F. *J. Chem. Phys.* **2008**, *129*, 114105.
- [304] Scuseria, G. E.; Henderson, T. M.; Sorensen, D. C. *J. Chem. Phys.* **2008**, *129*, 231101.
- [305] Henderson, T. M.; Scuseria, G. E. *Mol. Phys.* **2010**, *108*, 2511–2517.
- [306] Quintero-Monsebaiz, R.; Monino, E.; Marie, A.; Loos, P.-F. *J. Chem. Phys.* **2022**,
- [307] Furche, F. *Phys. Rev. B* **2001**, *64*.
- [308] Seeger, R.; Pople, J. A. *J. Chem. Phys.* **1977**, *66*, 3045–3050.
- [309] Grüneis, A.; Marsman, M.; Harl, J.; Schimka, L.; Kresse, G. *J. Chem. Phys.* **2009**, *131*, 154115.

- [310] Paier, J.; Janesko, B. G.; Henderson, T. M.; Scuseria, G. E.; Grüneis, A.; Kresse, G. *J. Chem. Phys.* **2010**, *132*, 094103.
- [311] Ren, X.; Marom, N.; Caruso, F.; Scheffler, M.; Rinke, P. *Phys. Rev. B* **2015**, *92*.
- [312] Bintrim, S. J.; Berkelbach, T. C. *J. Chem. Phys.* **2021**, *154*, 041101.
- [313] Foerster, D.; Koval, P.; Snchez-Portal, D. *J. Chem. Phys.* **2011**, *135*, 1–19.
- [314] Bruneval, F.; Marques, M. A. L. *J. Chem. Theory Comput.* **2013**, *9*, 324–329.
- [315] Liu, P.; Kaltak, M.; Klimeš, J. c. v.; Kresse, G. *Phys. Rev. B* **2016**, *94*, 165109.
- [316] Knight, J. W.; Wang, X.; Gallandi, L.; Dolgounitcheva, O.; Ren, X.; Ortiz, J. V.; Rinke, P.; Körzdörfer, T.; Marom, N. *J. Chem. Theory Comput.* **2016**, *12*, 615–626.
- [317] Maggio, E.; Liu, P.; van Setten, M. J.; Kresse, G. *J. Chem. Theory Comput.* **2017**, *13*, 635–648.
- [318] Bruneval, F.; Dattani, N.; van Setten, M. J. *Front. Chem.* **2021**, *9*.
- [319] von Barth, U.; Holm, B. *Phys. Rev. B* **1996**, *54*, 8411–8419.
- [320] Holm, B.; von Barth, U. *Phys. Rev. B* **1998**, *57*, 2108–2117.
- [321] Schöne, W.-D.; Eguiluz, A. G. *Phys. Rev. Lett.* **1998**, *81*, 1662–1665.
- [322] García-González, P.; Godby, R. W. *Phys. Rev. B* **2001**, *63*.
- [323] Faleev, S. V.; van Schilfgaarde, M.; Kotani, T. *Phys. Rev. Lett.* **2004**, *93*, 12–15.
- [324] van Schilfgaarde, M.; Kotani, T.; Faleev, S. *Phys. Rev. Lett.* **2006**, *96*, 226402.
- [325] Stan, A.; Dahlen, N. E.; van Leeuwen, R. *Europhys. Lett.* **2006**, *76*, 298–304.
- [326] Kotani, T.; van Schilfgaarde, M.; Faleev, S. V. *Phys. Rev. B* **2007**, *76*, 1–24.
- [327] Shishkin, M.; Kresse, G. *Phys. Rev. B* **2007**, *75*.
- [328] Caruso, F.; Rinke, P.; Ren, X.; Scheffler, M.; Rubio, A. *Phys. Rev. B* **2012**, *86*, 81102.
- [329] Bruneval, F.; Rangel, T.; Hamed, S. M.; Shao, M.; Yang, C.; Neaton, J. B. *Comput. Phys. Commun.* **2016**, *208*, 149–161.
- [330] Kaplan, F.; Harding, M. E.; Seiler, C.; Weigend, F.; Evers, F.; van Setten, M. J. *J. Chem. Theory Comput.* **2016**, *12*, 2528–2541.
- [331] Jin, Y.; Su, N. Q.; Yang, W. *J. Phys. Chem. Lett.* **2019**, *10*, 447–452.
- [332] Duchemin, I.; Blase, X. *J. Chem. Theory Comput.* **2020**, *16*, 1742–1756.
- [333] Duchemin, I.; Blase, X. *J. Chem. Theory Comput.* **2021**, *17*, 2383–2393.
- [334] Knowles, P. J.; Handy, N. C. *Chem. Phys. Lett.* **1984**, *111*, 315–321.
- [335] Booth, G. H.; Thom, A. J.; Alavi, A. *J. Chem. Phys.* **2009**, *131*, 54106.

- [336] Booth, G. H.; Grüneis, A.; Kresse, G.; Alavi, A. *Nature* **2013**, *493*, 365–370.
- [337] Li, J.; Otten, M.; Holmes, A. A.; Sharma, S.; Umrigar, C. J. *J. Chem. Phys.* **2018**, *149*, 214110.
- [338] Sriluckshmy, P. V.; Nusspickel, M.; Fertitta, E.; Booth, G. H. *Phys. Rev. B* **2021**, *103*, 085131.
- [339] Backhouse, O. J.; Booth, G. H. *J. Chem. Theory Comput.* **2022**, *18*, 6622–6636.
- [340] Arnoldi, W. E. *Q. Appl. Math.* **1951**, *9*, 17–29.
- [341] Iguchi, H.; Natori, M.; Imai, H. *Reorthogonalization in the Block Lanczos Algorithm*; 1992.
- [342] Cullum, J.; Donath, W. A block Lanczos algorithm for computing the  $q$  algebraically largest eigenvalues and a corresponding eigenspace of large, sparse, real symmetric matrices. 1974 IEEE Conference on Decision and Control including the 13th Symposium on Adaptive Processes. 1974.
- [343] Golub, G.; Underwood, R. *Mathematical Software*; Elsevier, 1977; pp 361–377.
- [344] Saad, Y. *SIAM J. Numer. Anal.* **1980**, *17*, 687–706.
- [345] Bai, Z.; Day, D.; Ye, Q. *SIAM J. Matrix Anal. Appl.* **1999**, *20*, 1060–1082.
- [346] Ruhe, A. *Math. Comput.* **1979**, *33*, 680–687.
- [347] Bai, Z.; Freund, R. W. *SIAM J. Sci. Comput.* **2001**, *23*, 542–562.
- [348] Fukaya, T.; Nakatsukasa, Y.; Yanagisawa, Y.; Yamamoto, Y. CholeskyQR2: A Simple and Communication-Avoiding Algorithm for Computing a Tall-Skinny QR Factorization on a Large-Scale Parallel System. 2014 5th Workshop on Latest Advances in Scalable Algorithms for Large-Scale Systems. 2014; pp 31–38.
- [349] Fukaya, T.; Kannan, R.; Nakatsukasa, Y.; Yamamoto, Y.; Yanagisawa, Y. *SIAM J. Sci. Comput.* **2020**, *42*, A477–a503.
- [350] Fertitta, E.; Booth, G. H. *Phys. Rev. B* **2018**, *98*, 235132.
- [351] Fertitta, E.; Booth, G. H. *J. Chem. Phys.* **2019**, *151*, 014115.
- [352] Kuijlaars, A. B. J. *SIAM J. Matrix Anal. Appl.* **2000**, *22*, 306–321.
- [353] Sharma, M.; Ahsan, M. A. H. A Davidson-Lanczos iteration method for computation of continued-fraction expansion of the Green’s function at very low temperatures: Applications to the dynamical mean field theory. 2014; <https://arxiv.org/abs/1409.3374>.
- [354] Hammerschmidt, T.; Seiser, B.; Ford, M.; Ladines, A.; Schreiber, S.; Wang, N.; Jenke, J.; Lysogorskiy, Y.; Teijeiro, C.; Mrovec, M.; Cak, M.; Margine, E.; Pettifor, D.; Drautz, R. *Comput. Phys. Commun.* **2019**, *235*, 221–233.
- [355] Dong, X.; Gull, E.; Strand, H. U. R. *Phys. Rev. B* **2022**, *106*.
- [356] van Leeuwen, R.; Dahlen, N. E.; Stan, A. *Phys. Rev. B* **2006**, *74*.
- [357] Pokhilko, P.; Zgid, D. *J. Chem. Phys.* **2021**, *155*, 024101.

- [358] Pulay, P. *Chem. Phys. Lett.* **1980**, *73*, 393–398.
- [359] Pulay, P. *J. Comput. Chem.* **1982**, *3*, 556–560.
- [360] Buth, C.; Birkenheuer, U.; Albrecht, M.; Fulde, P. *Phys. Rev. B* **2005**, *72*, 1–18.
- [361] Buth, C. *J. Chem. Phys.* **2006**, *125*.
- [362] McClain, J.; Sun, Q.; Chan, G. K.-L.; Berkelbach, T. C. *J. Chem. Theory Comput.* **2017**, *13*, 1209–1218.
- [363] Wang, X.; Berkelbach, T. C. *J. Chem. Theory Comput.* **2020**, *16*, 3095–3103.
- [364] Lange, M. F.; Berkelbach, T. C. *J. Chem. Phys.* **2021**, *155*, 081101.
- [365] Stan, A.; Romaniello, P.; Rigamonti, S.; Reining, L.; Berger, J. A. *New J. Phys.* **2015**, *17*, 093045.
- [366] Schäfer, T.; Ciuchi, S.; Wallerberger, M.; Thunström, P.; Gunnarsson, O.; Sangiovanni, G.; Rohringer, G.; Toschi, A. *Phys. Rev. B* **2016**, *94*.
- [367] Rossi, R.; Werner, F. *J. Phys. A* **2015**, *48*, 485202.
- [368] Gunnarsson, O.; Rohringer, G.; Schäfer, T.; Sangiovanni, G.; Toschi, A. *Phys. Rev. Lett.* **2017**, *119*.
- [369] Tarantino, W.; Romaniello, P.; Berger, J. A.; Reining, L. *Phys. Rev. B* **2017**, *96*.
- [370] VÉril, M.; Romaniello, P.; Berger, J. A.; Loos, P.-F. *J. Chem. Theory Comput.* **2018**, *14*, 5220–5228.
- [371] Reitner, M.; Chalupa, P.; Re, L. D.; Springer, D.; Ciuchi, S.; Sangiovanni, G.; Toschi, A. *Phys. Rev. Lett.* **2020**, *125*.
- [372] Berger, J. A.; Loos, P.-F.; Romaniello, P. *J. Chem. Theory Comput.* **2021**, *17*, 191–200.
- [373] Iskakov, S.; Gull, E. *Phys. Rev. B* **2022**, *105*.
- [374] Monino, E.; Loos, P.-F. *J. Chem. Phys.* **2022**, *156*, 231101.
- [375] Scott, C. J. C.; Booth, G. H. *Phys. Rev. B* **2021**, *104*, 245114.
- [376] Joyner, D.; Čertík, O.; Meurer, A.; Granger, B. E. *ACM Commun. Comput. Algebraic* **2012**, *45*, 225–234.
- [377] Meurer, A.; Smith, C. P.; Paprocki, M.; Čertík, O.; Kirpichev, S. B.; Rocklin, M.; Kumar, A.; Ivanov, S.; Moore, J. K.; Singh, S.; Rathnayake, T.; Vig, S.; Granger, B. E.; Muller, R. P.; Bonazzi, F.; Gupta, H.; Vats, S.; Johansson, F.; Pedregosa, F.; Curry, M. J.; Terrel, A. R.; Roučka, Š.; Saboo, A.; Fernando, I.; Kulal, S.; Cimrman, R.; Scopatz, A. *PeerJ Comput. Sci.* **2017**, *3*, e103.
- [378] White, A. F.; Gao, Y.; Minnich, A. J.; Chan, G. K.-L. *J. Chem. Phys.* **2020**, *153*, 224112.
- [379] Rubin, N. C.; DePrince, A. E. *Mol. Phys.* **2021**, *119*.
- [380] Evangelista, F. A. *J. Chem. Phys.* **2022**, *157*, 064111.



- [381] Backhouse, O. J.; Scott, C. J. C.; Booth, G. H. **ebcc**: Coupled cluster models for both purely electronic and coupled electron-boson models, with a focus on generality and model extensibility. <https://github.com/BoothGroup/ebcc>, 2022.
- [382] Thomas, S.; Hampe, F.; Stopkowicz, S.; Gauss, J. *Mol. Phys.* **2021**, *119*, e1968056.
- [383] Karton, A.; Daon, S.; Martin, J. M. *Chem. Phys. Lett.* **2011**, *510*, 165–178.
- [384] Goerigk, L.; Hansen, A.; Bauer, C.; Ehrlich, S.; Najibi, A.; Grimme, S. *Phys. Chem. Chem. Phys.* **2017**, *19*, 32184–32215.
- [385] Backhouse, O. J. **gmtkn**: GMTKN test sets in python. <https://github.com/obackhouse/gmtkn>, 2021.
- [386] Caruso, F.; Dauth, M.; van Setten, M. J.; Rinke, P. *J. Chem. Theory Comput.* **2016**, *12*, 5076–5087.
- [387] Cedérbaum, L.; Hohlneicher, G.; von Niessen, W. *Chem. Phys. Lett.* **1973**, *18*, 503–508.
- [388] Hättig, C. *Phys. Chem. Chem. Phys.* **2005**, *7*, 59–66.
- [389] Weigend, F.; Ahlrichs, R. *Phys. Chem. Chem. Phys.* **2005**, *7*, 3297.
- [390] Andrae, D.; Häußermann, U.; Dolg, M.; Stoll, H.; Preuß, H. *Theor. Chim. Acta* **1990**, *77*, 123–141.
- [391] Kaupp, M.; v. R. Schleyer, P.; Stoll, H.; Preuß, H. *J. Chem. Phys.* **1991**, *94*, 1360–1366.
- [392] Leininger, T.; Nicklass, A.; Stoll, H.; Dolg, M.; Schwerdtfeger, P. *J. Chem. Phys.* **1996**, *105*, 1052–1059.
- [393] Metz, B.; Stoll, H.; Dolg, M. *J. Chem. Phys.* **2000**, *113*, 2563–2569.
- [394] Peterson, K. A.; Figgen, D.; Goll, E.; Stoll, H.; Dolg, M. *J. Chem. Phys.* **2003**, *119*, 11113–11123.
- [395] Krause, K.; Harding, M. E.; Klopper, W. *Mol. Phys.* **2015**, *113*, 1952–1960.
- [396] Group, Q. A. C. R. *Chim. Med. J.* **1979**, *92*, 811–816.
- [397] White, N. J.; Hien, T. T.; Nosten, F. H. *Trends Parasitol.* **2015**, *31*, 607–610.
- [398] Novak, I.; Kovač, B. *J. Org. Chem.* **2003**, *68*, 5777–5779.
- [399] Galasso, V.; Kovač, B.; Modelli, A. *Chem. Phys.* **2007**, *335*, 141–154.
- [400] Groom, C. R.; Bruno, I. J.; Lightfoot, M. P.; Ward, S. C. *Acta Crystallogr. B: Struct. Sci. Cryst. Eng. Mater.* **2016**, *72*, 171–179.
- [401] Riplinger, C.; Neese, F. *J. Chem. Phys.* **2013**, *138*, 034106.
- [402] Riplinger, C.; Pinski, P.; Becker, U.; Valeev, E. F.; Neese, F. *J. Chem. Phys.* **2016**, *144*, 024109.
- [403] Borlido, P.; Aull, T.; Huran, A. W.; Tran, F.; Marques, M. A. L.; Botti, S. *J. Chem. Theory Comput.* **2019**, *15*, 5069–5079.

- [404] Kühne, T. D.; Iannuzzi, M.; Ben, M. D.; Rybkin, V. V.; Seewald, P.; Stein, F.; Laino, T.; Khaliullin, R. Z.; Schütt, O.; Schiffmann, F.; Golze, D.; Wilhelm, J.; Chulkov, S.; Bani-Hashemian, M. H.; Weber, V.; Borštnik, U.; Taillefumier, M.; Jakobovits, A. S.; Lazzaro, A.; Pabst, H.; Müller, T.; Schade, R.; Guidon, M.; Andermatt, S.; Holmberg, N.; Schenter, G. K.; Hehn, A.; Bussy, A.; Belleflamme, F.; Tabacchi, G.; Glöß, A.; Lass, M.; Bethune, I.; Mundy, C. J.; Plessl, C.; Watkins, M.; VandeVondele, J.; Krack, M.; Hutter, J. *J. Chem. Phys.* **2020**, *152*, 194103.
- [405] Perdew, J. P.; Ernzerhof, M.; Burke, K. *J. Chem. Phys.* **1996**, *105*, 9982–9985.
- [406] Perdew, J. P.; Levy, M. *Phys. Rev. Lett.* **1983**, *51*, 1884–1887.
- [407] Perdew, J. P.; Zunger, A. *Phys. Rev. B* **1981**, *23*, 5048–5079.
- [408] Sham, L. J.; Schlüter, M. *Phys. Rev. Lett.* **1983**, *51*, 1888–1891.
- [409] Mori-Sánchez, P.; Cohen, A. J.; Yang, W. *Phys. Rev. Lett.* **2008**, *100*.
- [410] Crowley, J. M.; Tahir-Kheli, J.; Goddard, W. A. *J. Phys. Chem. Lett.* **2016**, *7*, 1198–1203.
- [411] Madelung, O. *Semiconductors: Data Handbook*; Springer Berlin Heidelberg, 2004.
- [412] Kosugi, T.; Matsushita, Y.-i. *J. Chem. Phys.* **2019**, *150*, 114104.
- [413] Kovács, D. P.; van der Oord, C.; Kucera, J.; Allen, A. E. A.; Cole, D. J.; Ortner, C.; Csányi, G. *J. Chem. Theory Comput.* **2021**, *17*, 7696–7711.
- [414] Zhang, L.; Onat, B.; Dusson, G.; McSloy, A.; Anand, G.; Maurer, R. J.; Ortner, C.; Kermode, J. R. *Npj Comput. Mater.* **2022**, *8*.
- [415] Rath, Y.; Booth, G. H. *Phys. Rev. Res.* **2022**, *4*.
- [416] Sakurai, R.; Mizukami, W.; Shinaoka, H. *Phys. Rev. Res.* **2022**, *4*.
- [417] Lan, T. N.; Kananenka, A. A.; Zgid, D. *J. Chem. Phys.* **2015**, *143*, 241102.
- [418] Lan, T. N.; Zgid, D. *J. Phys. Chem. Lett.* **2017**, *8*, 2200–2205.
- [419] Lan, T. N.; Shee, A.; Li, J.; Gull, E.; Zgid, D. *Phys. Rev. B* **2017**, *96*.
- [420] Tran, L. N.; Isakov, S.; Zgid, D. *J. Phys. Chem. Lett.* **2018**, *9*, 4444–4450.
- [421] Rusakov, A. A.; Isakov, S.; Tran, L. N.; Zgid, D. *J. Chem. Theory Comput.* **2018**, *15*, 229–240.
- [422] Isakov, S.; Yeh, C.-N.; Gull, E.; Zgid, D. *Phys. Rev. B* **2020**, *102*.
- [423] Yeh, C.-N.; Isakov, S.; Zgid, D.; Gull, E. *Phys. Rev. B* **2021**, *103*.
- [424] Yeh, C.-N.; Shee, A.; Isakov, S.; Zgid, D. *Phys. Rev. B* **2021**, *103*.
- [425] Nusspickel, M.; Booth, G. H. *Phys. Rev. B* **2020**, *102*.
- [426] Nusspickel, M.; Booth, G. H. *Phys. Rev. X* **2022**, *12*.

- [427] Nusspickel, M.; Ibrahim, B.; Booth, G. H. On the effective reconstruction of expectation values from ab initio quantum embedding. 2022; <https://arxiv.org/abs/2210.14561>.
- [428] Nusspickel, M.; Scott, C. J. C.; Backhouse, O. J.; Ibrahim, B.; Santana-Bonilla, A.; Booth, G. H. **Vayesta**: A Python package for wave function-based quantum embedding. <https://github.com/BoothGroup/Vayesta>, 2022.
- [429] Condon, E. U. *Phys. Rev.* **1930**, *36*, 1121–1133.